# Interphase Formation During Curing Simulated by Reactive Molecular Dynamics

TECHNISCHE UNIVERSITÄT DARMSTADT

Vom Fachbereich Chemie
der Technischen Universität Darmstadt

zur Erlangung des akademischen Grades eines
Doktor rerum naturalium (Dr. rer. nat.)

genehmigte
**Dissertation**

vorgelegt von

**Karim Frédéric Farah, M.Sc of Physics**

aus Dakar, Sénégal

| | |
|---|---|
| Referent: | Prof. Dr. Florian Müller-Plathe |
| Korreferent: | Prof. Dr. Nico Van der Vegt |
| Tag der Einreichung: | |
| Tag der mündliche Prüfung: | |

Darmstadt 2011

**D 17**

# Summary

The present PhD thesis is part of a six year project initiated to tackle the issue of interphase formation in hybrid materials characterized by polymer-solid contacts. Interphases are regions "near" the solid surface boundaries where the polymer properties are modified in comparison to more distant regions. Experimental investigations on the nature and length scales of interphases have been hampered by the challenging task of setting up apparatus that spatially resolve polymer properties. Thus, unresolved questions on the role of interphases in polymer-based hybrid materials still remain. While a broad class of polymer-solid surface systems is currently being investigated in the framework of this six year project, our task has been to setup a simulation tool to tackle the question of interphase formation during curing. The final goal of the project is to simulate experimentally relevant polymer-solid systems. The present PhD thesis deals with the first three years of the project devoted to the development of the simulation tool, to the investigation of interphase formation at a generic level and to the search of suitable methods to develop interaction potentials to model experimental systems.

Curing denotes the formation of a polymer network from a reactive system which consists of components of lower molecular weight. It is an important class of reactions as many technical adhesives such as epoxy polymers are formulated as reactive liquids of monomers and curing agents. The polymer adhesives are generated from the reactive liquids in the presence of the adherend surfaces under specific thermodynamic conditions. Thus, a suitable modelling tool should allow the dynamics and chemical reactions occurring in the systems to be investigated under the desired thermodynamic conditions. These requirements can be satisfied by the use of Reactive Molecular Dynamics methods (RMD) reviewed in the first chapter of the thesis. The time scale accessible to atomistic RMD simulations is in some cases not sufficient to observe reactive events. At a coarser level, reactive simulations allow the treatment of bigger systems using simplified reaction schemes. Currently, the formation of an interphase during curing can not be simulated at the atomistic level in a reasonable amount of time. Thus, our systems are described at a coarser level with a simplified reaction scheme. Each monomer and polymer repeat unit is a coarse-grained (CG) bead that is formed by merging several atoms into "super-units".

In the second chapter we present our RMD approach. The possibility to perform reactive simulations with material-specific CG potentials has been exemplified by growing polystyrene chains from ethylbenzene as a model of styrene monomers. *Iterative Boltzmann Inversion* (IBI) [Reith, D.; Pütz, M.; Müller-Plathe, F.; *J. Comput. Chem.* **2003**, *24*, 1624.] has been employed to develop these potentials. Many properties of the samples grown with the RMD approach have been compared to the

results of equilibrium molecular dynamics simulations on identical polymer samples. An agreement between RMD-based and equilibrium simulation results has been found. Our RMD algorithm is based on alternating between bond formation steps driven by a reaction cutoff parameter and diffusion periods defined by a delay time parameter. We have performed a number of simulations varying the RMD parameters to understand their role and to gain insight into polymerization processes. We have correlated the final degree of polymerization distributions to the reaction conditions. Our reactive scheme is inspired by a RMD model proposed approximately ten years ago, which was however not material-specific [Akkermans, R. L. C.; Tøxvaerd, S.; Briels, W. J.; *J. Chem. Phys.* **1998,** *109*, 2929.].

The third chapter deals with the issue of material-specific force-fields for the simulation of experimental adhesive systems. From the investigations of the first chapter, IBI appeared as a suitable method to obtain material-specific potentials. To understand the challenges involved in developing such force-fields we have investigated the temperature transferability of IBI potentials optimized for liquid hexane. Temperature transferability is the capability of a CG force field to describe the system at a temperature far away from where it has been parameterized. This study has been a simplified way to gain experience on transferability issues of CG potentials before tackling the complex case of adhesive systems and surfaces. In this study we have also experienced the use of scaling factors that are currently a rather common solution to generate CG potentials suitable for different thermodynamic states and we have developed a novel, more robust scheme.

The fourth chapter presents generic simulations of curing processes in the presence of idealized surfaces. Here, the reactive liquid mixtures are first equilibrated in the presence of the surfaces prior to the curing process. The constituents of the reactive liquids are bifunctional beads and tetrafunctional curing agents. The surface interactions with the different constituents are tunable. In this way, preferential adsorption at the surfaces of one of the constituents can be promoted. In fact, the purpose was to investigate the impact of surface-induced segregation on interphase formation. From the RMD simulations it appears that densities and average bond orientation profiles are not affected by the segregation processes. In fact, the perturbations of these two properties remain similar with or without preferential surface interactions. In contrast, properties which depend on the spatial distribution of the curing species such as the average length of the polymer segments between two branching points (i.e. curing agents with more than two bonds) are affected by segregation processes. In fact, the average length of the polymer segments increases with increasing distance from the surfaces for a preferential adsorption of the curing agents. The opposite scenario is observed for a preferential adsorption of the bifunctional monomers. In the absence of segregation processes, the average length of polymer segments is rather constant in the polymer samples.

The fifth chapter summarizes some of the future steps in connection with the simulations of interphase formation. The possibility to extend the present RMD tool to simulate other reactive processes such as the growth of grafted polymer brushes is briefly discussed.

.

# Zusammenfassung

Die vorliegende Dissertation wurde im Rahmen eines sechs Jahre dauernden Projektes über die Ausbildung von Grenzflächen in Hybrid-Materialien mit Polymer-Festkörper-Kontakten durchgeführt. Als Grenzflächen bezeichnet man die Region nahe am Festkörper, in der sich Polymer-Eigenschaften von denen unterscheiden, die in größeren Entfernungen zur Oberfläche realisiert sind. Experimentelle Untersuchungen über die Natur und Ausdehnung dieser Grenzflächen werden durch technische Probleme, Polymer-Eigenschaften räumlich aufzulösen, erschwert. Dies hat dazu geführt, dass der Einfluss von Grenzflächen in Hybrid-Materialien auf Polymer-Basis nur ungenügend verstanden ist. Während im Rahmen des sechsjährigen Projektes viele Polymer-Festkörper-Systeme untersucht wurden/werden, bestand unsere Aufgabe in der Entwicklung eines Simulations-Verfahrens, mit dem sich die Ausbildung von Grenzflächen während des Aushärtens beschreiben lässt. Ziel unserer Arbeiten ist die Simulation experimentell relevanter Polymer-Festkörper-Systeme.

Die vorliegende Dissertation wurde in der ersten Hälfte des DFG-Schwerpunktes 1369 geschrieben. Inhalt der Arbeit ist die Entwicklung eines geeigneten Simulations-Werkzeugs, das Studium der Ausbildung von Grenzflächen auf Basis verallgemeinerter Modelle sowie die Suche nach geeigneten numerischen Verfahren, um Wechselwirkungs-Potentiale experimenteller Systeme zu bestimmen.

Unter dem Begriff „Aushärtung" versteht man die Ausbildung einer Polymer-Struktur in einem reaktiven System, das aus Komponenten mit niedrigerem molekularem Gewicht besteht. Die eben beschriebenen reaktiven Prozesse sind sehr wichtig, da viele technisch relevante Klebstoffe wie z.B. Epoxy-Polymere, in Form einer reaktiven Lösung von Monomeren und Aushärtungs-Reagenzien vorliegen. Die Polymer-Klebstoffe werden mithilfe einer reaktiven Lösung in Gegenwart einer behandelten Oberfläche unter genau definierten thermodynamischen Bedingungen hergestellt. Aus diesem Grund sollte es ein geeignetes Simulations-Werkzeug ermöglichen, die Dynamik sowie die reaktiven Prozesse eines gewählten Systems unter den gewünschten Bedingungen zu modellieren. Diese Anforderungen lassen sich durch so genannte reaktive Molekulardynamik (RMD)-Methoden erfüllen, die im ersten Kapitel dieser Dissertation beschrieben werden. Leider reicht die Zeitskala atomarer RMD-Simulationen oft nicht aus, um reaktive Prozesse zu detektieren. In einer vergröberten Beschreibung können reaktive MD-Simulationen verwendet werden, um größere Systeme mit einfachen Reaktionsschemata zu beschreiben. Zurzeit ist es nicht möglich, die Ausbildung einer Grenzfläche während eines Aushärtungsprozesses in einer atomaren Auflösung in einer realistischen

Zeitskala zu beschreiben. Deshalb haben wir die gewählten Modell-Systeme mit vergröberten Methoden und vereinfachten Reaktions-Schemata beschrieben. In unserer Näherung wird jedes Monomer sowie jede Polymereinheit als effektives Superatom (CG)-Teilchen beschrieben.

Im zweiten Kapitel der vorliegenden Dissertation präsentieren wir den von uns entwickelten RMD-Formalismus. Die Möglichkeit, reaktive Simulationen mithilfe von materialspezifischen CG-Potentialen zu beschreiben, wird am Wachstum von Polystyrol-Ketten auf Basis von Ethylbenzol-Monomeren erläutert. Die Ethylbenzol-Moleküle approximieren in unserer Näherung Styrol-Monomere. Die notwendigen Potentiale wurden mithilfe der iterativen Boltzmann-Inversion (IBI) berechnet [Reith, D.; Pütz, M.; Müller-Plathe, F.; *J. Comput. Chem.* **2003**, *24*, 1624]. Viele Eigenschaften von Proben, die während RMD-Simulationen „gewachsen" sind, wurden mit den Ergebnissen von konventionellen Gleichgewichts-Simulationen an identischen Systemen verglichen. In allen Fällen war die Übereinstimmung zwischen RMD-Daten und Gleichgewichts-Ergebnissen gut. Die von uns entwickelte RMD-Methode basiert auf einem Wechsel zwischen so genannten reaktiven Schritten, die durch einen Abstandsparameter zwischen den reagierenden Teilchen beschrieben werden und nichtreaktiven Diffusions-Perioden, die mithilfe einer charakteristischen Zeitkonstanten definiert sind.

Im Rahmen meiner Dissertation wurden systematische Simulationen als Funktion der oben erwähnten RMD-Parameter durchgeführt, um ihren Einfluss zu verstehen und um Einblick in Polymerisationsprozesse zu gewinnen. Die erhaltenen Massenverteilungen der Polymere wurden mit den numerischen Bedingungen der RMD-Simulationen (Wahl der Zeitskala, Wahl des Abstandsparameters) korreliert. Für unser reaktives MD-Schema haben wir Elemente einer über zehn Jahre alten Studie adaptiert, die allerdings nicht materialspezifisch war [Akkermann, R.L.C.; Tøxvaerd, S.; Briels, W.J.; *J. Chem. Phys.* **1998**, *109*, 2929].

Im dritten Kapitel stellen wir ein materialspezifisches Kraftfeld für die Simulation experimentell interessanter Systeme vor. Die Untersuchungen im ersten Kapitel haben gezeigt, dass IBI gut geeignet ist, solche Potentiale zu berechnen. Um die Schwierigkeiten bei der Entwicklung solcher Kraftfelder zu illustrieren, haben wir die Temperatur-Abhängigkeit und Übertragbarkeit von
CG-Potentialen für flüssiges Hexan untersucht. Unter dem Begriff (Temperatur-)Übertragbarkeit versteht man die Fähigkeit (Flexibilität) eines CG-Kraftfeldes, ein System bei Temperaturen zu beschreiben, die stark von der Temperatur abweichen, bei der das Potential parametrisiert wurde. Die beschriebenen Simulationen sind ein einfacher Ansatz, die Übertragbarkeit von CG-Potentialen zu

testen, bevor die Methode auf komplizierte Klebstoffe und Oberflächen übertragen werden kann. In diesem Zusammenhang haben wir auch die Genauigkeit von einfachen Skalierungsverfahren untersucht, die in der Literatur recht gebräuchlich sind und einen neuen, stabileren Formalismus vorgeschlagen.

Im vierten Kapitel beschreiben wir verallgemeinerte Simulationen eines Aushärte-Prozesses in Gegenwart einer idealisierten Oberfläche. Bestandteile der reaktiven Lösung sind „zweiwertige" Monomere und ein „vierwertiges" Aushärtungs-Reagenz. Die Wechselwirkung zwischen der Oberfläche und den Komponenten der Mischung wurde variabel gehalten. Auf diese Weise war es möglich, selektive Adsorptions-Prozesse für die Komponenten zu simulieren. Ziel dieser reaktiven Simulationen war es, den Einfluss einer räumlichen Trennung der Komponenten auf die sich entwickelnde Grenzfläche zu untersuchen. Unsere RMD-Simulationen legen nahe, dass die Massendichte sowie die Orientierung der Bindungen nicht durch diese Komponenten-Trennung beeinflusst werden. Beide Eigenschaften zeigen ein ähnliches Verhalten, unabhängig davon, ob die Komponenten räumlich unter dem Einfluss der Oberfläche getrennt wurden. Im Unterschied dazu werden Eigenschaften, die von der räumlichen Verteilung des Aushärte-Reagenzes abhängen, wie die Länge eines Polymer-Fragments zwischen zwei Verzweigungspunkten (Aushärte-Teilchen mit mehr als zwei chemischen Bindungen) durch Trennung der Komponenten beeinflusst. So nimmt z.B. die mittlere Länge von Polymer-Fragmenten zu, wenn der Abstand zu einer Oberfläche mit selektiver Adsorption des Aushärte-Reagenzes größer wird. Dieses Verhältnis wird umgekehrt, wenn bevorzugt die zweiwertigen Monomere adsorbiert werden. Ohne diese Komponenten-Trennung ist die mittlere Länge der Polymer-Fragmente in der Probe mehr oder weniger konstant.

Im fünften Kapitel werden einige zukünftige Schritte bei der Simulation von Grenzflächen referiert. Die Möglichkeit, das entwickelte RMD-Verfahren auf andere reaktive Prozesse wie z.B. dem Wachstum von chemisch gebundenen Polymer-Ketten zu übertragen, wird andiskutiert.

# Table of Contents

# 1. Classical Reactive Molecular Dynamics Implementations: State of the Art

## 1.1. Introduction

Quantum chemistry based on ab initio, density functional theory (DFT), or semi-empirical calculations has grown to a powerful level of theory to gain microscopic insight into chemical reactions. Computer-assisted quantum chemical calculations[1-15] have allowed the investigation of reactive processes[11, 12, 15] as well as equilibrium structures of compounds.[6] Nevertheless, there is a strong restriction in the number of atoms that can be treated by quantum chemical methods due to the strongly increasing computer time demand. To treat bigger systems, hybrid methods combining quantum mechanics and molecular mechanics (QM/MM) can be used;[16-18] however, they are also expensive. In such schemes the reactive region is described by QM while the non-reactive regions are described by MM approaches based on empirical potential energy functions, i.e. force-fields. Force-fields are analytical functions parameterized via quantum calculations on fragments of the system or via known experimental properties (geometrical parameters, density, heat of vaporization…). Such force-fields map the combined influence of electronic and nuclear interactions in a coarser manner. Their adoption leads to a dramatical computer time reduction. QM/MM methods and their applications to enzymatic reactions have been reviewed by Aqvist and Warshel already in 1993.[16] Many force-fields, such as CHARMM,[19] AMBER,[20] and MM3[21] have been developed for MM approaches. Most of the MM force-fields available, such as the ones just mentioned, describe particle interactions via potential energy functions that do not allow bond breaking or bond formation. They can be employed in pure MM methods only to investigate equilibrium properties[22] such as bond lengths, bond angles or conformational preferences of molecules. Nevertheless, reactive force-fields have also been implemented to investigate transition states of chemical reactions with pure MM methods. The latter subject has been thoroughly reviewed by Eksterowicz and Houk in 1993.[23] With QM, QM/MM and MM approaches it is however not possible to study the time-evolution (i.e. dynamics) of complex liquid, solid or polymer systems. Finite-temperature effects are often considered only in the simple harmonic approximation while pressure effects are beyond their scope. Quantum Monte-Carlo approaches can include finite-temperature effects.[24, 25] However, they remain expensive time-independent methods.

The time-evolution as well as finite-temperature or pressure effects in complex systems can be studied via molecular dynamics (MD) approaches.[26-30] MD is based on the resolution of Newton's equations of motion. During MD simulations, particles experience forces $\vec{F}$ that are computed from relation (1.1.),

$$\vec{F} = -\vec{\nabla}E_p \qquad (1.1.)$$

with $\vec{\nabla}E_p$ representing the gradient of the potential energy function $E_p$. The predictive power of MD simulations is determined by the accuracy of the force-field to reproduce the particle interactions.

Due to the difficulties in coupling MD-driven dynamics with reactive processes mapped by a force-field approach, simulations have been mainly restricted for many years to non-reactive conditions using force-fields such as CHARMM,[19] AMBER,[20] and MM3[21] already mentioned above. Several other non-reactive force-fields[31-35] based on the same philosophy have been described in the literature. In the present review we will classify these non-reactive force-fields as "standard MD force-fields". An alternative to simulate reactions via MD is the use of hybrid methods, such as the Car-Parinello molecular dynamics method (CAPMD), which combines MD with QM.[36-38] Nevertheless, the treatment of the reactive quantum regions in QM/MD approaches still remains demanding. Currently, MD simulations treating both the particle dynamics as well as reactive processes with a force-field are an efficient compromise to investigate the time-evolution of very huge systems under thermodynamic constraints with reasonable computer time demands. But, as already mentioned, such implementations are a challenging task. In the context of non-reactive MD simulations, the topology of the system is never altered. The equilibrium distances and angles are preserved by the force-field. In reactive simulations, an accurate and predictive force-field should, first of all, allow for the reproduction of the material properties under non-reactive conditions. Secondly, the extra features required to model a chemical reaction as realistically as possible must be incorporated into the force-field. This includes the capability of the reactive force-field to decide under which conditions the encounter of particles leads to a reactive step. The modelling of the transition state of a reaction is a challenge for any realistic reactive force-field. During such a transition, the geometry of the reacting species evolves. An accurate reactive force-field should guarantee a continuous transition from the equilibrium structures of the reactants to the product ones. Preferentially, the reactive part of the force field should be developed from first-principles approaches. The points mentioned above clearly highlight the additional challenges accompanying the development of a reactive force-field.

Nevertheless, the interest in reactive molecular dynamics (RMD) simulations is growing and a certain number of approaches are now available. In the present review we have divided the existing RMD approaches into two classes. The first class of RMD implementations comprises approaches that do not focus on a realistic description of the elementary chemical reaction. In this RMD branch, a connection between two particles is made if they are found within a pre-defined distance. In the present review, approaches that rely on a distance criterion are classified as “reaction cutoff distance” methods.[39-55] Here, the interaction between reacting particles switches from the nonbonded to the bonded one without transition. Historically, the purpose of reaction cutoff methods has been the generation of equilibrated polymer structures.[39-41, 44, 47, 50-52, 54] In later articles they have been used to provide qualitative insight into polymerization processes.[40, 42, 43, 45, 46, 48, 49, 53-55] The second class of implementations, intents to develop accurate and predictive reactive force-fields as discussed above. These approaches will be classified here as RMD methods based on “empirical reactive force-fields”. Reactive force fields such as the RMDff implementation of Nyden et al.[56-64] or the Adiabatic Reactive Molecular Dynamics (ARMD) approach of Meuwly et al.[65-68] are based on modified versions of available standard MD force-fields. The Stillinger-Weber (SW) potentials[69-94] adopt many-body interactions in their setup. The Abell-Tersoff-Brenner (ATB) potentials[95-128] as well as the force-field ReaxFF of van Duin et al.[129-154] are bond-order based potentials. The cited methods define the different subclasses that can be identified in the family of “empirical reactive force-fields”. In these schemes, a continuous transition region from the reactants to the products is implemented. In most of these approaches, this is ensured by the use of switching functions. For this purpose, the choice of functions based on the hyperbolic tangent seems to be common. It is worth mentioning that such functions have already been used as smooth bond interpolation functions in quantum chemical calculations.[2] The aim of empirical reactive force-field approaches is to reproduce certain aspects of the reaction kinetics as well as transition state geometries. The difference between methods based on empirical reactive force-fields and reaction cutoff techniques is illustrated in Figure 1.1.

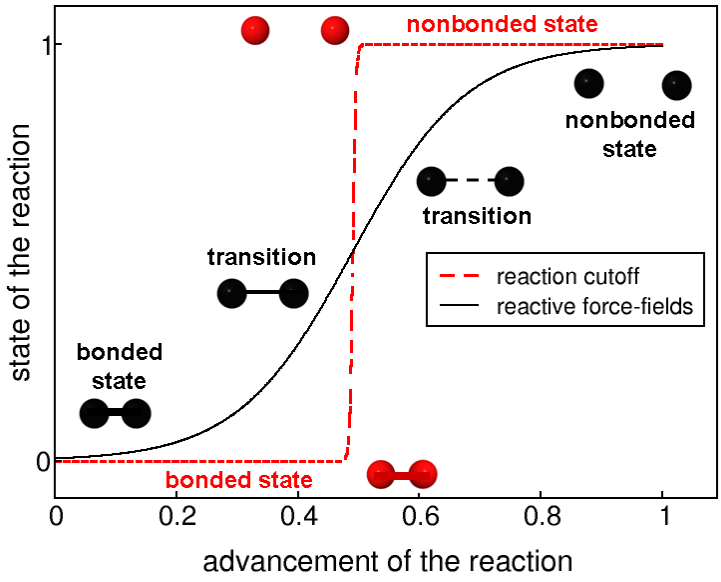


***Figure 1.1.*** *Illustration of a bond-breaking process either described by a reactive force-field method or a reaction cutoff distance approach. The x-axis is a generalized reaction coordinate that indicates the advancement of the reaction; x = 0 is the beginning of the reaction and x = 1 the end. The dimensionless y-axis maps the state of the reaction (y = 0 is the educt, y = 1 is the product). The black switching function symbolizes a continuous transition as interpolated by a reactive empirical force-field. For a reaction cutoff method, the red step-function indicates the abrupt change of the state.*

Two older reviews on reactive MD simulations are available in the literature. In the one by Garrison and Srivastava (1995),[155] chemical reactions of a few hydrogen or oxygen atoms with metallic surfaces, described with the London-Eyring-Polyani-Sato (LEPS) potential, have been summarized. In addition the SW and ATB potentials prevailingly adopted to simulate silicon surface etching and the Embedded Atom Model (EAM) for the description of metals have been discussed. Similar to SW potentials, EAM force-fields belongs to the family of many-body potentials. They have not been included in the present review because a more detailed description of the latest achievements of SW potentials has been reported. The second review published by Brenner (2000) is more focused on the theoretical fundaments of ATB potentials.[156]

A decade of research has elapsed since 2000 and - as foreseen by Garrison, Srivastava and Brenner - the interest in the development of RMD implementations has grown significantly. New achievements have been accomplished mainly in the field of polymer simulations. Topics such as the kinetics of the thermal decomposition of polymers, the bombardment of polymer materials with high-energy species, or qualitative investigations of polymer growth via generic potentials, have been discussed in the literature. As several new methods have emerged we feel that a new RMD classification, including the Stillinger-Weber and Tersoff approaches, is necessary. The present review

offers the possibility to estimate the role of RMD in material science by a comprehensive description of the available methods and their application fields. We discuss the capability of RMD implementations to reproduce or to explain experimental results.

In the second section, we present reaction cutoff distance models based on material-specific force-fields and on generic potentials. A discussion on empirical reactive force fields approaches follows in the third section. They have been regrouped into implementations based on modified standard MD force-fields, many-body and bond-order potentials. In the concluding section, we discuss the different advantages and limitations of the RMD approaches. Finally, we have grouped RMD simulations from our literature research as a function of their application domains in a table format that is provided at the end of the review.

## 1.2. Reactive Methods Based on a Reaction Cutoff Distance

In these methods, a reaction cutoff radius centered at a reactive particle determines the influence sphere where prospective reaction partners form new bonds. Figure 1.2. is a two-dimensional illustration of a chain-end propagation during a polymerization as simulated with a reaction cutoff method. In reaction cutoff methods, the bonded state between two particles is created by suddenly turning on the bonded interactions of the force-field while the nonbonded ones are turned off. Material-specific force-fields[39, 41, 44, 47, 51, 52, 54] generally require additional effort in contrast to generic CG potentials[40, 42, 43, 45, 46, 48-50, 53] as discussed below.

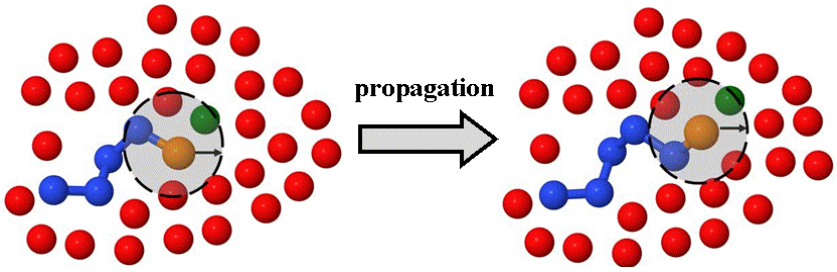


***Figure 1.2.*** *Two-dimensional representation of a propagation step for a chain-end polymerization. The red particles symbolize the free monomers and the blue the connected ones. The dotted circles centered at the brown particles symbolize the reactive state of the chain-ends. The green particles are the ones reacting with the active chain-ends. The green particle on the left picture is transformed into the brown one on the right picture. The black arrows represent the reaction cutoff distance.*

Material-specific potentials have characteristic features such as equilibrium distances and angles in the case of bonded interactions or, in the case of nonbonded interactions, specific excluded volumes. The differences in typical bonded and nonbonded distances imply that even the smallest value - defined by the excluded volume radius - allowed for a reaction cutoff distance will likely be found in the zone of strong forces of the bond-stretching potential. A bigger reaction cutoff speeds up the polymer generation but simultaneously introduces strong forces after switching to bonded interactions. The generation of states with high forces might require special care in the performance of RMD runs; this topic will be discussed in the next paragraph. In contrast to material-specific RMD approaches, implementations using generic models are generally easier to handle. Here, the bonded interactions often include a bond-stretching potential that is not restricted to realistic length scales.

As mentioned above, strong forces that might be introduced by a reaction cutoff approach can provoke instabilities. The common option to relax the system from such high energy configurations is to alternate bond formation steps with conventional MD moves controlled by a thermostat. Most implementations based on a reaction cutoff distance are composed by this alternation. Some implementations add more sophisticated relaxation techniques. In addition to the removal of forces, conventional MD steps also influence the final polymer length distributions as they define the diffusion time-scale between reactive steps.[40, 51] Below, we describe reaction cutoff distance methods that have been combined with standard MD force-fields or with tabulated potentials to simulate specific materials. Subsequently, we present the methods that have been applied in connection with generic potentials.

### 1.2.1. Reaction Cutoff Methods in Combination with Material-Specific Force-Fields

#### *1.2.1.1. Atomistic Standard MD Force-Fields*

As a set of representative studies, we present the investigations of Varshney et al.,[51] Wu et al.,[47] Bermejo et al.,[52] and Lin et al.[39] Varshney et al. have generated an epoxy polymer network from the resin monomer diglycidyl ether of bisphenol F and the cross-linker diethylene toluene diamine; see Figure 1.3., top. The reactive groups are the oxirane rings of the resin monomers and the amine fragments of the cross-linkers. The growth scheme is symbolized in Figure 1.4a. Four scenarios have been considered in this work. In the first one, all reactive groups have the same reactivity. In the second, the reactivity of primary amines is higher than the one of secondary amines. In the third, each nitrogen makes two bonds before considering another one. For these scenarios, one bond is formed at a time using a reaction cutoff of 1.0 nm. In the fourth scenario, all reactive sites react simultaneously

with an initial reaction cutoff of 0.4 nm that is enlarged by 0.025 nm after each unsuccessful reactive attempt. Here, a bonded potential is progressively introduced in association to an energy minimization via a multistep relaxation procedure (see Figure 1.4a).

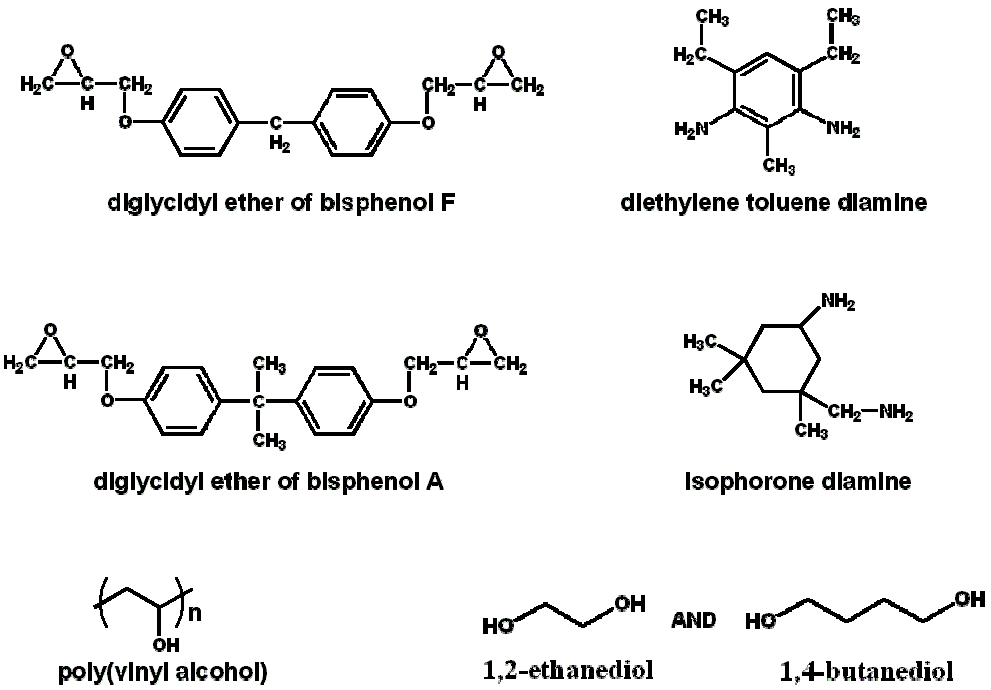


***Figure 1.3***. *Components employed in the RMD simulations of Varshney et al.*[51] *(top), Wu et al.*[47] *(center) and Bermejo et al.*[52] *(bottom).*

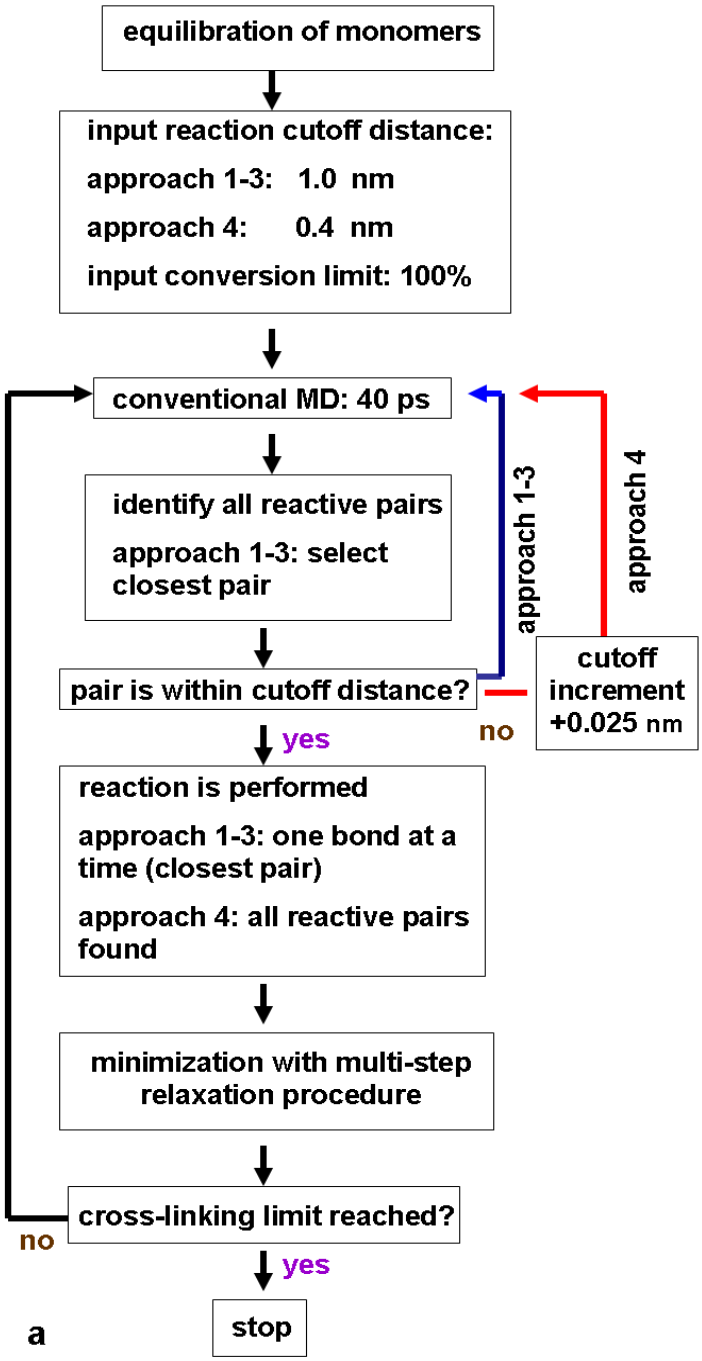
equilibration of monomers
input reaction cutoff distance:
approach 1-3: 1.0 nm
approach 4: 0.4 nm
input conversion limit: 100%
conventional MD: 40 ps
identify all reactive pairs
approach 1-3: select closest pair
pair is within cutoff distance?
approach 1-3
approach 4
cutoff increment +0.025 nm
no
yes
reaction is performed
approach 1-3: one bond at a time (closest pair)
approach 4: all reactive pairs found
minimization with multi-step relaxation procedure
cross-linking limit reached?
no
yes
stop
a

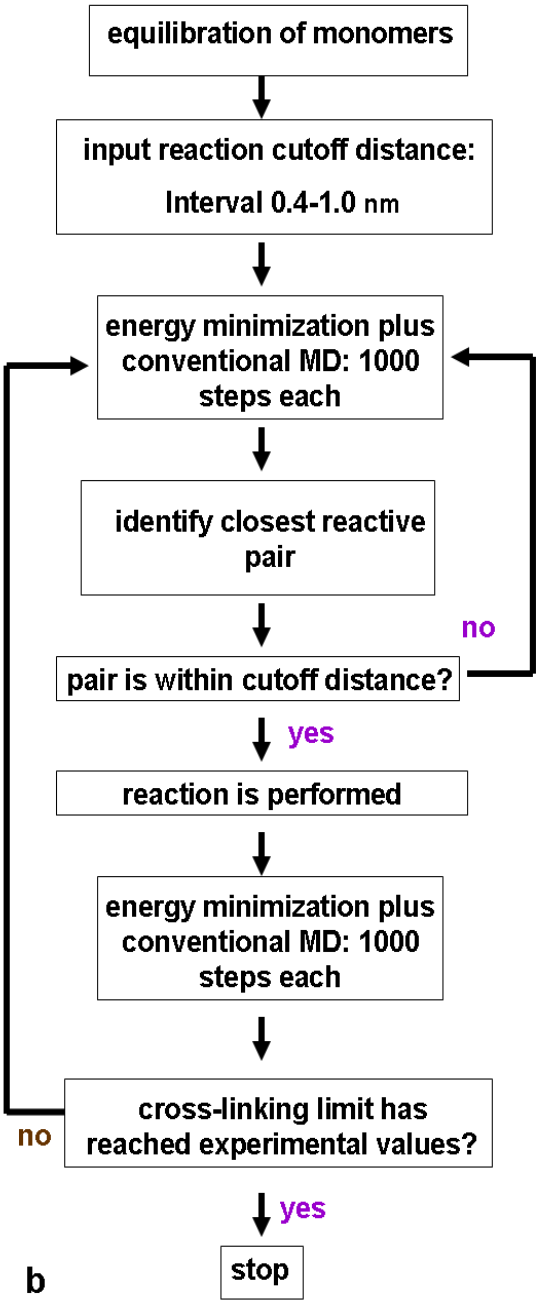
equilibration of monomers
input reaction cutoff distance:
Interval 0.4-1.0 nm
energy minimization plus conventional MD: 1000 steps each
identify closest reactive pair
pair is within cutoff distance?
no
yes
reaction is performed
energy minimization plus conventional MD: 1000 steps each
cross-linking limit has reached experimental values?
no
yes
stop

b

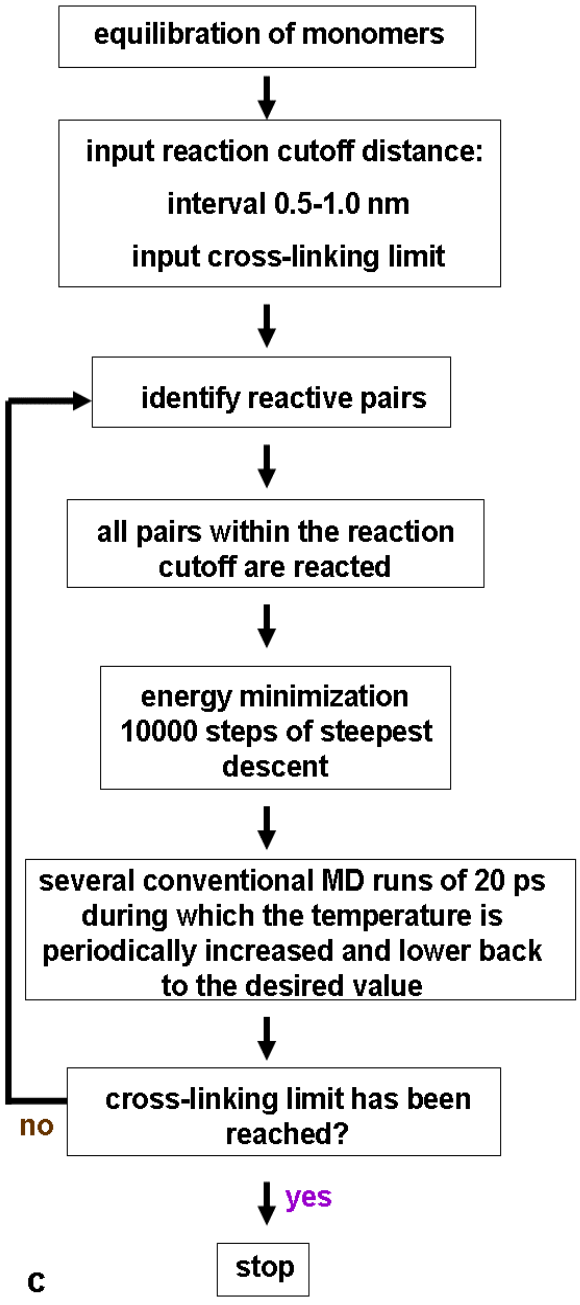
equilibration of monomers
input reaction cutoff distance:
interval 0.5-1.0 nm
input cross-linking limit
identify reactive pairs
all pairs within the reaction cutoff are reacted
energy minimization 10000 steps of steepest descent
several conventional MD runs of 20 ps during which the temperature is periodically increased and lower back to the desired value
cross-linking limit has been reached?
no
yes
stop

c

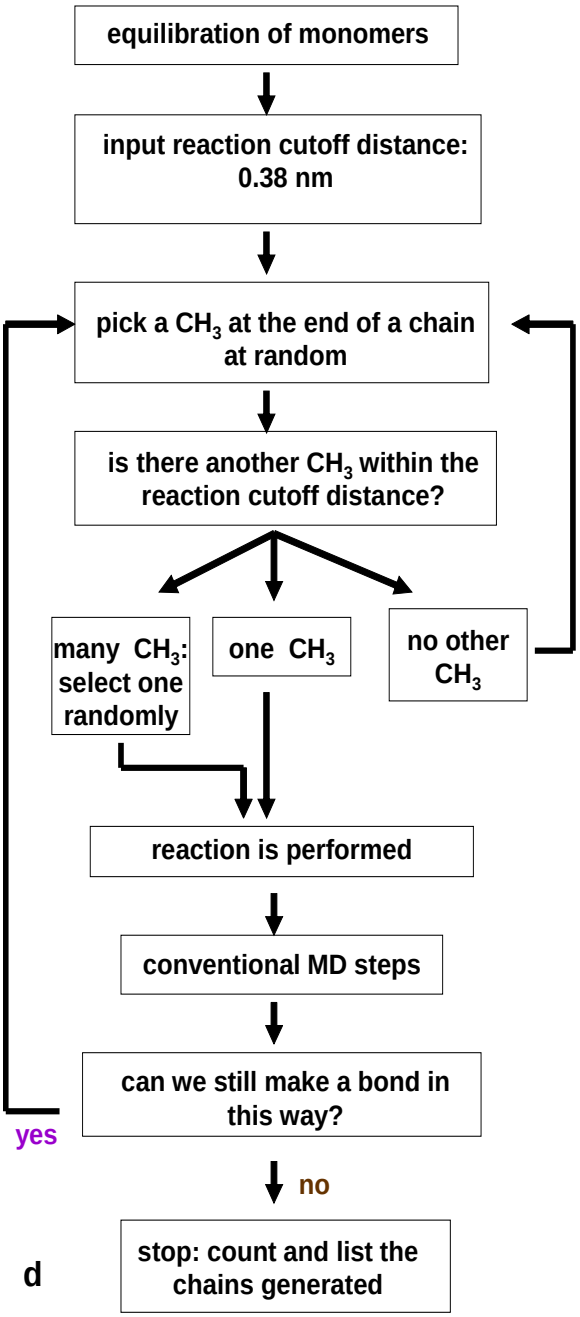


***Figure 1.4.*** *Schematic diagrams of the reaction cutoff distance methods implemented by a) Varshney et al.[51] for diglycidyl ether of bisphenol F as epoxy resin and the cross-linker diethylene toluene diamine, by b) Wu et al.[47] for diglycidyl ether of bisphenol A as epoxy resin and the cross-linker isophorone diamine, by c) Bermejo et al.[52] for poly(vinyl alcohol) chains and linear polyol cross-linkers and by d) Lin et al.[39] for poly(ethylene oxide) chains grown from dimethyl ether molecules. For detailed explanations of the diagrams see the text.*

The polymerization scheme of Wu et al.[47] is presented in Figure 1.4b. They have generated an epoxy polymer network from the resin monomer diglycidyl ether of bisphenol A and the cross-linker isophorone diamine; see Figure 1.3., center. The relaxation scheme of Wu et al. consists of energy minimization steps followed by conventional MD moves. Such a relaxation scheme has also been employed by Bermejo et al.[52] in a more sophisticated way. In the work of Bermejo et al., the conventional MD steps are performed as periodic cycles of temperature decrease and increase between 400 and 650 K (see Figure 1.4c). This temperature annealing process allows a gradual energy minimization that reduces the probability to trap the structure in a local energy minimum. For an early analysis of such annealing schemes, we refer to the work of Böhm et al.[3] Bermejo et al.[52] have generated a network from poly(vinyl alcohol) chains and polyol cross-linkers as displayed in the bottom part of Figure 1.3. Lin et al. have generated linear poly(ethylene oxide) chains. In their model, each of the $CH_3$ groups in the dimethyl ether and each of the $CH_2$ groups in poly(ethylene oxide) is treated as one “super-atom”. They have used conventional MD steps to relax the systems (see Figure 1.4d).

Varshney et al.[51] have implemented a quite involved multistep relaxation procedure in addition to conventional MD moves. In contrast, the poly(ethylene oxide) relaxation scheme of Lin et al.[39] uses only conventional MD steps. Unfortunately, general investigations on the merits and shortcomings of the different relaxation schemes do not exist. The comparison performed by Varshney et al. is - to our knowledge - one of the sparse attempts to correlate different approaches. They have compared the energies for the different force-field terms (bond stretching, angles, torsions, van der Waals…) of equilibrated configurations and found that the fourth approach leads to the lowest values.

The approaches discussed here all yield equilibrated samples with properties that are in agreement with experiments. The reference properties considered for the method validation are generally the density, the glass transition temperature, the volume shrinkage of the polymer or elastic constants. The grown samples are used to understand structure-property relationships. Bermejo and co-workers[52] have discussed the influence of the cross-linker size on network properties. In comparison to 1,4-butanediol, the shorter 1,2-ethanediol cross-linker leads to a poly(vinyl alcohol) network with a higher glass transition temperature. In fact, a more constrained motion of the polymer segments is induced by the shorter cross-linker. For the same reason, higher elastic constants reflecting a more rigid material have been observed when inserting the shorter 1,2-ethanediol.

It appears from the literature that at the atomistic or united atom level, reaction cutoff methods have been adopted prevailingly for the generation of equilibrated polymer samples. These methods are very useful and have highly contributed to reduce efforts to generate starting polymer configurations.

### *1.2.1.2. Coarse-Grained Implementations*

An RMD simulation using coarse-grained (CG) - but material-specific - potentials has recently been reported.[54] Coarse-graining involves regrouping a number of atoms into bigger units (i.e. beads) to reduce the number of interaction sites. In turn, MD time and length scales are strongly enhanced.[157] A number of techniques are now available to optimize material-specific CG potentials.[157-160] A tabulated set of CG potential has been employed in the RMD simulations of Farah et al.[161] They have been developed via the Iterative Boltzmann Inversion (IBI) technique.[158] Originally, they were used to model atactic polystyrene (PS), ethyl-benzene (EB) and their mixtures.[161] They can be scaled for the use at different temperatures and species concentrations. These CG potentials comprise bond stretching and angle-bending interactions in addition to the PS-PS, PS-EB and EB-EB nonbonded interactions. The CG beads either correspond to a PS repeat unit ($-(C_6H_5)C_2H_3-$) or to an EB molecule ($((C_6H_5)C_2H_5)$).[161]

In the work of Farah et al.,[54] reaction cutoff values are chosen inside the repulsive region of the nonbonded potentials. Smaller reaction cutoffs lower the probability to find reactive partners. The growth process is defined by initiation and propagation steps (see Figure 1.2.). Chain termination steps are not implemented. The reactive steps are represented below in Equation (1.2.),

$$\begin{aligned} &I^* + M \rightarrow I-P^* \\ &I-P^* + M \rightarrow I-P-P^* \\ &I-P_{n-1}-P^* + M \rightarrow I-P_n-P^*,\ n = 2,3,4,... \end{aligned} \qquad (1.2.)$$

The initiators are symbolized by I, the free monomers by M and the polymer beads by P. The symbol * defines the reactive centers. The relaxation steps are only based on conventional MD moves that are controlled by the Berendsen thermostat and barostat.[27]

One of the intentions in this RMD study was to test the capacity of the method to grow and equilibrate monodisperse polystyrene samples with chain lengths of 10, 30, 80 and 120 PS monomers at 500 K. Several properties such as densities, end-to-end distances, gyration radii, radial distribution functions, bond and angle distribution functions were extracted from the grown polymer samples. They agreed well with the results of non-reactive MD simulations performed on identical polymer systems, thus, validating the reactive implementation. As a second topic of the investigation, the relation between processing history and final polymer properties were analyzed. In this context, a benchmark for RMD-based polymer length distributions is the theoretical Poisson distribution

function.[40] It is observed for polymerizations only defined by initiation and propagation steps in an ideally mixed sample implying that reactive processes are not diffusion controlled. With these assumptions the analytical solution reads,[40]

$$P(N_L+1) = \frac{N(t)^{N_L}}{N_L!}\exp[(-N(t))] \quad N_L = 1,2,\ldots . \qquad (1.3.)$$

N(t) is the average number of bonds per chain (ratio between the total number of bonds formed and the total number of activated chains) at any time t and $P(N_L+1)$ the probability to observe a fraction of chains with length $N_L+1$ (i.e. degree of polymerization). In the literature, the comparison between RMD-based polymer length distributions and the Poisson solution is quite popular when relating polymer length profiles to the reaction conditions.[40, 53, 54] Any deviation from the Poisson solution indicates violations from the prerequisites mentioned above. The influence of the polymerization rate and of the initial spatial distribution of initiators (random or localized) on the final polymer length distribution $P(N_L)$ has been discussed by Farah et al.[54] For a random distribution of starters and a slow polymerization rate, a $P(N_L)$ profile in agreement with the Poisson distribution has been observed. A broader $P(N_L)$ profile has been derived from a faster polymerization with a random distribution of starters. This follows from the trapping in the polymer phase of some of the growing chains. An illustration of polymer length distributions $P(N_L)$ for a slow and fast polymerization is provided in the top part of Figure 1.5. A localized starting distribution of initiators, such as the one sketched in the left diagram of Figure 1.6., under fast polymerization conditions results in a strong deviation of the $P(N_L)$ profile from the Poisson solution. The polymer length distribution for such a starting configuration is displayed in the bottom of Figure 1.5. It follows from an initiator configuration with high steric hindrance due to the bead excluded volumes. As depicted in the right part of Figure 1.6., the polymer chains created by the outer initiators grow very fast inhibiting inner initiator reactions. From their simulations, Farah et al.[54] have highlighted starting conditions that result in highly inhomogeneous growth processes deviating completely from a Poisson-like profile.

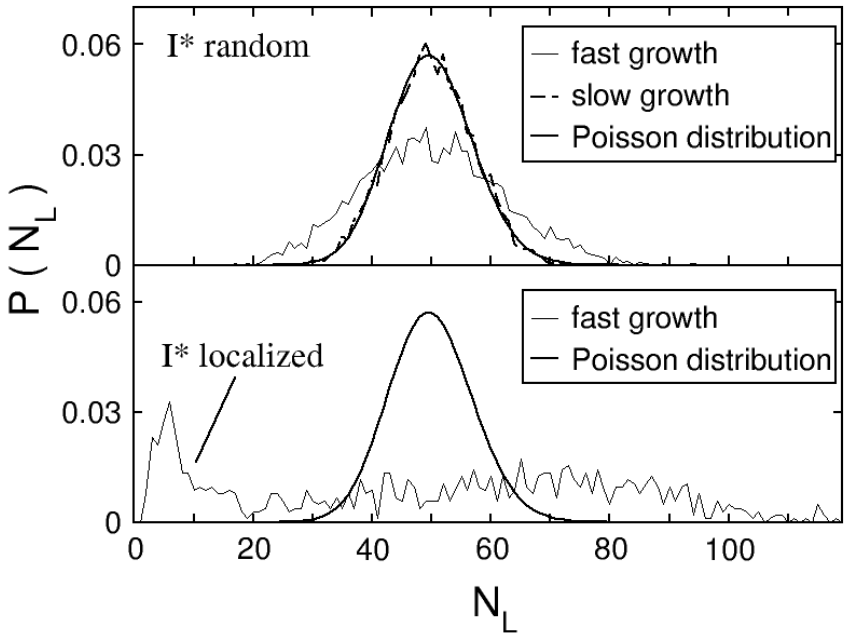


***Figure 1.5.*** *Polymer length distributions obtained from a fast and slow RMD polymerization. The top part shows the polymer length distributions in the case of an initial random distribution of initiators. The bottom refers to a localized distribution of initiators in the bulk of free monomers. The reference Poisson distribution is displayed in the top and bottom diagrams for comparison. The Figure has been taken from reference 54.*

Interestingly, the correlation between the spatial localization of initiators, the velocity of the reaction and the resulting polymer length distribution discussed here appears pertinent also in the case of a surface-initiated growth of polymer brushes.[53] The present RMD scheme has also been applied to study the formation of an interphase during a curing process in contact with an idealized surface.[55]

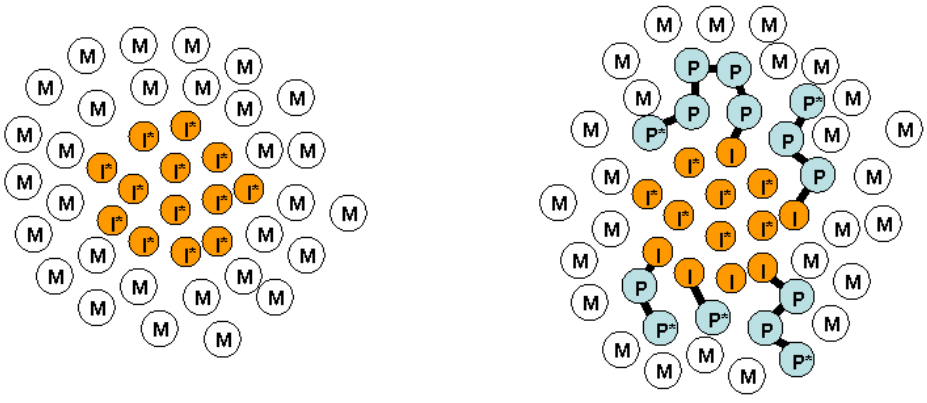

***Figure 1.6.*** *Trapping of initiators leading to very broad polymer length distribution ($P(N_L)$) in the case of a fast chain polymerization starting from a localized distribution of initiators. On the left: Droplet of initiators (I*) in the bulk of free monomers (M) prior to the reaction. On the right: Trapping of the inner droplet initiators after a certain number of reactive steps. P symbolizes a polymer repeat unit.*

## 1.2.2. Reaction Cutoff Methods in Combination with Generic Polymer Models

### *1.2.2.1. Finitely Extensible Non-Linear Elastic (FENE) Potential*

The FENE potential has been originally developed to perform generic simulations of polymer systems under non-reactive conditions.[162] Nevertheless, it has been employed also in RMD simulations. In this scheme, the bonding is described by a combination of the repulsive part of a Lennard-Jones interaction (Weeks-Chandler-Andersen (WCA) potential) and the attractive FENE potential (1.4.).

$$E_{FENE}(r) = \begin{cases} -\frac{1}{2} f_{const} (r_{max})^2 \ln(1-(\frac{r}{r_{max.}})^2), & r \le r_{max} \\ \infty, & r > r_{max} \end{cases} . \quad (1.4.)$$

$r_{max}$ is the maximum extension of the bond and $f_{const}$ the associated force-constant. The construction of the interaction potential has been plotted in the left diagram of Figure 1.7. The relation between the WCA and the FENE parameters is $r_{max} = 1.5\sigma$ and $f_{const} = (30\varepsilon)/\sigma^2$ with the Lennard-Jones parameters $\varepsilon$ (i.e. potential depth) and $\sigma$ (i.e. radius defining the excluded volume) set equal to unity.

The two studies discussed here model the polymerization scheme displayed in Figure 1.2. Perez et al.[50] have performed bulk linear-chain polymerizations while Liu et al.[53] studied the growth of chains grafted to a surface. The initiators at the beginning of the simulations were distributed randomly in a pure bulk phase in the work of Perez et al. while they have been located at a surface with a pre-defined density in the study of Liu et al. Both RMD studies start with the equilibration of the monomer liquids. The reaction cutoff in these implementations corresponds to the shell of the first neighbors surrounding a reactive particle. The bonding partner is chosen randomly in this shell among the particles that are still in the monomer state.

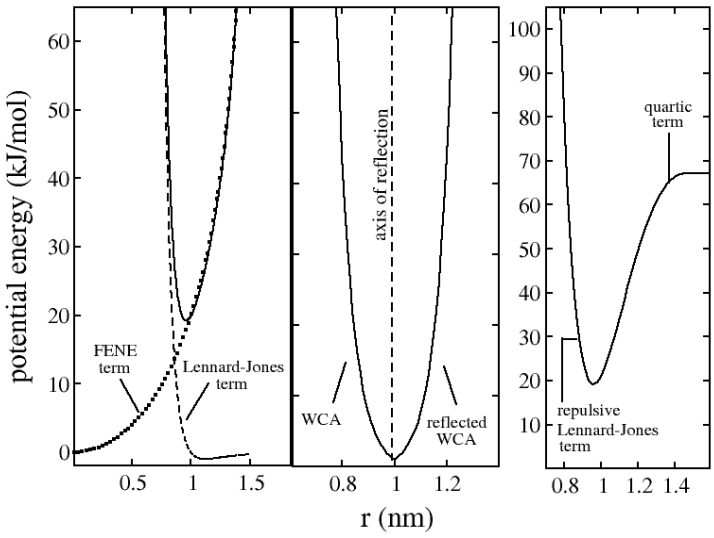


***Figure 1.7.*** *Potentials used in generic RMD simulations. Left: FENE potential combined with a Lennard-Jones element. Center: Reflection of a WCA potential. Right: Breakable quartic bond potential combined with a Lennard-Jones function.*

When the bonding partner has been selected, Liu et al.[53] control the polymerization rate of the grafting process by an additional probability. In the two implementations described, each reactive particle can bind one particle in a reactive step. Relaxation occurs during a number of conventional MD moves under the influence of a thermostat. The Nosé-Hoover technique[28, 29] for the thermostat and barostat has been employed by Perez et al.[50] while a Dissipative Particle Dynamics thermostat has been used by Liu et al.[53]

Perez et al.,[50] in agreement with Farah et al.,[54] have observed broader polymer length distributions for faster reactive processes. To validate their implementation, Perez et al. have generated reference polymer samples with the Fast Push-Off technique (FPO).[163] Within the FPO model the chains are generated randomly in the simulation box without accounting for their excluded volume. The resulting overlaps are progressively removed by soft repulsive interactions until the full nonbonded potential can be reinstalled. To validate their implementation Perez et al.[50] have compared the mean square internal displacement of the chains, the gyration radii and the entanglement length from their RMD simulations to FPO results. Good agreement was observed for all properties.

Liu et al.[53] have focused their simulations on the relation between the surface initiator density, the polymerization rate and the final polymer length distribution $P(N_L)$ of the polymer brushes. They have observed that an increasing surface initiator density augments the total number of monomers that are grafted to the chains. Nevertheless, above a certain threshold, the total number of initiators that can react is limited to a constant value. This threshold value follows from the close proximity of the growing chains. As a result, the number of growing chains and, thus, the total number of grafted monomers remains constant. The top diagram of Figure 1.8. illustrates the case of low surface initiator density where chain initiation is not yet prevented by steric hindrance. The high density case (Figure 1.8., bottom part) illustrates the hindrance of initiation due to the close proximity of the growing chains. Qualitatively, the generic model of Liu et al.[53] is in good agreement with experiments. Yamamoto et al.[164] have found that the number of grafted methyl methacrylate monomers exhibits a nearly constant evolution above a critical initiator density. Another experiment performed by Ma et al.[165] revealed a similar behavior for oligo(ethylene glycol) methyl methacrylate monomers grafted on a gold coated surface. Finally, Liu et al.[53] have correlated the polymer length distributions $P(N_L)$ of the grafted chains to the initiator density and the polymerization rate. At low initiator density and slow polymerization rate, they recovered distributions in line with a Poisson profile. A stronger deviation from this distribution has been observed when the initiator density and polymerization rate were high. This latter case is similar to the bulk polymerization with a localized distribution of initiators as studied by Farah et al.[54] In fact, in both cases a fast reaction is modeled with a high spatial proximity of the initiators.

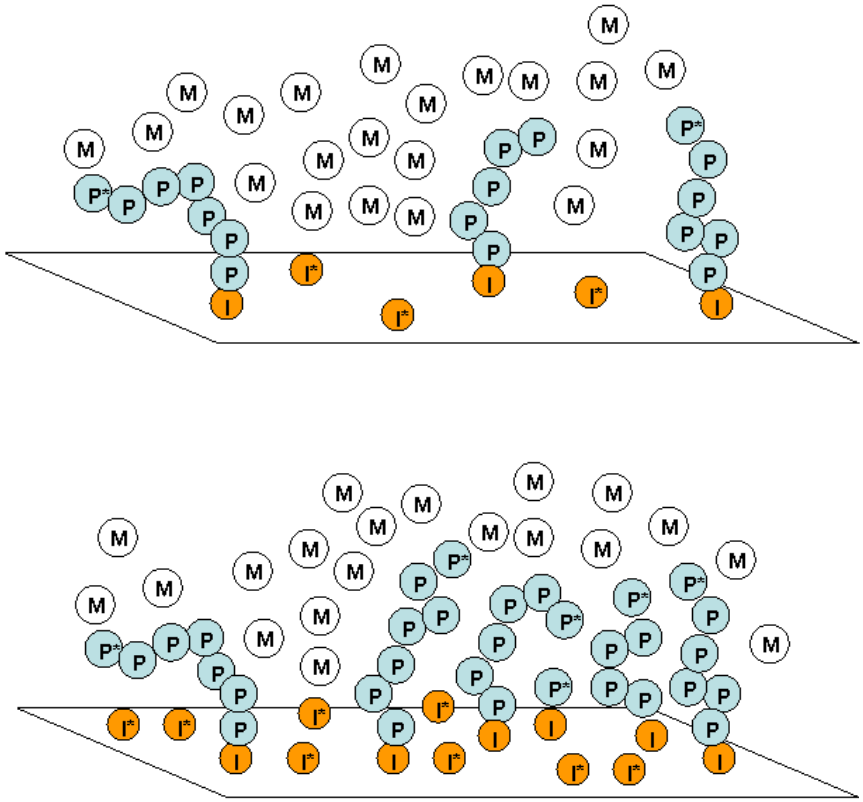


***Figure 1.8.*** *Representation of the polymer brushes for a low (top diagram) and a high (bottom diagram) surface initiator density. The free monomers are symbolized by the letter M, the initiators by I and the polymer beads by P. The star labels the reactive centers.*

### *1.2.2.2. Reflected Weeks-Chandler-Andersen (WCA) Potential.*

In the generic model implemented by Akkermans et al.,[40] the WCA potential[166] is used for the bond-stretching and the inter-molecular interactions (polymer-polymer, polymer-monomer and monomer-monomer). Irreversible bonding between two particles is ensured by a potential reflection that is centered at the distance $r_{center} = 2^{1/6}\sigma$ of the purely repulsive WCA function,

$$E_{reflected}(r) = E_{LJ}(r_{center} - |r - r_{center}|), \qquad 0 < r < 2r_{center}. \qquad (1.5.)$$

With this potential, bonds have a finite extensibility of $2r_{center}$; it is represented in the center part of Figure 1.7. The adoption of identical Lennard-Jones parameters for bonded and nonbonded interactions implies identical vibrational frequencies for connected and unconnected particles. Therefore, a larger time-step can be used in comparison to simulations that describe bond vibrations realistically.

Similar to references 50, 53 and 54 the chains are grown according to the polymerization scheme of Figure 1.2. The monomer liquid is first equilibrated; subsequently a random process chooses a subset of particles and labels them as initiators. Following this preparation stage the periodic alternation of reactive steps and conventional MD moves takes place. The Nosé-Hoover thermostat has been used here. The reaction cutoff is taken to be equal to $r_{center}$. Within the reaction cutoff, a random choice is made among the unconnected neighbors of a reactive centre. A probability is defined by the equation $P_r = m/m_{max}$ with $m_{max}$ being the maximum number of monomers that can surround a particle. The value m is the number of monomers currently found in the influence sphere of a reactive particle. The bonding state is established via the replacement of the repulsive inter-particle potential by the reflected WCA potential.

To validate the model, RMD-based end-to-end distances ($R_{ee}$) and gyration radii ($R_g$), obtained from the growth of single chains have been compared with the theoretical scaling law $X = b_x N_L^{\nu}$, with $X = R_{ee}$ or $R_g$. The prefactor $b_x$ has been evaluated from non-reactive simulations. The parameter $N_L$ is the number of monomers in the chain. $\nu = 0.588$ is observed for the scaling regime influenced by the excluded volume and $\nu = 1/2$ in the random walk regime. The $R_{ee}$ and $R_g$ obtained at different stages of single chain polymerizations agreed with the scaling law predictions. Following the validation part, Akkermans et al.[40] have followed the growth of multiple chains from the dilute regime to the polymer melt. An interesting attempt has been suggested to extract a polymerization rate constant k from the time interval $\tau_r$ separating reactive steps. The following expression has been proposed for the rate constant.

$$k = \frac{\int_0^{r_m} g_{MP^*}(r) 4\pi r^2 dr}{\tau_r m_{max}} \qquad (1.6.)$$

The integral refers to the radial distribution function that defines the average number of free monomers M around a reactive center P*. The parameter $m_{max}$ has been discussed above. In order to characterize the time evolution of the process a rate equation for the average number of bonds per chain formed at a time t (N(t)) obtained under the same assumptions as already adopted in the Poisson formula (see Equation (1.3.)) has been derived.[40]

$$N(t) = \frac{[M]_0}{[P^*]}(1 - \exp(-k[P^*]t)) \qquad (1.7.)$$

In Equation (1.7.), the rate constant k comes from Equation (1.6.). $[M_0]$ and [P*] refer to the initial monomer and reactive center concentrations. The analytical solution presented in Equation (1.7.) reproduces well the RMD based N(t) profiles at the beginning of the chain growth. Deviations are observed at the end of the process because the reactive simulations become diffusion controlled even for the biggest $\tau_r$ values. The correlation between reaction cutoff parameters and macroscopic rate equations in the work of Akkermans et al. is inspiring. The model is suitable to investigate the interplay between the velocity of reactive steps and diffusion (i.e. relaxation) that can have different time scales in polymerizations.

### *1.2.2.3. Breakable Quartic Bond Potential*

Stevens et al.[42, 43, 45, 46] have been focusing on the nature of adhesion failure in adhesive polymer networks. They transferred a FENE bond interaction into a quartic potential that provides the possibility of bond breaking events. The bonding potential is the sum of the repulsive part of a Lennard-Jones function and of the following breakable quartic bond potential,[42]

$$E_{quartic}(r) = \begin{cases} f_{const.}\,[(r-\Delta r)-P_1][(r-\Delta r)-P_2]\,(r-\Delta r)^2 + E_{shift} & r < r_c \\ E_{shift} & r > r_c \end{cases} \qquad (1.8.)$$

The determination of the parameters of Equation (1.8.) proceeds by a fitting process involving the initial FENE potential. $\Delta r$ adjusts the center of the quartic potential, $f_{const.}$ is the force-constant, and $P_1$ the inter-particle distance at the FENE minimum. $P_2$ is set equal to zero, and $E_{shift}$ is a shift in energy. The parameter $r_c$ is the interaction cutoff radius. The potential is plotted on the right hand side of Figure 1.7. The nonbonded polymer-polymer, polymer-monomer and monomer-monomer interactions are defined by a Lennard-Jones function. It is the repulsive part of this Lennard-Jones interaction that is used to describe the bonded potential (i.e. see above).

In their investigations Stevens et al. reproduce the curing process of epoxy resin monomers and curing agents that generate polymer network adhesives in the presence of adherend surfaces.[42, 43, 45, 46] The initial system of unconnected particles is composed of multifunctional curing agents (cross-linkers) and bifunctional monomers that are confined and equilibrated between two walls. The surface-

particle interactions are identical to the particle-particle ones. The network is formed during a constant temperature simulation. The reaction cutoff has been defined in Lennard-Jones units as equal to 1.3σ. In the first stage of the curing, only reactions between cross-linkers and surface beads occur. In the second stage, the cross-linkers and monomers are coupled. The authors did not mention any particular relaxation steps. After the completion of the network growth, the surface walls are moved with a uniform velocity and eventual bond breaking events in the adhesive system are tracked.

Tsige, Lorenz and Stevens have investigated the influence of mixed curing agents on the nature of the adhesion failure.[46] By mixing the curing agents with functionalities (i.e. number of bonds allowed) f = 3, 4 and 6 in different proportions, polymer networks with average functionalities $f_{av}$ increasing continuously from 3 to 6 have been generated. For a continuous increase of the average functionality from 3 to 6 Tsige et al. have shown that the failure mechanism evolves progressively from cohesive to interfacial. An interfacial failure results from bond breakings between the surface and the adhesive beads. Cohesive failure is due to the rupture of bonds in the adhesive material. Here, each curing agent can only make one bond with the surface beads. Tsige et al. have highlighted an interesting relation between the average functionality of the polymer adhesives and the nature of the adhesion failure.[46]

In another work, Tsige and Stevens[45] have tuned the number of bonds that are formed between the curing agents and the surface (i.e. interfacial bond density). By altering the interfacial bond density they could control the nature of the failure in the polymer networks. Three regimes have been observed as a function of the interfacial bond density. At high interfacial bond density they have found a cohesive failure. At low interfacial bond density the failure occurs at the surface. Figure 1.9. has been taken from the simulations of Tsige and Stevens[45] to illustrate these findings. The relation between the nature of the failure and the interfacial bond density as discussed by Tsige and Stevens has been observed also experimentally.[167]

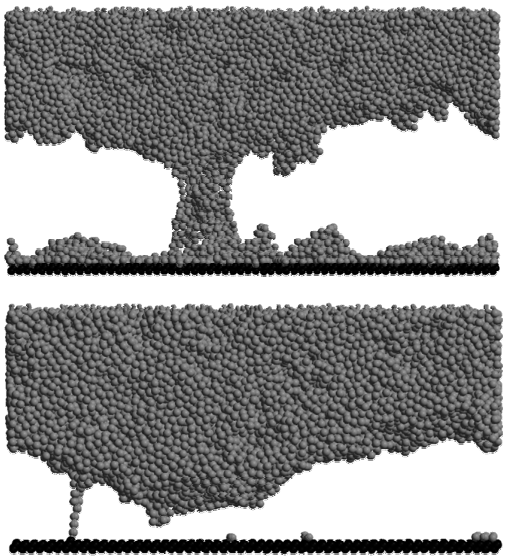

***Figure 1.9.*** *Cohesive failure (top) and interfacial failure (bottom) as a function of the interfacial bond density. The pictures are snapshots from the simulations of Stevens et al. (reference 45).*

## 1.3. RMD Methods Based on Reactive Empirical Force-Fields

### 1.3.1. Reactivity and Standard MD Force Fields

#### *1.3.1.1. The Adiabatic Reactive Molecular Dynamics (ARMD) Technique*

The ARMD[65-68] approach has been used mainly to investigate the rebinding process of NO molecules to myoglobin (Mb) proteins.[65-67] Mb proteins contain heme units with an iron atom that can rebind NO molecules. Factors influencing the reactivity of the Fe centre have been studied by one of the present author in the framework of a qualitative molecular orbital model.[9] It is known that only a subset of the atoms, i.e. the first and second neighbours of the irons is affected by the rebinding process. This subset of atoms that form the active centre of the Mb heme group is shown in Figure 1.10. It is defined by four pyrrole nitrogens (labelled $N_p$) that form a plane, the central Fe atom, the axial $N_\varepsilon 2$ of the proximal histidine fragment as well as the NO molecule.

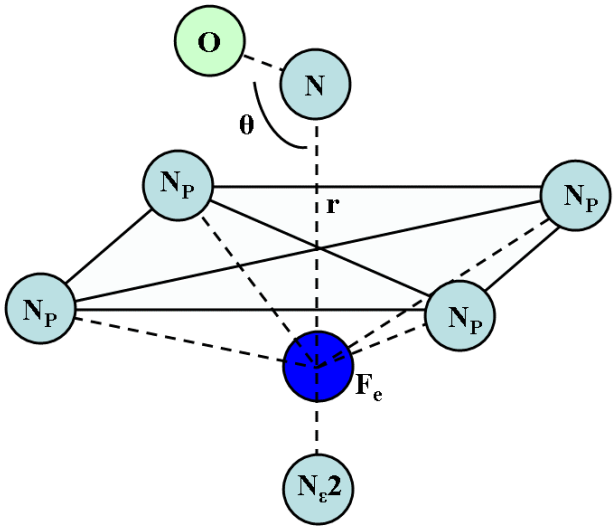


***Figure 1.10.*** *Subset of atoms in a myoglobin heme group which define the active region. Atoms in this region participate in - and are affected by - the rebinding process of Mb with NO molecules. The active region is shown in the bonded state (i.e. Fe-N bond formed). The dashed lines symbolize the bonds between the atoms in the active region. The full lines are drawn to emphasize the planar geometry adopted by the four $N_p$ atoms in the bonded state (i.e. when the Fe-N bond is formed). The diagram is directly inspired from reference 65.*

While the protein interactions outside the active regions are described by the CHARMM force-field,[19] other parameters have been used for the active region.[65-67] In the bonded state, the NO molecule is connected to the heme group via an Fe-N bond (cf. Figure 1.10). This bond is broken in the nonbonded state in which the NO molecule interacts with the active region through inter-molecular interactions. In the bonded state, the decisive interactions in the active region are intra-molecular (cf. Figure 1.10). To describe the reactivity of the system, only the potential energy in the active region is evaluated.[65-67] For the bonded state it is symbolized by $E_{bonded}$ and $E_{nb}$ in the nonbonded state.

The starting configuration of the RMD scheme corresponds to a state with a number of NO molecules dissociated from the Fe atoms.[65-67] Bond formation processes are based on the simultaneous evaluation of $E_{bonded}$ and $E_{nb}$. For an infinite separation between the NO nitrogen and the iron, $E_{nb}$ is below $E_{bonded}$. The opposite holds for small separations. The authors have defined a crossing point for a transition between the two configurations. It is obtained when $E_{bonded} + \Delta - E_{nb} < 0$ (i.e. change in the sign of the expression). The constant $\Delta$ allows defining a common "zero" of energy for $E_{bonded}$ and $E_{nb}$. Two time parameters $t_{cross}$ and $t_{mix}$ have been introduced to describe the reaction dynamics (see Equation 1.9.).[66, 67] The time at which a crossing has been detected is called the

crossing-time $t_{cross}$. The mixing time $t_{mix}$ specifies the time necessary to complete the transition from the state $E_{nb}$ to $E_{bonded}$.

When a crossing is detected the dynamics of the system controlled by $E_{nb}$ is halted to handle the transition. The dynamics is then restarted from the configuration observed at $t_{restart} = t_{cross} - t_{mix}/2$ (in fs). From this point the transition from $E_{nb}$ to $E_{bonded}$ is conducted by a time-dependent switching function S(t) defined as follows,[67]

$$S(t) = \frac{1}{2}[\tanh(\frac{a\,(t - t_{cross})}{t_{mix} - \delta t}) + 1]. \qquad (1.9.)$$

The tanh expression in Equation (1.9.) guarantees a smooth transition from the nonbonded to the bonded state. S(t) starts at zero and reaches an asymptotic limit at 1. The different interaction terms in the bonded state are introduced by weighting them with S(t). The function 1-S(t) decays from one to zero and is used to switch off the interactions in the nonbonded state. Thus, the van der Waals and electrostatic interactions of N and O with the Fe atom and its first neighbours are smoothly switched off by 1-S(t). The Fe-N bond as well as the forming angles and torsions involving these two atoms are introduced by S(t). Following the formation of the Fe-N bond, the proper geometry modifications in the active region are also ensured by the functions S(t) and 1-S(t). In fact, the parameters of the Fe-$N_{\varepsilon}2$ and the Fe-$N_P$ bonds and of the $N_P$-Fe-$N_P$ and the $N_P$-Fe- $N_{\varepsilon}2$ angles in the bonded and nonbonded states differ. An example for both S(t) and 1-S(t) is displayed on Figure 1.11. with the parameters a = 4.8 and $t_{mix}$ = 10 fs (i.e. parameters used in the work of Meuwly et al.[67]) assuming that the crossing has been observed at an arbitrary $t_{cross}$=80 fs.

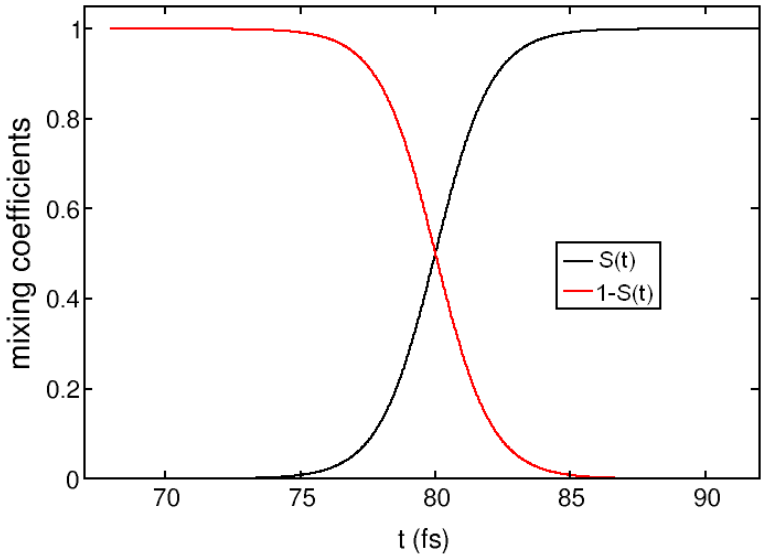


***Figure 1.11.*** *switching functions S(t) and 1-S(t) used in ARMD simulations as derived by the parameters defined in the text.*

For the electrostatic interactions, it is not the energy but the charges that are directly scaled. In this way, the compatibility of the method with the different ways to evaluate electrostatic interactions is maintained. Recrossing from the bonded to the nonbonded state is detected when the sign in the expression $(E_{bonded} + \Delta) - E_{nb}$ switches from a negative to a positive value.

The reactive interactions between NO ligands and heme proteins are decisive in many biological processes.[168-171] The first investigation of Meuwly et al. to understand the influence of the Mb heme relaxation dynamics on the rebinding time scales for NO ligands started in 2002.[65] Experiments show that the rebinding process of NO molecules with Mb, even at room temperature, has a sub-nanosecond timescale adequate for RMD simulations.[168, 169] The computed fraction of nonbonded NO ligands as a function of time (A(t)) has been compared to experiments which have shown that A(t) is well fitted to the double exponential of Equation (1.10.).[170, 171]

$$A(t) = w_1 e^{-\frac{t}{t_1}} + w_2 e^{-\frac{t}{t_2}} \quad \text{with} \quad w_1 + w_2 = 1 \qquad (1.10.)$$

The $w_1$ and $w_2$ factors as well as the two time constants $t_1$ and $t_2$ are adjustable parameters. The ARMD derived time constants[67] $t_1 = 3.6$ ps and $t_2 = 373$ ps are of the same order of magnitude as the experimental values $t_1 = 5.3$ ps, $t_2 = 133$ ps.[170, 171] Thus, a qualitative description of the rebinding process of NO molecules with Mb proteins is possible by RMD schemes. An analysis of the influence

1.of $\Delta$ on the time constants $t_1$ and $t_2$ and on the panel of rebinding geometries has been preformed.[67] Although $t_1$ and $t_2$ are influenced by $\Delta$, the double exponential law remains. The effect of $\Delta$ on the rebinding geometries is negligible. More recently, the ARMD method has been extended to the investigation of NO dioxygenation in truncated hemoglobin.[68]

#### *1.3.1.2. The Reactive Molecular Dynamics Force-Field (RMDff)*

The RMDff force-field has been employed to study the thermal decomposition of polymers at high temperatures.[56-64] It is a reactive force-field which aims at an accurate description of transition states.[63] Bond dissociation is achieved through a linear function defining the reaction coordinate (RC),[63]

$$RC = mr + b. \qquad (1.11.)$$

RC depends on the distance r between the dissociating atoms. m and b are parameterized to match RC = 0 and RC = 1 with values of 5 % and 99 % of the dissociation energy. RC = 0 is the beginning of the dissociation process and RC = 1 the end. The RMD based expression of RC in Equation (1.11.) responds to purely technical reasons and differs from the conventional quantum chemical or kinetic definitions.

With an ethane molecule, we illustrate how RMDff handles the transition states.[63] In analogy to the ARMD case of subsection 1.3.1.1, a bonded state is defined when the central C-C bond is formed. When it breaks (i.e. nonbonded state), the tetrahedral $sp^3$ carbons are transferred into planar $sp^2$ methyl radicals accompanied by changes in bond lengths and angles. The dissociating C-C bond as well as the angles and torsions involving these two carbons have to be gradually turned off and the nonbonded interactions introduced. The process is controlled with the help of two switching functions $S_1(RC)$ and $S_2(RC)$ both defined by Equation (1.12.).[63]

$$S_i(RC) = 0.5[1 - \tanh(a_i(RC - RC_{0,i}))] \text{ with } i = 1, 2. \qquad (1.12.)$$

The parameter $RC_{0,i}$ with i = 1, 2 defines the RC value where the interactions of the bonded and nonbonded states are equally weighted. In contrast to the ARMD case, the switching function $S_i(RC)$ with i = 1, 2 is equal to unity at RC=0 (i.e. dissociation begins) and decays to zero for RC=1 (i.e. dissociation ends). The functions $S_1(RC)$ and $S_2(RC)$ are used to weight the interaction terms in the

bonded state to turn them off.. The dissociation of the C-C central bond is ensured by $S_1(RC)$ while 1-$S_1(RC)$ introduces the nonbonded interactions between the methyl radicals. $S_1(RC)$ and 1-$S_1(RC)$ also handle the geometry modifications in the radicals (i.e. from $sp^3$ to $sp^2$). $S_2(RC)$ continuously suppresses the influence of the dissociating angles and torsions. Guided by quantum mechanical calculations, a faster decay of $S_2(RC)$ is implemented.[63] The RMD-based potential energy of ethane as a function of the central C-C separation is in very good agreement with quantum calculations.[63] RMDff is based on the MM3[21] standard MD force-field. In contrast to the time-dependent switching function defined in Equation (1.9.), $S_i(RC)$ has a spatial dependence through the RC parameter.

We have just presented the most recent and sophisticated version of the reactive force-field of Nyden and co-workers called RMDff and published in 2007.[63] Initial developments of RMDff started already in 1991.[56] At this time, the unimolecular thermal decomposition of single polyethylene chains, either stretched or coiled, with various molecular weights has been investigated by Nyden and Noid[56] (T = 2732 - 3054 K). The calculated decomposition rates have been in reasonable agreement with estimates from statistical theories.[56] Higher polymer stability was achieved with shorter chains and higher degree of coiling. Then, the possibility to reduce the flammability of polyethylene has been investigated by Nyden et al. (T = 500 - 5000 K).[57] They observed the formation of cross-links between the chains at T = 5000 K, a process which reduces the polymer flammability. Experimentally this temperature can be reached via radiation-induced decomposition.[57] Following their RMD simulations, Nyden et al. performed the radiation-induced experiments on poly(ethylene) chains and observed an agreement with their simulations.[57] In a different work, Nyden and Gilman have evaluated the thermal stability of polypropylene chains confined between graphite sheets.[58] The decomposition of these chains has been monitored as a function of the distance from the graphite layers. Stabilization due to polymer-graphite as well as polymer-polymer interactions close to the graphite surface has been observed. In agreement with experiments, stronger decomposition has been evaluated further away from the graphite sheets.[172] Subsequently, RMDff has been employed to study the thermal degradation of several commercial polymers such as poly(styrene),[59] poly(methyl methacrylate)[60] and poly(isobutylene).[61, 62] In a very recent publication (2011) Smith et al. have revisited the poly(ethylene) stability as a function of the molecular weight in a bulk phase formed by several chains.[64] The decreasing stability of polymer chains with increasing molecular weight has been explained by the accumulated strain in the longer polymer chains. The study of Smith et al. has shown that the common practice to adopt rate constants from measurements on small gas phase molecules in kinetic models of thermal polymer decomposition can lead to significant errors.[64]

### 1.3.2. The Many-Body Reactive Potential of Stillinger and Weber (SW)

The reactive potentials developed by Stillinger and Weber are non-additive.[69-74] In their approach, the inter-atomic interactions are described by a combination of two-body ($E_2$) and three body ($E_3$) terms. For a system of N atoms the overall potential $E_P$ has the form,

$$E_P(1,...,N) = \sum_{I<J} E_2(I,J) + \sum_{I<J<K} E_3(I,J,K). \qquad (1.13.)$$

Generally, Stillinger and Weber define the two-body interaction $E_2$ by the product of a distance-dependent function f(r) and an exponential cutoff function $g(r-r_c)$,

$$E_2 = f(r) \times g(r - r_c). \qquad (1.14.)$$

The term f(r) in the definition of $E_2$ reproduces the repulsive and attractive parts of the potential. The exponential-type cutoff function $g(r-r_c)$ ensures a smooth decay of $E_2$ to zero beyond a distance $r_c$. For instance, in the first investigation of the crystalline-liquid phase transition of silicon semiconductors, the following functional form was chosen for the two-body interaction,[69]

$$E_2(r) = \begin{cases} A\,(B\,r^{-p} - r^{-q})\exp((r-r_c)^{-1}), & r < r_c \\ 0, & r \geq r_c \end{cases} \qquad (1.15.)$$

with $f(r) = A(Br^{-p}-r^{-q})$ and $g(r-r_c)= \exp((r- r_c)^{-1})$. The formula contains four parameters adjusted via physical or chemical properties of the chosen system. The general form of the three-body term $E_3$ is,

$$E_3(r_I, r_J, r_K) = h(r_{IJ}, r_{IK}, \theta_{JIK}) + h(r_{JI}, r_{JK}, \theta_{IJK}) + h(r_{KI}, r_{KJ}, \theta_{IKJ}) \qquad (1.16.)$$

In this expression $\theta_{IJK}$ is the angle formed by the three atoms I, J, K considered. The functions h also depend on the distance between the central atom J of the angle and the two outer ones I, K. The most important role of the three-body interaction $E_3$ is to ensure that the desired number of bonds per atom is not surpassed. Below we express the first term $h(r_{IJ}, r_{IK}, \theta_{JIK})$ of (1.16.) employed in the first investigation of Stillinger and Weber, [69]

$$h(r_{IJ}, r_{IK}, \theta_{JIK}) = \lambda \exp[(r_{IJ} - r_c)^{-1} + \gamma (r_{IK} - r_c)^{-1}] \times (\cos\theta_{JIK} - \cos\theta_{tetra.})^2 \quad . (1.17.)$$

The two other terms $h(r_{JI}, r_{JK}, \theta_{IJK})$ and $h(r_{KI}, r_{KJ}, \theta_{IKJ})$ of Equation (1.16.) are obtained by replacing the angle $\theta_{JIK}$ in Equation (1.17.) by $\theta_{IJK}$ and $\theta_{IKJ}$. The function h has two adjustable parameters ($\lambda$, $\gamma$). The two- and three-body parts of the potential vanish at the same cutoff distance $r_c$. If one of the distances $r_{IJ}$ or $r_{IK}$ is beyond $r_c$ then $h(r_{IJ}, r_{IK}, \theta_{JIK})$ vanishes. The cosine terms of $h(r_{IJ}, r_{IK}, \theta_{JIK})$ guarantee the preferential weight of a tetrahedral coordination in the most stable diamond structure of Si crystals. Deviations from the diamond arrangement are penalized by the cosine of the tetrahedral angle employed in Equation (1.17.) ($\cos\theta_{tetra.} = -1/3$). In this way, a valence of four is preferred by the Si atoms.

The Stillinger and Weber method has been developed in 1985 to investigate the anomalous melting behaviour of silicon semiconductors.[69] Later, it has been extended to study liquid sulfur systems,[70-72] elemental fluorine in the liquid phase,[73] and finally the reaction of fluorine atoms with silicon.[74, 76] The latter parameterization has allowed investigating the etching of silicon surfaces as presented below.

Patterned surfaces for microelectronic applications can be generated by surface etching processes.[173-180] During an etching process, atoms, ions or molecules from a beam or a thermalized gas are propelled onto a surface.[173-180] The surface constituents are etched (i.e. detached) by the colliding species. RMD simulations intent is to provide insight into the reaction pathways leading to the experimentally etched products. For instance, in experimental etching of the dimer reconstructed silicon (100) surface (i.e. Si(100)(2×1)) with fluorine atoms, the main etched product is the fluorosilyl molecule $SiF_4$.[174] $SiF_2$, $SiF_3$ and $Si_2F_6$ appear in smaller amounts. The etched products observed in the reactive simulations of Schoolcraft and Garrison[77] were similar to the experimental ones. Nevertheless, the amount of $SiF_3$ has been overestimated and appeared as their main etched product. The RMD result has been attributed to a deficiency of the potential to stabilize sufficiently adsorbed $SiF_2$ fragments. The reaction pathways leading to etched $Si_2F_5$ fragments have also been investigated by Schoolcraft and Garrison[77] to find a pathway towards the formation of $Si_2F_6$ molecules. The RMD-based mechanisms for the formation of etched $Si_2F_5$ are explained in Figures 1.12. and 1.13. Figure 1.14. illustrates the $SiF_4$ formation.

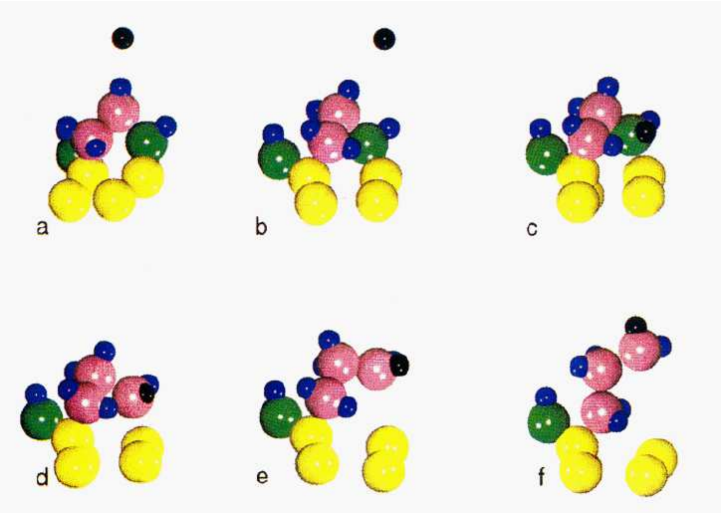


***Figure 1.12.*** *Formation of a tower structure from a fluorinated pyramid as observed in the RMD simulations of Schoolcraft and Garrison[77] with the SW potential. Yellow spheres: nonfluorinated Si atoms, green spheres: monofluorinated Si atoms, orchid spheres: difluorinated Si atoms, red spheres: trifluorinated Si atoms, blue spheres: adsorbed fluorine atoms, black sphere: incoming fluorine atom. (a) The fluorine atom approaches the pyramidal configuration. (b) The same situation as (a) but the view is rotated by 90°. (c) The fluorine atom starts to adsorb to the monofluorinated Si atom (green sphere). (d) Lengthening of the Si-Si bond between the Si atom that has adsorbed the fluorine and the Si atom of the surface dimer. (e) The tower moves to the final configuration. (f) Final structure of the tower. The picture has been taken from reference 77.*

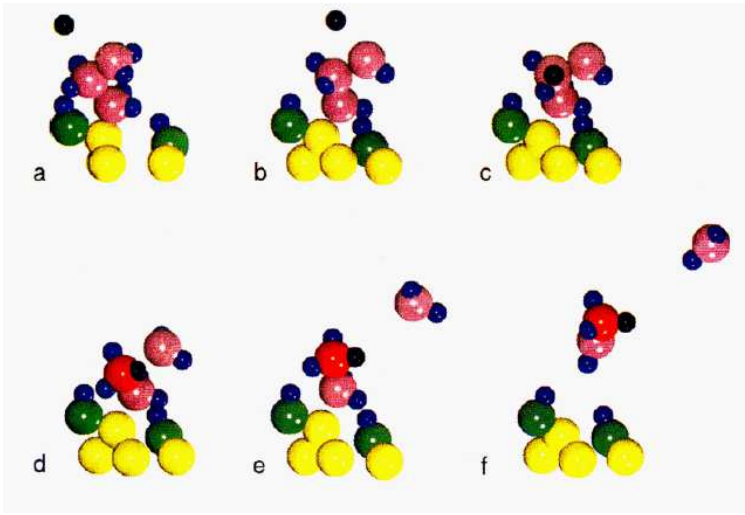


***Figure 1.13.*** *Formation of the $Si_2F_5$ gas phase molecule from the tower structure shown in Figure 1.12. as observed in the simulations of Schoolcraft and Garrison[77] with the SW potential. The colour scheme is identical to Figure 1.12. (a) Incoming fluorine approaching the tower structure. (b) Picture (a) rotated to show that the fluorine atom attacks the middle Si of the tower structure. (c) Fluorine atoms binding to the middle Si atom of the tower structure. At the same time, the Si-Si bond to the crystal lengthens. (d) Trifluorination of the middle Si of the tower structure provoking the etching of the $SiF_2$ fragment. (e) Reorganization of pentafluorodisilane $Si_2F_5$; lengthening of the Si-Si bond to the crystal. (f) The $Si_2F_5$ fragment finally desorbs from the surface. The picture has been taken from reference 77.*

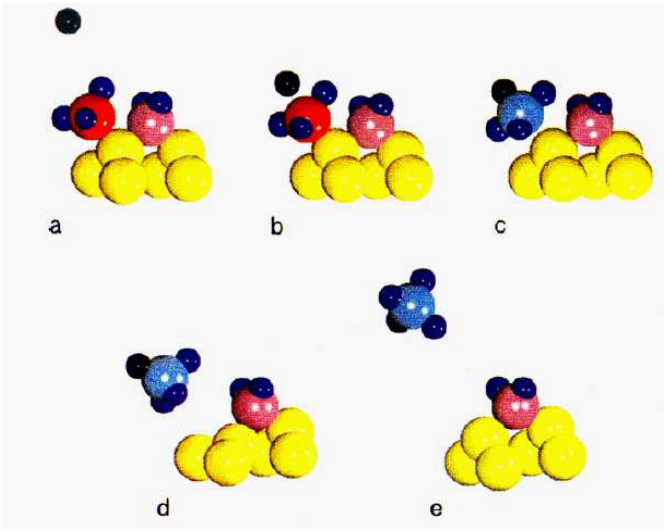


***Figure 1.14.*** *Formation of $SiF_4$ from the reaction of an incoming fluorine with $SiF_3$ adsorbed at the surface as observed in the simulations of Schoolcraft and Garrison[77] with the SW potential. The colour scheme is identical to Figure 1.12 except the turquoise colour that represents a tetrafluorinated Si atom. The picture has been taken from reference 77.*

In their simulations, Schoolcraft and Garrison have reproduced the experimentally determined arrangement of the chemisorbed fluorosilyl layer at the Si surface which is formed by SiF, $SiF_2$ and $SiF_3$ units.[77] It is worth mentioning that the interactions between surface Si and fluorine atoms have been initially optimized by Stillinger and Weber via experimental $SiF_x$ gas phase data.[74] As a main consequence of this gas phase approach, the Si-F bond at the surface was not attractive enough in the initial SW potential. Weakliem et al. have re-parameterized the Si-F interactions against ab initio calculations of fluorine atoms binded to Si surface clusters.[78, 80] A comparison between the original and the improved potential has shown that they agreed in the predicted pathways. In the last decade, DFT calculations[10] of the chemisorption of fluorine atoms and of the desorption barriers of $SiF_x$ units have been in agreement with the values derived by Srivastava et al.[88] using the SW potential. These DFT results reinforced the relevance of the SW potential and the capability of reactive empirical force-fields. Subsequently, the SW potential has been adapted to simulate the etching process of the dimer reconstructed Si surface with various etching species. For instance, Feil et al. have extended the SW potential to the dimer reconstructed Si(100) surface etched by monoatomic or diatomic chlorine.[79] This potential has been used by Hanson et al.[87] who obtained etching yields and a surface roughness in agreement with experiments.[178, 179] In the last decade, further developments have been made by Ohta et al. to simulate the etching process of silicon dioxide surfaces by fluorine and chlorine atoms.[89, 90] The etching of silicon dioxide with fluorocarbon fragments as colliding species has been studied by Smirnov et al.[93] On the basis of ab initio calculations, Nagaoka et al. have developed a version of the SW potential to simulate the etching of the Si(100) surface by HBr plasmas.[94]

### 1.3.3. Bond-Order Potentials

#### *1.3.3.1. Abel-Tersoff-Brenner (ATB) Potentials*

The study of Abell (1985)[181] had been conducted to explain experimental observations that binding energies follow universal relations.[182] The formalism of Abell makes use on the bond-order bond length relation introduced by Pauling already in 1938.[183] Abell represents the interaction between bonded atoms as the sum of parametrizable pair-wise repulsive and attractive functions. The attractive term is weighted by a bond-order function taking into account the influence of the neighboring environment on the strength of a bond.[181] Thus, it is an implicit many-body approach. The formalism of Abell has first been exploited by Tersoff, in 1986, to model elemental silicon.[95] As prescribed by Abell, the potential developed by Tersoff is as follows,

$$E_p = \left[E_2^{REP.}(r_{IJ}) - E_2^{ATT.}(r_{IJ})\right]. \qquad (1.18.)$$

$E_2^{REP.}(r_{IJ})$ and $E_2^{ATT.}(r_{IJ})$ are pair-wise repulsive and attractive Morse-type functions between the interacting particle IJ,

$$E_2^{REP.}(r_{IJ}) = A\exp(-\lambda_1 r_{IJ}) \qquad (1.19.)$$

$$E_2^{ATT.}(r_{IJ}) = BO_{IJ}\exp(-\lambda_2 r_{IJ}). \qquad (1.20.)$$

In formula (1.20.), $BO_{IJ}$ is the bond-order term that weights the strength of the attractive interaction. A, $\lambda_1$ and $\lambda_2$ are adjustable model parameters. The construction of Abell-Tersoff potentials uses chemical trends extracted either from theoretical calculations[181, 182] or experiments.[182, 183] For instance, the strength of the chemical bonds of an atom is reduced with the number of bonded neighbors.[181] Quantitatively, this is expressed by empirical formulas relating bond-order values to the coordination number for different atomic environments.[183] In the Tersoff potential, an exponential relation has been chosen to ensure a decrease of the bond-order term $BO_{IJ}$ as a function of the number of bonded neighbors,[95]

$$BO_{IJ} = B_0\exp(z_{IJ}/b). \qquad (1.21.)$$

In this expression, $z_{IJ}$ is a measure of the number of bonds that are in competition with the reference bond IJ. The parameter b specifies the reduction rate of the bond-order as a function of the number of neighbors and $B_0$ the maximum bond-order value. The term $z_{IJ}$ is expressed as follows,

$$z_{IJ} = \sum_{K\neq I,J}[w(r_{IK})/w(r_{IJ})]^n \times [c + \exp(-d\times\cos\theta_{IJK})]^{-1}. \qquad (1.22.)$$

The function $w(r) = f_c(r)\exp(-\lambda_2 r)$ is defined by the attractive exponential term of Equation (1.20.) weighted by a cutoff function $f_c(r)$. In Equation (1.22.) c and d are adjustable parameters. When bonds are competing, the exponent n in the first term of $z_{IJ}$ specifies how much the closest neighbors are favored with respect to more distant ones. The second term modulates the influence of a competing bond JK on the strength of a bond IJ depending on the angle IJK. In the Tersoff formalism, the local

geometry of the system is thus determined by coordination numbers. This particular feature allows the handling of geometrical modifications when bonds with new neighbors are formed or broken. The silicon potential initially optimized by Tersoff in 1986 did not establish the tetrahedral silicon geometry at the potential energy minimum.[95] An improvement had been proposed by Dodson[96] in 1987 and one year later by Tersoff.[98] The ability of the potential to reproduce elastic properties of silicon structures has been improved in a following work by Tersoff[97] which, however, has led to a less accurate description of certain silicon surfaces. Subsequently, optimizations for carbon and germanium as well as multi-component systems of these elements such as Si-C and Si-Ge have been performed by Tersoff.[100] The new parameterization accurately reproduced carbon single, double and triple bonds but had deficits in describing conjugated carbon bonds as well as the bonding in radicals. The ensuing improvements led to the Reactive Empirical Bond-Order potential (REBO) introduced by Brenner, essentially applied to simulate hydrocarbons and carbon systems.[101] A first version was published in 1990, followed by a second generation in 2002.[110] In the second generation, the attractive and repulsive functions were modified to enhance the simultaneous description of equilibrium distances, energies and force-constants of carbon-carbon bonds.[110] Inter-molecular and torsional terms had not been included in the development because they were not relevant for the systems originally studied, i.e. crystals characterized prevailingly by bonded interactions and small hydrocarbon molecules in the gas phase. Any attempt to transfer the REBO force-field to liquids or polymers has to consider such interactions. They were introduced by Stuart et al. in the Adaptative Inter-molecular Reactive Empirical Bond-order potential (AIREBO).[109] The challenge in the development of AIREBO was the incorporation of the nonbonded interactions and torsions while maintaining the reactive nature of REBO. Due to its universality, a Lennard-Jones potential has been chosen to map the nonbonded part while a cosine function has been used for the torsions. With this setup AIREBO follows the philosophy of most of the standard MD force-fields. Switching functions have been used to smoothly introduce or turn-off the nonbonded interaction during the reaction.[109]

The etching of Si surfaces has been treated not only by SW potentials but also via ATB force-fields. A comparison of the SW and a Tersoff potential developed by Abrams and Graves has been reported in 2000.[108] In this comparative simulation the Si(100) dimer reconstructed surface was etched with energy rich fluorine atoms. The same trends for the yield of ejected Si atoms as a function of the collision energy (10 to 50 eV) and for the saturation concentrations of surface fluorine atoms have been observed with both the SW and the Tersoff potential of Abrams and Graves.[108] Nevertheless, simulations on the spontaneous room temperature etching of Si surfaces performed by

Humbird and Graves[111, 112] using the potential of Abrams and Graves[108] led to a very high concentration of $SiF_3$. A re-parameterization was then performed by Humbird and Graves [111, 112] based on the DFT calculations of Walch.[10] The saturation concentration of fluorine atoms on the reconstructed Si surface agreed well with experimental findings of McFeely et al.[175] for $XeF_2$ which is expected to behave similarly. A reaction probability (number of Si etched per F atoms) of 0.03 was obtained by Humbird and Graves.[111, 112] This value differs not too much from experimental values < 0.001 by Flamm et al.,[173] of 0.025 by Ninomiya et al.,[176] and 0.021 by Vasile and Stevie.[174] From their reactive simulations, Humbird and Graves[111] proposed a mechanism for the formation of gas phase $SiF_4$ that is identical to the Schoolcraft and Garrison[77] suggestion (cf. Figure 1.14.) based on the SW potential. The formation of the gas phase unit $Si_2F_6$ is explained by an attack of an F atom on an adsorbed fluorinated Si tower-like structure. A similar mechanism has been proposed by Schoolcraft and Garrison[77] (cf. Figure 1.13.) for the formation of $Si_2F_5$. Gou et al [125] have used the improved potential of Humbird and Graves[111, 112] in a recent investigation of the etching on the Si(100) dimer reconstructed surface with energy rich Cl. The calculated Si etch yield per incident Cl ion was in good agreement with the simulations of Hanson et al.[87] (SW potential) and with the experiments of Chang and Sawin.[179] ATB investigations on film growths have been reported recently. The growth of diamond films has been investigated by Eckert et al. with the REBO potential (i.e. first generation).[117] The growth of an amorphous silicon layer deposited on the top of a crystalline silicon surface was simulated by Lampin and Krzeminski with the Tersoff potential.[119] A simulation on the deposition of fluorocarbons on a diamond surface has been reported by Devine et al.[124] They used an extension of the second generation REBO potential by Jang and Sinnott[114] to include fluorine atoms. In this study, the results of REBO and a coupled DFT-MD agreed with bare DFT findings. Nevertheless, as widely known from the development of force-fields, the REBO method is not free of shortcomings when treating charged systems. Due to a short interaction cutoff necessary to consider correctly bond-order contributions, some of the transition states observed in the DFT approaches did not appear in the REBO simulations. As a last example of growth reactions we want to cite Fichthorn et al.[127] who have optimized a potential to study the growth of GaAs(001) films. Further extensions of REBO (second generation) by Jang and Sinnott[114] have allowed simulations on the bombardment of polymer materials with high-energy species. In this context, Jang and Sinnott[114] and Végh et al.[118] have investigated chemical modifications of polystyrene as response to the deposition of fluorocarbons[114] and to the bombardment with argon species.[118] An extended version of the AIREBO potential including oxygen interactions has been used by Su et al.[121] to model the

bombardment of poly(methyl methacrylate) by deposition of energy-rich argon species. ATB studies of the bombardment of polymer materials have emerged during the last decade.

### *1.3.3.2. Stillinger and Weber Potential with Bond-Order Correction (SW-BOC)*

In subsection 1.3.2. on many-body potentials, we have cited an optimization of the SW potential by Feil et al.,[79] here denoted as SWF, to model the dimer reconstructed Si(100) surface etching with Cl. The SWF potential has been used by Hanson et al.[87] to predict surface roughnesses and etching yields that are in fair agreement with experiments. Nevertheless, with the SWF potential the strength of the Si-Si and Si-Cl bonds does not depend on the local environment. The limitations of these shortcomings have been quantified in quantum chemical calculations.[5, 8] The independence of the Si-Si and Si-Cl bonds upon local environment has been recognized as a deficiency of the SWF potential that influences the resulting distribution of etched species.[184, 185] The SW-BOC potential of Hanson et al. which intents to correct the SWF errors has the following form,[184, 185]

$$E_P(1,...,N) = \sum_I E_1(N_{Cl}) + \sum_{I<J} BO_{IJ} E_2(I,J) + \sum_{I<J<K} E_3(I,J,K). \quad (1.23.)$$

The main difference between Equation (1.23.) and the SW potential in expression (1.13.) is the presence of two new terms $E_1$ and $BO_{IJ}$ that weights the two-body potential $E_2$. The term $E_1$ maps the correction of the Si-Cl bond strength as a function of the number of Cl neighbours $N_{Cl}$ of an Si atom. The factor $BO_{IJ}$ is the bond-order correction to the Si-Si bond as a function of the number of Cl neighbours of the Si atoms. In comparison to the SWF potential, the SW-BOC corrections increased the amount of $SiCl_2$ by almost a factor of two for impacting atoms at 50 eV and by a factor of 3 at 100 eV. From surface etching experiments of Si(100) with 75 eV impacting argon in the presence of $Cl_2$, $SiCl_2$ is the major etched product obtained. Hanson et al.[184, 185] derived a relative concentration of surface adsorbed $SiCl_2$ of 0.29 and 0.22 with the SW-BOC and the SWF potential. A value of 0.34 was obtained experimentally for 40 eV Cl atom etching.[180] The relative concentrations of adsorbed SiCl were 0.03 (SW-BOC), 0.04 (SWF). A value of 0.087 has been observed experimentally.[180] The SW-BOC potential improves the proportion of adsorbed $SiCl_2$ but not the one of $SiCl_3$. The Si yield (Si atoms desorbed per Cl impact) has also been enhanced by the SW-BOC potential. The average yield obtained from the SW-BOC is 0.39±0.17 and 0.17±0.05 for SWF. An experimental value for reference is 0.39 at 55 eV.[179]

### *1.3.3.3. The ReaxFF Force-Field*

Initially developed by van Duin et al. for hydrocarbons,[129] ReaxFF covers now a broader class of materials. Since the optimization philosophy is always similar, we present here the force-field in its original form. The potential energy function $E_P$ is partitioned into several contributions.

$$E_P = E_b + E_{ang.} + E_{tors.} + E_{vdWaals} + E_{Coulomb} + E_{stability} + E_{conjugation} + E_{undercoordination} + E_{overcoordination}. \quad (1.24.)$$

The decomposition into bond stretching, angle bending, torsions, van der Waals and Coulomb terms in expression (1.24.) resembles the designs of standard MD force-fields. The four last terms are characteristic for the reactive character of the force-field. The bond term $E_b$ has the following form,[129]

$$E_b = -D_e \times BO_{IJ} \times \exp(p_1(1 - BO_{IJ}^{P_1})) \quad (1.25.)$$

where De is the dissociation energy, $BO_{IJ}$ the bond-order between two bonded atoms I and J and $P_1$ is a model parameter. The bond order value depends on the inter-atomic distance as follows,[129]

$$BO_{IJ} = BO_{IJ}^{\sigma} + BO_{IJ}^{\pi} + BO_{IJ}^{\pi\pi} = \exp[P_{bo,1}.(\frac{r_{ij}}{r_{0,\sigma}})^{P_{bo,2}}] + \exp[P_{bo,3}.(\frac{r_{ij}}{r_{0,\pi}})^{P_{bo,4}}] + \exp[P_{bo,5}.(\frac{r_{ij}}{r_{0,\pi\pi}})^{P_{bo,6}}]. \quad (1.26.)$$

$BO_{IJ}^{\sigma}$ is the distance dependence of the bond-order for the σ single bond, $BO_{IJ}^{\pi}$ and $BO_{IJ}^{\pi\pi}$ for the π double and triple bonds. $P_{bo,i}$ with $i = 1$ to $6$ are adjustable parameters. The lengths $r_{0,\sigma}$, $r_{0,\pi}$ and $r_{0,\pi\pi}$ are equilibrium distances for single and, if realized, double and triple bonds. In the case of the carbon-hydrogen or hydrogen-hydrogen bonds only the $BO_{IJ}^{\sigma}$ exponential survives. As an example, the optimized exponentials of Equation (1.26.) for carbon-carbon bonds are shown in Figure 1.15. It shows that the maximum bond-order for a carbon bond is 3 (i.e. triple bond). For quantum chemists, it might be somehow surprising that the maximum value of 3 for the sum of the bond-order terms is, in Figure 1.15., reached at a C-C distance normally not accessible (0.1 nm). It is here an example that shows the inevitable loss of chemical accuracy when using force-fields. This example also shows that the success of force-fields is determined by the flexibility of the functions. Manipulations of technical nature are also required to maintain a consistent chemical environment. For instance, residual interactions between second neighbors can yield hypervalent atoms i.e. more than four (one) bonds for C (H)

atoms. Complex correction functions are applied to remove these artificial residues.[129] As their presence is only related to technical reasons they are not commented here.

In Figure 1.16., we have plotted $E_b$ as a function of the bond distance. As can be seen $E_b$ alone does not consider atomic core repulsion. In fact, one peculiarity of ReaxFF is the combination of $E_b$ and $E_{vdWaals}$ for all pairs of atoms. The repulsive tail of the van der Waals interactions provides the missing atomic core repulsions. Later, we come back to this peculiarity of ReaxFF.

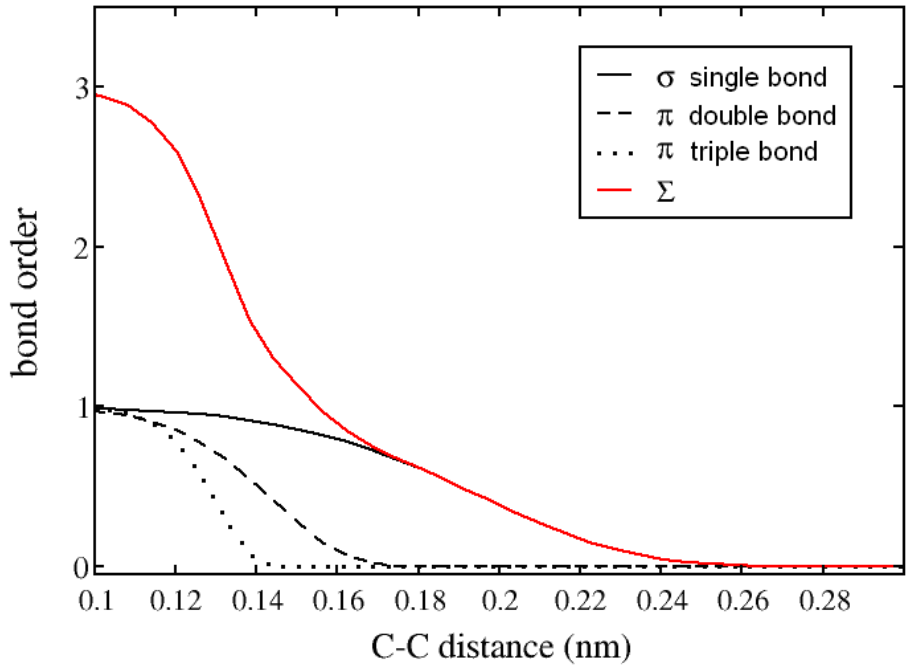


***Figure 1.15.*** *Dependence of the bond-order element for a C-C σ single, π double, and π triple bond as a function of the inter-nuclear separation with the parameters of reference 129. The Σ curve results from the summation of the C-C bond-order element of the σ single, π double, and π triple bond.*

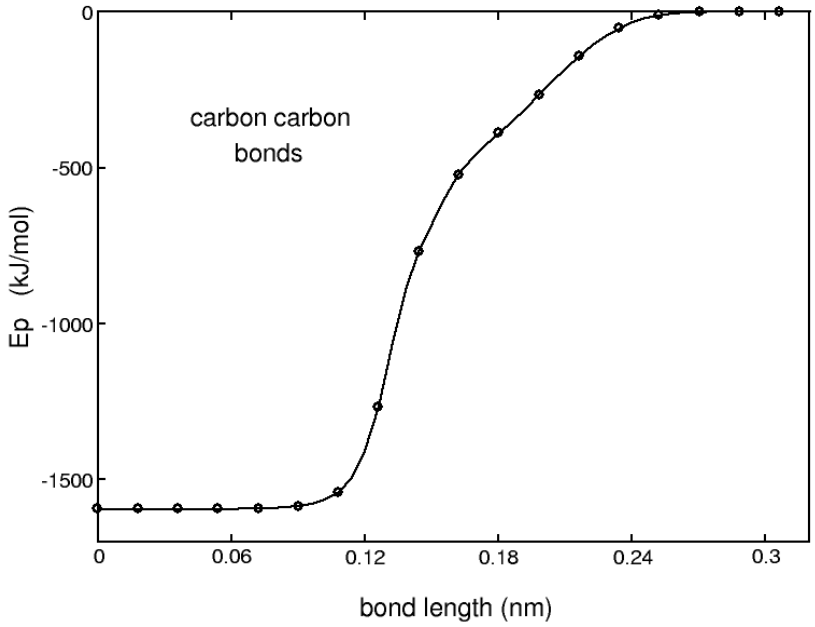


***Figure 1.16..*** *Potential energy from equation (25) as a function of the carbon-carbon bond length using the parameters optimized in reference 129.*

The angle term has the following form,[129]

$$E_{ang.} = f_{cutoff}(BO_{IJ}) \times f_{cutoff}(BO_{JK}) \times f_{correct}(\Delta_j) \times \left\{ f_{const} - f_{const} \exp\left[ -a(\theta_{eq.} - \theta_{ijk})^2 \right] \right\} \quad (1.27.)$$

The function $f_{cutoff}$ depends on the bond-order values of the bonds IJ and JK that form the angle IJK. They are of exponential character ensuring a smooth decay to zero of the angle interaction when the bond-order of the bonds IJ or JK goes to zero. The function $f_{correct}$ is a bond-order correction term that avoids unphysical valences. $f_{const}$ stands for the angle force constant. $\theta_{IJK}$ denotes the angle IJK with equilibrium value $\theta_{eq}$. The value of $\theta_{eq}$ depends on the number of π bonds (i.e. the sum of π bond-orders) formed by the central atom J,[129]

$$\theta_{eq.} = \pi - \theta_{0,0}\{1 - \exp[P_2(2 - SBO_\pi)]\}. \quad (1.28.)$$

$SBO_\pi$ is the sum of the π bond-orders while $P_2$ is a model parameter. $\Theta_{0,0}$ is chosen in a way to guarantee the proper angle for each valence state. With this scheme $\theta_{eq.}$= 109.47° is observed when the sum of the π-bond-orders is zero, $\theta_{eq.}$= 120° when the sum of π-bond-orders is one $\theta_{eq.}$= 180° when it

is equal to two. The specification of $\theta_{eq}$ is thus performed "on-the-fly" from the influence of the atomic environment. This allows the proper management of angle modifications during a reaction. $E_{stability}$ is an exponential bond-order dependent function that ensures the stability of valence angles of compounds such as allenes that share two $\pi$ bonds with a central atom. The torsional element $E_{tors}$ is as follows, [129]

$$E_{tors} = f_{cutoff}(BO_{IJ}, BO_{JK}, BO_{KL}) \times \sin\theta_{IJK} \times \sin\theta_{JKL} \left(\frac{V_2}{2} f_{mod.}(BO_{JK})(1-\cos 2\theta_{IJKL}) + \frac{V_3}{2}(1+\cos 3\theta_{IJKL})\right). \quad (1.29.)$$

Here again, the function $f_{cutoff}$ depends on the bond-order values of the bonds IJ, JK and KL involved in the torsional interaction spanning the atomic quartet IJKL. It ensures a smooth decay to zero if the bond-order value of the bonds IJ, JK or KL goes to zero. The sine terms imply that the energy $E_{tors}$ vanishes when the angles IJK and JKL both have a value of 180°. The last cosine terms allow a fine tuning of the torsional equilibrium angle as well as the torsional barriers. $V_2$ modulates the function $f_{mod.}(BO_{JK})$ that depends on the bond-order of the central bond JK. $f_{mod.}(BO_{JK})$ controls the increase in rotation barriers when the central bond JK has a bond-order value of two. $E_{tors}$ is used only for non-aromatic hydrocarbons. In the case of aromatic hydrocarbons, the rotation about a bond is described by the term $E_{conjugation}$, [129]

$$E_{conjugation} = f_{conj.}(BO_{IJ}, BO_{JK}, BO_{KL}) \times P_3 \times (1+\sin\theta_{IJK} \times \sin\theta_{JKL}(\cos^2\theta_{IJKL} - 1)) \quad (1.30.)$$

The function $f_{conj.}$ has a maximum when the bond-orders of the bonds IJ, JK and KL are simultaneously equal to 1.5 as in benzene and other aromatic hydrocarbons. $P_3$ is a model dependent constant. The sine functions ensure that there is no contribution of $E_{conjugation}$ on the forces when the angles IJK and JKL have both a value of 180º. The term $E_{undercoordination}$ takes into account the energy contribution of two undercoordinated atoms i.e. atoms that have not reached their full valence. $E_{overcoordination}$ refers to a correction term for unphysically high coordination numbers. As mentioned above, an important peculiarity of ReaxFF is the consideration of nonbonded interactions between all atom pairs including first, second and third neighbors. The van der Waals potential is described by a "shielded" Morse function. A distance dependent screening reducing interactions in the case of the first, second and third neighbor of an atom is incorporated. The Coulomb interaction is screened in a similar way. The inclusion of the nonbonded elements between all atom pairs ensures that the transition from bonded to nonbonded potentials is straightforward and smooth. Switching functions are not required.[129]

Once the interaction terms and bond-order functions have been defined in Equation (1.26.), ReaxFF parameters are optimized to reproduce properties of systems where the atoms of interest have different chemical environments. The target properties are derived from extensive quantum chemical calculations. In the case of hydrocarbons[129] the optimization has been performed considering non-saturated and saturated as well as conjugated and non-conjugated systems. Radicals and crystal structures of carbon (graphite, diamond) have also been included. The ensemble of parameters that yields the best compromise in the reproduction of the heats of formation, equilibrium bond lengths and bond angles for each of the hydrocarbon and carbon systems is accepted for the force-field.

As an example of ReaxFF applications, different steps in the formation of carbon nanotubes (CNTs) will be commented on. CNTs have become important materials due to their interesting mechanical properties. An important step in the growth of CNTs is the decomposition of hydrocarbon precursor fragments catalyzed by nickel nanoparticles. In this context, Mueller et al. have studied the decomposition of several saturated and unsaturated hydrocarbons.[148, 149] They have observed a lower activation energy for unsaturated hydrocarbons that are able to use their π electrons for chemisorption on nickel nanoparticles. For saturated hydrocarbons a C-H bond has to be broken first. A dehydrogenated carbon is released for a CNT growth due to the creation of four bonds with the nickel surface atoms involving a C-C bond breaking. Here, it is the first step of CNT growth that is simulated. In a different work[137] the capacity of Ni, Co and Cu catalysts to assemble acyclic and cyclic carbon chains has been compared. Nielson et al.[137] have observed a high catalytic activity of Ni and Co in branching carbon fragments and a very weak one for Cu. The simulation trends are in line with experiments[186-190] showing the predictive power of ReaxFF. Interesting snapshots from the work of Nielson et al.[137] are presented below. The initial system formed by linear and cyclic carbon chains and the Cu, Ni and Co catalysts is shown in Figure 1.17.[137] The configurations (a), (b), (c) and (d) in Figure 1.18. have been extracted after from the reactive simulations 90 ps.[137] The simulations without any catalysts (picture (a), Figure 1.18.) do not show any branching. Snapshots (b) and (c) exhibit a certain amount of branching resulting from the Co and Ni catalytic activities. Less branching is realized in snapshot (d) with a Cu catalyst. The configuartion (e) shows a high degree of carbon branching which has been obtained after 750 ps in the presence of Ni ((c) has been extracted after 90 ps).

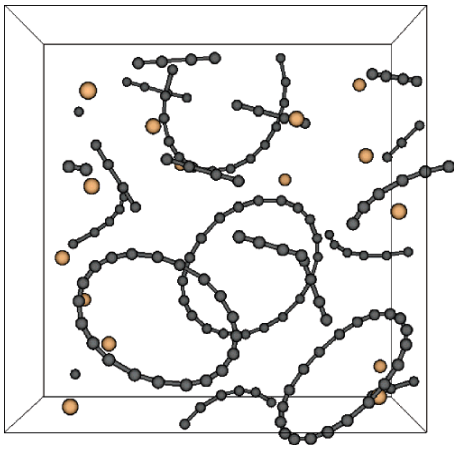

***Figure 1.17.*** *Initial system composed by acyclic and cyclic carbon units in the presence of Cu, Ni, or Co catalysts. The snapshot has been taken from reference 137.*

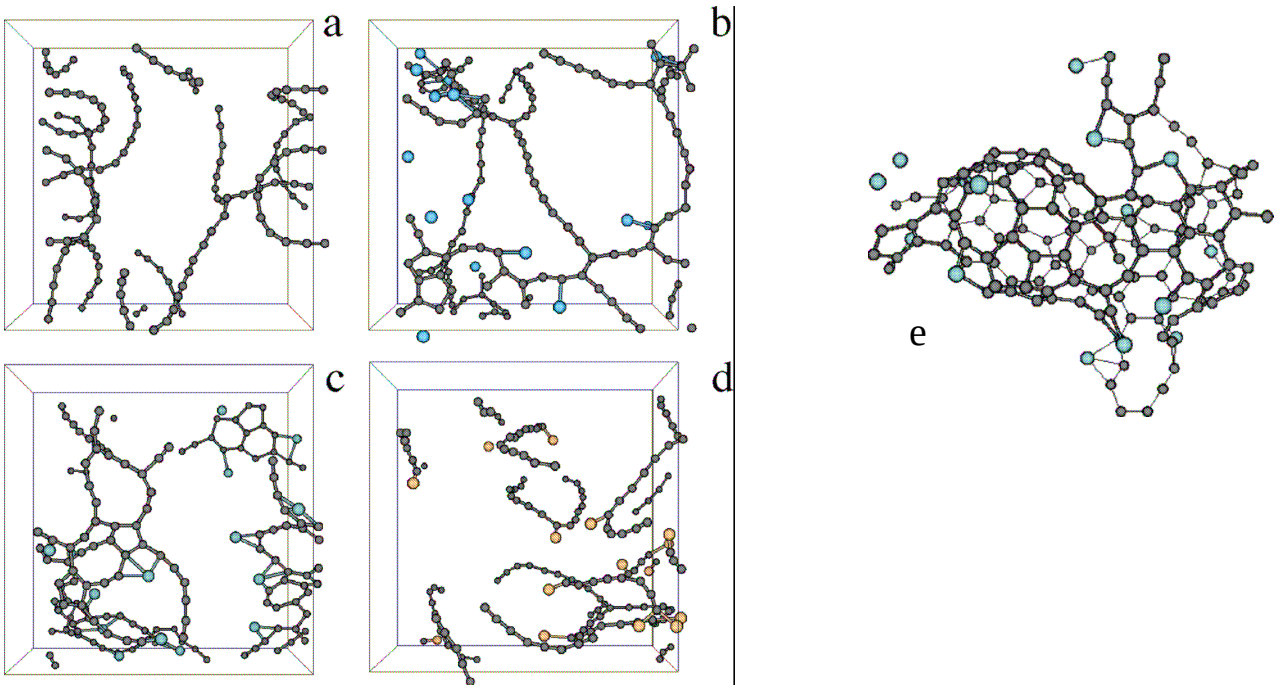


***Figure 1.18.*** *Degree of carbon branching in the absence of catalysts (a), and under the influence of the activity of Co (b), of Ni (c) and of Cu (d). (a), (b), (c) and (d) are obtained at 1500 K after 90 ps of simulation time. Picture (e) shows the high degree of carbon branching obtained after 750 ps with the Ni catalyst. (c) and (e) describes the same system at different times (90 and 750 ps) and highlight the capacity of the Ni catalyst to assemble nanotube-like structures. The snapshots have been taken from reference 137.*

These two examples illustrate impressively the power of ReaxFF to study catalyzed CNT growth. We would like to cite some other catalytic processes investigated by ReaxFF.[140, 151]

Hydrogen storage is a topic related to the current need of developing “clean” fuel sources. Due to its high hydrogen mass ratio, ammonia borane ($BH_3NH_3$) is a promising candidate for such applications. Weismiller et al [152] have studied a single ammonia borane molecule in a temperature range of 1000 - 1750 K highlighting the unimolecular release of the first hydrogen molecule ($H_2$). Then, investigations with several ammonia borane molecules (T= 300 - 5000 K) showed that the last hydrogen molecule is released through a polymerization step.[152] It is worth mentioning that the formation of polymeric aminoborane has been observed also in experiments.[191] Other RMD simulations on the capacity of chemical compounds to store hydrogen atoms have been reported in the literature.[133, 134, 136]

Sound knowledge on the detonation mechanisms of explosive materials is crucial for safety reasons. It is obvious that such scientific fields would undoubtedly profit from investigation methods that do not require direct contact with chemicals. Using ReaxFF, van Duin et al. have demonstrated that the thermal initiation of triacetonetriperoxide (TATP) is entropy-driven.[139] In fact, the similarity of the initial event for a single TATP molecule and for the condensed phase indicates its unimolecular kinetics. In another work, the decomposition mechanism in a pentaerythritol (PETN) (cf. Figure 1.19.) has been provoked by propagating weak and strong shock waves through an idealized crystalline form (i.e. absence of crystal defects).[142]

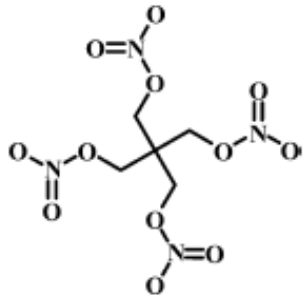

***Figure 1.19.*** *Representation of the pentaerythritol molecule simulated in the work of Budzien et al.[142] The picture is taken from reference 142.*

The calculated detonation velocity in the crystal[142] was in reasonable agreement with an experimentally established correlating the detonation velocity to the PETN crystal density.[192] From the reactive simulations, Budzien et al.[142] have observed primary reaction products close to the shock wave front and delayed secondary ones. According to the RMD simulations the initiation reaction pathway is non-unique. As main pathways the authors have suggested the release of $NO_2$, $NO_3$ and $CH_2NO_3$ (cf. Figure 1.19.). Other decomposition products were observed at the shock wave front.[142]

In the present paragraph we have summarized some representative topics analyzed with ReaxFF. Reactive simulations by Chenoweth et al[141]. have treated the gas-phase high-temperature oxidation of methane, propene, o-xylene and benzene. Still in the field of combustion, the formation of soot has been investigated by Kamat et al.[145] In a different field, the technological importance of polymers has promoted studies on their thermal degradation properties. In this context, poly(dimethylsiloxane) (PDMS) has been investigated by Chenoweth et al.[132] Reactions of water and dimethyl methylphosphonate at the interface with silica nanoparticles and surfaces have been simulated by Fogarty et al.[144] and Quenneville et al.[150] Finally, we want to cite an optimization of ReaxFF to simulate reactions in the presence of gold surfaces and nanoparticles that has been performed by Keith et al.[146]

## 1.4. Summary and Outlook

Reactive molecular dynamics has become a common name to designate molecular dynamics simulations implementing chemical reactions via a force-field approach. The present review has shown that the field of RMD is strongly growing since the pioneery works of Stillinger and Weber or Tersoff in the mid 1980s. These authors presented RMD schemes that dominated the literature for about twenty years. In the past decade a number of new methods have been brought to maturity. In our review, the first class of implementations covers all RMD methods using a reaction cutoff distance. With such methods the transition between educt and product states is sudden. They are based on the alternation of reactive and non-reactive conventional MD steps. The latter are required to remove eventual strong forces due to the sudden reactive transition and to define the diffusion time-scale between two reactive steps. Due to their simplicity, reaction cutoff methods can be used to study collective reactive processes such as chain-like or cross-linking polymerizations. The second class of RMD implementations uses empirical reactive force fields parameterized via quantum chemical calculations or experimental data. They have been developed to describe chemical reactions as realistically as possible with a force-field approach. Some of the reactive force-fields, such as RMDff

or ARMD, rely on the modification of widely adopted standard MD force-fields. Reactive force-fields can also be found in the form of many-body interactions, such as Stillinger and Weber potentials, or in the form of implicit many-body bond-order potentials such as Abell-Tersoff-Brenner force-fields or ReaxFF. The continuous and smooth transition from the educts to the products that is ensured by reactive force-fields requires a high degree of sophistication in the design of the force-fields. In contrast to the first class of RMD implementations, reaction kinetics or mechanisms as well as transient geometries can be investigated with reactive force-fields.

The large diversity of the topics that can be treated by the different empirical reactive force-fields offers an interesting insight into the strength and limitations of these schemes. Many topics have been treated with bond-order potentials such as Abell-Tersoff-Brenner force-fields or ReaxFF. During the last decade, ReaxFF has been already applied to different systems. Bond-order based approaches are easier to parameterize and to transfer than Stillinger and Weber or reactive potentials based on modified standard MD force-fields. Nevertheless, it is not obvious how reactive bond-order implementations can reproduce transient geometries. In this context, some advancement has been made with the RMDff implementation. In RMDff, the switching functions ensuring a smooth transition during dissociative reactions are parameterized via ab initio calculations to reproduce the energy of transient structures.[63]

Discussions on the validity and transferability of the results obtained via empirical reactive potentials have been pursued since the introduction of the Stillinger-Weber and Abell-Tersoff-Brenner potentials in 1985. From a quantitative point of view, the results of such RMD simulations are, in general, not yet satisfactory. Nevertheless, there is now ample evidence that the qualitative results are physically meaningful and trustable. For instance, the comparative study of Abrams and Graves[108] showed that a Stillinger-Weber and a Tersoff potential lead to the same trends. Furthermore, the etching mechanisms obtained from the Tersoff potential by Abrams and Graves[108] are the same as the ones described in 1991 by Schoolcraft and Garrison[77] with a Stillinger-Weber potential. When presenting the application domains of the other reactive force-fields (RMDff, ARMD, and ReaxFF) we could also cite many results that were in qualitative agreement with experiments.[58, 67, 137, 152] Therefore, further efforts in the field of reactive potentials seem be the refinement of the force-fields to match experimental results quantitatively. The SW-BOC method of Hanson et al.[184, 185] is an example of a refinement for the SW approach. Nevertheless, one has to accept that any refinement of reactive force-field parameters is coupled to the availability of quantum chemical or experimental data. Apart from the refinement of the potentials, technical improvements such as the parallelization of the reactive programs are also needed. Despite the tremendous gain in computing time achieved with

RMD implementations, some of the reactive processes investigated are still only accessible under extreme conditions. For instance, very high temperatures have to be used in the study of thermal polymer degradation with RMDff or in the different investigations performed with ReaxFF to observe reactive processes in the time scale of RMD. Among the future challenges of RMD simulations, polymerization processes via empirical reactive force-fields might be a suitable candidate. Up to now, only thermal polymer decomposition and beam irradiation of polymer materials have been studied. At present, polymerization reactions are studied only qualitatively with generic potentials. Nevertheless, reactive simulations such as the one of Liu et al.[53] on polymer brushes have shown how the underlying physics of experimental growth reactions can be revealed by generic models.

At the end of this review, we propose in Table 1.1. a summary of representative RMD simulations for a broad spectrum of applications. The purpose of the present review has not been to present all RMD simulations that have been performed. Instead, from a representative literature research our intention has been to classify the most important RMD approaches and to exemplify how RMD simulations can lead to an understanding of experimental results. From our point of view, the field of RMD opens promising perspectives for large-scale reactive simulations.

| REACTION CUTOFF DISTANCE METHODS | | |
|---|---|---|
| **Application:** Generation of equilibrated polymer structures | | |
| **System** | **Force-field** | **References** |
| Cross-linked atomistic epoxies | Standard MD force-field | 44, 47, 51 |
| Cross-linked atomistic poly(methacrylate) | Standard MD force-field | 41 |
| Cross-linked atomistic poly(vinyl alcohol) | Standard MD force-field | 52 |
| Amorphous atomistic poly(ethylene oxide) | Standard MD force-field | 39 |
| Coarse-grained polystyrene | Tabulated potentials | 54 |
| Generic polymer systems | Reflected WCA<br>FENE | 40<br>50 |
| **Application:** Qualitative investigations of cross-linking and chain polymerizations | | |
| **System** | **Force-field** | **References** |
| Fracture in polymer networks | Quartic potential | 42, 43, 45, 46 |
| Growth history of bulk polymerizations | Reflected WCA<br>Tabulated potentials | 40<br>54 |
| Surface-initiated growth of polymer brushes | FENE | 53 |
| Polymerization-induced phase separation in mixtures | Reflected WCA | 48 |
| **EMPIRICAL REACTIVE FORCE-FIELDS** | | |
| **Application:** Biophysical processes | | |
| **System** | **Force-field** | **References** |
| Rebinding process of NO to myoglobin | ARMD | 65, 66, 67 |
| NO dioxygenation in truncated hemoglobin | ARMD | 68 |
| **Application:** Thermal decomposition of polymers | | |
| **System** | **Force-field** | **References** |
| Poly(ethylene) | RMDff | 56, 57, 61,64 |
| Poly(styrene) | RMDff | 59 |
| Single chain or nano-confined poly(propylene) | RMDff | 58, 61 |
| Poly(methyl methacrylate) | RMDff | 60 |
| Poly(isobutylene) | RMDff | 61, 62 |
| Poly(dimethyl siloxane) | ReaxFF | 132 |

| **Application:** Silicon surface etching | | |
|---|---|---|
| **System** | **Force-field** | **References** |
| Si(100) / fluorine or chlorine | SW<br>ATB | 78, 80, 83<br>108 |
| Si(100) / argon | ATB | 99 |
| Si(100) / HBr or Br | SW | 94 |
| Si(100)/ fluorocarbons | ATB | 107 |
| Si(100)/ argon + CF2 and F | ATB | 113 |
| Si(100)( chlorinated or fluorinated) / argon | SW | 81, 82 |
| Si(100)(fluorinated) / F2 | SW | 84 |
| Si(100)(methylated) / hydrogen | ATB | 122 |
| Si(100)(2×1) / fluorine or chlorine | SW<br>ATB | 74, 75, 76, 77<br>112, 111, 125 |
| Si(100)(2×1) / argon + fluorine or chlorine | SW | 92 |
| Si(100) (2×1) / argon | ATB | 99 |
| Si(100) (2×1)(fluorinated) / argon , F or F2 | SW | 84, 85 |
| Si(001) / chlorine | SW | 87 |
| Si(001)(2×1) / chlorine | SW<br>SW-BOC | 87<br>184, 185 |
| Si(110) / argon | ATB | 99 |
| Si(111)(chlorinated) / argon | SW | 79 |
| SiO2 / chlorine, fluorine or fluorocarbons | SW | 89, 90, 93 |
| **Application:** Beam deposition of chemical species on polymer materials | | |
| **System** | **Force-field** | **References** |
| Poly(styrene) + fluorocarbons | ATB | 114 |
| Poly(styrene ) + argon<br>Poly(styrene ) + argon + hydrogen or | ATB | 118 |
| Poly(methyl methacrylate) + argon | ATB | 121 |
| **Application:** Interaction of chemical species with diamond surfaces | | |
| **System** | **Force-field** | **References** |
| Growth of diamond films | ATB | 101, 102 |
| Diamond (100) surface bombarded by C2H5 | ATB | 120 |
| Deposition of polyatomic fluorocarbons on diamond surface | ATB | 124 |

| | | |
|---|---|---|
| Hydrogen terminated (111) diamond surface bombarded by molecular clusters | ATB | 105 |
| **Application:** Detonation mechanisms in high-energy materials | | |
| **System** | **Force-field** | **References** |
| Thermal decomposition of cyclic-$[CH_2N(NO_2)]_3$ | ReaxFF | 138 |
| Thermal initiation of triacetonetriperoxide | ReaxFF | 139 |
| Shock propagation through a pentaerythritol tetranitrate crystal | ReaxFF | 142 |
| Detonation chemistry with model systems | ATB | 103, 106 |
| **Application:** Energy storage in hydrogenated compounds | | |
| **System** | **Force-field** | **References** |
| Interaction of H with single-walled boron nitride nanotubes | ReaxFF | 134, 136 |
| Abstraction of H2 from magnesium hydride systems | ReaxFF | 133 |
| Dehydrogenation of ammonia borane | ReaxFF | 152 |
| **Application:** Metal-catalyzed reactions | | |
| **System** | **Force-field** | **References** |
| Nickel-catalyzed hydrocarbon reactions | ReaxFF | 148, 149 |
| Vanadium oxide-catalyzed hydrocarbon reactions. | ReaxFF | 140 |
| Cobalt, nickel, copper-catalyzed formation of carbon nanotubes | ReaxFF | 137 |
| Hydrogen dissociation on Pd surfaces | ATB | 126 |
| **Application:** Combustion reactions | | |
| **System** | **Force-field** | **References** |
| Oxidation reactions of hydrocarbons | ReaxFF | 141 |
| **Application:** Epitaxial growth | | |
| **System** | **Force-field** | **References** |
| Solid phase epitaxy of Si(100), (110) and (111) | ATB | 119 |
| Homoepitaxial growth of GaAs (001) | ATB | 127 |

***Table 1.1.*** *Collection of representative reactive molecular dynamics simulations. The table is subdivided into the main RMD classes (i.e. reaction cutoff distance methods and empirical reactive*

*force-field approaches). For each of these two classes, different reactive processes are cited in the table. The first column lists the system studied, the second one defines the force-field in the RMD method used and the last one provides corresponding references. In case of the surface etching simulations, the systems are presented by citing first the surface and then the etching species using the symbol / as a separator. Labels such as (2×1) and (1×1) symbolize the symmetry of reconstructed surfaces.*

## References


[1] M. T. Yin, M. L. Cohen, *phys. Rev. Lett.* **1980**, *45*, 1004.

[2] M. C. Böhm, R. Gleiter, *Theor. Chim. Acta* **1981**, *59*, 127.

[3] M. C. Böhm, C. Elsässer, M. Fähnle, E. H. Brandt, *Chem. Phys.* **1989**, *130*, 65.

[4] C. J. Wu, E. A. Carter, *J. Am. Chem. Soc.* **1991**, *113*, 9061.

[5] M. D. Allendorf, C. F. Melius, *J. Phys. Chem.* **1993**, *97*, 720.

[6] G. D. Smith, R. L. Jaffe, *J. Phys. Chem.* **1996**, *100*, 18718.

[7] M. Akbulut, W. C. Ermler, D. M. Kalyon, *Comp. and Theor. Polymer Science* **1997**, *7*, 75.

[8] R. C. Boehm, J. D. Kress, R. L. Martin, P. J. Hay, *J. Comput. Chem.* **1998**, *19*, 2075.

[9] C. Kollmar, S. F. Fischer, M. C. Böhm, *Z. Naturforsch.* **1998**, *53a*, 755.

[10] S. P. Walch, *Surf. Sci.* **2002**, *496*, 271.

[11] K. V. Cauter, V. V. Speybroek, M. Waroquier, *ChemPhysChem* **2007**, *8*, 541.

[12] H. Li, L. Zhang, Z.-X. Wang, Y. Hu, *J. Phys. Chem. A* **2010**, *114*, 2697.

[13] M. D. Miller, A. J. Holder, *J. Phys. Chem. A* **2010**, *114*, 10988.

[14] H.-C. Fang, Z. H. Li, K.-N. Fan, *Phys. Chem. Chem. Phys.* **2011**, *13*, 13358.

[15] D.-M. Han, G.-L. Dai, H. Chen, Y. Wang, A.-G. Zhong, C.-P. Lin, D. Chen, *Int. J. Quant. Chem.* **2011**, *111*, 2898.

[16] J. Aqvist, A. Warshel, *Chem. Rev.* **1993**, *93*, 2523.

[17] F. Ahmadi, N. Jamali, S. Jahangard-Yekta, B. Jafari, S. Nouri, F. Najafi, M. Rahimi-Nasrabadi, *Spectrochim. Acta, Part A* **2011**, *79*, 1004.

[18] P. M. Zimmerman, M. Head-Gordon, A. T. Bell, *J. Chem. Theory. Comput.* **2011**, *7*, 1695.

[19] B. R. Brooks, R. E. Bruccoleri, B. D. Olafson, D. J. States, S. Swaminathan, M. Karplus, *J. Comput. Chem.* **1983**, *4*, 187.

[20] S. J. Weiner, P. A. Kollman, D. A. Case, U. C. Singh, C. Ghio, G. Alagona, S. Profeta, P. Weiner, *J. Am. Chem. Soc.* **1984**, *106*, 765.

[21] N. L. Allinger, Y. H. Yuh, J. H. Lii, *J. Am. Chem. Soc.* **1989**, *111*, 8551.

[22] F. H. Westheimer, J. E. Mayer, *J. Chem. Phys.* **1946**, *14*, 733.

[23] J. E. Eksterowicz, K. N. Houk, *Chem. Rev.* **1993**, *93*, 2439.

[24] M. C. Böhm, R. Ramírez, J. Schulte, *Mol. Phys.* **2005**, *103*, 2407.

[25] M. C. Böhm, R. Ramírez, J. Schulte, *Chem. Phys.* **2007**, *342*, 1.

[26] B. J. Alder, T. E. Wainwright, *J. Chem. Phys.* **1959**, *31*, 459.

[27] H. J. C. Berendsen, J. P. M. Postma, W. F. van Gunsteren, A. DiNola, J. R. Haak, *J. Chem. Phys.* **1984**, *81*, 3684.

[28] S. Nosé, *J. Chem. Phys.* **1984**, *81*, 511.

[29] W. G. Hoover, *Phys. Rev. A* **1985**, *31*, 1695.

[30] R. D. Groot, P. B. Warren, *J. Chem. Phys.* **1997**, *107*, 4423.

[31] M. Clark, R. D. Cramer III, N. van Opdenbosch, *J. Comput. Chem.* **1989**, *10*, 982.

[32] S. L. Mayo, B. D. Olafson, W. A. Goddard III, *J. Phys. Chem.* **1990**, *94*, 8897.

[33] A. K. Rappe, C. J. Casewit, K. S. Colwell, W. A. Goddard III, W. M. Skiff, *J. Am. Chem. Soc.* **1992**, *114*, 10024.

[34] W. L. Jorgensen, D. S. Maxwell, J. Tirado-Rives, *J. Am. Chem. Soc.* **1996**, *118*, 11225.

[35] H. Sun, *J. Phys. Chem. B* **1998**, *102*, 7338.

[36] S. Izvekov, G. A. Voth, *J. Chem. Phys.* **2002**, *116*, 10372.

[37] Y. Wu, C. J. Mundy, M. E. Colvin, R. Car, *J. Phys. Chem. A* **2004**, *108*, 2922.

[38] K. Kwac, E. Geva, *J. Phys. Chem. B* **2011**, *115*, 9184.

[39] B. Lin, P. T. Boinske, J. W. Halley, *J. Chem. Phys.* **1996**, *105*, 1668.

[40] R. L. C. Akkermans, S. Tøxvaerd, W. J. Briels, *J. Chem. Phys.* **1998**, *109*, 2929.

[41] D. C. Doherty, B. N. Holmes, P. Leung, R. B. Ross, *Comp. and Theor. Polymer Science* **1998**, *8*, 169.

[42] M. J. Stevens, *Macromolecules* **2001**, *34*, 2710.

[43] M. J. Stevens, *Macromolecules* **2001**, *34*, 1411.

[44] I. Yarovsky, E. Evans, *Polymer* **2002**, *43*, 963.

[45] M. Tsige, M. J. Stevens, *Macomolecules* **2004**, *37*, 630.

[46] M. Tsige, C. D. Lorenz, M. J. Stevens, *Macomolecules* **2004**, *37*, 8466.

[47] C. Wu, W. Xu, *Polymer* **2006**, *47*, 6004.

[48] H. Liu, H.-J. Qian, Y. Zhao, Z.-Y. Lu, *J. Chem. Phys.* **2007**, *127*, 144903.

[49] S. Corezzi, C. de Michele, E. Zaccarelli, D. Fioretto, F. Sciortino, *Soft Matter* **2008**, *4*, 1173.

[50] M. Perez, O. Lame, F. Leonforte, J. L. Barrat, *J. Chem. Phys.* **2008**, *128*, 234904.

[51] V. Varshney, S. S. Patnaik, A. K. Roy, B. L. Farmer, *Macomolecules* **2008**, *41*, 6837.

[52] J. S. Bermejo, C. M. Ugarte, *Macromol. Theory Simul.* **2009**, *18*, 259.

[53] H. Liu, M. Li, Z.-Y. Lu, Z.-G. Zhang, C.-C. Sun, *Macromolecules* **2009**, *42*, 2863.

[54] K. Farah, H. A. Karimi-Varzaneh, F. Müller-Plathe, M. C. Böhm, *J. Phys. Chem. B* **2010**, *114*, 13656.

[55] K. Farah, F. Leroy, F. Müller-Plathe, M. C. Böhm, *J. Phys. Chem. C* **2011**, *115*, 16451.

[56] M. R. Nyden, D. W. Noid, *J. Phys. Chem.* **1991**, *95*, 940.

[57] M. R. Nyden, G. P. Forney, J. E. Brown, *Macomolecules* **1992**, *25*, 1658.

[58] M. R. Nyden, J. W. Gilman, *Comp. and. Theor. Polymer Science* **1997**, *7*, 191.

[59] M. R. Nyden, T. R. Coley, S. Mumby, *Polym. Eng. Sci.* **1997**, *37*, 1496.

[60] S. I. Stoliarov, P. R. Westmoreland, M. R. Nyden, G. P. Forney, *Polymer* **2003**, *44*, 883.

[61] M. R. Nyden, S. I. Stoliarov, P. R. Westmoreland, Z. X. Guo, C. Jee, *Mat. Sci. Eng.* **2004**, *A365*, 114.

[62] S. I. Stoliarov, R. E. Lyon, M. R. Nyden, *Polymer* **2004**, *45*, 8613.

[63] K. D. Smith, S. I. Stoliarov, M. R. Nyden, P. R. Westmoreland, *Mol. Simul.* **2007**, *33*, 361.

[64] K. D. Smith, M. Bruns, S. I. Stoliarov, M. R. Nyden, O. A. Ezekoye, P. R. Westmoreland, *Polymer* **2011**, *52*, 3104.

[65] M. Meuwly, O. M. Becker, R. Stote, M. Karplus, *Biophys. Chem.* **2002**, *98*, 183.

[66] D. R. Nutt, M. Meuwly, *Biophys. J.* **2006**, *90*, 1191.

[67] J. Danielsson, M. Meuwly, *J. Chem. Theory Comput.* **2008**, *4*, 1083.

[68] S. Mishra, M. Meuwly, *J. Am. Chem. Soc.* **2010**, *132*, 2968.

[69] F. H. Stillinger, T. A. Weber, *Phys. Rev. B* **1985**, *31*, 5262.

[70] F. H. Stillinger, *Physica* **1986**, *140A*, 142.

[71] F. H. Stillinger, T. A. Weber, R. A. LaViolette, *J. Chem. Phys.* **1986**, *85*, 6460.

[72] F. H. Stillinger, T. A. Weber, *J. Phys. Chem* **1987**, *91*, 4899.

[73] F. H. Stillinger, T. A. Weber, *J. Chem. Phys.* **1988**, *88*, 5123.

[74] F. H. Stillinger, T. A. Weber, *Phys. Rev. Lett.* **1989**, *62*, 2144.

[75] T. A. Schoolcraft, B. J. Garrison, *J. Vac. Sci. Technol. A* **1990**, *8*, 3496.

[76] T. A. Weber, F. H. Stillinger, *J. Chem. Phys.* **1990**, *92*, 6239.

[77] T. A. Schoolcraft, B. J. Garrison, *J. Am. Chem. Soc.* **1991**, *113*, 8221.

[78] P. C. Weakliem, C. J. Wu, E. A. Carter, *Phys. Rev. Lett.* **1992**, *69*, 200.

[79] H. Feil, J. Dieleman, B. J. Garrison, *J. App. Phys.* **1993**, *74*, 1303.

[80] P. C. Weakliem, E. A. Carter, *J. Chem. Phys.* **1993**, *98*, 737.

[81] S. D. Athavale, D. J. Economou, *J. Vac. Sci. Technol. A* **1995**, *13*, 966.

[82] M. E. Barone, D. B. Graves, *J. App. Phys.* **1995**, *77*, 1263.

[83] M. E. Barone, D. B. Graves, *J. App. Phys.* **1995**, *78*, 6604.

[84] L. E. Carter, E. A. Carter, *J. Phys. Chem* **1996**, *100*, 873.

[85] A. Darcy, A. Galijatovic, R. Barth, T. Kenny, K. D. Krantzman, T. A. Schoolcraft, *J. Mol. Graphics* **1996**, *14*, 260.

[86] P. C. L. Stephenson, M. W. Radny, P. V. Smith, *Surf. Sci.* **1996**, *366*, 177.

[87] D. E. Hanson, A. F. Voter, J. D. Kress, *J. Appl. Phys.* **1997**, *82*, 3552.

[88] D. Srivastava, T. Halicioglu, T. A. Schoolcraft, *J. Vac. Sci. Technol. A* **1999**, *17*, 657.

[89] H. Ohta, S. Hamaguchi, *J. Chem. Phys.* **2001**, *115*, 6679.

[90] H. Ohta, S. Hamaguchi, *J. Vac. Sci. Technol. A* **2001**, *19*, 2373.

[91] D. B. Graves, D. Humbird, *App. Surf. Sci.* **2002**, *192*, 72.

[92] D. Humbird, D. B. Graves, *J. Vac. Sci. Technol. A* **2005**, *23*, 31.

[93] V. V. Smirnov, A. V. Stengach, K. G. Gaynullin, V. A. Pavlovsky, *J. App. Phys.* **2005**, *97*, 093302.

[94] T. Nagaoka, K. Eriguchi, K. Ono, H. Ohta, *J. App. Phys.* **2009**, *105*, 023302.

[95] J. Tersoff, *Phys. Rev. Lett.* **1986**, *56*, 632.

[96] B. W. Dodson, *Phys. Rev. B* **1987**, *35*, 2795.

[97] J. Tersoff, *Phys. Rev. B* **1988**, *38*, 9902.

[98] J. Tersoff, *Phys. Rev. B* **1988**, *37*, 6991.

[99] R. Smith, D. E. Harrison, B. J. Garrison, *Phys. Rev. B* **1989**, *40*, 93.

[100] J. Tersoff, *Phys. Rev. B* **1989**, *39*, 5566.

[101] D. W. Brenner, *Phys. Rev. B* **1990**, *42*, 9458.

[102] H.-P. Kaukonnen, R. M. Nieminen, *Phys. Rev. Lett.* **1992**, *68*, 620.

[103] D. W. Brenner, D. H. Robertson, M. L. Elert, C. T. White, *Phys. Rev. Lett.* **1993**, *14*, 2174.

[104] M. V. R. Murty, H. A. Atwater, *Phys. Rev. B* **1995**, *51*, 4889.

[105] L. Qi, S. B. Sinnott, *J. Phys. Chem. B* **1997**, *101*, 6883.

[106] B. M. Rice, W. Mattson, S. F. Trevino, *Phys. Rev. E* **1998**, *57*, 5106.

[107] C. F. Abrams, D. B. Graves, *J. App. Phys.* **1999**, *86*, 5938.

[108] C. F. Abrams, D. B. Graves, *J. App. Phys.* **2000**, *88*, 3734.

[109] S. J. Stuart, B. Tutein, J. A. Harrison, *J. Chem. Phys.* **2000**, *112*, 6472.

[110] D. W. Brenner, O. A. Shenderova, J. A. Harrison, S. J. Stuart, B. Ni, S. B. Sinnott, *J. Phys.: Condens. Matter* **2002**, *14*, 783.

[111] D. Humbird, D. B. Graves, *J. App. Phys.* **2004**, *96*, 791.

[112] D. Humbird, D. B. Graves, *J. Chem. Phys.* **2004**, *120*, 2405.

[113] D. Humbird, D. B. Graves, *J. App. Phys.* **2004**, *96*, 65.

[114] I. Jang, S. B. Sinnott, *J. Phys .Chem. B* **2004**, *108*, 18993.

[115] I. Jang, S. B. Sinnott, D. Danailov, P. Keblinski, *Nano Lett.* **2004**, *4*, 109.

[116] B. Ni, K.-H. Lee, S. B. Sinnott, *J. Phys.: Condens. Matter* **2004**, *16*, 7261.

[117] M. Eckert, E. Neyts, A. Bogaerts, *Chem. Vap. Deposition* **2008**, *14*, 213.

[118] J. J. Végh, D. Nest, D. B. Graves, R. Bruce, S. Engelmann, T. Kwon, R. J. Phaneuf, G. S. Oehrlein, B. K. Long, C. G. Willson, *J. App. Phys.* **2008**, *104*, 034308.

[119] E. Lampin, C. Krzeminski, *J. App. Phys.* **2009**, *106*, 063519.

[120] X. D. Lu, Y. Qin, J. Ning, T. Zhou, C. Y. Deng, C. Meng, Q. Qiu, F. Gou, Z. Chuanwu, Y. Ying, J. Ming, *Nuc. Instrum. Met. Phys. Res. B* **2009**, *267*, 3238.

[121] Y.-T. Su, T.-R. Shan, S. B. Sinnott, *Nucl. Instrum. Phys. Res. B* **2009**, *267*, 2525–2531.

[122] J. J. Végh, D. B. Graves, *J. Phys. D: Appl. Phys.* **2009**, *42*, 222001.

[123] L. Yang, G. Pourtois, M. Caymax, A. Ceulemans, M. Heyns, *Phys. Rev. B* **2009**, *79*, 165312.

[124] B. Devine, I. Jang, T. Kemper, D. Lee, J. D. Gale, N. Iordanova, S. B. Sinnott, *J. Phys. Chem. C* **2010**, *114*, 12535.

[125] F. Gou, E. Neyts, M. Eckert, S. Tinck, A. Bogaerts, *J. App. Phys.* **2010**, *107*, 113305.

[126] Y. Xiao, W. Dong, H. F. Busnengo, *J. Chem. Phys.* **2010**, *132*, 014704.

[127] K. A. Fichthorn, Y. Tiwary, T. Hammerschmidt, P. Kratzer, M. Scheffler, *Phys. Rev. B* **2011**, *83*, 195328.

[128] P. T. Mikulski, K. V. Workum, G. M. Chateauneuf, G. Gao, J. D. Schall, J. A. Harrison, *Tribol. Lett.* **2011**, *42*, 37.

[129] A. C. T. van Duin, S. Dasgupta, F. Lorant, W. A. Goddard III, *J. Phys. Chem. A* **2001**, *105*, 9396.

[130] A. C. T. van Duin, A. Strachan, S. Stewman, Q. Zhang, X. Xu, W. A. Goddard III, *J. Phys. Chem. A* **2003**, *107*, 3803.

[131] Q. Zhang, T. Çagin, A. C. T. van Duin, W. A. Goddard III, Y. Qi, L. G. Hector, *Phys. Rev. B* **2004**, *69*, 045423.

[132] K. Chenoweth, S. Cheung, A. C. T. van Duin, W. A. Goddard III, E. M. Kober, *J. Am. Chem. Soc.* **2005**, *127*, 7192.

[133] S. Cheung, W.-Q. Deng, A. C. T. van Duin, W. A. Goddard III, *J. Phys .Chem. A* **2005**, *109*, 851.

[134] S. S. Han, J. K. Kang, H. M. Lee, A. C. T. van Duin, W. A. Goddard III, *J. Chem. Phys.* **2005**, *123*, 114703.

[135] S. S. Han, A. C. T. van Duin, W. A. Goddard III, H. M. Lee, *J. Phys .Chem. A* **2005**, *109*, 4575.

[136] S. S. Han, J. K. Kang, H. M. Lee, A. C. T. van Duin, W. A. Goddard III, *J. Chem. Phys.* **2005**, *123*, 114704.

[137] K. D. Nielson, A. C. T. van Duin, J. Oxgaard, W.-Q. Deng, W. A. Goddard III, *J. Phys. Chem. A* **2005**, *109*, 493.

[138] A. Strachan, E. M. Kober, A. C. T. van Duin, J. Oxgaard, W. A. Goddard III, *J. Chem. Phys.* **2005**, *122*, 054502.

[139] A. C. T. van Duin, Y. Zeiri, F. Dubnikova, R. Kosloff, W. A. Goddard III, *J. Am. Chem. Soc.* **2005**, *127*, 11053.

[140] K. Chenoweth, A. C. T. van Duin, P. Persson, M. J. Cheng, J. Oxgaard, W. A. Goddard III, *J. Phys. Chem. C* **2008**, *112*, 14645.

[141] K. Chenoweth, A. C. T. van Duin, W. A. Goddard III, *J. Phys. Chem. A* **2008**, *112*, 1040.

[142] J. Budzien, A. P. Thompson, S. V. Zybin, *J. Phys. Chem. B* **2009**, *113*, 13142.

[143] H.-P. Chen, R. K. Kalia, E. Kaxiras, G. Lu, A. Nakano, K.-i. Nomura, A. C. T. van Duin, P. Vashishta, Z. Yuan, *Phys. Rev. Lett.* **2010**, *104*, 155502.

[144] J. C. Fogarty, H. M. Aktulga, A. Y. Grama, A. C. T. van Duin, S. A. Pandit, *J. Chem. Phys.* **2010**, *132*, 174704.

[145] A. M. Kamat, A. C. T. van Duin, A. Yakovlev, *J. Phys. Chem. A* **2010**, *114*, 12561.

[146] J. A. Keith, D. Fantauzzi, T. Jacob, A. C. T. van Duin, *Phys. Rev. B* **2010**, *81*, 235404.

[147] M. R. LaBrosse, J. K. Johnson, A. C. T. van Duin, *J. Phys. Chem. A* **2010**, *114*, 5855.

[148] J. E. Mueller, A. C. T. van Duin, W. A. Goddard III, *J. Phys. Chem. C* **2010**, *114*, 5675.

[149] J. E. Mueller, A. C. T. van Duin, W. A. Goddard III, *J. Phys. Chem. C* **2010**, *114*, 4939.

[150] J. Quenneville, R. S. Taylor, A. C. T. van Duin, *J. Phys .Chem. C* **2010**, *114*, 18894.

[151] C. F. Sanz-Navarro, P.-O. Åstrand, D. Chen, M. Rønning, A. C. T. van Duin, W. A. Goddard III, *J. Phys. Chem. C* **2010**, *114*, 3522.

[152] M. R. Weismiller, A. C. T. van Duin, J. Lee, R. A. Yetter, *J. Phys. Chem. A* **2010**, *114*, 5485–5492.

[153] S. Agrawalla, A. C. T. van Duin, *J. Phys. Chem. A* **2011**, *115*, 960.

[154] O. Rahaman, A. C. T. van Duin, W. A. Goddard III, D. J. Doren, *J. Phys. Chem. B* **2011**, *115*, 249.

[155] B. J. Garrison, D. Srivastava, *Annu. Rev. Phys. Chem.* **1995**, *46*, 373.

[156] D. W. Brenner, *phys. stat. sol. (b)* **2000**, *217*, 23.

[157] F. Müller-Plathe, *ChemPhysChem* **2002**, *3*, 754.

[158] D. Reith, M. Pütz, F. Müller-Plathe, *J. Comput. Chem.* **2003**, *24*, 1624.

[159] S. J. Marrink, H. J. Risselada, S. Yefimov, D. P. Tieleman, A. H. Vries, *J. Phys. Chem. B* **2007**, *111*, 7812.

[160] C. Peter, K. Kremer, *soft matter* **2009**, *5*, 4357.

[161] H.-J. Qian, P. Carbone, X. Chen, H. A. Karimi-Varzaneh, C. C. Liew, F. Müller-Plathe, *Macromolecules* **2008**, *41*, 9919.

[162] K. Kremer, G. S. Grest, *J. Chem. Phys* **1990**, *92*, 5057.

[163] R. Auhl, R. Everaers, G. S. Grest, K. Kremer, S. J. Plimpton, *J. Chem. Phys.* **2003**, *119*, 12718.

[164] S. Yamamoto, Y. Tsujii, T. Fukuda, *Macromolecules* **2000**, *33*, 5995.

[165] H.-W. Ma, J.-H. Hyun, P. Stiller, A. Chilkoti, *Adv. Mater.* **2004**, *16*, 338.

[166] J. D. Weeks, D. Chandler, H. C. Andersen, *J. Chem. Phys* **1971**, *54*, 5237.

[167] M. S. Kent, H. Yim, A. Matheson, C. Cogdill, G. Nelson, E. D. Reedy, *J. Adhes.* **2001**, *75*, 267.

[168] A. Ansari, J. Berendzen, D. Braunstein, *Biophys. Chem.* **1987**, *26*, 337.

[169] P. Anfinrud, C. Han, R. Hochstrasser, *Proc. Natl. Acad. Sci.* **1989**, *86*, 8387.

[170] J. W. Petrich, J.-C. Lambry, K. Kuczera, M. Karplus, C. Poyart, J.-L. Martin, *Biochem.* **1991**, *30*, 3975.

[171] S. Kim, G. Jin, M. Lim, *J. Phys. Chem. B* **2004**, *108*, 20336.

[172] J. W. Gilman, T. Kashiwagi, S. Lomakin, J. D. Lichtenham, P. Jones, E. Giannelis, E. Manias, *Proceedings of the 6th European meeting on Fire Retardancy of Polymeric Materials, Lille, France, September 1997.*

[173] D. L. Flamm, V. M. Donnelly, J. A. Mucha, *J. Appl. Phys.* **1981**, *52*, 3633.

[174] M. J. Vasile, F. A. Stevie, *J. Appl. Phys.* **1982**, *53*, 3799.

[175] F. R. McFeely, J. F. Morar, N. D. Shinn, G. Landgren, F. J. Himpsel, *Phys. Rev. B* **1984**, *30*, 764.

[176] K. Ninomiya, K. Suzuki, S. Nishimatsu, O. Okada, *J. Appl. Phys.* **1985**, *58*, 1177.

[177] D. J. Oostra, A. Haring, R. P. Vaningen, A. E. Devries, *J. Appl. Phys.* **1988**, *64*, 315.

[178] K. Sung, S. Pang, *Jpn. J. Appl. Phys., Part 1* **1994**, *33*, 7112.

[179] J. P. Chang, H. H. Sawin, *J. Vac. Sci. Technol. A* **1997**, *15*, 610.

[180] N. Layadi, V. M. Donnelly, J. T. C. Lee, *J. Appl. Phys.* **1997**, *81*, 6738.

[181] G. C. Abell, *Phys. Rev. B* **1985**, *31*, 6184.

[182] J. Ferrante, J. R. Smith, J. H. Rose, *Phys. Rev. Lett.* **1983**, *50*, 1385.

[183] L. Pauling, *Phys. Rev.* **1938**, *54*, 899.

[184] D. E. Hanson, J. D. Kress, A. F. Voter, *J. Vac. Sci. Technol. A* **1999**, *17*, 1510.

[185] D. E. Hanson, J. D. Kress, A. F. Voter, *J. Chem. Phys.* **1999**, *110*, 5983.

[186] C. H. Kiang, W. A. Goddard III, R. Beyers, J. R. Salem, D. S. Bethune, *J. Phys. Chem* **1994**, *98*, 6612.

[187] C. H. Kiang, *J. Phys. Chem. A* **2000**, *104*, 2454.

[188] R. L. Vander Wal, T. M. Ticich, *J. Phys. Chem. B* **2001**, *105*, 10249.

[189] R. L. Vander Wal, T. M. Ticich, V. E. Curtis, *Carbon* **2001**, *39*, 2277.

[190] G. H. Luo, Z. F. Li, F. Wei, X. Y. Deng, J. Yong, *Physica B* **2002**, *323*, 314.

[191] G. Wolf, J. Baumann, F. Baitalow, F. P. Hoffmann, *Thermochim. Acta* **2000**, *343*, 19.

[192] L. G. Green, E. L. Lee, *Detonation Pressure Measurements on PETN. Proceedings of 13th International Detonation Symposium, Norfolk, VA, July 2006.*

# 2. Reactive Molecular Dynamics with Material-Specific Coarse-Grained Potentials: Growth of Polystyrene Chains from Styrene Monomers

## 2.1. Introduction

For quite a long time the development of connectivity-altering molecular dynamics (MD) and Monte Carlo (MC) methods had not been in the focus of computer simulation studies. The expected prohibitively long computer time demands of reactive MD (RMD) and MC (RMC) calculations seemed to be an obstacle for scientific activities in this direction. The increasing computational facilities in the past 15 years, however, initiated the development of reactive simulation techniques. The first RMD and RMC simulations aimed at generating equilibrated structures of chain-like and cross-linked polymers. [1-8] Khare et al. combined atomistic MD simulations with periodic MC trials to connect monomer units.[9] The approach of these authors as well as similar studies[1-8] has been performed with the intention to build up glassy structures. Successful RMD approaches on the basis of generic bead-and-spring models have been suggested by several groups to study the polymerization kinetics of linear chains as well as the structural properties of the resulting melts.[10-12] The efficient simulation method of Svaneborg et al. rendered possible the formation of topologically disordered polymer networks.[13] At roughly the same time, a first MC realization under consideration of translational, orientational and reactive moves has been published.[14] The end- and double-bridging MC algorithms of Theodorou et al. have grown into powerful methods for the generation of well-equilibrated polymer samples with chain-like or even more complex architectures.[15-18] In the approach of Liu et al. a dissipative particle dynamics has been used to study phase separation which is coupled with polymerization.[19]

In more recent contributions, new RMD and RMC methods have been suggested. A generic MD model using hard ellipsoids to map irreversible polymerization has been described by Correzzi et al.[20] An RMD scheme in a coarse-grained (CG) resolution to study the formation of polymer chains has been developed by Perez et al.[21] In addition to a Lennard-Jones interaction these authors have coupled adjacent beads via the anharmonic finite extensible non-linear elastic potential. In analogy to the RMD work of Akkermans et al.[11], a capture radius had to be defined in the latter formalism to model reactive steps; see below. These reactive simulations[11,21] can be considered as an extension of the pioneering work of Gao.[10]

Outside the context of polymerization, RMD simulations on the basis of a local equilibrium have been described for very simple processes.[22-24] Smith et al.[25] have developed a RMD formalism to simulate the thermal decomposition of polymers and nanostructures. Similar processes have been studied by other groups.[26,27] Reactive force-fields of quantum chemical accuracy, however, have not been combined yet with reactive MD or MC schemes in the study of polymerization processes.[28,29] Finally we want to mention the Reactive Ensemble Monte Carlo method[30] developed to study the equilibrium behavior of reacting systems. On the basis of the existing RMD literature the following picture appears. While simple local reactions in polymers can be modeled with system-specific force-fields at an atomistic level, the majority of polymerization reactions have been described only at the CG level with generic potentials.[11, 21]

It is the purpose of the present study to make new steps towards RMD simulations using CG potentials of specific systems. We have modeled the polymerization of styrene (parameterized and from here on denoted as ethylbenzene (EB)) to atactic polystyrene (PS). The CG mapping scheme employed is displayed in Figure 2.1. Each ethylbenzene monomer as well as each repeat unit of PS has been identified with a CG bead. The labels R and S in the schematic diagram characterize the two enantiomeric orientations of the -CHPh- group with Ph abbreviating a phenyl ring.

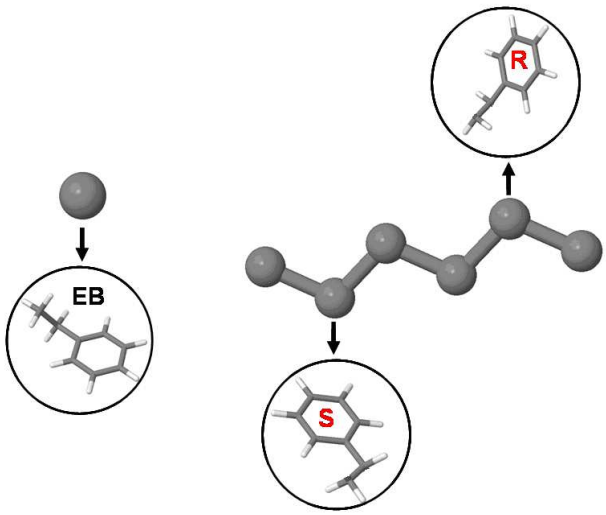


***Figure 2.1***. *Coarse-grained mapping scheme for ethylbenzene (EB, left) as a model of styrene and polystyrene (PS, right). A coarse-grained bead encompasses either one EB molecule* $((C_6H_5)C_2H_5)$ *or one repeat unit of PS* $(-(C_6H_5)C_2H_3-)$. *In a PS chain, the two absolute configurations of the carbon center substituted by the phenyl rings give rise to CG beads symbolized by R and S. In atactic PS the sequence of the R and S beads is random.*

The selection of CG polystyrene in our first RMD investigation is due to our recent simulation studies of this polymer.[31-34] A Coarse-grained model for ethylbenzene and polystyrene as well as their mixtures has been tested in detail. Their temperature (T) transferability has been investigated in comprehensive equilibrium simulations.[31] In atomistic non-equilibrium calculations of PS and PS-$CO_2$ mixtures we have analyzed the thermal conductivity of these species. [33, 34] Crystalline syndiotactic PS has been chosen to study the correlation between the calculated thermal conductivity and degrees of freedom in a given force-field.[32] The published CG potential of PS[31] adopted in the present work offers the possibility to compare RMD data for monodisperse PS samples with results of non-reactive equilibrium MD simulations on melts of a given chain length. Note that the CG potentials derived by Qian et al. were optimized to generate the same structure as the atomistic MD simulation. It should be noted that the present reactive MD implementation is an extension of the RMD model of Akkermans et al.[11] So far, the model has only been applied in connection with generic potentials which offer enough flexibility to simplify the implementation of a reactive MD scheme.[11,21] Employing specific potentials in RMD simulations is less straightforward as will be shown in the second and third sections. In contrast to former RMD studies, the focus is here more oriented on the growth history of the polymer samples. The present simulations show that qualitative features of polymerization experiments are already in reach.

The organization of the present chapter is as follows. In the next section we explain the background of the developed RMD formalism. All simulations have been performed with the program IBIsCO which has been written in our group for CG studies of polymers.[35] The reactive MD extension of IBIsCO has lead to the R-IBIsCO code. The computational conditions for the RMD calculations are given in the third section. In the fourth, we compare RMD results for monodisperse PS with the output of equilibrium simulations.[31] Before the conclusion, the growth history of the PS formation in polydisperse samples is related to experimental results in section 5.

## 2.2. Theoretical Background

The theoretical setup chosen allows the mapping of a so-called living polymerization with irreversible bond formation.[36.37] Before the polymerization of the monomers (M) can start (in the present work the polymerization of EB to PS), we have to define a certain number of monomer beads ($N_I$) which act as initiators (I*). Such an internal initiation occurs, e.g., in photo-polymerizations. Each I* can bind one free monomer. In the succeeding polymerization steps the terminal monomer (P*) of a polymer chain can react with a free monomer. Thus the irreversible polymerization leads to the following reactive scheme with the symbol * denoting a reactive unit:

$$\begin{aligned} &I^* + M \rightarrow I-P^* \\ &I-P^* + M \rightarrow I-P-P^* \\ &I-P_{n-1}-P^* + M \rightarrow I-P_n-P^*, n = 2,3,4,... \end{aligned} \qquad (2.1.)$$

Suitable descriptors for such processes are the polymer size (degree of polymerization) $N_L$, its mean value $\langle N_L \rangle$, the underlying distribution function $P(N_L)$ as well as the polydispersity index $I_P$. These quantities have been determined in the present reactive MD simulations. To emphasize this origin in the following discussions they have been labeled with the index "sim". $\langle N_L \rangle_{sim}$ and $I_{Psim}$ are defined as

$$< N_L >_{sim} = \sum n_{N_L} N_L \qquad (2.2.)$$

$$I_{Psim} = \frac{N_w}{< N_L >_{sim}} \text{ with } N_w = \sum w_{N_L} N_L \, . \qquad (2.3.)$$

The symbols $n_{N_L}$ and $w_{N_L}$ denote the number fraction and weight fraction.[38] The summations in relations (2.2.) and (2.3.) are performed over all possible values of $N_L$.

It has been mentioned in the introduction that the present RMD implementation exhibits certain similarities with polymerization models suggested by Akkermans et al.[11] as well as Perez et al.[21] But in contrast to these generic schemes we have employed a realistic CG potential derived for EB, PS and EB-PS mixtures.[31] The present CG potential is defined by nonbonded interactions as well as by

bonded radial and angle terms. These degrees of freedom are not considered in generic RMD schemes with potential functions that are not system-specific.

Reactive steps in the present RMD formalism are implemented as follows. We define two tuning parameters controlling the polymerization. The first is a characteristic delay time ( $\tau_r$ ) separating two succeeding time steps in which reactions are allowed to take place. The interval $\tau_r$ between such steps is reserved for normal MD without connectivity alteration, e.g. for the relaxation and diffusion of the particles. In order to simplify the implementation of the reactive processes the parameter $\tau_r$ is kept constant during the simulations and is independent of the chain length. For small $\tau_r$ the particles do not have enough time to reach equilibrium via dynamic processes. RMD simulations under these conditions have been denoted as "static".[11,21] For large $\tau_r$ the system has more time to relax and diffuse before new bonds can be formed. The time interval required for relaxation by molecular motions of course depends on the polymer weight fraction and the degree of polymerization. In contrast to the "static" processes in the limit of small $\tau_r$, the descriptor "dynamic" has been employed in the RMD literature to classify simulations performed for large values of $\tau_r$.[11,21] In the present RMD formalism the number of reactive time steps separated by $\tau_r$ is not limited. Each propagating chain as well as each initiator is allowed to form only one bond per reactive step. The maximum number of chains that can propagate simultaneously in a reactive step is equal to the initial number of starters $N_I$.

In addition to the delay time $\tau_r$ we employ a geometric criterion compatible with bond formation at reactive time steps. This leads us to the second tunable parameter of our method. Bonding - at the allowed time steps - takes place whenever a free monomer is found in a sphere of radius $r_I$ of an initiator bead I* or $r_P$ of a terminal unit P* of a growing chain. If more than one free monomer lies within the capture radius of a reactive center a bond is formed with the closest one. A schematic display for the reactive steps is shown in Figure 2.2. In the left (center) diagram characterizing the starting reaction the initiator can bind (has bound) a free EB monomer, in the right one a terminal monomer P* of the growing chain has formed a new bond (propagation).Whenever a new bond is formed, the CG potential - to be described below - switches instantaneously from a nonbonded interaction to a bonded one

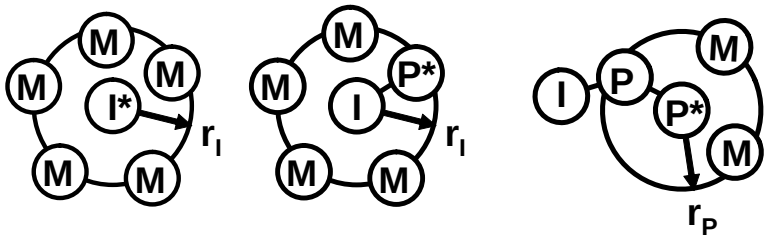


***Figure 2.2.*** *Schematic representation of the initiation step of the polymerization (left and center diagrams) as well as the chain propagation (right). The center diagram symbolizes the formation of a new I-P* bond. The two different reactive processes are characterized by capture radii* $r_I$ *and* $r_P$. *The reaction can take place whenever a free monomer bead M comes into the interaction sphere* $r_I$ *of an initiator I* or* $r_P$ *of a terminal reactive chain monomer P*.*

described by bond and angle terms. In contrast to the other reactive simulations employing such a geometric criterion[11,21] we have used a force-field where $r_I$ ($r_P$) lies inside the repulsive part of the potential. The R-IBIsCO program written for the present research allows the definition of individual capture radii $r_I$ ($r_P$) for the starting reaction and chain propagation. Thus we can model different reactivities at the two topology-altering centers. For the reactive parameters $r_I$ ($r_P$) as well as for the delay time $\tau_r$, we had to choose values that lead to simulation times accessible with the present computational facilities. In our simulations we have adopted capture radii between 0.55 and 0.40 nm. The nonbonded interactions at these $r_I$ ($r_P$) values lead to energy barriers of 0.47 and 16.30 kJ/mol. They measure the difference between the minimum of the pair-wise nonbonded potential and the energy derived at $r_I$ ($r_P$). Modifications of this energy under the influence of the reactive process are not considered in our simple setup. Nevertheless we suggest identifying these numbers in the context of the present RMD scheme as the activation energy $E_A$ of the polymerization reaction. Note that these numbers are smaller than the $E_A$ of living polymerizations. We expect, however, that qualitative aspects of the polymerization procedure can be reproduced by the present approach.

To sum up, in addition to the number $N_I$ and position of the initiator beads I*, the present RMD scheme is controlled by two tuning parameters. The delay time $\tau_r$ separates two reactive MD steps where bond formations are possible. In principle there is no limitation in the overall number of new bonds formed at reactive MD steps, as long as free monomers are available. Nevertheless, a reaction can only take place if the two reacting beads are located within a sphere of radius $r_I$ (I-P* bonds) or $r_P$ (P-P* bonds). The capture radii determine the activation energy for the polymerization. The delay time $\tau_r$ controls the degree of relaxation and diffusion between reactive MD steps, i.e. it is an element

characteristic for the simulation method. Although of different physical meaning the influence of $r_I$ ($r_P$) and thus of $E_A$, on the one hand, and $\tau_r$ on the other hand, cannot be considered as completely independent. With the above choice of parameters, the present MD simulations have approximately the same time scale for the polymer dynamics and the chemical activation in the reactive steps. Although differing by many orders of magnitude in reality, they nevertheless allow the simulation of a living polymerization which provides insight on growth mechanisms. The introduction of the parameters $N_I$, $r_I$ ($r_P$), $\tau_r$ indicates that RMD simulations of polydisperse samples can be considered as a case study to test the sensitivity of the approach to these parameters. The present analysis of polydisperse samples, however, goes beyond the recent generic RMD simulations as it offers a qualitative access to experimental features; see the discussion in a later section.

We now come to the CG mapping of the chosen systems. We have employed an existing CG potential[31] derived via the iterative Boltzmann inversion (IBI) method, a highly stable algorithm developed by one of the present authors.[39] As target functions Qian et al. made use of inter- and intramolecular distribution functions from atomistic simulations.[31] Atactic PS is characterized by a random arrangement of so-called R and S beads. The sequence of the two repeat units was determined by a random number generator with equal probabilities. There are two terms for the bonded "two-bead" interaction R-R (= S-S) and R-S (= S-R). The different types of angular potentials are symbolized by R-R-R (= S-S-S), R-R-S (= S-R-R = S-S-R = R-S-S) and R-S-R (= S-R-S). The nonbonded interactions are described by potential terms denoted R-R (= S-S) and R-S (= S-R). In analogy to non-reactive IBIsCO simulations, all potentials in R-IBIsCO are stored in tabulated form.

The correlation between RMD results for monodisperse PS and equilibrium data reported recently[31] is used as benchmark to estimate the capability of the present simulation scheme in generating equilibrated polymer structures. Even in conventional equilibrium MD calculations of complex systems the possible trapping in quasi-degenerate configurations which may differ in certain physical properties, requires a high computational effort.[40-42] A detailed discussion of such phenomena in non-equilibrium simulations of PS can be found in one of our recent articles.[33] It cannot be ruled out a priori that such problems are even enhanced in the presence of reactive processes. Thus the comparison of RMD and equilibrium data can be considered as an additional test to recognize and – if necessary – to suppress the implications of such quasi-degeneracies.

## 2.3. Computational Conditions

All RMD simulations were performed in the constant-NPT ensemble where the particle number $N = N_M$ includes all beads in the system i.e. the free monomer and initiator beads as well as the ones in the polymer chains. For simulations of monodisperse PS samples we have chosen the temperature T = 500 K and the pressure P = 101.3 kPa to meet the conditions of the equilibrium runs which served as reference.[31] The total number of CG beads adopted in the benchmark studies amounts to $N_M$ = 3840. Monodisperse samples have been generated with the help of a predefined chain length $N_L$. If a growing chain has reached this limit, further reactive processes are forbidden by definition. At the end of the simulation we have $N_I$ polymer chains with identical length $N_L$. A complete list of the parameters defining the present RMD approach can be found in Table 2.1. For the monodisperse simulations, the initial number of initiators is determined by the ratio $N_I = N_M / N_L$ with $N_L$ = 10, 30, 80 and 120. In a first stage, growth and equilibration of the monodisperse samples are performed until all free monomers have been captured. The values of the capture radius and delay time adopted here are $r_I = r_P$ = 0.40 nm and $\tau_r = 5\times10^{-4}$ ns. Long equilibration runs are subsequently performed for these monodisperse samples from which the quantities of interest are extracted.

| | |
|---|---|
| $N_M$ | total number of monomer beads including the initiators I* |
| $N_I = N_P$ | total number of initiators $N_I$ which coincides with the total number of chains $N_P$ |
| $N_{ir}$ | number of initiators that have reacted at a certain polymerization time |
| $N_L$ | degree of polymerization of a polymer chain |
| $D_P$ | conversion (percentage of monomers converted into polymer beads) |
| $r_I$ ( $r_P$ ) | capture radius of the initiator I* (terminal monomer bead P* of a chain) |
| $I_P$ | polydispersity index |
| $N_G$ | total number of growth steps, i.e. number of reactive MD steps |
| $\tau_r$ | time interval (ns) between two reactive MD steps |
| $t_{1/2}$ | time to reach a 50% conversion of the free monomers M into polymer beads P |
| $t_\infty$ | time to complete the polymerization $D_P$ ( $t_\infty$ ) = 100 % |

***Table 2.1.*** *Summary of input parameters and quantities used in the present RMD simulations of a living polymerization.*

In the simulation of polydisperse samples, the constraint of a common $N_L$ is simply removed. These calculations have been performed at P = 101.3 kPa and T = 400 K which is a characteristic condition for the living polymerization of styrene to PS.[43,44] To derive the CG potential for this temperature we have used the temperature-dependent scaling factor of reference[31], $f(T) = \sqrt{T/T_0}$ where $T_0$ = 500 K is the temperature for the development of the CG force-field. The CG potential at T = 400 K requires a simple transformation of the potential by the multiplicative factor $f(T) \approx 0.894$. A qualitative justification of the square-root dependence of the factor f(T) can be found in reference 28. The polydisperse samples have been modeled by considering $N_M$ = 4000 including an initiator number $N_I$ of 80 beads. The chosen $N_M / N_I$ ratio is quite close to the relative concentrations of the components in experiments.[43,44] All reactive MD simulations (monodisperse and polydisperse samples) have been continued until the last free monomer had been captured by one of the growing chains.

Constant time steps of 5 fs have been employed in the reactive simulations. The Berendsen thermostat[45] is used with a coupling time of 0.5 ps while a coupling time of 5 ps has been chosen for the barostat. These time constants are combined with an isothermal compressibility of $1\times10^{-6}$ $kPa^{-1}$. The cut-off for the nonbonded interactions has been set to 1.6 nm and the associated Verlet neighbor list cut-off value is 1.7 nm. The updating procedure for the neighbor list has to be at least equal to the delay time $\tau_r$ to monitor the time evolution of the system topology correctly. The values for the capture radius $r_I$ ($r_P$) and the delay time $\tau_r$ employed in the different RMD simulations are quoted in the fourth and fifth sections.

The alteration of the particle connectivity requires a permanent control of the system. Whenever a new bond is formed, the interaction potential between the reacting beads is switched instantaneously from a nonbonded to a bonded interaction. The implications of this process for the entries in the neighbor list are evident: the RMD code has to guarantee that the newly connected beads do not feel nonbonded interactions up to the second neighbors in the chain. All simulations have been performed under periodic boundary conditions and the minimum image convention.

At the end of this section we analyze the stability of the present RMD implementation. We just have emphasized that each reactive event between two beads is accompanied by a spontaneous switch of the CG potential from a nonbonded to a bonded interaction. In Figure 2.3. we show that the excess heat produced in these processes does not lead to significant changes in the temperature fluctuations. The target temperature adopted in these reactive MD runs is 500 K. The top diagram provides the T fluctuations in a conventional equilibrium simulation (i.e. absence of reactive processes).

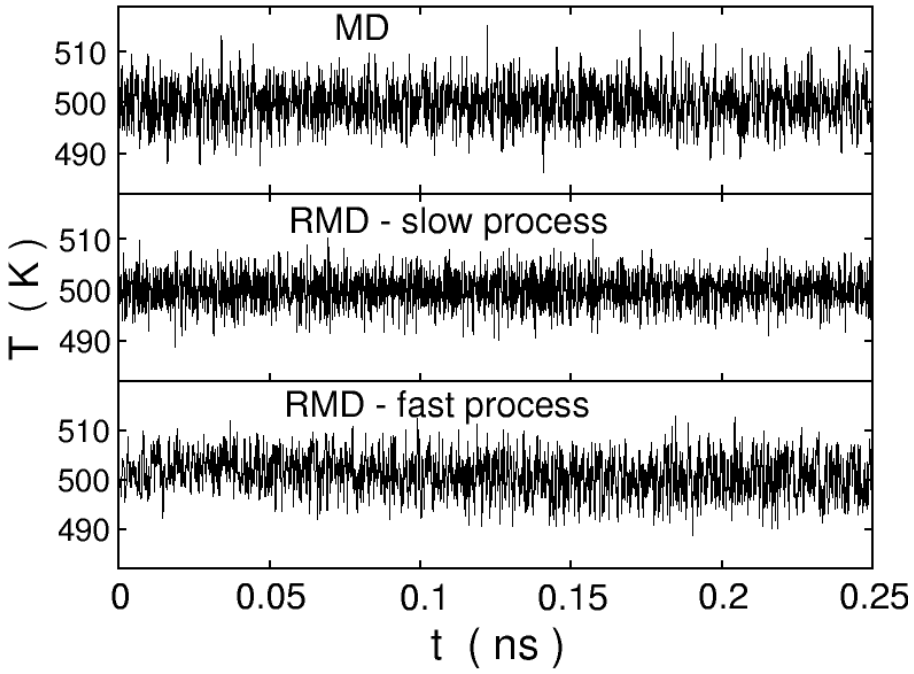


***Figure 2.3.*** *Temperature fluctuations as a function of the simulation time t. The top diagram represents the T dependence of a conventional equilibrium MD simulation of a monodisperse sample with $N_L$ = 80. The T fluctuations in the other diagrams refer to reactive MD simulations. Center plot: $D_P$ = 30 %, $r_I = r_P$ = 0.40 nm, $\tau_r = 5\times10^{-4}$ ns; bottom plot: $D_P$ = 90 %, $r_I = r_P$ = 0.55 nm, $\tau_r = 5\times10^{-4}$ ns. The target temperature is T = 500 K.*

In the middle diagram we have plotted the temperature fluctuations in a polydisperse sample at a conversion of 30 %. The RMD runs are performed with $r_I = r_P$ = 0.40 nm and $\tau_r = 5\times10^{-4}$ ns, i.e. we follow a slow process. It can be seen that the formation of new bonds does not lead to any increase of the temperature. The same behavior is found when increasing the conversion continuously i.e. in the limit of complete polymerization. In the faster process shown in the bottom diagram ($r_I = r_P$ = 0.55 nm and $\tau_r = 5\times10^{-4}$ ns) only a slight increase of T of roughly 2 K near the time origin can be detected. This increase is due to the switching from the nonbonded to the bonded potentials when bonds are being formed in this fast process. But even this excess energy is quickly removed from the system by the Berendsen thermostat with standard settings. In analogy to the middle diagram the bottom T profile is characteristic for the whole reactive process. Finally, we also have checked the length fluctuations of a bond formed at a certain time t = 0 up to the end of the reactive simulation (results not shown here). The length fluctuations of the bonds formed during the reactive simulations are similar to those experienced by the same system simulated with standard MD (i.e. topology of the system fixed at the beginning of the simulation).

## 2.4. Growth of Monodisperse Systems: Validation of the Method

We have chosen the density (ρ) as the first quantity to present the correlation between equilibrium MD and RMD data for monodisperse PS samples. All non-reactive equilibrium simulations reported below have been repeated for the present work by adopting the setup described by Qian et al.[31]. In the top diagram of Figure 2.4. we have plotted the density of PS as a function of the predefined chain length $N_L$. The agreement between MD and RMD data is very good. The equilibrium MD and RMD densities for $N_L$ = 10, 30, 80, 120 differ by less than 1 %. The 500 K density of the initial EB sample amounts to 631.1 kg/m$^3$.

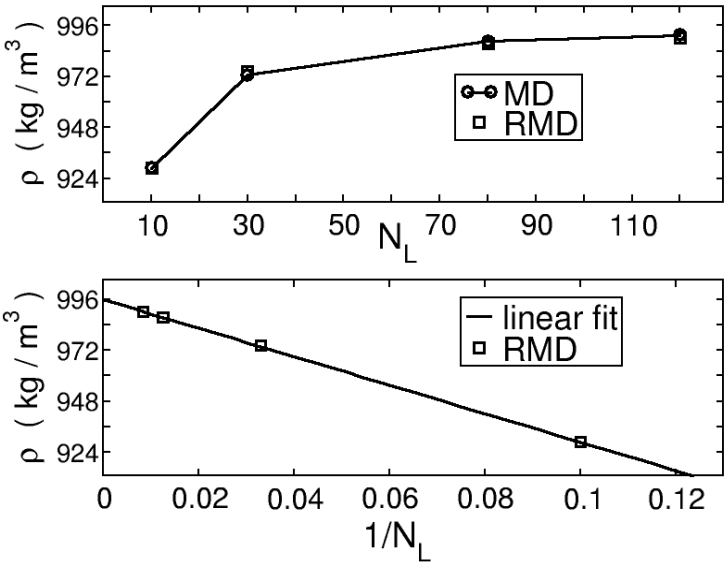


***Figure 2.4.*** *Density ρ of monodisperse polystyrene samples as a function of the predefined chain length $N_L$ (top diagram) and as a function of $1/N_L$ (bottom diagram). The data points of the standard equilibrium MD simulations (circles) in the top diagram have been connected by a full line as a guide to the eye, the reactive MD (RMD) derived data are represented by squares. The bottom diagram shows the RMD data (squares) along with the fitted linear curve used for an extrapolation of the density of a monodisperse system with an average chain length of 500 monomers.*

With increasing length of the polymer the density increases. The present MD and RMD densities are of the same order of magnitude as experimentally determined values. In reference 46 a density of 950 kg/m$^3$ at T = 500 K has been reported for atactic PS. It refers to a polymer sample with an average molecular weight of 51000 g/mol corresponding to an averaged chain length of 500. The bottom diagram of Figure 2.4. contains the RMD based densities as a function of the inverse polymer size $N_L$.

In this linear correlation the limit $1/N_L \rightarrow 0$ can be used to estimate the density of polymers with long chains. For $N_L$ = 500 the extrapolation leads to a density of 995 kg/m$^3$ which differs by less than 5 % from the experimental value.

The same good agreement between equilibrium and RMD results for PS is observed for the root-mean-square end-to-end distance $R_{ee} = \left\langle R_E^2 \right\rangle^{1/2}$ and gyration radius $R_g = \left\langle R_G^2 \right\rangle^{1/2}$. $R_E$ ($R_G$) symbolizes the end-to-end distance (radius of gyration). The $N_L$ dependence of $R_{ee}$ is shown in Figure 2.5. (top diagram) along with the simulation results of Qian et al..[28] The RMD-based scaling exponent $\upsilon$ in the relation $R_{ee} \propto N_L^{\upsilon}$ of 0.571 differs by less than 3% from the theoretical estimate for self-avoiding walks of $\upsilon$ = 0.588. This value of $\upsilon$ is characteristic for the excluded volume behavior of short chains.[11,47] For the radius of gyration (Figure 2.5., bottom diagram) we have correlated the present RMD and MD results with two equilibrium simulations from the literature.[31,48] As expected on the basis of the $R_{ee}$ plot we again observe a linear relation between $R_g$ and $N_L$ when plotted in a double-logarithmic scale. All equilibrium results considered in the benchmark studies are reproduced perfectly by the reactive MD approach. Thus it seems that sampling problems[40,41] are small for the quantities derived for monodisperse PS samples by the two different MD techniques.

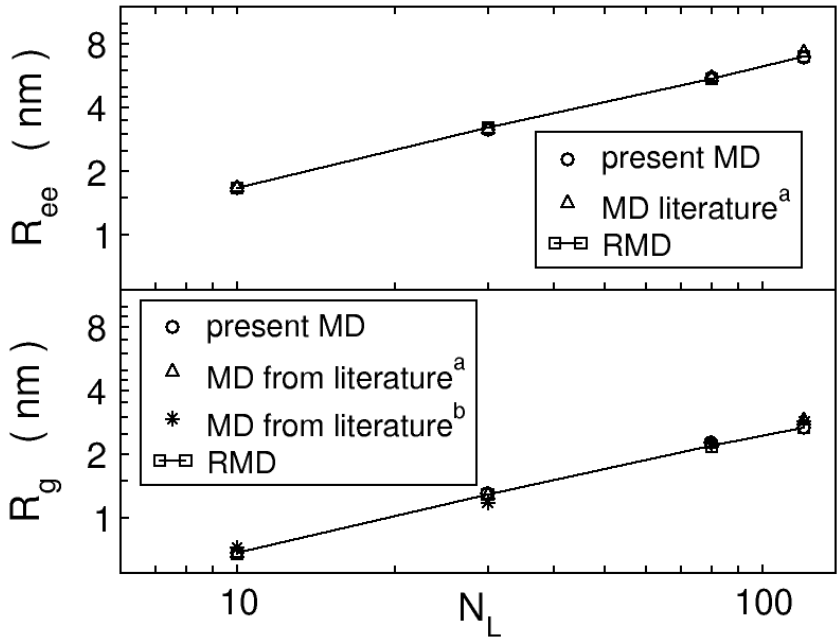


***Figure 2.5***. *Root-mean-square end-to-end distance* $R_{ee}$ *(top) and radius of gyration* $R_g$ *(bottom) for monodisperse PS of chain lengths* $N_L$ *= 10, 30, 80 and 120 as derived by standard and reactive MD simulations. All simulations have been performed at T = 500 K. Note the double logarithmic representation of the plot. The literature data labeled by a (b) have been taken from reference 31 (2.48.).*

We continue our comparative analysis of monodisperse PS in CG resolution with distribution functions for the bonds and angles. In Figure 2.6. we show the length distribution between the centers of mass of bonded beads as derived under RMD and conventional equilibrium MD conditions. The same comparison between the two computational schemes for the angle distributions of the bonded beads is reported in Figure 2.7. The curves in both figures have been evaluated for a predefined chain length $N_L$ of 120 beads. Again we notice an excellent agreement between the connectivity-altering and the equilibrium MD runs. The same is valid for the angle distributions in Figure 2.7. From Figures 2.6. and 2.7. we deduce that intramolecular length and angle distributions are correctly determined by the present RMD method. The same agreement between the two MD codes has been observed for the other chain lengths studied ($N_L$ = 10, 30, 80). The intramolecular distributions plotted in Figures 2.6. and 2.7. confirm the trends already formulated in connection with the density as well as the $R_{ee}$ and $R_g$ profiles.

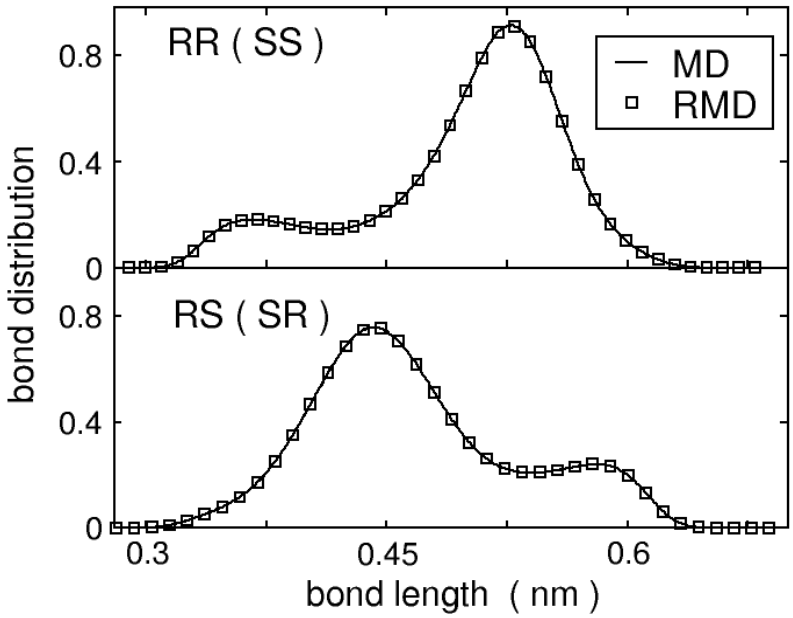


***Figure 2.6.*** *Bond length distribution between the centers of mass of RR (SS) and RS (SR) beads in atactic polystyrene (top, bottom) from the present RMD approach and a conventional equilibrium MD simulation. The data refer to $N_L$ = 120 and T = 500 K.*

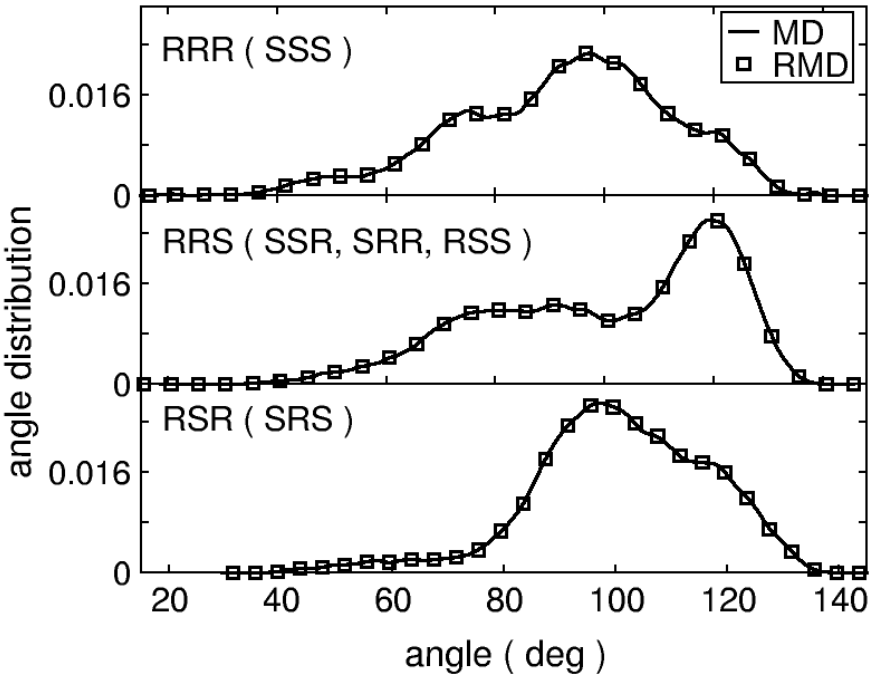


***Figure 2.7.*** *Angle distribution between three adjacent repeat units of atactic PS from the present RMD approach and in standard equilibrium MD simulations. The data refer to NL = 120 and T = 500 K*

A comparison of the nonbonded radial distribution function g(r) between RR (SS) beads for monodisperse PS chains with $N_L$ = 120 and 10 concludes our validation of the RMD implementation. In analogy to the bonded distribution curves also the nonbonded ones in Figure 2.8. are correctly reproduced by the RMD method. Thus, the present connectivity altering MD code is an efficient tool to derive equilibrated structures of monodisperse polymer samples. On the basis of the above simulation results we strongly feel that the RMD approach should be also a useful tool to study the properties of polydisperse systems under different growth conditions.

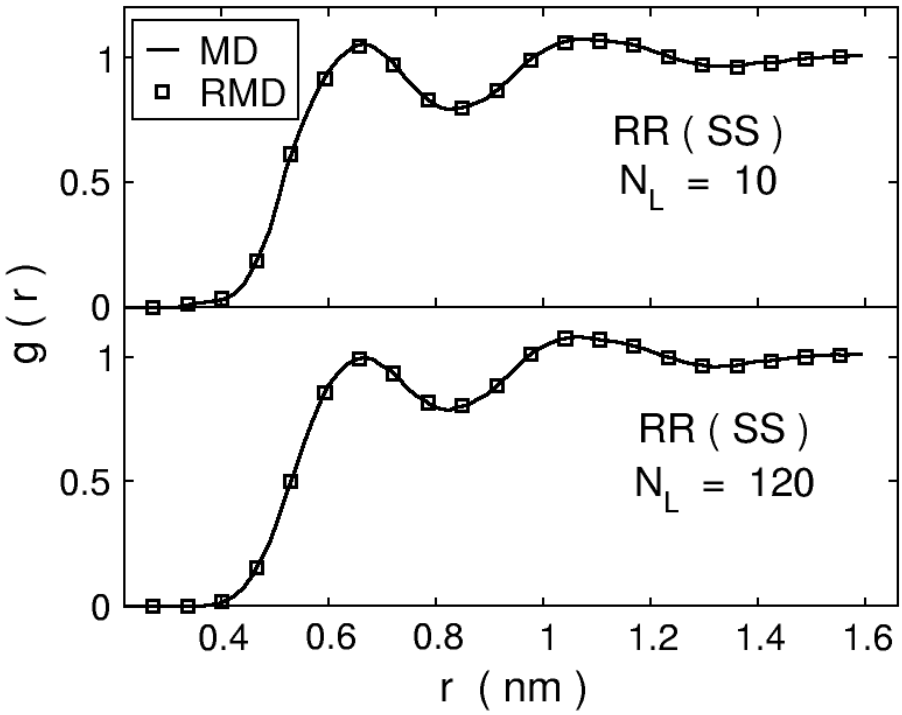


***Figure 2.8.*** *Nonbonded radial distribution functions g(r) between RR (SS) beads of atactic PS with $N_L$ = 10 (top) and $N_L$ = 120 (bottom) from the present RMD approach and conventional equilibrium MD simulation at T = 500 K.*

## 2.5. Growth History in Polydisperse Samples

The polymer growth in the monodisperse samples of the last section has been terminated by the predefined parameter $N_L$ which defines the common length of all chains. In the simulations described below, this constraint on $N_L$ has been removed in order to allow a free growth of the $N_I$ different polymer chains. In analogy to monodisperse samples, we have again a good agreement between the calculated $\rho$ of 1025 kg/m$^3$ and measured values of 1005 kg/m$^3$ and 1013 kg/m$^3$. The experimental data refer to samples with an averaged chain length of 500 monomers[46,49] while the RMD results correspond to a value of roughly 50 at T = 400 K. The literature data have been recorded at T = 408 K.

### 2.5.1 Influence of the Capture Radius and Delay Time

In this section, the initiator positions have been distributed randomly in the simulation box. First we have chosen a common capture radius r ($r = r_I = r_P$) for the initiator I* and the terminal polymer bead P* in the chains at a constant value of the delay time $\tau_r = 5\times10^{-4}$ ns. Numerical results on the correlation between r and characteristic polymerization times are given in Table 2.2. where we have collected the parameters $t_{1/2}$ and $t_\infty$ as a function of r. The time $t_{1/2}$ indicates that one half of the initial free monomers M has been converted into polymer beads P (i.e. $D_P$ = 50 %), while $t_\infty$ denotes that the polymerization process has been completed (i.e. $D_P$ = 100 %).

| $r_I = r_P$ | $t_{1/2}$ | $t_\infty$ |
|---|---|---|
| 0.40 | 6.00 | 29.6 |
| 0.45 | 0.40 | 2.5 |
| 0.48 | 0.13 | 1.2 |
| 0.55 | 0.03 | 0.86 |

***Table 2.2.*** *Characteristic times (half life $t_{1/2}$ and time to full conversion $t_\infty$) as a function of the capture radius $r = r_I = r_P$ in RMD simulations of polydisperse samples. The delay time is $\tau_r = 5\times10^{-4}$ ns. The values $t_{1/2}$ and $t_\infty$ are given in ns, $r_I$ and $r_P$ in nm.*

The $t_{1/2}$ numbers indicate that an increase of r from 0.40 to 0.55 nm leads to an enhancement of the reaction velocity by a factor of 200. This acceleration is a manifestation of the higher probability to find a monomer in the vicinity of a terminal chain bead if the capture radius is enlarged. This can be quantified by averaging the number of free beads within the capture radius of a reactive bead during a certain simulation time. For r = 0.55 nm the averaged number of free beads in the reactive sphere of the chain-end during 0.03 ns is 0.63. Note that 0.03 ns refer to the time to reach $D_P$ = 50 %. For the same time of simulation (i.e. 0.03 ns) the averaged number of free beads found within a capture radius of 0.40 nm is reduced to 0.0125. In contrast to $t_{1/2}$ the time to full conversion $t_\infty$, however, differs by only a factor of roughly 34. This leveling indicates the decelerating influence of equilibration and diffusion steps in the end phase of a polymerization even if these factors are unimportant at the beginning of a fast reaction. We come to the influence of r on the degree of polymerization $N_L$ of the $N_I$ polymer chains. The final chain length distribution $P(N_L)$ derived for $\tau_r = 5\times10^{-4}$ ns has been plotted in Figure 2.9. for the two limiting r considered (0.40 and 0.55 nm). The fast reaction (large r) leads to a broader $P(N_L)$ profile. The small activation energy associated to r = 0.55 nm allows reactive steps in configurations only partially relaxed that are characterized by a trapping of initiator units or terminal polymer beads in a non-reactive surrounding.

Under certain assumptions it is possible to solve the kinetic equations for a polymerization process analytically. In this framework it is assumed that the reaction rate coefficient for the bimolecular reaction ($I\text{-}P_{n-1}\text{-}P^* + M$) is independent of $N_L$. This is fulfilled under the following conditions. i) The reactants have to be ideally mixed preventing a diffusion control. ii) The initiation kinetics has to be fast relative to the chain propagation. Condition ii) will be examined in more detail in following subsections. The analytical solution for $P(N_L+1)$ corresponds to the following Poisson distribution function.

$$P(N_L+1) = \frac{N(t)^{N_L}}{N_L!}\exp[(-N(t))] \quad N_L = 1,2,... \qquad (2.4.)$$

N(t) is the average number of bonds per chain (ratio between the total number of bonds formed and the total number of activated chains) at any time t . The recurrence formula offers an access to the fraction of polymers with polymerization degree $N_L+1$ (number of polymer chains with length $N_L+1$ divided by the total number of growing chains).

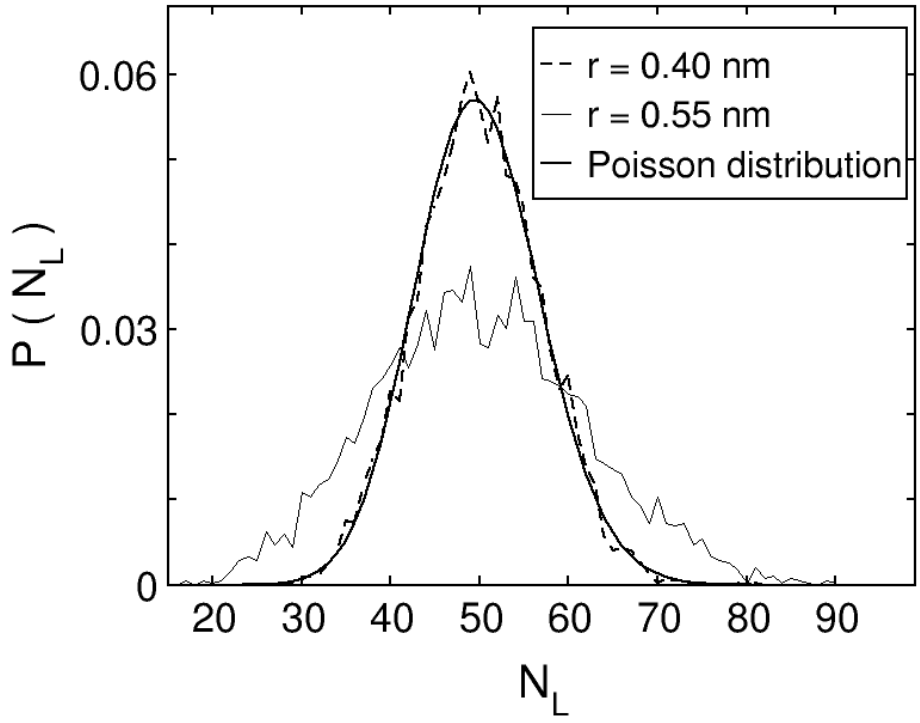


***Figure 2.9.*** *Distribution function* $P(N_L)$ *for the polymer size* $N_L$ *from RMD simulations with* $r = 0.40$ *nm and with* $r = 0.55$ *nm* ($r = r_I = r_P$). *The value of the delay time is* $\tau_r = 5\times10^{-4}$ *ns. Both RMD curves have been averaged over 55 simulations. Each simulation starts with a different random initial distribution of the starters in the box. The bold curve is a Poisson profile (analytical solution (2.4.)) derived by assuming that all polymerization steps can be described by the same rate law and rate constant.*

In addition to the two RMD curves in Figure 2.9. we have displayed the $P(N_L)$ profile using the above Poisson formula. For more information we refer to the literature.[11] Figure 2.9. indicates that the r = 0.40 nm simulations follow a Poisson-like behavior. Thus we can conclude that equilibration and diffusion seem to be fast compared to the polymerization rate with this small r value. In the r = 0.55 nm case the deviation of the $P(N_L)$ profile from the Poisson-like behavior is due to trapping effects as described in the following paragraph.

To emphasize differences in the growth history of the polymers as a function of r we have calculated the length $N_L$ for the two longest and shortest chains as a function of the conversion $D_P$. The curves in the top and middle diagrams of Figure 2.10. refer again to the limiting capture radii r of 0.40 and 0.55 nm combined with $\tau_r = 5\times10^{-4}$ ns. The bottom diagram of Figure 2.10. will be considered later in this subsection. It appears from the top and center diagrams that up to $D_P \approx 30$ % there is no large difference in the growth history of the fast and slow polymerization. For $D_P > 30$ % trapping processes appear in the simulation with r = 0.55 nm and $\tau_r = 5\times10^{-4}$ ns. They cause a split between the

$N_L$ profiles of the short and long chains which increases as polymerization proceeds. The implications of such processes in the presence of a small energy barrier have been visualized already in Figure 2.9.

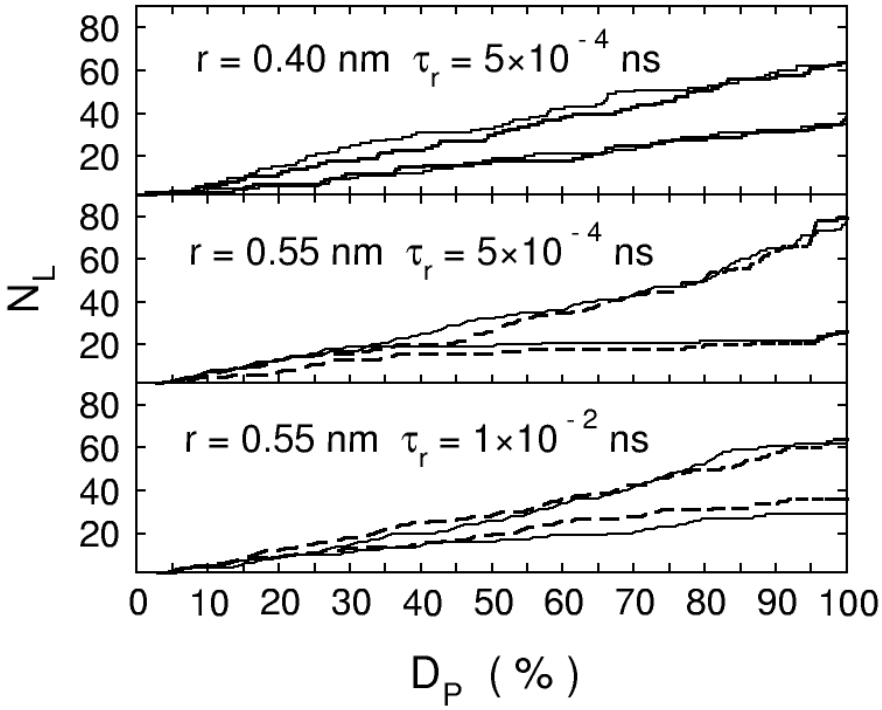


***Figure 2.10.*** *Evolution of the polymer size NL for the two shortest and the two longest chains as a function of the conversion DP in RMD simulations performed with* $r$ *= 0.40 nm (top) and* $r$ *= 0.55 nm (center) associated with* $\tau_r = 5\times10^{-4}$ *ns. The bottom diagram has been evaluated with r = 0.55 nm and* $\tau_r = 1\times10^{-2}$ *ns.*

For the polymerization simulated with r = 0.55 nm and $\tau_r$ = 5×10-4 ns Equation (2.3.) leads to a polydispersity index $I_{P_{sim}}$ of 1.058. The relaxation and diffusion processes allowed under r = 0.40 nm imply a small reduction of $I_{P_{sim}}$ to 1.020. These polydispersity indices are the results of an average over 55 RMD simulations for each of these two cases. Considering the differences in the chain lengths of experimental systems and the present simulations, the splitting between the calculated $I_{P_{sim}}$ and experimental numbers of roughly 1.3 for living polymerization is not unexpected.[21] Nevertheless we feel that the calculated $I_{P_{sim}}$ numbers emphasize that the present RMD simulations of a living polymerization in a CG resolution offer a reliable description of the kinetics. By means of the local reaction parameter r it has been possible to simulate a transition from a "static" polymerization (r large, $\tau_r$ small) to a "dynamic" scheme (r and $\tau_r$ small). From the simulations it appears that r = 0.40 nm ($E_A$ = 16.3 kJ/mol) seems to be sufficient for a proper consideration of equilibration and diffusion processes in the sample of growing polymer chains.

In order to investigate the influence of the delay time we have adopted two different $\tau_r$ values of $5\times10^{-4}$ and $1\times10^{-2}$ ns with a constant capture radius r = 0.55 nm. In Figure 2.11. we have plotted the conversion as a function of the simulation time. Of course the polymerization is faster when using the

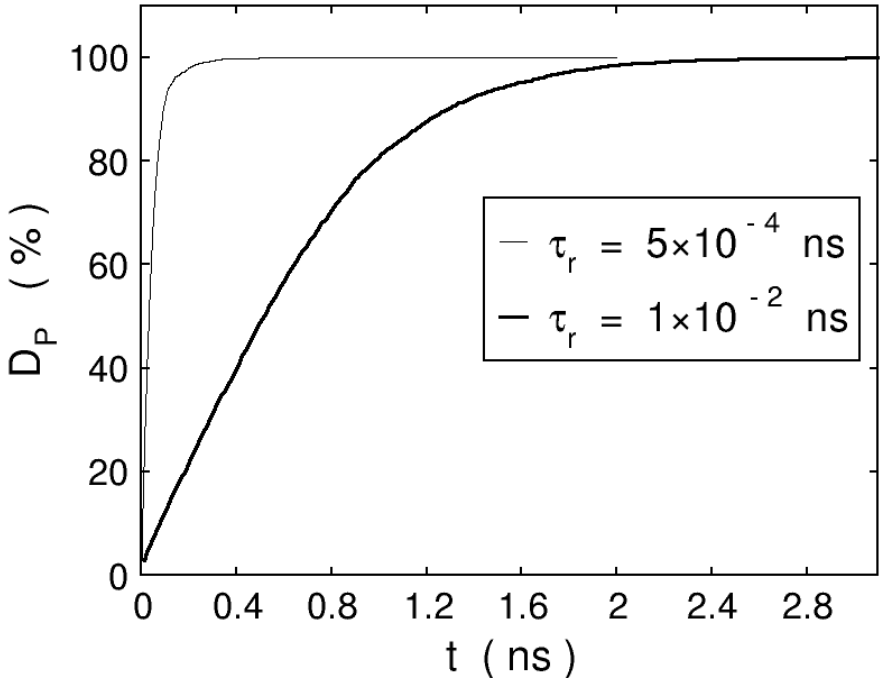


***Figure 2.11.*** *Time dependence of the conversion $D_P$ ( % ) for $\tau_r = 5\times10^{-4}$ ns (thin curve) and $1\times10^{-2}$ ns (bold curve). Both RMD curves use* r *= 0.55 nm for all reactive centers.*

smaller $\tau_r$ value of $5\times10^{-4}$ ns. Here the polymerization is finished after 0.86 ns while $t_\infty$ in the $\tau_r$ = $1\times10^{-2}$ ns equals 3.20 ns. In analogy to the r dependent simulations let us now follow the growth history of the two longest and shortest PS chains as a function of $\tau_r$. The curves in the bottom diagram of Figure 2.10. have been derived for r = 0.55 nm and $\tau_r = 1\times10^{-2}$ ns. The results of this diagram are compared to the evolution of the curves in the center diagram derived with the same capture radius r but a smaller $\tau_r$. As could be expected on the basis of the above findings, trapping effects are more or less absent in the "dynamic" simulation with $\tau_r = 1\times10^{-2}$ ns.

The RMD results presented up to now suggest - as expected - that r and $\tau_r$ cannot be considered as completely independent control parameters. This means that similar growth histories of the polymer chains can be modeled by different combinations of the delay time between reactive steps $\tau_r$ and the capture radius r. This computational degree of freedom can be extracted from Figure 2.12 where we have plotted the probability function $P(N_L)$ for two $(r, \tau_r)$ combinations: (0.55 nm, $1\times10^{-2}$ ns) and (0.40 nm, $5\times10^{-4}$ ns). Both reactive MD runs lead to almost identical $P(N_L)$ profiles. The

advantage of this one-to-one mapping under different simulation conditions is evident. In fact, the simulation with (0.55 nm, $1\times10^{-2}$ ns) is approximately ten times faster.

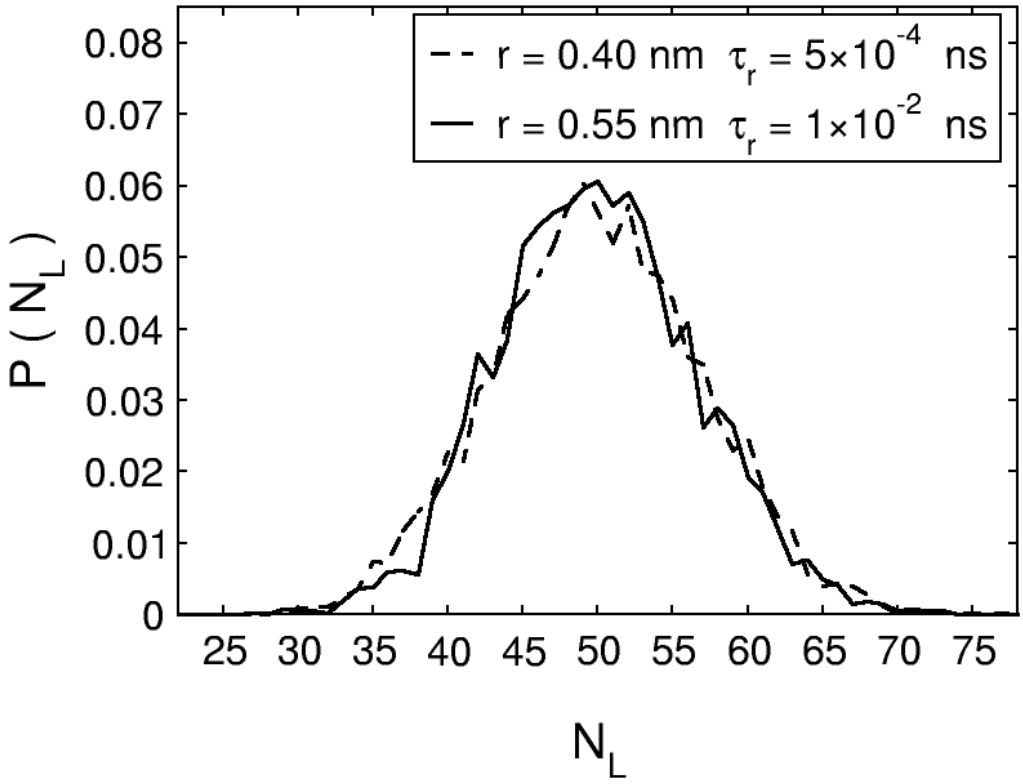


***Figure 2.12.*** *Distribution* $P(N_L)$ *of the polymer size* $N_L$ *on the basis of two different* $(r, \tau_r)$ *combinations. The full curve corresponds to* $r = 0.55$ *nm,* $\tau_r = 1\times10^{-2}$ *ns, the broken one to the combination* $r = 0.40$ *nm,* $\tau_r = 5\times10^{-4}$ *ns.*

### 2.5.2. Influence of the Spatial Distribution of the Initiator Beads

All RMD simulations discussed up to now have been performed for samples with a random distribution of the initiator beads I*. Now we relate these data to RMD runs starting from a spatially localized distribution of the I*. Experimentally, such an arrangement can be generated by a local photo-initiation or by the proper arrangement of the entrance slots for the initiators in the reactor. From technical polymerizations it is known that the size of the reaction vessel, its geometry and the velocity of the component mixing can have a strong influence on the chain lengths and polydispersity index.[36] By changing the localization of the initiators I* in the simulation box, a case study for such an experimental control element can be performed. A localized concentration of the I* is generated as follows. Before starting the RMD run, one EB bead is randomly chosen as initiator I*. The remaining members of the initiator ensemble are then selected on the basis of a simple cut-off criterion (i.e. the 79 beads closest to the chosen starter serve as the remaining I*).

Let us first consider the influence of the localization of the initiator beads on the number of I* forming an I-P$^*$ bond ($N_{Ir}$) as a function of the number of reactive MD steps ($N_G$). In Figure 2.13. we have plotted such curves for a random and a spatially localized distribution of the 80 initiators. The RMD results have been derived for $\tau_r = 5\times10^{-4}$ ns and $r = 0.55\,\text{nm}$. From the figure we see that only $N_G = 5$ reactive MD time steps are required in the sample with randomly distributed I* to allow the 80

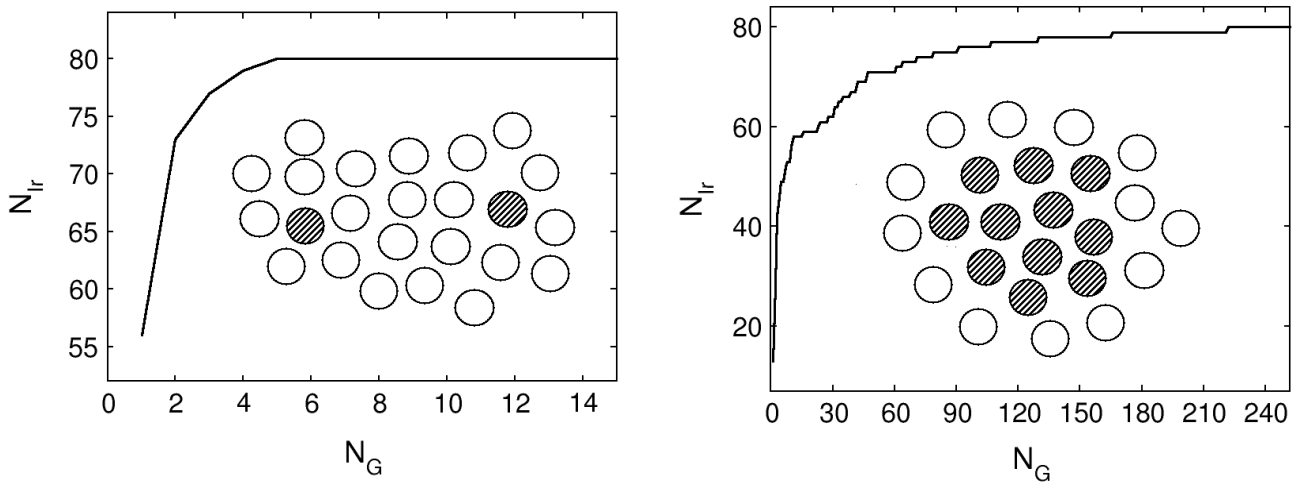


***Figure 2.13.*** *Number of initiators that have reacted $N_{Ir}$ as a function of the number of reactive steps $N_G$. The top curve has been derived for a random distribution of the initiators, while the bottom one refers to a spatially localized initial configuration of the initiators. Both RMD simulations have been performed with $r = 0.55$ nm and $\tau_r = 5\times10^{-4}$ ns.*

initiators I* to bind a monomer. $N_G$ = 5 corresponds to a simulation time of 25 fs. The spatially localized I* distribution needs roughly 220 reactive steps to generate 80 growing chains. The simulation time associated to $N_G$ = 220 amounts to 1100 fs. The different behavior between the two consumption curves of I* is easy to explain. For the localized I* arrangement, only the I* at the surface of the initiator droplet can find a reactive partner; the inner ones are trapped. Possible trapping effects as a function of the reactive parameters r and $\tau_r$ have been commented on above. From the discussion of the growth history of the chains under the influence of these parameters (previous section) we expect that trapping leads to broadened polymer size distributions. This is confirmed by the $P(N_L)$ curves in Figure 2.14. They are either based on $\tau_r = 5\times10^{-4}$ ns (top) or on $1\times10^{-2}$ ns (bottom). The $P(N_L)$ profiles have been derived for the two extremal I* distributions considered (random and localized arrangements).

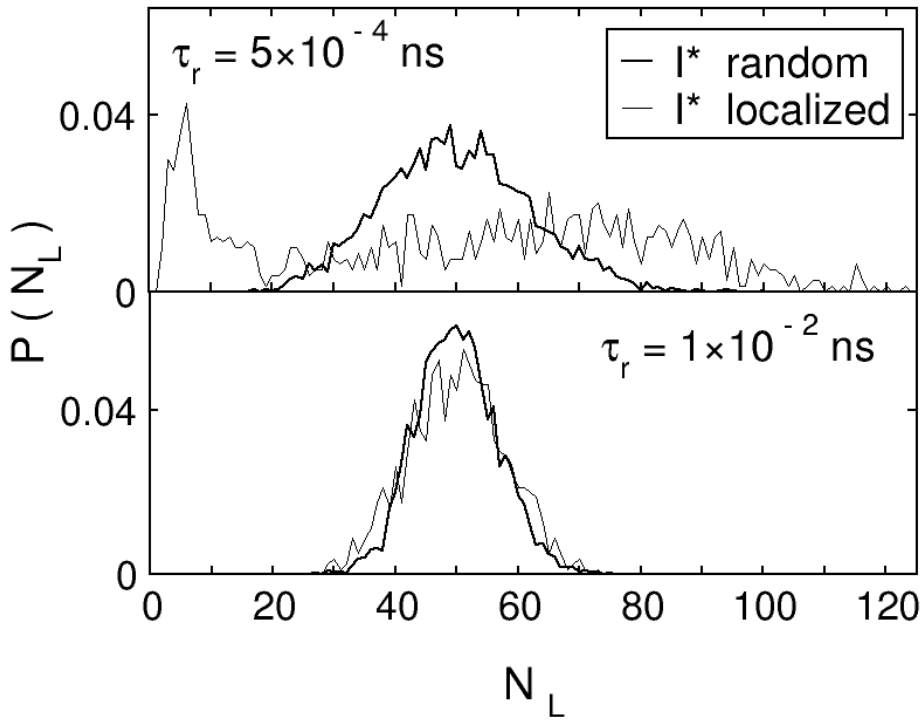


***Figure 2.14.*** *Distribution* $P(N_L)$ *of the polymer size* $N_L$ *calculated with a random (bold curves) and a spatially localized (thin curves) distribution of the initiator beads I*. The curves in the top diagram are based on* $\tau_r = 5\times10^{-4}$ *ns, the curves in the bottom one on* $\tau_r = 1\times10^{-2}$ *ns. All simulations have been performed with* $r = 0.55$ *nm.*

The $\tau_r = 5\times10^{-4}$ ns polymerization with the smaller time interval for relaxation and diffusion between the reactive steps leads to large differences between the two $P(N_L)$ profiles. The non-reactive surrounding of the inner I* in the droplet is responsible for an extremely broad $P(N_L)$ curve with two

maxima. The first one occurs for $N_L$ slightly below 10. It indicates that - as expected - some of the initiator beads have been captured in a non-reactive surrounding for a rather long time. The second $P(N_L)$ maximum in the curve derived for localized I* appears at $P(N_L) \approx 70$. The double-peak structure of the $P(N_L)$ profile obtained for the spatially localized I* reflects that the trapping of some I* enables the growth of long polymer chains in the subset of untrapped reactive polymer ends.

From Figure 2.14. we deduce that a spatial localization of initiator beads can lead to a length or mass profile of the chains strongly different from the Poisson-like distribution shown above. A Poisson-like profile occurs under conditions where relaxation and diffusion in the sample are fast in comparison to the chain propagation. The double-peak curve in Figure 2.14. can be considered as an extreme example where this balance is violated. It remains an open question whether such a mass distribution could be obtained in an experiment. We are aware that the polymerization dynamics modeled by the present RMD approach is much faster than any experimental one. But if there was a chance to achieve this limit, two conditions would have to be fulfilled. The activation energy has to be very low and high sample viscosities would help to decelerate relaxation and diffusion. The lower diagram in Figure 2.14. emphasizes that the difference between the two $P(N_L)$ profiles disappears when performing the RMD runs under "dynamic" conditions ($\tau_r = 1\times10^{-2}$ ns). Both curves are quite similar and have their maximum at $N_L \approx 50$. The longer delay time $\tau_r$ between reactive MD steps allows the I* to spread into reactive domains of the sample before chain elongation under non-equilibrium conditions takes place.

In analogy to the forgoing calculations, the simulations starting from spatially localized initiators should provide insight into conditions supporting trapping. Figure 2.15. contains the length of the two shortest chains obtained under $\tau_r = 5\times10^{-4}$ ns (bold curves) and $\tau_r = 1\times10^{-2}$ ns (thin curves). Trapping is almost absent under "dynamic" conditions compatible with $\tau_r = 1\times10^{-2}$ ns. Here even the shortest chains contain more than 30 monomers. The $N_L$ increase continuously with increasing polymerization.

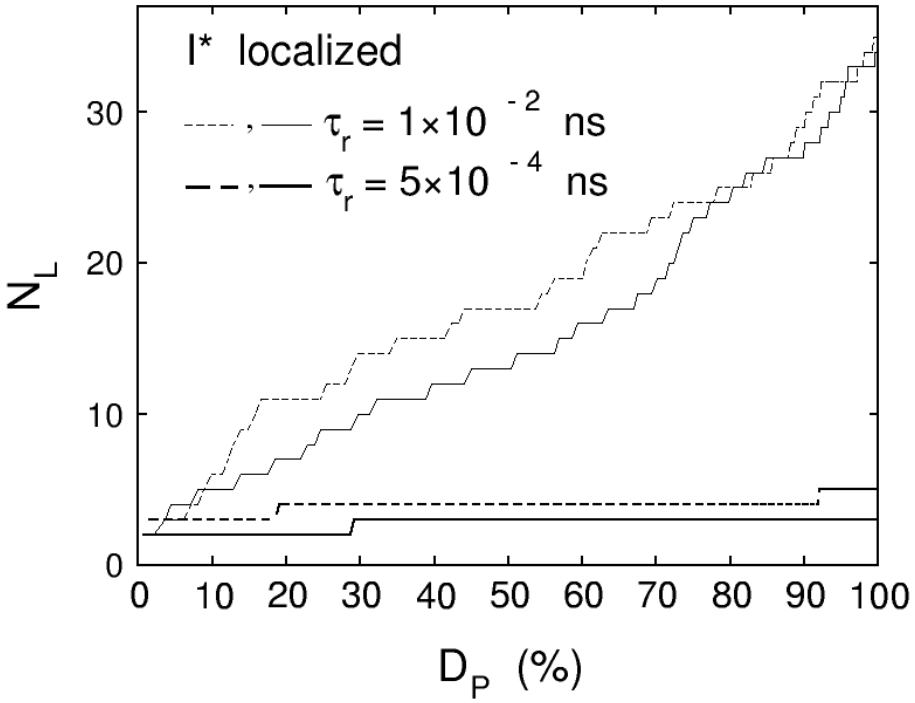


***Figure 2.15.*** *Evolution of the size $N_L$ of the two shortest chains in RMD simulations starting from a localized initiator concentration for $\tau_r = 5\times10^{-4}$ ns and $\tau_r = 1\times10^{-2}$ ns. All simulations employ* r = *0.55 nm.*

The reduction of $\tau_r$ from $1\times10^{-2}$ ns to $5\times10^{-4}$ ns is responsible for an almost perfect trapping of the reactive terminal beads of the chains. At the end of the polymerization, chains with only three or five monomers are left. We believe that Figures 2.14 and 2.15 provide useful information on the implications of localized initiator concentrations in living polymerizations.

### 2.5.3. Different Capture Radii for the Initiation and Chain Propagation

We now relate polymerizations performed under $r_I = r_P$ to $r_I \neq r_P$ ones, i.e. we consider different activation energies for the reaction of the initiator I* with a monomer and the chain propagation. In this section the term "homogeneous" is used to denote simulations performed with r = $r_I = r_P$. In polymerization reactions one usually has lower activation energies for the initiation step than for the propagation.[37] With the present RMD model this can be mapped by setting $r_I > r_P$. Let us go to the top diagram of Figure 2.16. where we have plotted the probability $P(N_L)$ of a process modeled by $r_I$ = 0.55 nm and $r_P$ = 0.40 nm together with two homogeneous profiles evaluated for common radii ($r_I = r_P$) of either 0.55 nm or 0.40 nm. All RMD results have been obtained for $\tau_r = 5\times10^{-4}$ ns.

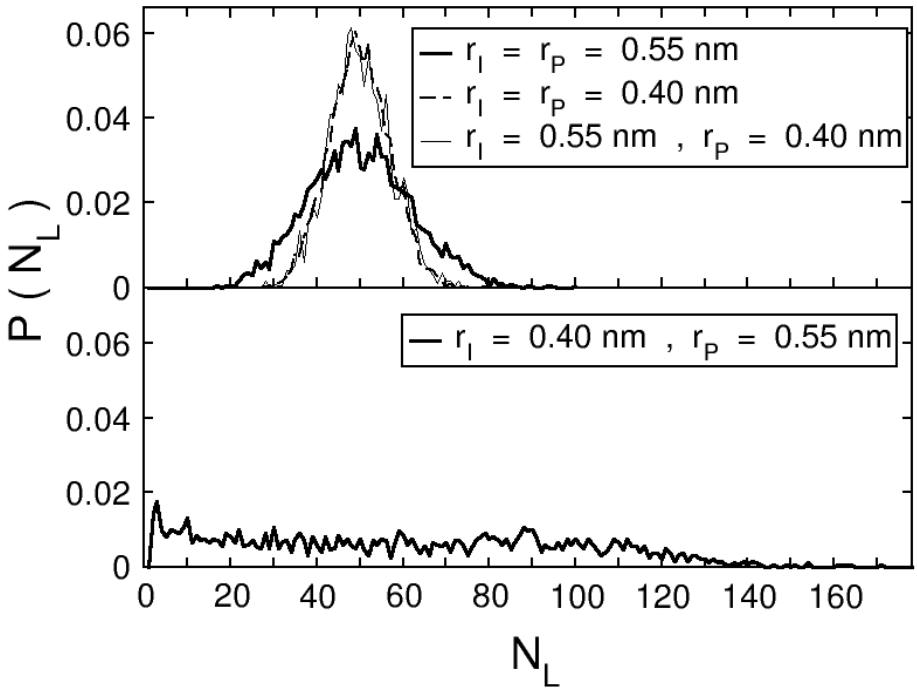


***Figure 2.16.*** *Distribution* $P(N_L)$ *of the polymer size* $N_L$ *for a RMD run with* $r_I = 0.55$ *nm and* $r_P = 0.40$ *nm as well as for two homogenous processes with* $r_I = r_P = 0.40$ *nm and 0.55 nm (top diagram). The* $P(N_L)$ *distribution in the bottom diagram has been evaluated for* $r_I = 0.40$ *nm and* $r_P = 0.55$ *nm. All simulations have been performed with a delay time* $\tau_r$ *of 5×10-4 ns.*

The simulations show that the energy demand for the starting reaction is without influence on the size distribution and polydispersity index if the chain propagation requires a higher or equal activation energy. The $r_I \neq r_P$ curve and the homogeneous one with high activation energy are similar; both reproduce a Poisson-like behavior. The reasons leading to the broad $P(N_L)$ for the homogeneous runs with $r_I = r_P = 0.55$ nm have been commented on in the foregoing discussion.

The time demand for the formation of 80 growing polymer chains for simulations with $r_I = 0.55$ nm and $r_P = 0.40$ nm differs from the ones with $r_I = r_P = 0.40$ nm. In the RMD study with $r_I = 0.55$ nm only five reactive MD steps are necessary to initiate the 80 growing chains. This amounts to roughly 0.02 % of the complete polymerization time $t_\infty$. When choosing a capture radius of 0.40 nm for the initiation 1174 reactive time steps are required for the initiation of the 80 growing chains. Here, the completion of the starting process covers 2 % of $t_\infty$. The slow propagation rate in both systems attenuates any difference in the initiation. In the case of $r_I = r_P = 0.40$ nm, the coupled initiation and propagation steps do not prevent the latest chains initiated from finding free monomers. For $r_I > r_P$ the 80 growing chains that were started already within 0.02 % of the reaction will grow uniformly. The

discussion in this last subsection has shown that the present RMD results are in line with basic principles of reaction (polymerization) kinetics. It is the slowest step of a process that determines the final product profile.[37] This is impressively seen in the bottom diagram of Figure 2.16. Here we have plotted the probability function $P(N_L)$ now derived for a polymerization where the formation of the I-P* is slower than the chain propagation. The RMD calculation leads to an extremely broad profile. Polymer chains containing more than 150 monomers are formed in this simulation. The small initiation radius $r_I$ = 0.40 nm leads to an increase in the time required for all initiators to bind a monomer. Thus, the initiation step is extended over a long period. At the same time, the large propagation value $r_P$ = 0.55 nm guarantees a fast chain growth whenever a I-P* unit has been formed. Therefore, a large amount of monomers are connected by the first growing chains while few remain for the growth of the latest chains formed.

### 2.5.4. Comparison with experiments and analytical results

In the discussion of the RMD results of polydisperse samples we have emphasized that the tuning parameters $r_I$, $r_P$ and $\tau_r$ have a sizeable influence on the molecular weight distribution $P(N_L)$, its mean value $< N_L >_{sim}$ and the polydispersity index $I_{Psim}$. In this section, we relate the RMD based quantities to simple analytical expressions ($N_{La}$, $I_{Pa}$) that are valid for a living/controlled polymerization as well as to experimental trends. We will show that the absence of termination reactions is only one condition for a living/controlled polymerization. The proximity to the limit of a living/controlled process is also determined by the absolute and relative speed for initiation and chain propagation; see below. If the initiation step is slow relative to the propagation we will always have a deficit of I* leading to the formation of long chains (large polydispersity indices). This has been confirmed experimentally.[50-52] We next consider the overall speed of the polymerization under the assumption that the initiation and propagation steps require approximately the same time. In this case, the polydispersity increases with the speed. This has been observed experimentally in an Atom Transfer Radical Polymerization (ATRP) of styrene, whose reaction speed was modulated by using different iron halide complexes as catalysts.[52] For the fastest reactions, $I_P$ values between 1.4 and 1.3 have been measured. A slight reduction of the speed has lowered $I_P$ to 1.3, while a slow polymerization has been accompanied by a further decrease of $I_P$ to 1.2. Conversions of 60 and 80 % were reached in this ATRP study.

Let us continue with analytical formulas that are employed in experiments to discuss the living/controlled character of a polymerization process.[50-52] For a well controlled polymerization (i.e. a process that yields narrow polymer size distribution) the expected average degree of polymerization $N_{La}$ and polydispersity index $I_{Pa}$ can be determined[38,52] theoretically by the ratio between the monomers that have reacted ($\Delta M$) at a given time and the number of initiators $N_I$. For a conversion of 100 % in our RMD simulations $\Delta M = N_M - N_I$ is the number of monomers at the beginning of the reaction. We have

$$N_{La} = \frac{\Delta M}{N_I} \qquad (2.5.)$$

and

$$I_{Pa} = 1 + \frac{1}{N_{La}} - \frac{1}{(N_{La})^2}. \qquad (2.6.)$$

The computational conditions adopted for the polydisperse samples imply $N_{La}$ = 3920/80 = 49 and $I_{Pa}$ = 1.02 ($D_P$ = 100 %).

On the basis of the given experimental information and the analytical expressions (2.5.) and (2.6.) let us reconsider the RMD results derived for polydisperse samples. First we want to highlight some peculiarities of the simulations with the help of figures. In one RMD run starting from a localized initiator distribution (r = 0.55 nm, $\tau_r$ = $5\times10^{-4}$ ns) we have modeled an extremely inefficient condition for a controlled polymerization (see top diagram in Figure 2.14.). The small number of I* accessible at the beginning of the reaction strongly restricts the number of growing polymer chains. The outcome of such a condition is the formation of broad P($N_L$) profiles. In our special case a distribution with two maxima has been observed. The first one has been found at a $N_L$ value of roughly 10, the second one at $N_L \approx 70$. But also in connection with a random distribution of the I*, a very broad P($N_L$) profile has been detected (see bottom diagram in Figure 2.16.). Prerequisite for this curve shape is again an initiation step that is slow in comparison to the propagation. In our RMD simulations it had been generated by capture radii fulfilling $r_I < r_P$. Already the results in Figures 2.14. and 2.16. have indicated that the RMD approach is able to reproduce general experimental trends of living polymerization reactions. Inefficient starting reactions imply broad P($N_L$) profiles (large $I_P$ numbers). In the present approach two mechanisms forcing such a polymerization process have been suggested: i.) inefficient starting reaction (here modeled by $r_I < r_P$) and ii.) localized starting

configuration of the initiators which implies that many of the I* are in the inner region of the initiator droplet.

We continue our discussion with the RMD data in Table 2.3. It summarizes $< N_L >_{sim}$ and $I_{P_{sim}}$ (Equations (2.2) and (2.3)) values that have been derived from single simulations under different conditions.

| Example | Reactive conditions | $< N_L >_{sim}$ | $I_{Psim}$ |
|---|---|---|---|
| 1 | $r_I = r_P = 0.55, \tau_r = 5\times10^{-4}$ | 49.99 | 1.06 |
| 2 | $r_I = r_P = 0.55, \tau_r = 1\times10^{-2}$ | 49.99 | 1.015 |
| 3 | $r_I = r_P = 0.40, \tau_r = 5\times10^{-4}$ | 50.79 | 1.016 |
| 4 | $r_I = 0.55, r_P = 0.40, \tau_r = 5\times10^{-4}$ | 50 | 1.026 |
| 5 | $r_I = 0.40, r_P = 0.55, \tau_r = 5\times10^{-4}$ | 58.65 | 1.47 |

***Table 2.3.*** *Simulated average degree of polymerization < NL >sim and polydispersity index IPsim for RMD simulations under different conditions. The quantities are derived for a conversion DP = 100 %. They are compared with $N_{La}$ = 49 and $I_{Pa}$ = 1.02 (equations (2.5.) and (2.6.)). All simulations considered in this table are based on a random distribution of the initiators. The delay time τr is given in ns, r in nm.*

Case studies 1, 2, 3 and 4 are close to the boundary of a living/controlled polymerization. Nevertheless examples 1 and 3 show that an enhanced velocity (r = 0.55 nm in 1 relative to r = 0.40 nm in 3) implies a larger deviation from Ipa = 1.02 (i.e. 1.06 versus 1.016). In example 4 we are again closer to 1.02 due to the small $r_P$ = 0.40 nm. The largest deviation from this limit is observed for example 5, where the slow starting reaction ($r_I$ = 0.40 nm) compared to the propagation ($r_p$ = 0.55 nm) leads to $< N_L >_{sim}$ = 58.65 and $I_{P_{sim}}$ = 1.47. In contrast to the case study of the previous subsection, which led to a bimodal $P(N_L)$ curve, a random distribution of the I* has been adopted in example 5.

The results of the present section can be summarized as follows. 1.) The correlation of the RMD data with limiting values derived analytically for a living/controlled polymerization has shown that we are able to reproduce this limit by properly designed tuning parameters. 2.) The RMD approach reproduces a general experimental trend, i.e. the increase of the polydispersity index for slow initiation and for high propagation speed. 3.) It seems to be an advantage of the RMD simulations in

the range of nanoseconds that they reproduce experimental trends derived for reaction times in the range of minutes. The present findings let us hope that the simulations on polydisperse samples go beyond a bare case study. In analogy to the RMD data derived for monodisperse samples, also the quantities calculated for polydisperse ones offer insight into experimental control parameters of a living polymerization.

## 2.6. Conclusions

In the present contribution we have introduced a reactive MD approach equipped with a material-specific CG potential. We have chosen the polymerization of styrene monomers (represented by ethylbenzene) to polystyrene as a model. To simulate a living polymerization, irreversible bond formation and the absence of chain termination reactions have been assumed. For the mapping of the CG beads we have employed a potential optimized on the basis of atomistic equilibrium MD simulations. It is characterized by system-specific radial and angle terms that are less straightforward to implement than generic potentials. The different degrees of sophistication in the potential are perhaps the strongest discriminator between recent generic models and the present implementation.

The RMD scheme developed requires the introduction of two input parameters. The first is the delay time $\tau_r$ between two reactive MD steps, which is characteristic for simulation methods of the MD or MC type. The second parameter is related to an activation term for bond formation. The activation energy for this process is indirectly determined by so-called capture radii $r_I$ and $r_P$ defining the possibility that two nonbonded monomers form a chemical bond in a reactive step. This process is implemented as the transition from a nonbonded to a bonded CG potential. In our first numerical study we have allowed an instantaneous transition from a nonbonded to a bonded potential in a reactive process. The simulations discussed in the third section have verified that there is no heat up in the sample that exceeds the fluctuations in conventional equilibrium simulations. The largest T enhancement found in the case of fast reaction dynamics is still too small to be significant.

The capability of the present RMD formalism has been validated for monodisperse samples. The reactive MD code reproduces the results of equilibrium simulations. Densities, end-to-end distances, radii of gyration as well as different geometrical distribution functions have been chosen for the comparison of RMD and MD results. In this part of our work we have shown that the present RMD approach offers a straightforward access to equilibrated polymer configurations, which is an additional application for it. Previous coarse-grained RMD studies were more oriented in generating equilibrated polymer structures. Thus, the natural possibility to track the polymerization dynamics by RMD

simulations had not been fully explored. Despite all simplifications, the present model has been successful in reproducing the basic characteristics of living polymerization. The results derived for polydisperse samples have also been correlated favorably to experimental trends. The different case studies clearly emphasized the power of future RMD studies for (living) polymerizations.

## References


[1] Leung, Y.K.; Eichinger, B.E. J. Chem. Phys. 1984, 32, 3877.

[2] Faulon, J.L. J. Comput. Chem. 2001, 22, 580.

[3] Alperstein, D.; Dodiuk, H.; Kenig, S. Acta Polym. 1998, 49, 594.

[4] Zhang, Z.; Yamashita, T.; Wong, C.P. Macromol. Chem. Phys 2005, 206, 869.

[5] Cheng, K.-C.; Don, T.-M.; Rwei, S.P.; Li, Y.-C.; Duann, Y.-F. J. Polym. Sci.: Part B: Polym. Phys. 2002, 40, 1857.

[6] Wen, M.; Scriven, L.E.; McCormick, A.V. Macromolecules 2003, 36, 4140.

[7] Gupta, S.; Westermann-Clark, G.B.; Bitsanis, I. J. Chem. Phys. 1993, 98, 634.

[8] Milchev, A.; Wittmer, J.P.; Landau, D.P. J. Chem. Phys. 2000, 112, 1606.

[9] Khare, K.; Paulaitis, M.; Lustig, S.R. Macromolecules 1993, 26, 7203.

[10] Gao, J. J. Chem. Phys. 1995, 102, 1074.

[11] Akkermans, R.L.C.; Toxvaerd, S.; Briels, W.J. J. Chem. Phys. 1998, 109, 2929.

[12] Toxvaerd, S. J. Mol. Liq. 2000, 84, 99.

[13] Svaneborg, C.; Grest, G.C.; Everaers, R. Polymer 2005, 46, 4283.

[14] Berardi, R.; Micheletti, D.; Muccioli, L.; Ricci, M.; Zannoni, C. J. Chem. Phys. 2004, 121, 9123.

[15] Mavrantzas, V.G.; Boone, T.D.; Zervopoulo, E.; Theodorou, D.N. Macromolecules 1999, 32, 5072.

[16] Auhl, R.; Everaers, R.; Grest, G.S.; Kremer, K.; Plimpton, S.J. J. Chem. Phys. 2003, 119, 2718.

[17] Pant, P.V.K.; Theodorou, D.N. Macromolecules 1995, 28, 7224.

[18] Karayiannis, N.C.; Mavrantzas, V.G.; Theodorou, D.N. Phys. Rev. Lett. 2002, 88, 105503.

[19] ] Liu, H.; Qian, H.-J.; Zhao, Y.; Lu, Z.-Y. J. Chem. Phys. 2007, 127, 144903.

[20] Corezzi, S.; De Michele, C.; Zaccarelli, E.; Fioretto, D.; Sciortino, F. Soft Matter. 2008, 4, 1173.

[21] Perez, M.; Lame, O.; Leonforte, F.; Barrat, J.-L. J. Chem. Phys. 2008, 128, 234904.

[22] Sciortino, F.; De Michele, C.; Douglas, J.F.; Tartaglia, P. J. Chem. Phys. 2007, 126, 194903.

[23] Sciortino, F.; De Michele, C.; Douglas, J.F. J. Phys.: Condens. Mat. 2008 , 20, 155101.

[24] Xu, J.; Kjelstrup, S.; Bedeaux, D. Phys. Chem. Chem . Phys. 2006, 8, 2017.

[25] Smith, K.D.; Stoliarov, S.I.; Nyden, M.R.; Westmoreland, P.R. Mol. Sim. 2007, 33, 361.

[26] Jiang, B.; Selvan, M.E.; Keffer, D.J.; Edwards, B. J. J. Phys. Chem. B 2009, 113, 13670.

[27] Nyden, M.R.; Stolianov, S.I.; Westmoreland, P.R.; Guo, T.X.; Jee, C. Nat. Sci. & Engin. A 2004, 365, 114.

[28] van Duin, A.C.T.; Dasgupta, S.; Lorant, F.; Goddard III, W.A. J. Phys. Chem. A 2001, 105, 9396.

[29] van Duin, A.C.T.; Strachan, A.; Stewman, S.; Zhang, Q.; Xu, X.; Goddard III, W.A. J. Phys. Chem. A 2007,107, 3803.

[30] Turner, H.C.; Brennan, J.K.; Lísal, M.; Smith, W.R.; Johnson, J.K.; Gubbins, K.E. Mol. Simul. 2008, 34, 119.

[31] Qian, H.-J.; Carbone, P.; Chen, X.; Karimi-Varzaneh, H.A.; Liew, C.C.; Müller-Plathe, F. Macromolecules 2008, 24, 9919.

[32] Rossinsky, E.; Müller-Plathe, F. J. Chem Phys. 2009, 130, 134905.

[33] Algaer, E.; Alaghemandi, M.; Böhm, M.C.; Müller-Plathe, F. J. Phys. Chem. A 2009, 113, 11487.

[34] Algaer, E.; Alaghemandi, M.; Böhm, M.C.; Müller-Plathe, F. J. Phys. Chem. B 2009, 113, 14596.

[35] Theoretical Physical Chemistry TU-Darmstadt Home Page.

[36] http: //www.theo.chemie.tu-darmstadt.de

[37] Szwak, M.; van Beylen, M. Ionic Polymerization Living Polymers; Chapmans Hall: New York: 1993

[38] Allen, P.E.M, Patrick, C.R. Kinetics and Mechanism of Polymerization Reactions; Ellis Horwood: Chichester: 1974

[39] Rubinstein, M.; Colby, R.H. Polymer Physics; Oxford University Press: 2006

[40] Reith, D.; Pütz, M.; Müller-Plathe, F. J. Comput. Chem. 2003, 24, 1624.

[41] Binder, K.; Stauffer, D. Application of the Monte Carlo Method in Statistical Physics; Springer Verlag: Berlin: 1987.

[42] Böhm, M.C.; Elsässer, C.; Fähnle, M.; Brandt, E.H. Chem. Phys. 1989, 130, 65.

[43] Sujita,Y.; Okamoto, Y. Chem. Phys. Lett. 1999, 314, 141.

[44] Dollin, M.; Szkuhran, A.R.; Georges, M.K. J. Polym. Sci.: Part A: Polym. Chem. 2007, 45, 5487

[45] Miura, Y.; Mibae, S.; Moto, H.; Nakamura, N.; Yamada, B. Polymer Bulletin 1999, 42, 17.

[46] Berendsen, H.J.C.; Postma, P.M.; van Gunsteren, W.F.; Di Nola, A.; Haak, J.R. J. Chem. Phys. 1984, 81, 3684.

[47] Höcker, H.; Blake, G.J.; Flory, P.J. Trans. Faraday Soc. 1971, 67, 2251.

[48] Des Cloiseaux, J.; Jannink, G. Polymers in Solution; Their Modelling and Structure; Clarendon: Oxford: 1990.

[49] Sun, Q.; Faller, R. Macromolecules 2006, 39, 812.

[50] Fox, T.G.; Flory, P.J. J. Appl. Phys. 1950, 21, 581.

[51] Matyjaszewski, K. In controlled Radical Polymerization Chapter 1, ACS Symposium Series; American Chemical Society: Washington, DC: 1998

[52] Matyjaszewski, K.; Wang, J.L.; Grimaud, T.; Devon, A.S. Macromolecules 1998, 31, 1527.

[53] Matyjaszewski, K.; Wei, M.L.; Xia, J.; McDermott N.E. Macromolecules 1997, 30, 8161.

# 3. Temperature Dependence of Coarse-Grained Potentials for Liquid Hexane

## 3.1. Introduction

Atomistically resolved molecular dynamics (MD) simulations of complex liquids and polymers are often beyond current computational capacities.[1,2] Thus, there has been a strong need to develop simple and fast alternative methods to study such systems under conservation of the predictive capability of atomistic MD simulations. Several coarse-graining techniques meeting these requirements have been developed. In coarse-grained (CG) models, a number of atoms or characteristic functional groups are combined into superatoms denoted as CG beads.[1] This coarser description of the system provides a significant increase in the simulation speed.[2, 3]

A broad variety of CG mapping schemes has been described in detail in the literature for different polymer systems.[2-17] The simplest CG studies of polymers have been performed with spring potentials connecting the beads.[4] Universal properties of polymers can be successfully described by these generic bead-and-spring models.[5, 6, 7] Recent years have seen the emergence of methods enabling the development of material-specific CG potentials.[1, 8] Polystyrene (PS) has served as a prominent reference system in benchmark studies intended to demonstrate the predictive power of different CG mapping schemes.[9-15] In the CG approach of Milano et al.[11] developed for atactic PS at a temperature of 500 K and ambient pressure, the PS dyads (of either m or r stereochemistry) were considered as superatoms. The model successfully reproduced the structural and dynamic properties of PS for different chain lengths. The intramolecular potential in this method was described by multi-centered Gaussians.[10] To derive the tabulated nonbonded potential, the Iterative Boltzmann Inversion[8] (IBI) has been employed. The CG simulations of Harmandaris et al. using different PS mapping schemes [2, 12, 15] have also been successful in predicting structural and dynamic quantities. The IBI optimization was used in the work of Milano et al. and Harmandaris et al. A successful application of the Iterative Boltzmann Inversion in the challenging field of coarse-graining of biomolecular systems has recently been reported by Wang et al.[18] The inverse Monte Carlo technique (IMC) of Murtola et al. is also a powerful method that has been used to coarse-grain phospholipids/cholesterol bilayers.[19] The IMC technique differs from the IBI method in the way of extracting the effective pair-wise potentials from the target distribution functions. The present state of-

the-art has been reviewed in an article of Peter and Kremer.[20] Beside these structure-based techniques (i.e. IBI and IMC) other methods to optimize CG force-fields from atomistic simulations have been reported in the literature. Force matching approaches such as the "multi-scale coarse-graining" [21] of Voth et al. (MS-CG) or the MARTINI force-field [22] are successful approaches for coarse-graining simulations of biomolecular systems such as lipid bilayers. Outside the context of polymers and biomolecular systems, coarse-grained models for simple systems such as water and benzene can be found in the literature.[23, 24, 25]

In structure-based coarse-graining methods, the potentials are often determined on the basis of distribution functions for bond lengths, angle bending, and torsional angles, as well as for nonbonded distributions that have been evaluated at atomistic resolution. The IBI is a powerful and stable algorithm for the optimization of such CG potentials. However, when performing CG simulations with IBI one has to take into account that the potentials have been optimized for a certain thermodynamic state characterized by the reference temperature $T_0$, pressure $P_0$, and - in some applications - concentration(s). Thus, there is no guarantee that a CG potential developed at a reference temperature $T_0$ can be adopted successfully for temperatures $T \neq T_0$.[26] As a matter of fact, the transferability of CG potentials between different thermodynamic states has been widely investigated. In the CG model of Gosh and Faller for ortho-terphenyl, the potentials developed were significantly temperature dependent and non-transferable while the distribution functions showed weak temperature dependence.[27] In contrast, Vettorel and Mayer have optimized a CG model for short polyethylene chains[16] and as a result obtained temperature transferable potentials. The variationnal principle used in the MS-CG method allowed Krishna et al.[28] to generate potentials suitable for simulations at different T for a Lennard-Jones liquid and a simple water system. The same method with small modifications has been used to study the transferability of CG potentials for several compounds.[29] The MS-CG technique has very recently been adapted to perform potential optimizations in the NPT ensemble.[30] A recent coarse-grained model optimized to simulate PS, ethylbenzene (EB) and their mixtures has been reported by Qian et al.[13] They have found that the CG potential of PS is temperature-independent over a range of 100 K. The transferability of the EB coarse-grained potential over an interval of 142 K was ensured by scaling the potential optimized at $T_0$ with the factor $f(T) = (T/T_0)^{1/2}$ when performing MD simulations at other temperatures $T \neq T_0$.

It is the purpose of the present MD simulations to analyze the temperature dependence of CG potentials of molecular fluids, in order to deepen understanding of this concept and to determine its range of applicability. As an example, we have chosen liquid n-hexane, because, unlike the rather rigid ethylbenzene of our previous study[13], n-hexane is a flexible molecule. This flexibility must be translated into the CG mapping, which therefore needs intramolecular bond and angle terms. This

scheme differs from the single-site model for EB where the CG potential is exclusively composed - due to the mapping scheme - of nonbonded terms. We have applied the method proposed by Qian et al. to the present hexane CG model and detected that the analytic form of the T-dependent prefactor differs from the $f(T) = (T/T_0)^{1/2}$ behavior that has been reported for ethylbenzene. Furthermore, we have found that different forms of the prefactor must be used for the same system (here hexane) depending on the temperature $T_0$ at which the CG potential was optimized. In the present work, we modify the approach of the EB work. We have extended the single-reference model to a scheme where the CG potentials at temperature T are determined by a linear superposition of two reference CG potentials. These reference potentials are optimized at the limiting points $T_L$ and $T_U$ which bracket the temperature range investigated: $T_L \leq T \leq T_U$. We have found that the choice of $T_L$ and $T_U$ has no influence on the functional form of the interpolation formula as long as we explore a region of homogeneous phases. This will be shown by varying the limiting points $T_L$ and $T_U$ in the temperature range investigated here. The functional form would certainly depend on the choice of $T_L$ and $T_U$ in the presence of any phase transitions such as clustering, entrance into a glassy state, etc… In the same line the consideration of quantum fluctuations[31] would require modifications of the present simple interpolation. In this study, these boundaries are not met; the system is investigated by a classical MD approach in its pure liquid state.

One additional motivation for the present research has been our recent effort in the development of a reactive MD (RMD) code for so-called living polymerization in a CG resolution.[32] RMD simulations as a function of temperature and solvent (such as hexane) should provide useful information on the influence of a solvent during a polymerization process. With CG potentials that are transferable to a larger range of temperatures, such RMD simulations can be performed more efficiently.

## 3.2. Generation of Coarse-Grained Potentials

In the framework of the single-reference approach, the potentials from IBI optimizations at different $T_0$ are employed to generate other hexane CG potentials that are suitable for a temperature $T \neq T_0$ in the liquid phase. The scaling procedure previously suggested[13] was expressed as with $U(r, T_0)$ denoting the nonbonded CG potential developed at the reference temperature $T_0$.

$$U(r, T) = U(r, T_0) \times f(T) \qquad (3.1.)$$

$U(r,T)$ is the nonbonded potential at temperature $T \neq T_0$, while $f(T)$ is the scaling function. In reference 13, the model only consisted of nonbonded interactions. There, it was empirically found that, with the scaling function $f(T) = (T/T_0)^{1/2}$, it was possible to obtain accurate CG potentials for ethylbenzene at temperatures $T \neq T_0$. In the fifth section we analyze the accuracy of Equation (3.1.) for hexane in connection with a CG potential containing both intramolecular and nonbonded terms. In analogy to the previous study on EB, only the nonbonded hexane potentials have been scaled when adopting Equation (3.1.). The bonded potentials were left as they had been parameterized at $T_0$. For this model, we have studied a possible dependence on the choice of $T_0$ and of the scaling function $f(T)$.

The extended interpolation scheme of the present work uses two CG potentials $U(r,T_L)$ and $U(r,T_U)$ to estimate $U(r,T)$ in the intervening temperature range.

$$U(r,T) = C_L \times U(r,T_L) + C_U \times U(r,T_U) \text{ with } T_L \leq T \leq T_U \qquad (3.2.)$$

$U(r,T_L)$ and $U(r,T_U)$ can be any potentials of the CG force-field i.e. intra- or intermolecular terms. Thus, the 2-point interpolation (3.2.) is used to derive both inter- and intramolecular potentials suitable for use at any temperature T in the above interval. $C_L$ and $C_U$ are T-dependent mixing coefficients that generate the CG potential between $T_L$ and $T_U$. In the present study, we apply the simple linear relations (3.3.).

$$C_L = \frac{|T_U - T|}{T_U - T_L} \qquad C_U = \frac{|T_L - T|}{T_U - T_L} \quad . \qquad (3.3.)$$

With this definition, the sum of the two coefficients is always equal to 1. For $T = T_L$ ($T = T_U$), $C_U$ ($C_L$) does not contribute to the CG potential. As emphasized above it is expected that the 2-point interpolation (Equation (3.2.)) will lead to accurate CG potentials within a T interval in the absence of phase transitions. For hexane this is fulfilled in the temperature range 190 – 338 K[33] (liquid phase under atmospheric pressure). Finally we should mention that neither Equation (3.1.) or Equation (3.2.) can be traced back to a microscopic theory. Some qualitative considerations justifying Equation (3.1.) have been given in reference 13. We have accepted Equation (3.2.) as a useful empirical interpolation scheme that has been confirmed a posteriori by its computational accuracy.

## 3.3. Atomistic Simulations

To derive the target functions (distributions of bond distances, bond angles and non-bonded distances) for the coarse-graining optimization we have performed a number of atomistic MD simulations of liquid n-hexane in the temperature range 220 – 330 K at ambient pressure (101.3 kPa). The atomistic molecular dynamics package YASP was used.[34] NPT simulations were carried out with 250 molecules of hexane. We used a coupling time of 0.2 ps for the Berendsen thermostat and 2.0 ps for the barostat with an isothermal compressibility of 1.6 $kPa^{-1}$. A Verlet neighbor list cut-off of 1.1 nm in combination with a 1.0 nm cut-off for the nonbonded interactions was chosen. The neighbor list was updated every 10 simulation steps. The intramolecular bonded interactions of hexane were described by the OPLS-AA force-field.[35] The nonbonded Lennard-Jones parameters came from a force-field optimized for uncharged 2-methylpentane (isomer of hexane) via the simplex algorithm.[36] In our simulations the reduction of the 2-methylpentane hydrogen sigma parameter to 0.252 nm has led to a better accuracy for the density (ρ) and the diffusion coefficient. Our MD value of 655.56 $kg/m^3$ derived at 300 K agrees within 1 % with the experimental room-temperature densities[37-41] of 652.9 and 654.9 $kg/m^3$. The MD based diffusion coefficient of $3.26\times10^{-5}$ $cm^2/s$ derived at T = 300 K is of the same order of magnitude as the experimental[41] coefficient of $4.14\times10^{-5}$ $cm^2/s$. In a series of simulations at different temperatures (T = 220 – 330 K) we have calculated the hexane densities and distribution functions required for comparison with CG results. The good agreement between calculated and experimental densities can be observed in Table 3.1.

| T (K) | Atomistic simulation ($kg/m^3$) | experiments ($kg/m^3$) |
|---|---|---|
| 330 | 628.2 | 625.97 |
| 324 | 633.8 | 631.39 |
| 316 | 638.6 | 641.1 |
| 308 | 648.3 | 645.77 |
| 300 | 655.6 | 652.9 |
| 280 | 673.7 | 670.73 |
| 260 | 692.2 | 688.35 |
| 240 | 710.1 | 705.8 |
| 220 | 729.0 | 723.13 |

***Table 3.1.*** *Temperature dependence of the density of liquid hexane in the range 220-330 K from experiments[37-41] and atomistic simulations.*

## 3.4. Development of Coarse-Grained Potentials by Iterative Boltzmann Inversion

We have adopted a CG three-bead mapping for hexane (Figure 3.1.). The two terminal beads (type 1) comprise $C_2H_5$ groups while the central bead (type 2) is defined by the $C_2H_4$ fragment. The bead centers are placed at the center of mass of the respective group of atoms (symbolized in Figure 3.1. by the red dots). The present mapping scheme implies one bond type (between beads of type 1 and 2) and one 1-2-1 angle type parameter as intramolecular interactions. By means of the separation between the center of mass of the beads as well as the 1-2-1 angle, discrimination between atomistic trans, gauche or cis conformations is still possible. The nonbonded interaction between two hexane molecules is described by three intermolecular interactions: 1-1, 1-2 (= 2-1) and 2-2.

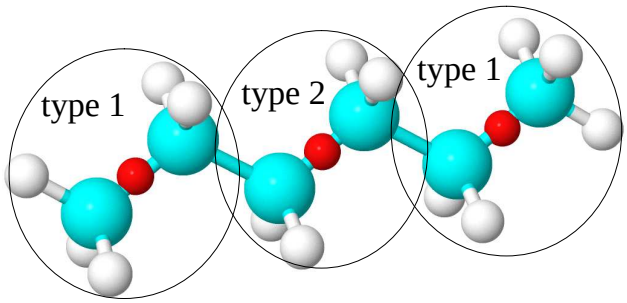


***Figure 3.1.*** *Coarse-grained mapping scheme for hexane with two types of beads. A type 1 bead represents a terminal $C_2H_5$ group, the central type 2 bead the $C_2H_4$ unit. The red dots symbolize the centers of mass of each group of atoms.*

The MD code IBIsCO[42] was used to derive the CG potential of hexane at three reference temperatures: $T_0$ = 220, 300 and 330 K. All inter- and intramolecular potentials optimized via the IBI algorithm with ramp corrections were tabulated. With the optimized CG potentials, simulations were carried out in the NPT ensemble at ambient pressure. The coupling times for the Berendsen thermostat and barostat were 0.2 and 5.0 ps, respectively, with the isothermal compressibility being 1.6 $kPa^{-1}$. The cut-off for the nonbonded interactions was 0.9 nm and the neighbor list cut-off 1.0 nm. The neighbor list was updated every 10 time steps. The optimized CG potentials used in the NPT simulations led to densities of 725.5, 655.6 and 628.3 $kg/m^3$ at $T_0$ = 220, 300 and 330 K. For each optimization temperature $T_0$ the atomistic and CG values differed by less than 1 %.

Figures 3.2. and 3.3. show the intramolecular bond length and bond angle distributions of the hexane beads derived from atomistic and CG trajectories. The maximum in the bond distributions at

$r_{max}$ = 0.267 nm indicates the dominance of atomistic *trans* configurations. The smaller maximum around 0.245 nm arises from a *gauche*-like alkane structure. A *cis* arrangement is not observed; it would occur at about 0.22 nm. The bond angle distribution has a maximum at an angle (α) somewhat smaller than 180°. Note that α = 180° between the centers of the beads refers to an alkane all-*trans* configuration. We notice that the present CG simulations reproduce the bonded distributions of the atomistic simulations with sufficient accuracy. The agreement between angle distributions for both simulation types is somewhat better than for the bonds. The atomistic radial distribution functions (rdfs, g(r)) are correctly reproduced by the CG simulations at any $T_0$ considered in the present series of simulations (Figure 3.4.). The figure shows only one example of the rdfs at each optimization temperature. The reduction of the first rdf maximum in the sequence $1{-}1 \rightarrow 1{-}2\ (= 2{-}1) \rightarrow 2{-}2$ is a manifestation of the decreasing probability of forming intermolecular contacts with participation of the central $C_2H_4$ bead. They are hindered by the excluded volume of the terminal $C_2H_5$ beads. The CG results of the present section can be summarized as follows: For each thermodynamic state chosen, we have shown that the CG potentials are accurate enough to reproduce MD results, such as densities and different distribution functions, which have been derived in atomistic resolution.

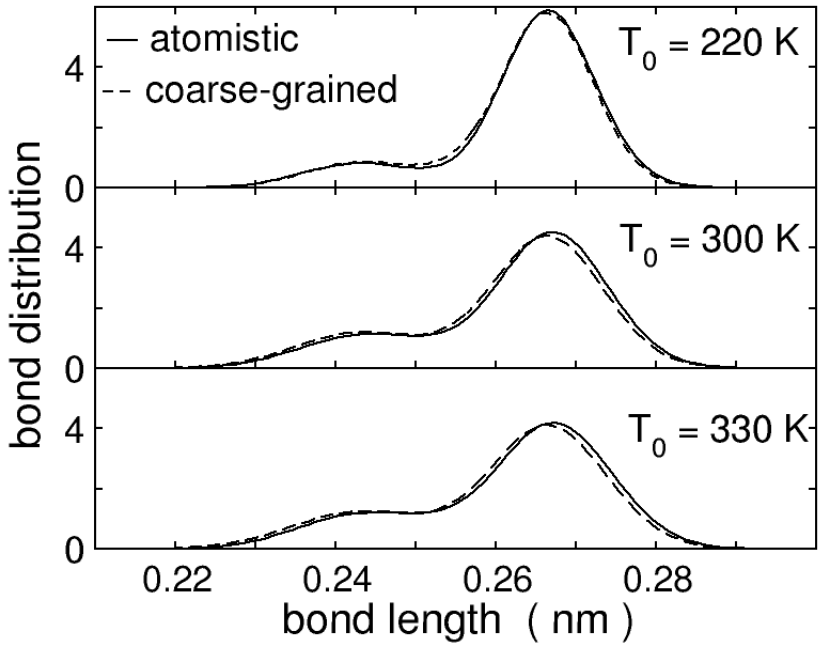


***Figure 3.2.*** *Bond length distributions between the centers of mass of hexane beads from atomistic and coarse-grained MD simulations. The CG potentials are optimized at $T_0$ = 220, 300 and 330 K.*

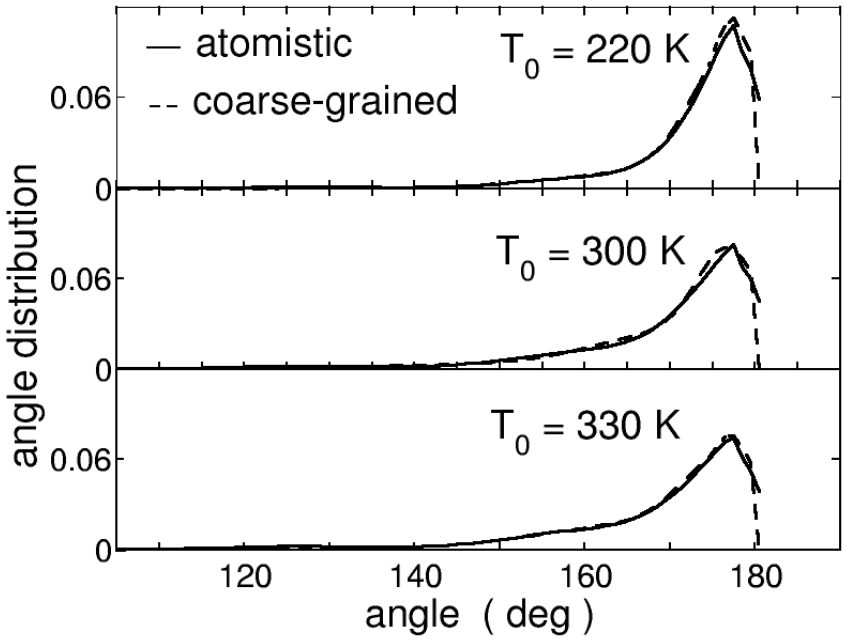


***Figure 3.3.*** *Angle distributions between the centers of mass of hexane beads from atomistic and coarse-grained MD simulations. The CG potentials are optimized at $T_0$ = 220, 300 and 330 K.*

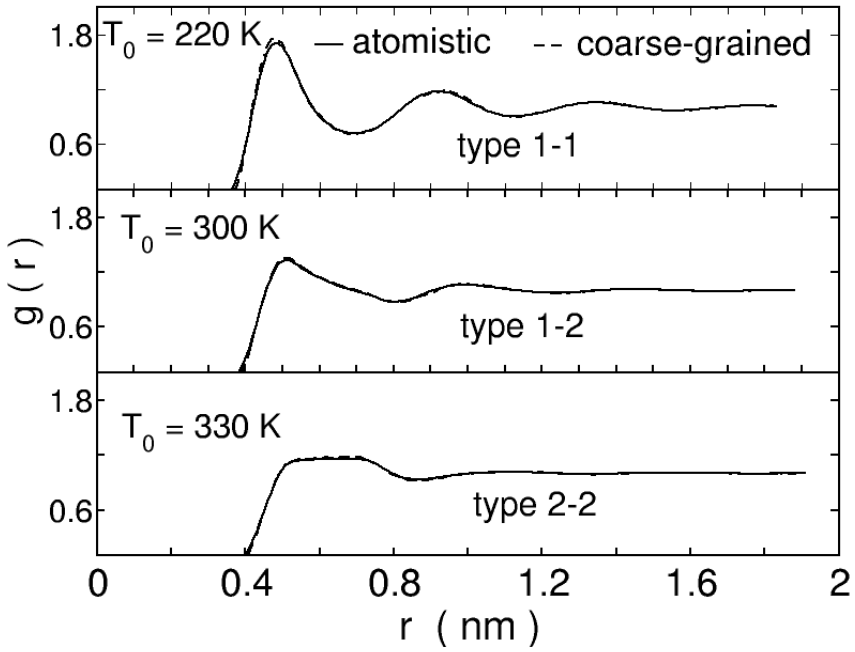


***Figure 3.4.*** *Nonbonded radial distribution functions g(r) between 1-1 ($T_0$ = 220 K), 1-2 ($T_0$ = 300 K) and 2-2 hexane beads ($T_0$ = 330 K) as derived by atomistic and CG simulations.*

## 3.5. Temperature Dependence of the Coarse-Grained Potentials

In this section, we compare the two Equations (3.1.) and (3.2.) for their ability to generate accurate potentials at temperatures other than the optimization temperatures. The criterion used to judge the accuracy of a potential is, in turn, its capability to reproduce the atomistic density and distribution functions at a particular temperature. To this end, coarse-grained simulations have been performed in two different T windows. The first range between 220 and 330 K was later extended to a second temperature range between 190 and 338 K. The reference temperatures $T_0$ in connection with the single-reference formula (Equation (3.1)) are 220, 300 and 330 K. The values for $T_L$ and $T_U$ in Equation (3.2.) for the first T range studied are 220 and 330 K. We have performed NPT simulations with the parameters developed in the foregoing sections. The transferability test of the coarse-grained potentials at temperatures $T \neq T_0$ or $T \neq T_U$, $T_L$ or has been performed under three different conditions. Firstly, we assumed that the CG potentials are T-independent. This approximation is described by $f(T) = 1$ in Equation (3.1.). The second type of simulation makes use of the single-reference formula (Equation (3.1.)) to calculate CG potentials at temperatures $T \neq T_0$. The function $f(T)$ has been chosen to reproduce densities in the T window between 220 and 330 K with an accuracy of ±1 %. However we have realized that with Equation (3.1.), the form of $f(T)$ depends on the optimization temperature

$T_0$. Finally we have checked the accuracy of the new interpolation formula (3.2.) which makes use of two thermodynamic reference states ($T_L$, $T_U$).

CG simulations under the assumption of T-independent potentials ( $f(T) = 1$) are accurate enough only in a narrow range around $T_0$. An exception in this series is the $T_0$ = 220 K case. With this reference temperature rather accurate distribution functions in the entire T window ranging from 220 to 330 K have been observed. This transferability does, however, not hold for the density (see Figure 3.5.). In Figure 3.5., CG densities derived using $f(T) = 1.0$, $f(T) = T_0/T$ and $f(T) = (T_0/T)^{1/2}$ are shown together with the experimental results (which are very close to the densities of the parent atomistic model, cf. Table 3.1.). In the bottom-right panel of Figure 3.5. we compare experimental densities to the results derived from the interpolation formula (Equation (3.2.)). The following message can be extracted from Figure 3.5.: Simulations based on $f(T) = 1.0$ (i.e. identical potentials for T and $T_0$) are valid only within a few K around $T_0$ (up-triangles). It can be deduced from the good matching between experimental and CG densities that the best factor for $T_0$ = 330 and 300 K is $f(T) = T_0/T$ (star symbols). We also observe that this factor is not suitable for $T_0$ = 220 K. In fact, the best scaling factor for $T_0$ =220 K is $f(T) = (T_0/T)^{1/2}$ (down-triangles). When scaling the potentials optimized at $T_0$ = 330 and 300 K with $f(T) = (T_0/T)^{1/2}$ the agreement between CG and experimental densities is reduced with decreasing temperatures (down-triangles on Figure 3.5.). We want to mention that the use of the ethylbenzene factor $f(T) = (T/T_0)^{1/2}$ has led to less accurate results for all optimization temperatures $T_0$ in the present case. By properly choosing a scaling function $f(T) \neq 1$ it is possible to reproduce the target experimental ρ values over the entire T interval considered, but we see that the analytic form of $f(T)$ depends on $T_0$. The bottom-right panel shows that the CG potentials derived with the help of the 2-point interpolation (Equation (3.2.)) lead to densities that coincide with the experimental ρ over the whole temperature range.

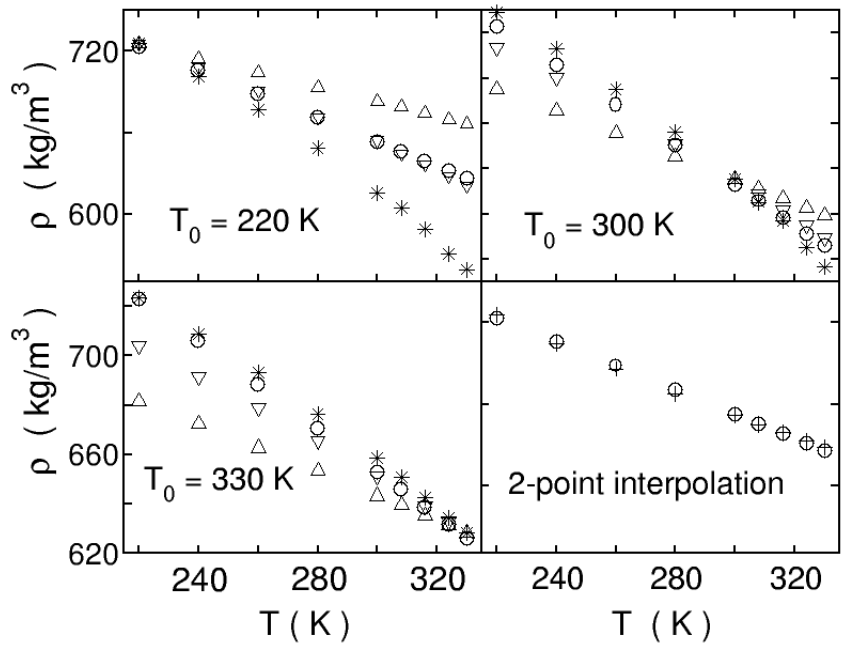


***Figure 3.5.*** *Temperature dependence of the hexane density (ρ). The circles (*O*) indicate experimental results. The up-triangles (Δ) denote the CG potentials derived with f(T) = 1 and the stars (∗) the application of f(T) = $T_0/T$. The down-triangles* (∇) *denote the use of f(T) = $(T_0/T)^{1/2}$. The crosses (+) are used in connection with the 2-point interpolation formula (3.2.) ($T_L$ = 220 K, $T_U$ = 330 K).*

The ability of the CG potentials to reproduce the distribution functions in the range 220-330 K has been estimated by the absolute root-mean-squared deviation (RMSD) between the target distributions and the simulated ones. A plot of the RMSD values as a function of T is shown on Figure 3.6. The blue symbols in all frames of the figure correspond to the RMSD that we have evaluated in the CG optimization via the IBI method (previous section). In the case of the frames a, b and c, the black symbols represent the RMSD between the atomistic target and distribution functions obtained when the transferability is tested with the assumption of T-independent potentials (f(T) = 1). In the case of frame d the black symbols are the RMSD resulting from the 2-point interpolation. Finally the deviation from target distributions resulting from the use of the CG potentials scaled with their best factors (see Figure 3.5.) is shown by the red symbols. We see from the blue symbols in the four diagrams of Figure 3.6. that the RMSD values for the nonbonded rdfs and angular distributions (blue circle, square, diamond and left-triangle in each frame a, b and c) resulting from the IBI optimization are smaller than for the bond distribution (blue up-triangle). Figures 3.2, 3.3, and 3.4 of the previous section can be consulted for a representative picture of these numbers. From graphs a, b and c it appears that the adoption of the best factors f(T) to scale the nonbonded potentials does not affect the

distribution functions significantly while the density turned out to be very sensitive to it (see Figure 3.5.). Only for $T_0$ = 300 K and $T_0$ = 330 K the bond distributions reveal a sensitivity to the use of the scaling factor $f(T) = T_0/T$ when approaching T = 280 K. In the case of $T_0$ = 220 K the RMSD values obtained from either the scaled ($f(T) = (T_0/T)^{1/2}$) or non-scaled (f (T) = 1) potentials are very close to the RMSD values resulting from the IBI optimization (blue symbols). This holds for all distributions and temperatures T. Note that the RMSD obtained for $T_0$ = 220 K increases slowly with increasing T. In the case of the 2-point interpolation scheme (graph d) the reproduction of all distribution functions is more stable. Its accuracy becomes evident especially when considering the scattering of the RMSD values of the single-point scheme with increasing separation from the optimization temperature $T_0$ (plot a, b and c). In Figure 3.7. we have plotted intramolecular bond distributions as derived by atomistic simulations and via Equation (3.1.) and (3.2.). The bond distributions in connection with Equation (3.1.) are derived using the best factor f(T) of each optimization temperature $T_0$ considered (see above). As expected from the RMSD plot of Figure 3.6., the bond distributions at higher temperatures (T = 308 K and 324 K) are well reproduced by choosing $T_0$ = 300 or 330 K combined with $f(T) = T_0/T$ as well as by the potentials optimized at $T_0$ = 220 K and scaled with $f(T) = (T_0/T)^{1/2}$. At T = 260 K the target distribution is nevertheless best reproduced by choosing $T_0$ = 220 K with $f(T) = (T_0/T)^{1/2}$ rather than $T_0$ = 300 or 330 K. Figure 3.7. also shows that a good agreement is observed between the target distribution functions and the CG profiles derived with the 2-point interpolation (3.2.).

Encouraged by the results of the 2-point interpolation (Equation (3.2.)) and the application of the best scaling factor $f(T) = (T_0/T)^{1/2}$ associated with $T_0$ = 220 K (Equation (3.1.)), we have extended the T window in the CG simulations. In the case of the single-point method two new simulations at T = 190 and 338 K had been performed after scaling the potentials optimized at $T_0$ = 220 K with the factor $f(T) = (T_0/T)^{1/2}$. In the case of the 2-point interpolation scheme, we have shifted $T_L$ to 190 K while $T_U$ has been raised to 338 K. Two additional IBI optimizations have been carried out at these two reference temperatures.

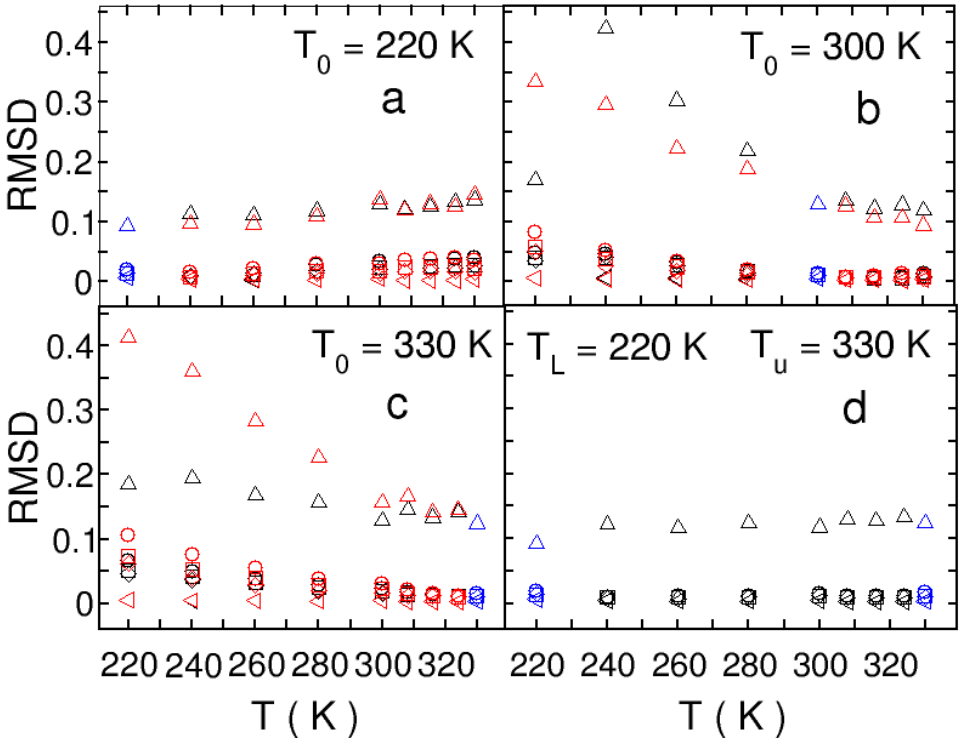


***Figure 3.6.*** *Absolute root-mean-squared deviation (RMSD) between target and simulated distribution functions as a function of T. In all four diagrams the blue symbols represent the RMSD values resulting from the IBI optimization process. In a, b and c the black and red symbols refer to the direct use of the potentials (f(T) = 1) at $T \neq T_0$ and to the adoption of the best scaling factor f(T) for each $T_0$. The black symbols in d correspond to the performance of the 2-point interpolation method. In all four diagrams the circles refer to the RMSD between target and simulated rdfs for the nonbonded interaction of the 1-1 type, the squares refer to the 1-2 and the diamonds to the 2-2 interaction type. The RMSD values for the bond and angle distributions are shown by up- and left-triangles.*

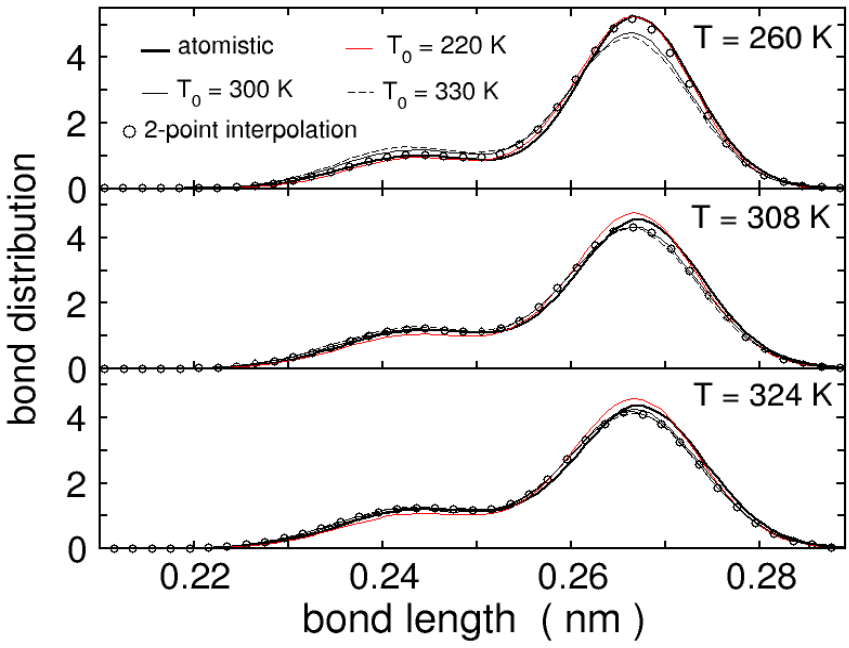


***Figure 3.7.*** *Bond distributions at temperatures T of 260, 308 and 324 K (from top to bottom) from atomistic simulations and different CG variants. The single-reference distributions are based on CG potentials optimized at $T_0$ = 220, 300 and 330 K. The function $f(T) = (T_0/T)^{1/2}$ is used for the simulations with reference temperature $T_0$ = 220 K. The linear function $f(T) = T_0/T$ has been used for $T_0$ = 300 and 330 K. The 2-point interpolation are derived from equation (2) with $T_L$ = 220 K and $T_U$ = 330 K.*

Hexane is still in the liquid phase in this 148 K interval (at P = 101.3 kPa). Here, we show that the same relation (3.2.) can still be used when varying the optimization temperatures $T_L$ and $T_U$. In analogy to the investigations carried out for the temperature window 200 – 330 K, good accuracy is again observed with relation (3.2.) as well as with the optimized potentials at $T_0$ = 220 K when scaled with $f(T) = (T_0/T)^{1/2}$. In analogy to Figure 3.6. we have plotted in Figure 3.8. the RMSD between the target and simulated distributions in the range 190 – 338 K for the 2-point interpolation (black symbols) and for the two temperatures 190 and 338 K which have been chosen in the single-point method (red symbols). Figure 3.8. clearly shows that the good accuracy of the two models as already observed in Figure 3.6. still holds for the distributions when a wider temperature range is considered. The 2-point interpolation yields a somewhat higher accuracy than the single-point approach. For a representative example, the intermolecular g(r) for the 1-1, 1-2 and 2-2 beads at T = 260 K as derived by atomistic MD simulations and by the 2-point interpolation (Equation (3.2.)) with the larger [$T_L$, $T_U$] interval are displayed on Figure 3.9. The agreement between both simulations is perfect. The intramolecular bond and angle distributions calculated under the same conditions and at the same T =

260 K as realized for the intermolecular rdfs are shown in Figure 3.10. Although the agreement between target values and scaled CG data is not as good as for the rdfs, the 2-point interpolation is still of sufficient accuracy.

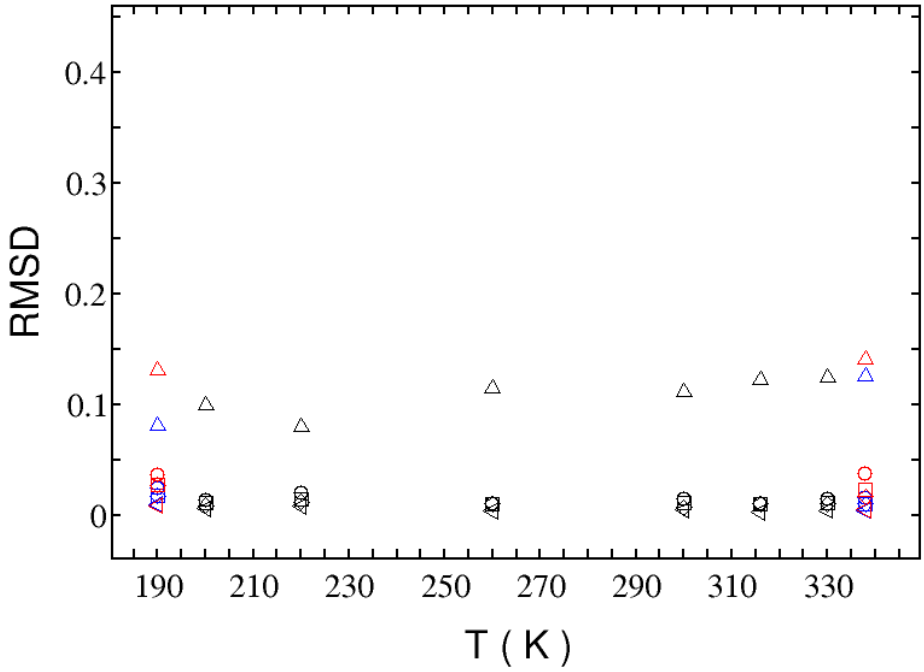


***Figure 3.8.*** *Absolute root-mean-squared deviation (RMSD) between target and simulated distribution functions as a function of T. The blue symbols represent the RMSD values resulting from the IBI optimization at $T_0$ = 190 and 338 K. The black symbols refer to the 2-point interpolation method with $T_L$ = 190 K and $T_U$ = 338 K. The red ones indicate refer the use of potentials optimized at $T_0$ = 220 K and scaled with $f(T) = (T_0/T)^{1/2}$. The circles symbolize the RMSD values between target and simulated rdfs for the nonbonded interaction of the 1-1 type, the squares characterize the 1-2 and the diamonds the 2-2 type interaction. The RMSD values for the bond and angle distributions are shown by up- and left-triangles.*

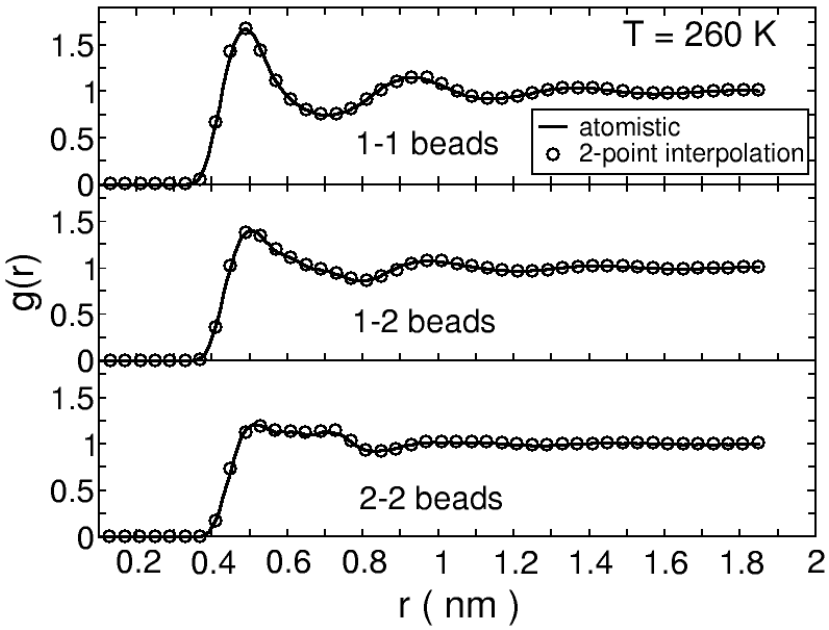


***Figure 3.9.*** *Radial distribution functions g(r) for 1-1, 1-2 (= 2-1) and 2-2 pairs at T = 260 K from atomistic simulations and the 2-point interpolation (Equation (3.2.)) with $T_L$ = 190 K and $T_U$ = 338 K.*

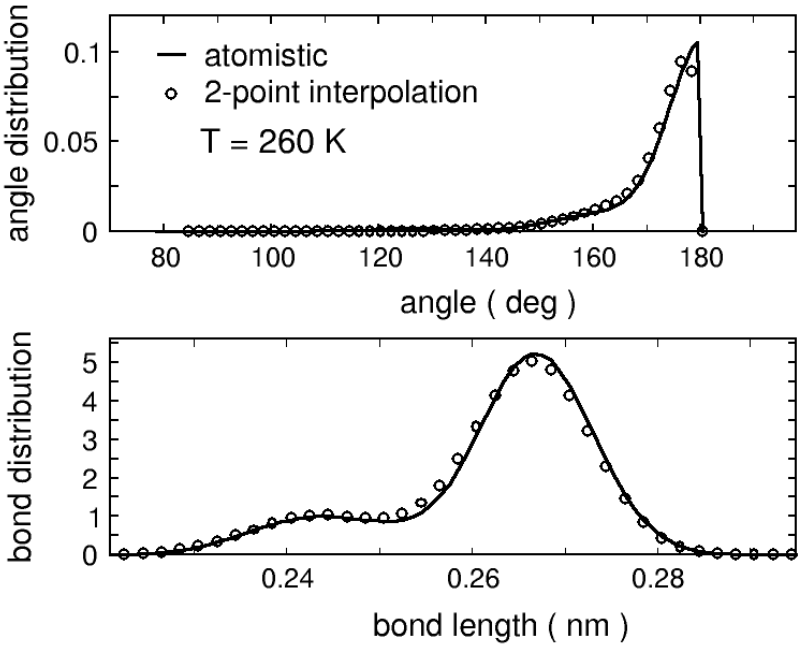


***Figure 3.10.*** *Angle (top diagram) and bond length (bottom diagram) distributions at T = 260 K from atomistic simulations and the 2-point interpolation (Equation (3.2.)) with $T_L$ = 190 K and $T_U$ = 338 K.*

The temperature dependence of the hexane density is presented in Figure 3.11. for the single-point and 2-point interpolation methods. It is an extension of Figure 3.5. to a larger T interval. We see that an increase of the T interval from 110 K to 148 K does not lead to a reduction in the accuracy of the 2-point interpolation (Equation 3.2.). The target and CG densities agree - on the average - within 1 %. Only for T = 260 K and 300 K the error is slightly increased to 1.2 %. In consideration of the simplicity of the interpolation scheme, the agreement observed for the densities is completely sufficient. The single-point method also provides very good accuracy by reproducing the target densities within 1 %.

## 3.6. Discussion

The optimized potentials and the target distribution functions of our hexane mapping scheme are all T-dependent, irrespective of the optimization temperature $T_0$ (Figures A.3.1. and A.3.2. in Appendix Section). When directly used at $T \neq T_0$ the optimized potentials fail to reproduce the density in the temperature range investigated. This agrees with the experience derived for the EB system.[13] similarly, we find that the use of scaling factors is a prerequisite in the present T dependent CG simulations. Nevertheless a more detailed investigation shows that the suitable functional form to be used depends on $T_0$ (see Figure 3.5.). Here, we have only scaled the nonbonded CG potentials with the factor f(T). This was justified a posteriori by the fact that the bonded CG potentials appeared – with a small exception (see below) - rather insensitive to the use of f(T) in their ability to reproduce structural properties. As shown in Figsure 3.5, 3.6 and 3.8 the model optimized at $T_0$ = 220 K and scaled with $f(T) = (T_0/T)^{1/2}$ matches the densities and all structural target functions in the range 190 - 338 K with sufficient accuracy. The potentials from the optimization at $T_0$ = 330 and 300 K scaled with $f(T) = T_0/T$ are sensitive to the scaling process in their ability to reproduce the structural target functions - especially the bond distribution - when approaching lower temperatures. Figure 3.6. shows that the sensitivity to the scaling process in the high temperature range (300 – 338 K) is less pronounced than at lower temperatures. For the potentials optimized at T = 330 and 300 K, Figure 3.6. shows a reduced accuracy to reproduce distributions when going down in temperature. Figure A.3.6. of the Appendix Section illustrates the sensitivity as well as the accuracy of the scaling process in matching the bond distribution at low temperature (T = 240 K). This type of unexpected behavior in addition to the $T_0$ dependence of f(T) makes the single-reference model - despite its computational success - very difficult to generalize.

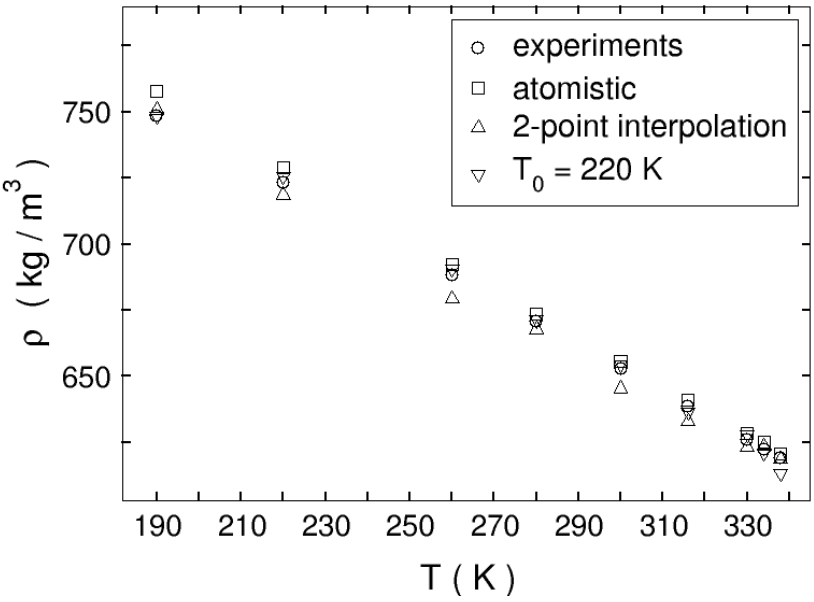


***Figure 3.11.*** *Temperature dependence of the hexane density from experiments[37-41], atomistic and coarse-grained simulations. The coarse-graining simulations use the 2-point interpolation method (Equation (3.2.)) with $T_L$ = 190 K and $T_U$ = 338 K and the optimized potentials at $T_0$ = 220 K scaled with $f(T) = (T_0/T)^{1/2}$ to derive the CG potentials at a temperature T.*

To further illustrate this feature we made unsuccessful attempts to find a suitable factor f(T) for $T_0$ = 190 K. The factors f(T) = 1, $f(T) = T_0/T$, $f(T) = T/T_0$, $f(T) = (T_0/T)^{1/2}$ and $f(T) = (T/T_0)^{1/2}$ (used for EB) failed to reproduce the density as a function of T; see Figure 3.12. The determination of a new factor f(T) would be necessary in this example. The 2-point interpolation requires the absence of a phase transition in the temperature window investigated (pure liquid phase here). It appears that the linear combination (Equation (3.2.)) used to derive the CG potentials for a temperature T is independent of the limiting points $T_L$ and $T_U$ of the window investigated in this study. With only one formula the densities and distribution functions were well reproduced in the two T windows between 220-330 K and 190-338 K (Figure 3.6. and 3.8.).

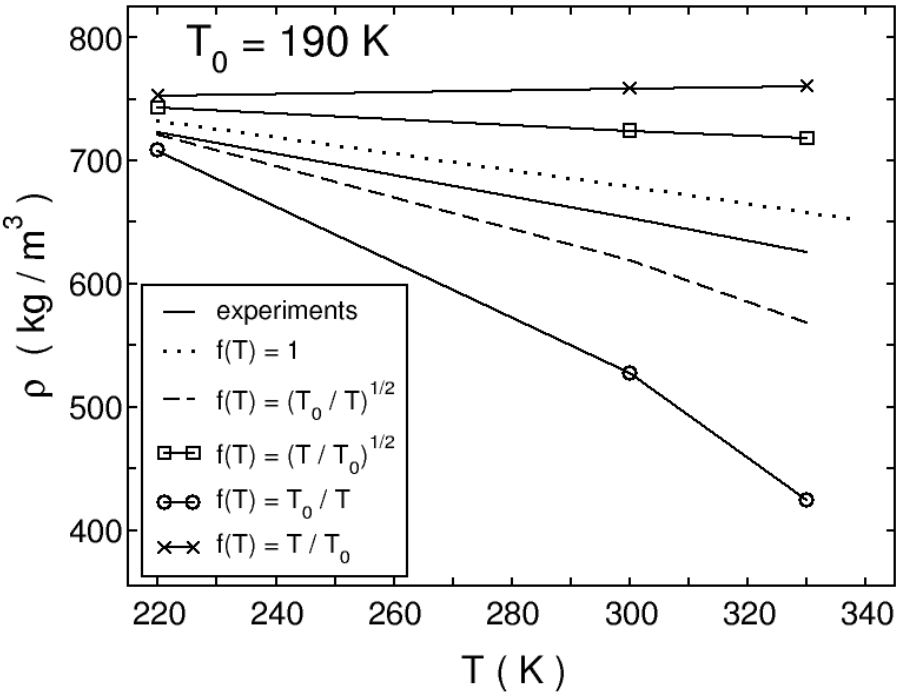


***Figure 3.12.*** *Temperature dependence of the hexane density (ρ) for the CG potentials optimized at $T_0$ = 190 K and scaled with different factors f(T). The simulated densities are compared with experiments.*

We now investigate the effect of the different scaling factors f(T) on the CG potentials that have been optimized via the Iterative Boltzmann Inversion at $T_0$ = 220, 300 and 330 K. The factor f(T) = $(T_0/T)^{1/2}$ leads - for any T – to a shift of the minimum of the nonbonded potentials (1-1, 1-2 and 2-2) towards positive values. Therefore, densities derived via $T_0$ = 220 K and f(T) = $(T_0/T)^{1/2}$ are sufficiently lowered. They are of better agreement with experiments than the densities determined via $T_0$ = 220 K and f(T) = 1 (see Figure 3.5.). An example of such a shift-up of the minimum of nonbonded potential is provided in Figure A.3.4 of the Appendix Section. The factor f(T) = $T_0/T$ has the inverse effect on the potentials that have been optimized at $T_0$ = 330 K. We can see from Figure 3.5. that the densities before potential scaling (triangle-up symbols) are lower than the experimental values (circles). The factor f(T) = $T_0/T$ shifts - for any T - the minimum of the nonbonded potentials towards negative values (see Figure A.3.5. of Appendix Section). The scaled nonbonded potentials are thus less soft than the non-scaled ones and the simulated densities increase towards the experimental ones. For the potentials optimized at $T_0$ = 300 K the correction of the nonbonded potentials depends on the actual position of T. The minimum of the nonbonded potentials is shifted in the direction of positive values when T > 300 K while the contrary happens when T < 300 K (Appendix Section, Figure A.3.6. and A.3.7.). The single-reference scaling factors f(T) therefore tune the depth of the

potentials that have been optimized with the IBI method in a way to reproduce the correct densities. However, we have also seen that potentials at a given $T_0$ scaled with the best factor f(T) yield nonbonded potentials that differ from the optimized IBI ones at this T. Figures A.3.4., A.3.5., A.3.6. and A.3.7. of the Appendix Section illustrate this point. In contrast with the single-reference scaling method, the 2-point interpolation reproduces the IBI optimized potentials for any $T = T_0$ with high accuracy. The 2-point interpolation seems, nevertheless, to be less accurate in reproducing the high energy domain of the angular potential while it is rather accurate in the relevant low energy region between 120 and 180 degrees. As a matter of fact the deviation between the 2-point interpolation and IBI optimized angular potentials in the high energy domain does not influence the corresponding distribution. The ability of the two-point interpolation to generate potentials similar to the IBI potentials at the same T is demonstrated in Figures A.3.8. and A.3.9. of the Appendix Section. The examples just discussed are clear evidence favoring the two-point interpolation in the derivation of temperature dependent CG potentials.

The use of scaling factors is necessary when the CG mapping scheme for a given system does not lead to temperature independent potentials. For example, in the framework of the MS-CG technique a powerful temperature rescaling process has been formally established.[28] Nevertheless, this scaling process requires expensive sampling of the configurations to be efficient.[28,29] This process might become difficult for complex polymeric or biomolecular systems. A complement to this MS-CG model (i.e. the EF-CG method) has been used by Wang et al. to test the transferability of effective potentials for number of properties[29] (symmetry and size of the system, temperature…) of several compounds including an ionic liquid. To our knowledge this work belongs to the sparse studies where a set of CG potentials for a low molecular weight system has been transferred with reasonable success and in the absence of scaling factors to different temperatures. More examples for CG systems of higher molecular weight for which the potentials are temperature independent over a wide window can be found in the literature.[3, 13, 16] Of particular relevance for our work is the approach of Vettorel et al.[16] on the temperature transferability of CG potentials for polyethylene chains containing 8 to 44 carbon atoms. In contrast to our short alkane chains they have developed via IBI optimizations a T-independent set of potentials. The group of atoms composing the bead has been the $C_2H_4$ fragment which is similar to the hexane beads defined in this work. It is interesting to see that it differs from the present hexane model prevailingly in the length of the alkane chain and the choice of the center of the bead. In our case, the bead center corresponds to the center of mass of the bead while in the polyethylene work it has been located at any second carbon atom of the chain backbone. It would be

interesting to evaluate the relative importance of the size of the system and the choice of the bead center location by applying their CG scheme to our short alkane system.

## 3.7. Conclusion

In the present MD study we have analyzed the temperature dependence of coarse-grained potentials for liquid n-hexane that are defined both by intramolecular and intermolecular contributions. A temperature interval of up to 148 K (the entire liquid range from 190 to 338 K) has been investigated. It was shown that a CG potential derived by a linear interpolation between two CG potentials optimized at the boundaries of the T interval was able to reproduce the density, the distributions of bond lengths and angles and the different nonbonded radial distribution functions in the entire temperature range. As reference we have chosen the parent atomistic simulation or the experiment. The use of the 2-point interpolation proved to be robust. We also showed that the old 1-point extrapolation (ref. 13), which uses extrapolated CG potentials from a single reference temperature, can only be made predictive if the potentials are scaled by a T dependent factor. This function needs to be determined empirically, is different for different system, and seems to depend in an unpredictable way on the reference temperature $T_0$. Nevertheless, accurate potentials could be generated in the T range 190 – 338 K with the potentials optimized at $T_0$ = 220 K and scaled with the factor f(T) = ($T_0$/T)1/2. It was shown here that the new two-point interpolation also works for a molecular liquid with internal flexibility. We will apply the interpolation procedure to other systems, in order to further test its range of applicability.

## References


[1] F. Müller-Plathe, ChemPhysChem, 2002, 3, 754.

[2] V.A. Harmandaris, D. Reith, N.F.A. van der Vegt and K. Kremer, Macromol. Chem. Phys., 2007, 208, 2109.

[3] P. Carbone, H.A. Karimi-Varzaneh, X. Chen and F. Müller-Plathe, J. Chem. Phys., 2008, 128, 064904.

[4] K. Kremer and G.S. Grest, J.Chem.Phys., 1990, 92, 5057.

[5] J.G.H. Cifre, S. Hess and M. Kröger, Macromol. Theory Simul., 2004, 13, 748-753.

[6] R.L.C. Akkermans, S. Toxvaerd and W.J. Briels, J.Chem. Phys., 1998, 109, 2929.

[7] M. Perez, O. Lame, F. Leonforte and J.L. Barrat, J.Chem. Phys., 2008, 128, 234904.

[8] D. Reith, M. Pütz and F. Müller-Plathe, J. Comput. Chem., 2003, 24, 1624.

[9] Q. Sun and R. Faller, Macromolecules, 2006, 39, 812.

[10] G. Milano, S. Goudeau and F. Müller-Plathe, J. Polym. Sci., Part B : Polym. Phys., 2005, 43, 871.

[11] Milano, G. and Müller-Plathe, F. J. Phys. Chem. B, 2005, 109, 18609.

[12] V.A. Harmandaris, N.P. Adhikari, N.F.A. van der Vegt and K. Kremer, Macromolecules 2006, 39, 6708.

[13] H.J. Qian, P. Carbone, X. Chen, H.A. Karimi-Varzaneh, C.C. Liew and F. Müller-Plathe, Macromolecules, 2008, 41, 9919.

[14] T. Spyriouni, C. Tzoumanekas, D. Theodorou, F. Müller-Plathe and G. Milano Macromolecules, 2007, 40, 3876-3885.

[15] D. Fritz, V.A. Harmandaris, K. Kremer and N.F.A van der Vegt, Macromolecules, 2009, 42, 7579-7588

[16] T. Vettorel and H. Meyer, Chem. Theory Comput., 2006, 2, 616.

[17] D. Reith, H. Meyer and F. Müller-Plathe, Macromolecules, 2001, 34, 2335.

[18] Z.J.,Wang and D.Markus, J. Phys. Chem. B, 2010, 114, 11207.

[19] T. Murtola, E. Falck, M. Karttunen and L. Vattulainen, J. Chem. Phys., 2007, 126, 075101.

[20] C. Peter and K. Kremer, soft matter, 2009, 5, 4357.

[21] S. Izvekov and A.G. Voth, J. Phys. Chem. B, 2005, 109, 2469.

[22] S.J. Marrink, H.J. Risselada, S. Yefimov, D.P. Tieleman and A.H. Vries, J. Phys. Chem. B, 2007, 111,7812.

[23] N. Zacharopoulos, N. Vergadou and D.N. Theodorou, J. Chem. Phys., 2005, 122, 244111.

[24] M.E. Johnson, T. Head-Gordon and A.A. Louis, J. Chem. Phys., 2007, 126, 144509.

[25] H. Wang, C. Junghans and K. Kremer, Eur. Phys. J. E., 2009, 28, 221.

[26] D. Reith, F. Müller-Plathe and S.Wiegand, J. Chem. Phys., 2002, 116, 9100.

[27] J. Ghosh and R. Faller, Mol. Sim., 2007, 33, 759.

[28] V. Krishna, W.G. Noid and G.A.Voth, J. Chem. Phys., 2009, 131, 024103.

[29] Y. Wang, W.G. Noid, P. Liu and G.A. Voth, Phys. Chem. Chem. Phys., 2009, 11, 2002.

[30] A. Das and H.C. Andersen, J. Chem. Phys., 2010, 132, 164106.

[31] M.C. Böhm, J. Schulte, E. Hernandez and R. Ramirez, Chem. Phys., 2001, 264, 371.

[32] K. Farah, H.A. Karimi-Varzaneh, F. Müller-Plathe and M.C. Böhm, J. Phys. Chem. B, in press.

[33] CRC Press, Handbook of Chemistry and physics 75$^{th}$ edition, 1994.

[34] F. Müller-Plathe, Comput. Phys. Commun., 1993, 78, 77.

[35] W.L. Jorgensen, J. Am. Chem. Soc., 1996, 118, 11225.

[36] R.J. Faller, Comput. Chem., 1999, 20, 1009.

[37] A.D. Sen, V.G. Anicich, T. Arakelian, J. Phys. D: Appl. Phys., 1992, 25, 516.

[38] D.M. Peña and G. Tardajos, J. Chem. Thermodynamics, 1978, 10, 19-24.

[39] E. Aicart and E. Junquer, J. Chem. Eng. Data, 1995, 40, 1225-1227.

[40] G.M. Mikhailov, V.G. Mikhailov, L.S. Reva and G.V. Ryabchuk, Russian Journal of Applied Chemistry, 2005, 78, 1067.

[41] R.K. Harris, J. Chem. Soc. Faraday Trans. 1, 1982, 78, 2265-2274.

[42] H.A. Karimi-Varzaneh, H-J. Qian, X. Chen, P. Carbone and F. Müller-Plathe, “IBIsCO: A molecular dynamics package for coarse-grained simulation”, J. Comput. Chem., in press.

# 4. Interphase Formation during Curing: Reactive Coarse-Grained Molecular Dynamics Simulations

## 4.1. Introduction

The ability of polymer materials to adhere to solid substrates has been intensively exploited in the design of polymer matrix composites, in coating processes and in the adhesive joining of surfaces.[1-11] Polymer adhesion onto solid surfaces originates from interactions spanning the range from weak van der Waals forces to chemical bond formation with surface constituents.[1] Adhesion is generally accompanied by a modification of the polymer properties near the adhesive-substrate interface region. Polymer-substrate interactions determine the polymer properties in these particular domains denoted as "interphases".[1-11] They are considered as important regions influencing the durability of adhesive-substrate systems. Thus, intense experimental efforts have been devoted to the characterization of interphases.[1-11] The development of experimental techniques for their investigation, however, is rather challenging. Measurements are particularly difficult for so-called "closed" joint configurations in which the adhesive part is covered by two solid surfaces.[1] "Open" joints offer an easier experimental access; these are polymer films coating only one surface. Properties are then measured for different film thicknesses. The interphase behavior is observed for thin polymer films while bulk properties are found for thick ones.[1, 3, 6, 7, 11, 12]

Epoxies and polyurethanes belong to two popular classes of polymers for coating as well as for the adhesive joining of surfaces.[1, 5, 7, 8, 10-12] These adhesives are frequently prepared as reactive liquid mixtures of monomers and linkers. In the initial step, the surface is coated with the reactive mixture. Subsequently, the cross-linking reaction is initiated and an adhesive polymer network is generated.[7, 11, 12] The interphase properties of epoxy and polyurethane adhesives cured onto various substrates have been a subject of detailed experimental investigations. Wehlack et al.[1] described the formation of organometallic bonds near the interface region of gold, aluminum and copper coated by epoxy and polyurethane network films. Bockenheimer et al.[11] analyzed the influence of mechanically pretreated aluminum surfaces that have been blasted either with alumina grit or glass beads on the formation of epoxy films. They showed a correlation between the nature of the surface pretreatment and the degree of cross-linker conversion in the resulting polymer films. Both the network morphology and the mobility of the particles at the interface were related to the surface pretreatment. With the help of

scanning force microscopy and energy dispersive X-ray analysis, Chung et al.[7] revealed a mechanical interphase for epoxy resins cured with amine compounds on a copper surface. In their study the interphase could be divided into a high-stiffness region close to the surface and a low-stiffness region in its direct neighborhood. In contrast to Chung et al.[7] who have discussed a stiffness gradient, Safavi-Ardebili et al.[8] extracted from an energy dispersive X-ray analysis and nano-indentation tests the formation of a hard homogeneous interphase when curing an epoxy adhesive onto an aluminum surface. All of these investigations highlight the complexity of interphase regions which are subject to chemical, dynamical and morphological alterations leading to properties that differ from bulk behavior.

Complex interfacial processes are thought to be responsible for the properties of the polymer interphase. Experiments[1, 5, 11, 12] and electronic structure calculations[13] emphasized the possibility of preferential interactions between the surface and one of the adhesive components leading to selective enrichment or even segregation. This preference is particularly important for adhesives which are applied as liquid mixtures. They can be easily influenced by surface-induced segregation prior to the curing process. The current opinion is that such segregation processes are one of the principal effects that influence the interphase properties in polymeric adhesive compounds. [1-11]

As a result of certain experimental uncertainties, molecular dynamics (MD) simulations have become an important tool to investigate interphase properties. MD offers access to static structural and dynamic properties of molecular and polymer systems. The method has been used extensively to study polymers in contact with solid surfaces.[14-23] In the present approach, we simulate a cross-linking reaction of an adhesive formed by reactive monomers and linkers in the presence of a surface. The study is performed in the framework of a reactive molecular dynamics (RMD) scheme. In this method a conventional MD implementation is augmented to allow connectivity-altering processes.[24-32] RMD has been used previously to study reactive processes in systems with a surface region. Fogarty et al.[33] have described reactions at a silica-water interface using the reactive force-field ReaxFF developed by van Duin and Goddard.[29, 34] With a different reactive force-field the same process has been modeled by Mahadevan and Garofalini.[35] ReaxFF has been employed also by Quenneville et al.[36] to study the interaction of dimethyl methylphosphonate with amorphous hydroxylated silica particles. In contrast to these RMD studies on the formation of only one or a few new bond(s), Liu et al.[37] have modeled a polymerization process in the vicinity of a surface. They investigated the properties of grafted polymer brushes as a function of the initiator density in a surface-initiated polymerization. Their generic polymer model was described by the finitely extensible nonlinear elastic (FENE) potential[38] combined with a Weeks-Chandler-Andersen potential[39] for the intermolecular interactions. In analogy to other reactive MD simulations on the basis of generic interactions or in coarse grained (CG)

resolution, the bond formation in the latter work has been described with the help of a distance-dependent criterion, i.e. a so-called capture radius, and a characteristic time for the relaxation of the system between two connectivity-altering steps.[28, 31, 37] While ref. 37 is one of the few RMD simulations of a surface-induced polymerization, bulk polymerizations have been analyzed in a number of reactive MD approaches.[28, 31, 40] In the majority of these computer experiments, generic polymer models have been used. In the simulations of the Stevens group, monomers and linkers were placed between two walls; then they were equilibrated.[15, 20] The chemisorption processes between the adhesive components and the surface have been modeled via a distance-based criterion. A Lennard-Jones potential and a modified FENE potential were adopted to describe the network. The modified potential allowed bond breaking in the adhesive as a function of the simulation conditions as well as of the model parameters of the RMD scheme. No interphase investigation was attempted in these studies. The present manuscript focuses on the impact of segregation processes caused by selective surfaces on interphase formation during the curing of adhesives.

In a recent RMD study[40] we have simulated the polymerization of styrene molecules (modeled as ethylbenzene (EB)) to polystyrene (PS) chains with the help of realistic CG potentials that have been generated from atomistic calculations via iterative Boltzmann inversion (IBI).[41] In the optimization of the CG potential, PS, EB and their mixtures have been considered. Despite the unavoidable approximations of any reactive MD scheme, we have been able to reproduce some basic features of “living polymerization”. This term describes polymerizations that do not experience any termination mechanisms such as chain or initiator recombination. Indeed, in our precursor study the polymer chains could grow until no free monomer beads were left in the reactive mixtures. Furthermore, we have shown that the RMD method is highly efficient to derive equilibrated structures of monodisperse polymer samples. This capability of our reactive MD tool encouraged the present extension to a more complex process. With the recent extensions in our RMD code we can simulate three-dimensional network formation in the presence of a surface. For this purpose, additional reactive steps have been implemented into the computer program, the cross-linking process being the most important one; see below. In this first RMD study of interphase formation during curing we have employed the CG potentials already used in our recent polymerization study of EB to PS.[40] For the curing process in contact with a surface, this potential has been supplemented by a tunable surface potential. By means of a preferential surface interaction for one of the reactive species, enrichment processes have been simulated.

## 4.2. Theoretical Tools

### 4.2.1 Coarse-Grained Model

Experimental data have demonstrated that interphase thicknesses can vary from several nanometers up to the micrometer range.[1, 8, 9] Such length scales preclude MD simulations at the atomistic level. To study the present polymer-surface systems with their large number of monomer units we have chosen an RMD variant in a coarse grained resolution. The iterative Boltzmann inversion (IBI) has been used to derive the CG potentials presently employed.[41, 42] IBI is a structure-based method that allows the optimization of CG potentials retaining - to some extent - chemical features of a compound. In our recent work[40] we have combined the RMD algorithm with the IBI-based potentials of ethylbenzene, polystyrene and their mixtures. We adopted a mapping scheme where each EB molecule and PS monomer is represented by one CG bead. In our previous work, the polymerization of PS chains proceeded from an initial liquid of EB beads. The adopted CG potentials were defined by three types of intermolecular interactions (PS-EB, PS-PS and EB-EB). Intramolecular interactions were described by bond stretching and angle bending potentials.

The same set of coarse-grained potentials is adopted in the present simulation. The monomers, initiators and cross-linkers are simply EB beads turned into bifunctional, monofunctional and tetrafunctional units. The intermolecular potential between the unconnected units is modeled via the EB-EB potential. The PS-PS intermolecular potential is used between connected units. The PS-EB cross-potential serves as interaction potential between the polymerized beads and the yet unconnected ones. Polystyrene networks are - to our knowledge - not employed as technical adhesives. Our intention in the present simulation thus has not been the reproduction of a real chemical system but to model some general principles of curing processes with surface selectivity to one species. The chain propagation considered in our recent reactive simulations[40] has been extended by a cross-linking step. Additionally, a generic surface with adjustable interactions toward the different species has been implemented.

### 4.2.2. Polymerization and Cross-linking Processes

A detailed description of the RMD method presently adopted has been given elsewhere.[40] In the following, only its main features will be summarized. As the different reactions contributing to a curing process are specific to the chosen systems, it is necessary to define the connectivity-altering

steps presently implemented. Chain reactions and cluster reactions of the cross-linking type are performed in this reactive scheme. A cluster is defined as a fragment comprising a linker with at least three bonds. The chain reactions consist of initiation, propagation and termination. Cross-linking reactions happen when two growing clusters react via their active centers. Cross-linking is the prerequisite of curing finally leading to percolating clusters. In our computation scheme we have allowed the formation of linker-linker bonds. Termination occurs when two polymer chains react via their active centers. Recombination of two initiators is not included in the set of predefined reactions. All bond formations are irreversible.

At the beginning of the curing reaction, only the initiators are active centers. As the reaction proceeds new activated centers are created via the propagation steps. Therefore, a list of the active centers is updated in course of the reactive simulation. Active centers that have reached their maximum number of bonds are removed from the reactive list. After each propagation and cross-linking step, the active centers are appropriately transferred to the ends of the growing chains. As pointed out above we have employed a common set of CG beads which only differ in their connectivity. The mass of the beads equals 104 a.m.u.

The two parameters required to control the reactive simulation are the capture radius r and the delay time $\tau_r$.[40] New bonds between reactive centers and beads in the mixture are allowed to be formed only in so-called reactive steps that are separated by the delay time $\tau_r$. Prospective bonding partners are searched in the neighbor list of the active centers. Within each list, the beads inside the capture radius r of the active centers are possible candidates for bond formation. The new bond is formed with the bead closest to the active center if its maximum number of allowed bonds has not yet been reached. The bonded state is created by turning on the relevant intramolecular interactions between the newly connected beads. Nonbonded interactions between them are turned off. Each active center can bind only one bead during a reactive step. Following a bond formation step, conventional MD steps are performed during the delay time $\tau_r$ in order to relax the system. The present RMD scheme is thus a succession of reactive steps separated by relaxation periods for the growing system. From our first study with the present connectivity-altering method it appeared that the velocity of a reaction is prevailingly determined by the value of the capture radius r. The smaller the capture radius, the slower the reactive process becomes. With a smaller impact, a delay time increase also causes slower reactions. The combination of the two parameters in the present reactive simulations leads to curing processes that are much faster than in experiments i.e. that occur within a time-scale feasible via MD. For more details we refer to our recent RMD study.[40] The curing processes take place here in the range of nanoseconds while they occur experimentally in the regime of hours.

### 4.2.3. Surface-Particle Interactions

Adherend surfaces that are used experimentally cover a broad variety in their structural features. In experiments both rough and rather smooth surfaces have been adopted to investigate the nature of the induced interphases.[1, 11, 12] The surfaces in the present model are continuous, unstructured, and flat. For a schematic representation of the simulation cell see Figure 4.1. The following generic potential has been used to model the surface-adhesive interactions [18]

$$E_p(z) = \varepsilon\left[\left(\frac{D}{z}\right)^9 - \left(\frac{D}{z}\right)^3\right] \quad (4.1.)$$

where ε is the potential depth and D = 0.38 nm the size of the excluded distance between the surface and the different adhesive species. The coordinate z measures the distance between the center-of-mass of a bead in the mixture and the surface plane. The equation defines an averaged potential resulting from an integration of a 12-6 Lennard-Jones function parallel to the x, y surface and in the vertical z direction. [18]

The flat surfaces in the simulation box are implemented by two additional "beads" initially positioned at (0, 0, $d_z/2$) and (0, 0, $-d_z/2$). The coordinates of the two beads along the z axis locate the position of the flat surface layers. The interaction with a surface layer is one-dimensional and depends only on the distance between the particle and the layer position in the z direction (Equation 4.1.). The equilibrium distance $d_z$ between the two surfaces defines the thickness of the solid substrate. The surface model has been inspired by a recent article from our group.[43] The two surfaces are connected by a harmonic potential (Equation 4.2.) with k denoting the force constant.

$$U(d) = \frac{1}{2}k(d - d_z)^2 \quad (4.2.)$$

An equilibrium distance $d_z$ of 2 nm which is bigger than the cutoff distance for the nonbonded interactions (1.6 nm) has been adopted. The value adopted for k is equal to $50.10^3$ kJ/mol; it guarantees that no large oscillations of the surface layers around $d_z$ = 2 nm occur. In fact, with this k value the magnitude of the layer oscillations in the z direction is not bigger than 1% of the imposed equilibrium distance of 2 nm. With the present setup no additional conditions have been necessary to fix the two surface-beads to the lab-origin. Spatial displacements of the surface "beads" are caused by the forces exerted by the particles in the system and the spring imposed to maintain the surface layers separation. The quantity d in equation (2) measures the instantaneous distance between the two surfaces in the z direction. They are mobile only in the z direction. However they do not participate in bond formation

restricting the interaction with the monomeric and polymeric particles to physisorption. For simplicity we have chosen the masses of the surfaces equal to the PS monomer masses.

Periodic boundary conditions (PBC) are employed in all Cartesian directions. All beads with $z > +d_z/2$ occupy the upper region of the box, beads with $z < -d_z/2$ the lower one (see Figure 4.1.). There are no beads between the surfaces. Beads leaving the central box at the top of the upper region re-enter it from below; vice versa for the beads in the lower half which feel the second flat surface at $(0, 0, -d_z/2)$. Constant pressure is maintained by coupling the z dimension of the periodic box to the desired normal pressure by a Berendsen barostat.[44] The positions of the two-surface beads are also included in the barostat rescaling process. In order to derive reference values, bulk simulations (i.e. absence of a surface) are also carried out both for the starting mixture and for the cured networks. Periodic boundary conditions in the three cartesian directions have been adopted for the cubic boxes of the reference bulk simulations. Here, the position rescaling due to the Berendsen barostat has been performed in the three cartesian directions, too. The virial has been adopted to calculate the pressure both in the surface and bulk simulations. The average values for the different pressure components were all found to be within a common set of error bars for all the surface simulations (i.e. polymer network; starting mixtures). Since a clear discrimination in the magnitude of pressure components did not appear; it seems that no pressure anisotropy was observed in the systems.

## 4.3. Simulation Details

All simulations have been performed in the NPT ensemble at a temperature T of 400 K and a normal pressure P of 101.3 kPa with a total of 20002 coarse-grained particles. Two of these beads are used to define the z positions of the flat surfaces as explained above. The time-step is 5 fs and the coupling time for Berendsen thermostat and barostat are 0.5 and 5 ps. A cutoff of 1.6 nm has been chosen for the nonbonded interactions while the Verlet neighbor list cutoff is 1.7 nm.

Two attractive surface potentials (Equation 4.1.) have been used with effective potential depths ε of 8 and 20 kJ/mol (At T = 400 K, the thermal energy corresponds to kT = 3.33 kJ/mol). Two series of simulations have been performed. In the first series, the beads in the reactive mixture feel the same surface potential irrespective of their chemical identity. In the second series, the surface-monomer potential differs from the surface-linker one. Two different combinations have been considered in this second series of simulations.

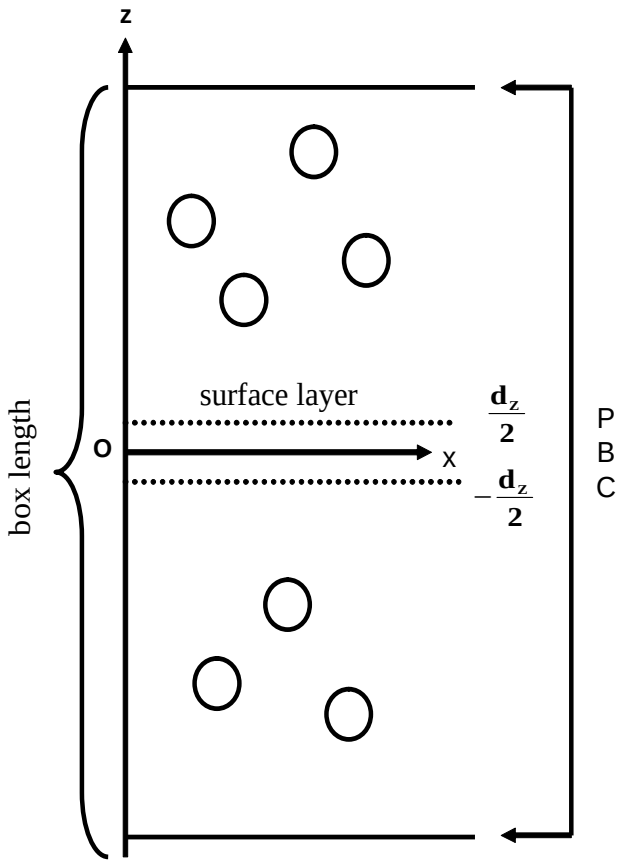


***Figure 4.1.*** *Two-dimensional (x, z) representation of the simulation box with two flat continuous surface layers separated by the distance $d_z$. The continuous surfaces are connected by a harmonic spring. Periodic boundary conditions are only shown for the z direction. However they are also present in the x, y directions.*

The first is linker-selective;: the 8 kJ/mol potential is used for the surface-monomer interaction while the linkers are attracted by the stronger surface potential. The second variant is monomer-selective; the monomers interact with the surface via the 20 kJ/mol potential while the linkers feel the 8 kJ/mol potential. For convenience, we will use the notation $Ep_{M,L}$ with M, L = 8, 20 kJ/mol to label the different simulations. The first index M characterizes the surface-monomer interaction, the second index L the surface-linker interaction. The surface-initiator interaction is identical to the surface-monomer one. Throughout the simulation, the interaction between a component of the reactive mixture and the surface is conserved even if the bead is incorporated into a polymer molecule.

The area of the surface layers is constant; it is equal to 10×10 $nm^2$ in the x and y directions. The thickness of the fluid layer is about 50 nm; it shrinks during network formation to about 36 nm. In all RMD simulations the capture radius is r = 0.55 nm and the delay time $\tau_r = 5\times10^{-2}$ ns. The given r value has been used already in our previous study[40] while $\tau_r$ has been increased in comparison to our

recent RMD work to allow better relaxation of the system between two reactive steps. In the starting mixture, 10% of beads were chosen as linkers and 7.5 % as initiators. When properties have been analyzed as a function of the separation z from the surface, the thickness of the slabs equalled 0.8 nm which represents 50% of the cutoff distance.

Prior to the curing process, the liquid starting mixture with monomers, initiators and linkers is prepared. In all simulation types, the linkers and initiators are randomly assigned in the starting mixtures. Nevertheless, this random distribution is subsequently slightly altered in the case of simulations with preferential surface interactions to accelerate equilibration. For preferential surface-linker interactions, a slightly enhanced linker concentration in the surface regions has been generated. From the previous random assignment 20 bifunctional monomers are relabeled as linkers within a 2 nm separation from each surface region augmenting the linker concentration. In the rest of the box, the same amount of linkers is randomly relabeled as bifunctional beads. This allows conserving the total number of linkers initially introduced. For the opposite case, the surface region is slightly depleted in the linker concentration. Within a 2 nm distance from each surface layer 20 linkers are randomly relabeled as bifunctional monomers and an equal amount is relabeled as linkers in the rest of the box. After the preparation of the different starting mixtures, equilibration runs driven by MD were performed up to the appearance of stable linker distributions; see below. After the establishment of these stable configurations we have assumed that the equilibration of the starting mixtures has been achieved.

During the equilibration runs of the liquid starting mixture, the distribution of the linkers and the bifunctional monomers in the simulation box is monitored. To do so we define in each slab the local linker mole fraction as $X = N_{linker} / (N_{linker} + N_{mon} + N_{init})$ and the normalized local mole fraction $X_N = X/X_{bulk}$. The local linker mole fraction X is the ratio between the number of linkers $N_{linker}$ and the sum of the number of monomers $N_{mon}$, initiators $N_{init}$ and linkers $N_{linker.}$ When an averaged X is evaluated via the amount of each species introduced in the whole box ($N_{linker}$ = 2000, $N_{mon}$ = 16500 and $N_{init}$ = 1500), the reference value $X_{bulk}$ = 0.10 is obtained. Normalized local mole fraction values $X_N$ are given by the ratio between local linker mole fraction values X and the reference linker mole fraction $X_{bulk}$. The simulation box is divided into slabs and $X_N$ is computed in each of them. Spatially resolved $X_N$ values are recorded at different times of the equilibration runs. The profile of the normalized local mole fraction of the starting mixture is considered as equilibrated when concentration changes become negligible. Once the state of negligible changes of the spatially resolved $X_N$ profiles is attained, production runs of 2 ns are additionally performed to evaluate the equilibrated $X_N$ profiles. They will be discussed in the Results section. Final equilibrated configurations are used as starting point for the RMD curing runs. After curing simulations of 8 ns the polymer-surface systems are

subjected to equilibration (5 ns) and production runs (2 ns) for the extraction of the properties. The quantities have been averaged over five different simulations. For the reference bulk simulations the amount of initiators and linkers is identical to the simulations with the surfaces. The reference bulk networks are also created via RMD. In the bulk simulations, the linkers and initiators are randomly distributed in the starting mixture.

## 4.4. Results and Discussion

In this section the properties of the cured samples resulting from the different starting mixtures are analyzed. During the curing of the systems (bulk, uniform and selective surface) the reactions become more and more diffusion controlled as clusters of higher molecular weight are created. In all simulations of curing systems (bulk, uniform and selective surface) the above mentioned 8 ns interval for curing has been sufficient to generate a size distribution that does not change with extension of the curing interval. Thus we have analyzed all systems after 8 ns of curing. For all systems, all bifunctional monomers, linkers and starters have taken part in the reactive process. All final products (bulk, uniform and selective surface simulations) are composed only by clusters and free terminated chains (i.e. terminated chains not connected to any cluster). These chains are no longer reactive. Irrespective of the simulation type a percolating cluster that fills almost the entire box is observed in every RMD run. In all reactive simulations, these percolating clusters have incorporated more than 18000 beads. Each percolating cluster is accompanied by few smaller clusters that did not percolate because of the diffusion-controlled nature of the reaction in the end phase. To give an idea on the size (i.e. number of beads) and the number of remaining smaller clusters we have averaged these two quantities over the total number of reactive simulations (bulk, uniform and non-uniform surface simulations). On average the number of small clusters is equal to 3.0 with a standard deviation of 3.0. The average number of beads in the smaller clusters is between 27 and 28 with a standard deviation of 8.0. We have averaged in the same way the number of linkers incorporated in the small clusters and a value of 1.0 with a standard deviation of 1.2 is obtained. This number shows that nearly 100% of the linkers are found in the percolating clusters irrespective of the curing simulation type. In the same way, we have considered the terminated free chains that are present in the final products irrespective of the simulation type. An average of 159.0 terminated free chains with a standard deviation of 13.5 is calculated. These averaged numbers and their standard deviations show that the final cured samples do not differ much. A number of 5 simulations have been performed for each simulation type. For all cured systems the last configuration is equilibrated during 5 ns. Following the equilibration, the analysis of the mass-density profiles, normalized mole fractions, segment orientation angles and

average chain length are performed on the cured products after a production run of 2 ns with a trajectory output frequency of 50 steps (8000 trajectory frames). For each simulation type the time-averaging of a property is followed by an average over the 5 simulations. For all the following graphs, the properties are analyzed as a function of the separation z relative to the top surface layer.

### 4.4.1 Density Profiles

Mass density profiles resulting from the simulations $Ep_{8,8}$ and $Ep_{20,20}$ with identical interactions between the surface and the component beads are displayed in Figure 4.2. Figure 4.2a shows the profiles for the reactive starting mixtures and Figure 4. 2b the RMD results for the cured network. The top surface layer ($d_z/2$) is located at the graph origin z = 0 of Figure 4.2. For the discussion we use normalized mass densities $\rho^*$ defined as $\rho^* = \rho / \rho_{bulk}$. The quantity $\rho$ represents the absolute mass density which is calculated as a function of the distance from the surface z and $\rho_{bulk}$ the average mass density of the bulk samples. Maxima and depletion zones in the starting mixtures and the cured products indicate layering that is noticeable within 2.7 nm from the surface. The influence of the surface potentials leads to two pronounced maxima in the density profiles of the starting mixtures (Figure 4.2a). For the stronger surface potential, the first peak is enhanced by a factor of five relative to the bulk density. This drops to a factor slightly larger than 2 in the $Ep_{8,8}$ simulation. In the cured samples (Figure 4.2b) the density oscillations near the surface are less pronounced. Here the first maximum in the $Ep_{20,20}$ run exceeds the bulk density only by a factor of about 3. The second and third maxima are roughly of the same intensity. The higher flexibility of the beads in the starting mixtures (i.e. no bonds) leads to a more efficient layering than in the cured network for the stronger surface attraction. The difference between uncured and cured systems becomes much smaller when the surface attraction is reduced to 8 kJ/mol. In the uncured mixture three small peaks are clearly distinguishable for z > 1.4 nm in the $Ep_{20,20}$ simulations, whereas only small density fluctuations are observed in the $Ep_{8,8}$ simulation. For the polymerized system two weak peaks are found for z > 1.5 nm for both surface potentials. They differ less than in the reactive starting mixtures.

Density profiles for the simulations $Ep_{8,20}$ and $Ep_{20,8}$ with selective surface interactions are not shown; they are similar to the profiles in Figure 4.2. for both the starting mixtures and the cured samples. In the $Ep_{8,20}$ simulations the bifunctional monomers and initiators which represent more than 90% of the total number of beads are attracted by the 8 kJ/mol potential. Thus it is not surprising that the density profile of the $Ep_{8,20}$ simulations is similar to the one derived from the $Ep_{8,8}$ simulations. For the same reason the normalized density profile derived with the $Ep_{20,8}$ potential is similar to the $Ep_{20,20}$ distribution. The segregation process in the present simulations has, therefore, little influence on the

resulting density profiles of the different systems. This is not so surprising, since all bead types have the same mass and interactions. In all simulations performed the surface induced mass density oscillations persist to a z distance of roughly 2.7 nm. The range of this perturbation by the interface depends neither on the type of the sample (starting mixture or cured network) nor on the strength of the surface attraction. In consideration of the present CG potential evaluated for PS-EB mixtures it is not surprising that the same interphase dimensions, when measured via mass density fluctuations, have been observed in atomistic and equilibrium MD simulations of nano-composites formed by atactic PS and a spherical silica nano-particle.[45, 46] An interphase dimension of about 2.0 nm for the density oscillations has been observed also by Maguire et al. in atomistic simulations of an epoxy polymer network onto an alumina surface.[9]

In Table 4.1. we compare bulk densities simulated for the pure bulk starting mixtures with the densities in the centre of the fluid phase (z > 2.7 nm) from simulations with a surface potential; we find them in close agreement. Curing is accompanied by a significant densification (volume shrink). The average density for the pure bulk starting mixture is 735.4 kg/m$^3$ (Table 4.1 - left column). This value is increased to 1060.8 kg/m$^3$ when the pure polymer network is formed (Table 4.1 – right column). These densities reflect the experimental densities of ethyl benzene and polystyrene, against which the coarse-grained potential was originally parameterized.[42] The pure bulk network has been generated by RMD simulations with the different species in identical amounts as in the corresponding surface simulations. Table 4.1. shows a good agreement between the pure bulk and the surface bulk-densities for all surface types (uniform and non uniform surface potentials) and systems (starting mixture and polymer).

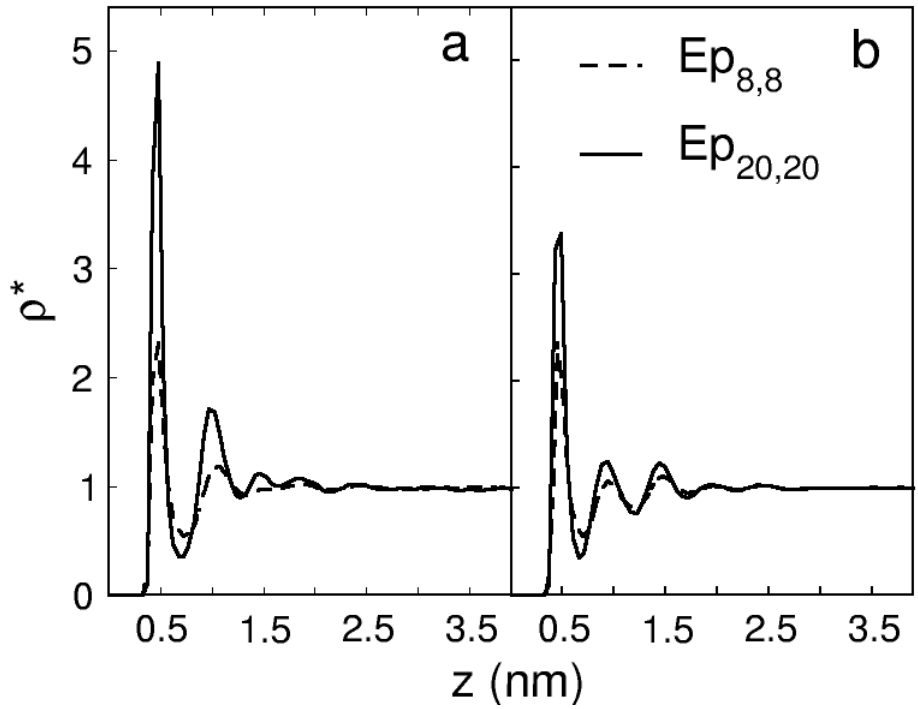


***Figure 4.2.*** *Normalized mass-density $\rho^* = \rho / \rho_{bulk}$ for (a) starting mixtures and (b) cured polymers as a function of the distance from the surface z at 400 K for the uniform potentials $Ep_{8,8}$ (broken curves) and $Ep_{20,20}$ (full curves). The top surface layer is located at the graph origin z = 0.*

| system | ρ ( kg/m$^3$) starting mixture | ρ ( kg/m$^3$) cured polymer |
|---|---|---|
| bulk | 735.4 | 1060.8 |
| $Ep_{8,8}$ | 735.8 | 1062.4 |
| $Ep_{20,20}$ | 736.5 | 1060.4 |
| $Ep_{8,20}$ | 735.9 | 1059.5 |
| $Ep_{20,8}$ | 734.1 | 1059.2 |

***Table 4.1.*** *Comparison of the bulk densities (T = 400 K) in the starting mixtures (first column) and in the cured networks (second column).The mass-densities have been derived for the pure bulk (second row) and in surface samples with the potentials $E_{M,L}$ (remaining rows). For the surface systems the bulk density was evaluated in the region z > 2.7 nm for both starting mixtures and cured systems.*

### 4.4.2. Local Composition

We now analyze the normalized local mole fraction of the linker $X_N = [N_{linker} / (N_{linker} + N_{mon} + N_{init})]/X_{bulk}$ for equilibrated starting mixtures and cured networks as a function of the distance from the surface. The local mole fraction has been calculated in each slab and time-averaged over a number of trajectory frames. We have also used the same slab construction for the bulk system. The time-averaged values obtained in the different slabs of the bulk system were again averaged over the number of slabs. We first analyze the starting mixtures. We derive the expected mean value $X_{bulk}$ = 0.10 (see simulation details section) with a standard deviation of 0.06. The same sampling process over the number of trajectory frames and the number of slabs is applied for the normalized local mole fraction $X_N$ in the case of the simulations with the uniform surface potentials $Ep_{8,8}$ and $Ep_{20,20}$. Standard deviations of 0.04 ($Ep_{8,8}$) and 0.03 ($Ep_{20,20}$) around the normalized value $X_N$ = 1.00 is derived for these samples. The normalized linker mole fraction for the bulk and the simulations with the uniform surface potentials ($Ep_{8,8}$ and $Ep_{20,20}$) is symbolized by the horizontal line at a value of 1.00 in Figure 4.3.

In the $Ep_{8,20}$ and $Ep_{20,8}$ simulations with selective surface interactions a segregation of the components in the starting mixtures is expected. The local composition as a function of the distance from the surface is shown in Figure 4. 3a. In $Ep_{8,20}$ simulations, $X_N$ is enhanced over the bulk value inside the surface cutoff interaction (1.6 nm) due to the linker-selective interactions with the surface. At z = 0.8 nm (first data point) a strong increase of the linker concentration ($X_N$ = 4.77) is found. In the opposite case $Ep_{20,8}$, a linker depletion is found at the same distance ($X_N$ = 0.17). For the linker-selective and the monomer-selective surface, Boltzmann inversion of the two probabilities gives local excess chemical potentials for the linkers in the first layer of -5.2 kJ/mol and +5.85 kJ/mol, respectively. Beyond the surface cutoff distance (1.6 nm), the $X_N$ values of the $Ep_{8,20}$ ($Ep_{20,8}$) simulation are slightly below (above) the bulk value due to the surface enrichment (depletion) in linkers. But they are nevertheless very close to the bulk values and the uniform $Ep_{8,8}$ and $Ep_{20,20}$ simulations.

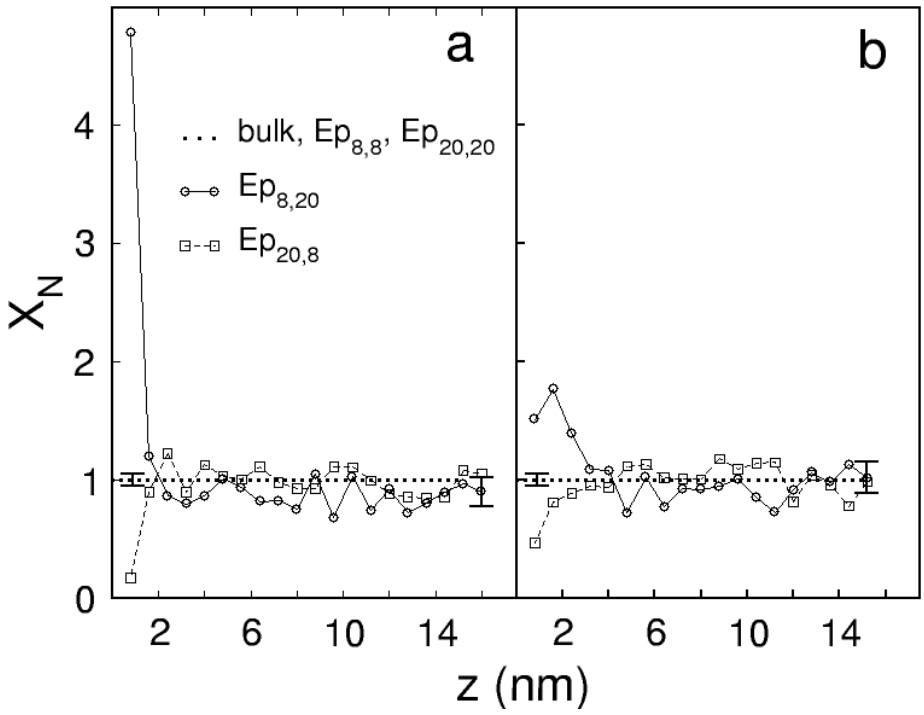


***Figure 4.3.*** *Normalized local mole fraction of linkers $X_N = X/X_{bulk}$ as a function of the distance z from the surface for (a) the uncured monomer mixtures and (b) the cured polymers. Uniform and selected surface potentials are considered as well as pure bulk systems are considered, too. $Ep_{8,20}$ indicates a preferential adsorption of the linkers, and $Ep_{20,8}$ a preferential adsorption for all non-linker entities. A value $X_N > 1$ indicates an enrichment of linkers over the expected bulk value, a value $X_N < 1$ a depletion. Also indicated is a typical standard deviation bar for the pure bulk and one for the bulk region in the $Ep_{8,20}$ simulation. The two bars are given at the left and right margin of the two plots. The top surface layer is located at the graph origin z = 0.*

In analogy to the reactive starting mixtures we have analyzed the normalized local mole fraction $X_N$ in the cured networks as a function of the separation z from the surface. The normalized local mole fraction in the present case is a good indicator of the localization of the linkers in the cured networks. A time averaging followed by an averaging over the number of slabs of the mole fraction values is again performed here in the case of the bulk and the $Ep_{8,8}$ and $Ep_{20,20}$ simulations. For the reference polymer bulk, the mean value $X_{bulk} = 0.10$ with a standard deviation of 0.05 is obtained. For the simulations with uniform surface potentials the normalized mole fraction $X_N = 1.00$ with deviations of 0.06 ($Ep_{8,8}$) and 0.08 ($Ep_{20,20}$) is calculated. The distribution of linkers in the cured network with uniform surface potentials is similar to the bulk network, i.e. uniform. The starting mixtures reacted in the presence of selective surfaces ($Ep_{20,8}$ and $Ep_{8,20}$) generate a cured network with a distinct linker

distribution. For a preferential attraction of the monomers in the $Ep_{20,8}$ simulations, $X_N$ falls to roughly 0.47 near the surface (z = 0.8 nm) , see Figure 4. 3b. This indicates a decrease in the local linker concentration in the polymer network. An opposite linker distribution is found for the linker-selective surface ($Ep_{8,20}$) with a maximum of $X_N$ = 1.8 at a distance of z = 1.6 nm. The values can be translated into "excess chemical potentials" for the linkers. Here, we use the term "excess chemical potentials" although the RMD based configurations refers to a frozen non-equilibrium state due to sudden bond formations. Thus, $X_N$ = 0,47 and $X_N$ = 1.8 at the surface correspond to local "excess chemical potentials" of +2.5 kJ/mol and –2.0 kJ/mol for the monomer-selective and the linker-selective surfaces, respectively. As the RMD steps of sudden bond formation arrest the conformations, one can expect a certain degree of frozen non-equilibrium here, in contrast to the fluid starting mixtures. The implications of such sudden bond formations on the "excess chemical potentials" for the linkers will be studied in future simulations as a function of the delay time $\tau_r$.

When comparing the $X_N$ profiles of starting mixtures and cured networks in Figure 4.3., some general differences between both systems become immediately apparent. The surface enrichment or depletion of linkers is much smaller in the cured networks than in the starting mixtures. Apparently, the initial concentration profile of the different components in the starting mixtures is strongly perturbed by the reactive processes. When measured in terms of the normalized mole fraction $X_{N,}$ the curing process leads to a broadening of the interphase relative to the initial system. The bulk value 1.00 is now approached for a separation from the surface of roughly 4 nm, rather than 1.6 nm in the unreacted mixture. This is a consequence of the broadening of the initially enriched or depleted regions by the network formation. More investigations of this broadening effect are also part of future simulations. A possible hypothesis is that the interphase broadening is caused by diffusion processes of unconnected linkers towards the surface (monomer-selective simulations) or into the interphase region (linker-selective simulations). This hypothesis will be confirmed or rejected on the basis of our future simulations. The snapshots in Figures.4.4. and 4.5. can be considered as a complement of Figure 4.3. that illustrates the interphase broadening just discussed. Figure 4.4. refers to a preferential attraction of the linkers towards the surface while the opposite case is represented in Figure 4.5. To visualize clearly the linker distributions in the simulation boxes the starters and bifunctional monomers are not shown in the pictures. As the upper and lower halves of the simulation boxes were symmetric, the snapshots have been restricted to the upper parts. The green bead symbolizes the top surface layer. The left pictures in Figures 4.4. and 4.5. show the linker distributions (red beads) in the starting mixtures prior to curing. The right pictures illustrate the linker distributions in the cured polymer networks. The left picture in Figure 4.4. clearly shows an accumulation of linkers at the surface in the starting mixture. This accumulation creates a very pronounced and ordered thin film in the vicinity of the surface. An

accumulation of the linkers is still visible in the case of the polymer network (Figure 4.4., right picture) even if this effect is weaker than in the starting mixture. We also see that the accumulation in the polymer network has extended more into the sample. The left picture of Figure 4.5. shows that the linkers are less present at the surface than in the starting mixture in Figure 4.4. In this case the starters and bifunctional monomers are predominantly occupying the surface-near region. A comparison with the resulting polymer (Figure 4.5., right picture) shows that the linkers have a higher concentration close to the surface after the formation of the network.

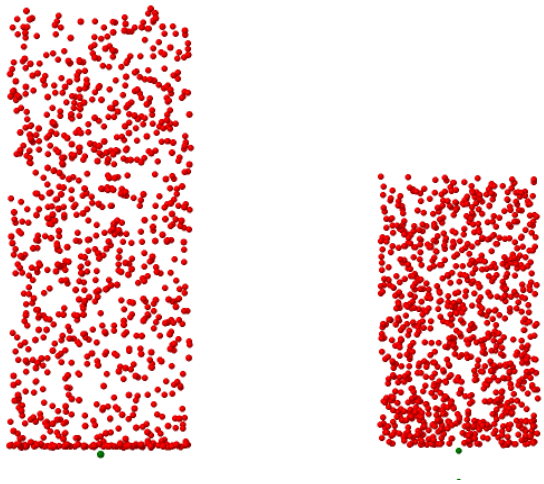

***Figure 4.4.*** *Snapshots of simulations with preferential surface attraction of the linkers. The linkers are represented by the red beads. The green bead symbolizes the top surface layer. Only the top half of the box is shown for the starting mixture (left picture) and the polymer network (right picture). The starters and bifunctional monomers have not been displayed for a better visualization of the linker distribution.*

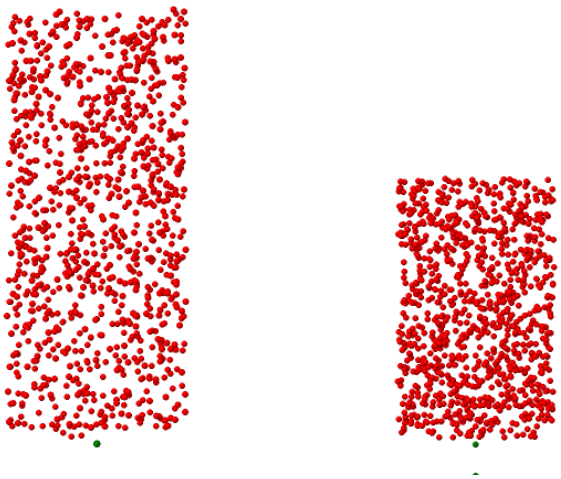

***Figure 4.5.*** *Snapshots of simulations with preferential surface attraction for the bifunctional monomers and starters. The linkers are represented by the red beads. The green bead symbolizes the top surface layer. Only the top half of the box is shown for the starting mixture (left picture) and the polymer network (right picture). The starters and bifunctional monomers have not been displayed for a better visualization of the linker distribution.*

### 4.4.3 Segment Orientation

The orientation of a pair of connected beads relative to the surface can be defined by the absolute value of the angle |θ| between their bond vector and its projection onto the x, y surface plane. With this definition a bond vector with an orientation angle of $0^o$ lies parallel to the surface. The midpoints of the bond vectors are used to assign them to different slabs. In addition to the simulations of the surface systems the bond orientation angle has been also calculated for the bulk material (projection onto the x, y plane). The calculated average of $32.7^o$ equals the theoretical value for a random orientation of bonds. In Figure 4.6. this value is represented by the horizontal line. Added to the graph are the orientation profiles for the two uniform surface potentials $Ep_{8,8}$ and $Ep_{20,20}$. Both attractive surface potentials induce an alignment parallel to the surface in the first layer (distance ≤ 2 nm), with an alignment being more pronounced for the stronger $Ep_{20,20}$. The deviation from the random value is about $-10^o$ for $Ep_{20,20}$ versus $-7^o$ for $Ep_{8,8}$.

From Figure 4.6. we deduce that the bond orientation converges to the (random) bulk value for z ≈ 2.4 nm. Within the error limits of the simulation method we observe roughly the same interphase thickness as estimated from the density oscillations. In recent non-reactive equilibrium MD simulations of PS – silica nanocomposites with spherical surfaces in atomistic resolution we have found that the bond orientation converges to the bulk value at shorter distances than the mass density.[45] The present network data might indicate that the formation of additional bonds during curing implies a somewhat stronger orientational ordering in the structure than for the linear polystyrene employed in the nanocomposites. Reactive simulations with selective attractions for the constituents have again led to angle profiles very similar to their uniform counterparts, as they are dominated by the majority component.

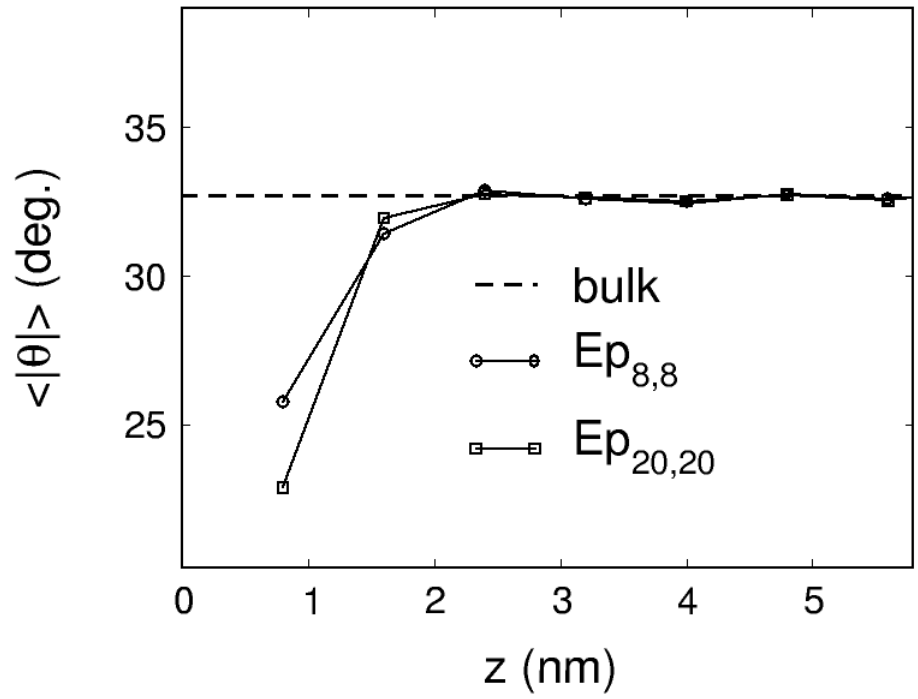


***Figure 4.6.*** *Average bond orientation angle <|θ|> (T = 400 K) as a function of the separation z from the surface. <|θ|> = 0° (90°) denotes an alignment parallel (perpendicular) to the surface. The broken horizontal line refers to the pure bulk value with random orientation of the vectors (<|θ|> = 32.7°) while the two others refer to simulations with uniform surface potentials ($Ep_{8,8}$, $Ep_{20,20}$) for the components. The top surface layer is located at the graph origin z = 0.*

### 4.4.4. Average Chain Length between Cross-links

Another property of interest is the number of beads in the chains between two branching points. Cross-linkers with at least three bonds (maximum connectivity is four) are considered as branching points. A chain is defined by a sequence of beads with two bonds (bifunctional monomers or cross-linkers) between two branching points. Its length $N_L$ is defined by the number of its beads, excluding the cross-link beads. Criterion for the assignment of a chain to a slab is the location of its center-of-mass. The length of each chain is calculated. From a branching point three or four chains can originate. The same analysis has been performed for the bulk network averaging over the entire box volume. Here we derive a mean value $<N_L> = 4.06$ with a standard error of ±0.04. In Figure 4.7. this limiting value appears as the horizontal line.

In this graph, we have compared the distance dependence of $<N_L>$ in the surface systems with the bulk material. For the simulation runs with uniform $Ep_{8,8}$ and $Ep_{20,20}$ potentials, the average chain lengths in the different slabs are close to each other. Averaging over the slabs yields a value of 4.07± 0.08 which is similar to the bulk material. There was no noticeable deviation near the surface for the

two simulations with uniform surface potentials. This changes for the cured network with selective surface interactions $Ep_{8,20}$ and $Ep_{20,8}$. The linker-selective surface $Ep_{8,20}$ induces an average length smaller than the bulk value for $z \leq 4$ nm. Conversely, the monomer-selective surface $Ep_{20,8}$ leads to chains longer than in the bulk for $z \leq 4$ nm. Beyond 4 nm, the chain lengths $<N_L>$ of both simulations fluctuate around the bulk value. This result could be expected on the basis of the normalized local mole fraction profiles of the linkers in the cross-linked polymer samples resulting from the simulations with surface selectivity (Figure 4.3.). Also the linker concentration approaches bulk behavior at about 4 nm in both cases. Thus, the chain length distribution observed in the cured network is a consequence of the surface-induced distribution of linkers and monomers (Figure 4.7.). In a more general sense, the average chain length in polymer networks is expected to correlate with the availability of reactive units. For the non-selective surfaces, homogeneous normalized mole fraction profiles are found for the starting mixtures and the bulk. As a result, similar chain length distributions are found for the bulk and for the surface systems. The starting mixtures equilibrated under the influence of selective surfaces show a deviation from the bulk network. Preferential attraction of the linkers to the surface causes the average chain length to be smaller ($Ep_{8,20}$ in Figure 4.7.). When the bifunctional monomers are more attracted the reduction of linkers near the surface causes the average chain length to be larger ($Ep_{20,8}$ in Figure 4.7.).

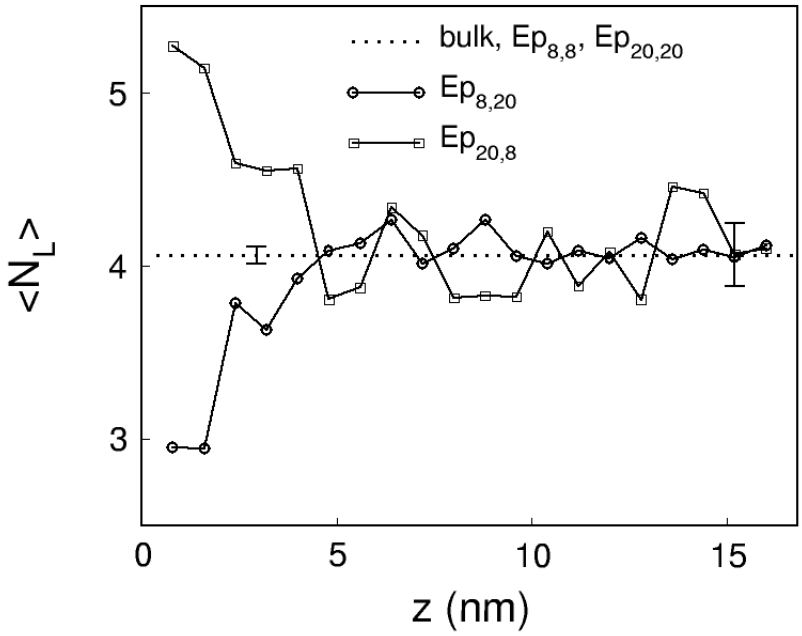


***Figure 4.7.*** *Average chain length <$N_L$> as a function of the distance z from the surface (T = 400 K). The reference bulk value $N_L$ = 4.06 is shown as horizontal line. In analogy to Figure 4. 3, typical error bars for the pure bulk (left symbol) and the bulk region of the surface selective simulations $Ep_{20,8}$ (right symbol) are shown. The top surface layer is located at the graph origin (z = 0).*

## 4.5. Conclusions and Outlook

In the present work we have adopted reactive MD simulations in coarse grained resolution to model a polymerization process leading to cross-linked networks near an interface. Starting point of our analysis has been the preparation of liquid reactive mixtures that have been equilibrated in the presence of flat surfaces with tunable potentials to vary their adsorption strength and selectivity. This approach mimics the experimental situation that the reactive starting mixture is for some time exposed to the influence of a surface prior to the activation of the curing process. The surface interactions have enough time to influence the local distribution of the different chemical species in the initial starting mixture. Our simulations show that non-selective surfaces yield concentration profiles that correspond to a homogeneous bulk-like mixture. This is no longer the case when the surface-linker and the surface-monomer interactions are different. In such simulations, the regions near the surface show an enrichment of one species and a depletion of the other. These different starting mixtures are subsequently cured to examine the influence of the surface selectivity on the final polymer network.

For the cured polymer networks, we have observed that properties like mass-density profiles and bond orientation distribution do not depend on the surface selectivity. For these properties, the range of the surface perturbation is independent of the selectivity and short. In fact, bulk behavior

is recovered beyond 2.7 nm (density) or 2.4 nm (bond orientation). In contrast, the mole fraction profiles of the linkers and bifunctional monomers as well as the average chain length between cross-links are influenced by the surface selectivity. They differ from the bulk behavior within 4 nm of the solid interface. The fact that these two quantities are coupled is no surprise, since surface selectivity determines the concentration profiles in the final cured network and, in turn, the concentration profiles determine the chain lengths. A higher local concentration of linkers leads to shorter chains and vice versa. The fact that different properties converge to their respective bulk values at different distances from the surface is a nice illustration of the phenomenon that the measured thickness of a polymer interphase near a solid surface strongly depends on the probed quantity.

This study has shown that RMD is an adequate tool to analyze the influence of the surface for adhesives formulated as reactive mixtures. In the present RMD simulations we are in the regime of typical van der Waals interactions with potential depths of 8 and 20 kJ/mol. It can be expected that for stronger surface potentials the perturbation in the composition may extend farther into the bulk affecting all properties that are related (i.e. average chain length). This range of surface-induced changes of the network properties (i.e. the interphase thickness) may be further increased by unlike interactions between monomeric species (in the present simulation all unconnected beads have the same interaction potentials), or by lower linker concentrations in the reactive mixture. These possible factors for a stronger extension of the interphase into the bulk will be considered in future simulations.

## References


[1] Wehlack, C.; Possart, W.; Krüger, J. K.; Müller, U. *Soft Materials* **2007,** *5***,** 87.

[2] Sharpe, L.H. *J. Adhesion* **1972,** *4*, 51.

[3] Possart, W.; Schlett, V. *J. Adhesion* **1995,** *48*, 25.

[4] Possart, W.; Diekhoff, S. *Int. J. Adhes. Adhes.* **1999,** *19*, 425.

[5] Montois, P.; Nassiet, V.; Petit, J.A.; Baziard, Y. *Int. J. Adhes. Adhes.* **2006,** *26*, 391.

[6] Possart, W.; Fanter, D. *J. Adhesion* **1996,** *57*, 227.

[7] Chung, J.; Munz, M.; Sturm, H. *Surf. Interface Anal.* **2007,** *39*, 624.

[8] Safavi-Ardebili, V.; Sinclair, A.N.; Spelt, J.K. *J. Adhesion* **1997**, *62*, 93.

[9] Maguire, J. F.; Talley, P.L.; Lupkowski, M. *J. Adhesion* **1993**, *45*, 269.

[10] Labrousse, M. G. B. *J. Adhesion* **1996,** *57***,** 65.

[11] Bockenheimer, C.; Valeske, B.; Possart, W. *Int. J. Adhes. Adhes.* **2002**, *22*, 349.

[12] Chung, J.; Munz, M.; Sturm, H. *J. Adhesion. Sci. Tecnol.* **2005**, 19, 1263.

[13] Knaup, J.M.; Köhler, C.; Frauenheim, T.; Blumenau, A.T.; Amkreutz, M.; Schiffels, P.; Schneider, B.; Hennemann, O.D. *J. Phys. Chem. B* **2006**, *110*, 20460.

[14] Baljon, A.R.C.; Robbins, M.O. *Macromolecules* **2001**, *34*, 4200.

[15] Stevens, M.J. *Macromolecules* **2001**, *34*, 2710.

[16] Frankland, S. J. V.; Caglar, A.; Brenner, D. W.; Griebel, M. *J. Phys. Chem. B* **2002**, *106*, 3046.

[17] Sides, S.W.; Grest, G.S.; Stevens, M.J. *Macromolecules* **2002**, *35*, 566.

[18] Baschnagel, J.; Meyer, H.; Varnik, F.; Metzger, S.; Aichele, M.; Müller, M.; Binder, K. *Interface Sci.* **2003**, *11*, 159.

[19] Smith, K.A.; Vladkov, M.; Barrat, J.-L. *Macromolecules* **2005**, *38*, 571.

[20] Tsige, M.; Stevens,M.J. *Macromolecules* **2007**, *37*, 630.

[21] Varnik, F.; Binder, K. *IJMR*, **2009,** *11***,** 1494.

[22] Eslami, H.; Müller-Plathe, F. *J. Phys. Chem. B* **2009**, *113*, 5568.

[23] Peter, S.; Meyer, H.; Baschnagel, J. *J. Chem. Phys.* **2009**, *131*, 014902.

[24] Stillinger, F.H.; Weber, T.A.; Laviolette, R.A. *J. Chem. Phys.* **1986**, *85*, 11.

[25] Stillinger, F.H.; Weber, T.A. *J. Chem. Phys.* **1987**, *91*, 4899.

[26] Schoolcraft, T. A.; Garrison, B.J. *J. Am. Chem. Soc.* **1991**, *113*, 8221.

[27] Barone, M.E.; Graves, D.B. *J. Appl. Phys.* **1995,** *78*, 6604.

[28] Akkermans, R. L. C.; Tøxvaerd, S.; Briels, W.J. *J. Chem. Phys.* **1998**, *109*, 2929.

[29] van Duin, A. C. T.; Siddharth, D.; Lorant, F.; Goddard III, W.A. *J. Phys.Chem. A* **2001**, *105*, 9396.

[30] Stoliarov, S. I.; Westmoreland, P.R.; Nyden, M.R.; Forney, G.P. *Polymer* **2003**, *44*, 883.

[31] Perez, M.; Lame, O.; Leonforte, F.; Barrat, J.-L. *J. Chem. Phys.* **2008**, *12*, 234904.

[32] Corezzi, S.; de Michele, C.; Zaccarelli, E.; Fioretto, D.; Sciortino, F. *Soft Matter* **2008**, *4*, 1173.

[33] Fogarty, J. C.; Aktulga, H. M.; Grama, A. Y.; van Duin, A.C.T. *J. Chem. Phys.* **2010**, *132*, 174704.

[34] van Duin, A. C. T.; Strachan, A.; Stewman, S.; Zhang, Q.; Xu, X.; Goddard III, W.A. *J. Phys.Chem. A* **2003**, *107*, 3803.

[35] Mahadevan, T.S.; Garofalini, S.H. *J. Phys. Chem. C* **2008,** *112***,** 1507.

[36] Quenneville, J.; Taylor, R.S.; van Duin, A.C.T. *J. Phys. Chem. C* **2010**, *114*, 18894.

[37] Liu, H.; Li, M.; Lu, Z.-Y.; Zhang, Z.-G.; Sun, C.-C. *Macromolecules* **2009**, *42*, 2863.

[38] Kremer, K.; Grest, G.S. *J. Chem. Phys* **1990,** *92***,** 5057.

[39] Weeks, J.D.; Chandler, D.; Andersen, H.C. *J. Chem. Phys* **1971,** *54*, 5237.

[40] Farah, K.; Karimi-Varzaneh, H.A.; Müller-Plathe, F.; Böhm, M.C. *J. Phys. Chem. B* **2010**, *114*, 13656.

[41] Reith, D.; Pütz, M.; Müller-Plathe, F. *J. Comput. Chem.* **2003**, *24*, 1624.

[42] Qian, H,-J.; Carbone, P.; Chen, X.; Karimi-Varzaneh, H.A.; Liew, C.C.; Müller- Plathe, F. *Macromolecules* **2008**, *41*, 9919.

[43] Leroy, F.; dos Santos, D.J.V.A; Müller-Plathe, F. *Macromol. Rapid Commun.* **2009**, *30*, 864.

[44] Berendsen, H. J. C.; Postma, P.M.; van Gunsteren, W.F.; Di Nola, A.; Haak, J.R. *J. Chem. Phys.* **1984,** *81*, 3684.

[45] Ndoro, T. V. M.;Voyiatzis, E.; Ghanbari, A.; Theodorou, D.N.; Böhm, M.C.; Müller-Plathe, F. *Macromolecules* **2011**, *44*, 2316.

[46] Ghanbari, A.; Böhm, M.C.; Müller-Plathe, F. *Macromolecules* **2011**, *44*, 5520

# 5. Outlook

The present PhD thesis has been focused on developing the Reactive Molecular Dynamics (RMD) tool to investigate the formation of interphases at a generic level and on making first steps towards the use of material-specific coarse-grained potentials. Following these preliminary steps, many new challenges still await to be tackled.

Among the challenges that can be tackled at the generic level, the investigation of locally resolved mechanical properties in systems having an interphase belongs to the most important ones. Experiments found that the largest interphase thicknesses are observed for the mechanical properties. In the context of mechanical properties, we would like to mention the RMD model of Tsige et al.,[1] commented on in detail in the first chapter. Their generic simulations deal with the failure mechanisms in adhesive polymer networks cured in contact with surface layers. Performing simulations of the Stevens et al. types with samples having properties, such as their cross-link density, perturbed (i.e. following segregation processes) would lead to very interesting insight. In fact, bond breaking events in the interphase region could be compared to the failure events in more distant regions. This would be a way of tackling the influence of interphases in the durability of hybrid-materials.

One of the most difficult challenges of the future is certainly the development of coarse-grained potentials to model experimental adhesive/surface systems such as epoxies cured onto copper or alumina surfaces. In the third chapter, we have emphasized that Iterative Boltzmann Inversion (IBI) approach can be used to optimize such material-specific potentials. Nevertheless, IBI optimizations rely on sampling structural properties from parent atomistic simulations of the adhesive/surface systems. This means that the first effort to obtain specific coarse-grained potentials reside in setting up atomistic systems with "realistic" interactions. Temperature transferability issues of the IBI-potentials can be avoided by simply performing the simulations at one thermodynamic state of interest. In contrast, the transferability of the IBI-potentials for different concentrations of the reacting species is more problematic. In fact, in the most rigorous case the IBI-potentials should reproduce the structural properties at different growth stages from the monomer liquids to the polymer adhesives. The ethylbenzene/polystyrene coarse-grained model of Qian et al.[2] offers an interesting discussion on this particular point. While IBI-potentials are able to yield realistic structural properties of polymers that can be followed as a function of growth processes, the investigation of dynamical and mechanical properties will remain qualitative at the coarse-grained level. In this context, reinserting the atomistic details of the parent simulations at the end of the growth via a back-mapping procedure could be an alternative.

Outside the context of interphase formation the present RMD tool would certainly be adequate to simulate the grafting of polymer brushes from nanoparticles or flat surfaces. Generic models already show how the underlying physics of such processes can be revealed via RMD simulations.[3] Nevertheless, the use of IBI-potentials in such type of growth could allow one to follow the structural evolution of specific polymer brushes at different stages of the growth as a function of the surface initiator density. In fact, the structural configurations of polymer brushes rely on the conformations of the grafted chains and, generally, a relatively good description of such properties can be achieved by IBI-potentials.

## References


[1] M. Tsige, M. J. Stevens, *Macomolecules* **2004**, *37*, 630.

[2] H.-J. Qian, P. Carbone, X. Chen, H. A. Karimi-Varzaneh, C. C. Liew, F. Müller-Plathe, *Macromolecules* **2008**, *41*, 9919.

[3] H. Liu, M. Li, Z.-Y. Lu, Z.-G. Zhang, C.-C. Sun, *Macromolecules* **2009**, *42*, 2863.

# 6. Appendix

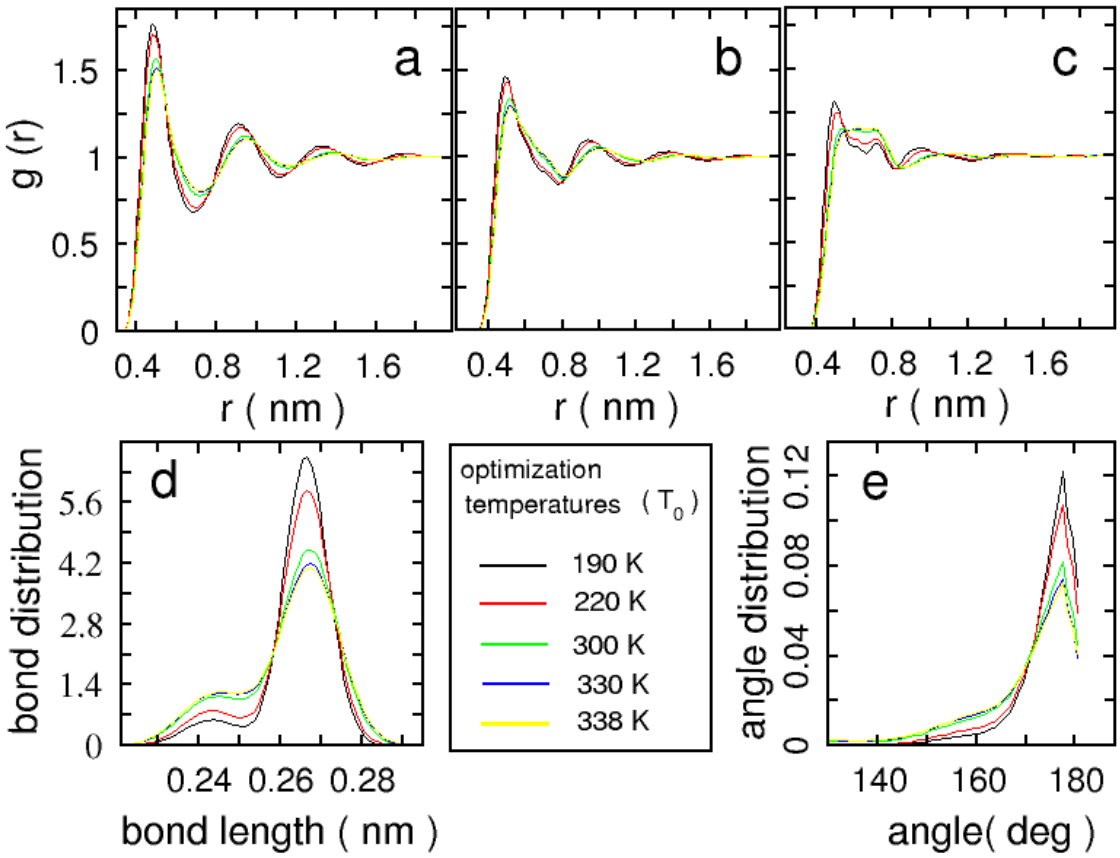


***Figure A.3.1.*** *Target distribution functions calculated from the atomistic trajectories for five different optimization temperatures $T_0$. The mapping scheme employed is displayed in Figure 3.1. of chapter 3. In diagrams a, b and c the target nonbonded radial distributions g(r) between the beads of type 1-1, 1-2 and 2-2 are shown. The target bond and angle functions are displayed in diagrams d and e.*

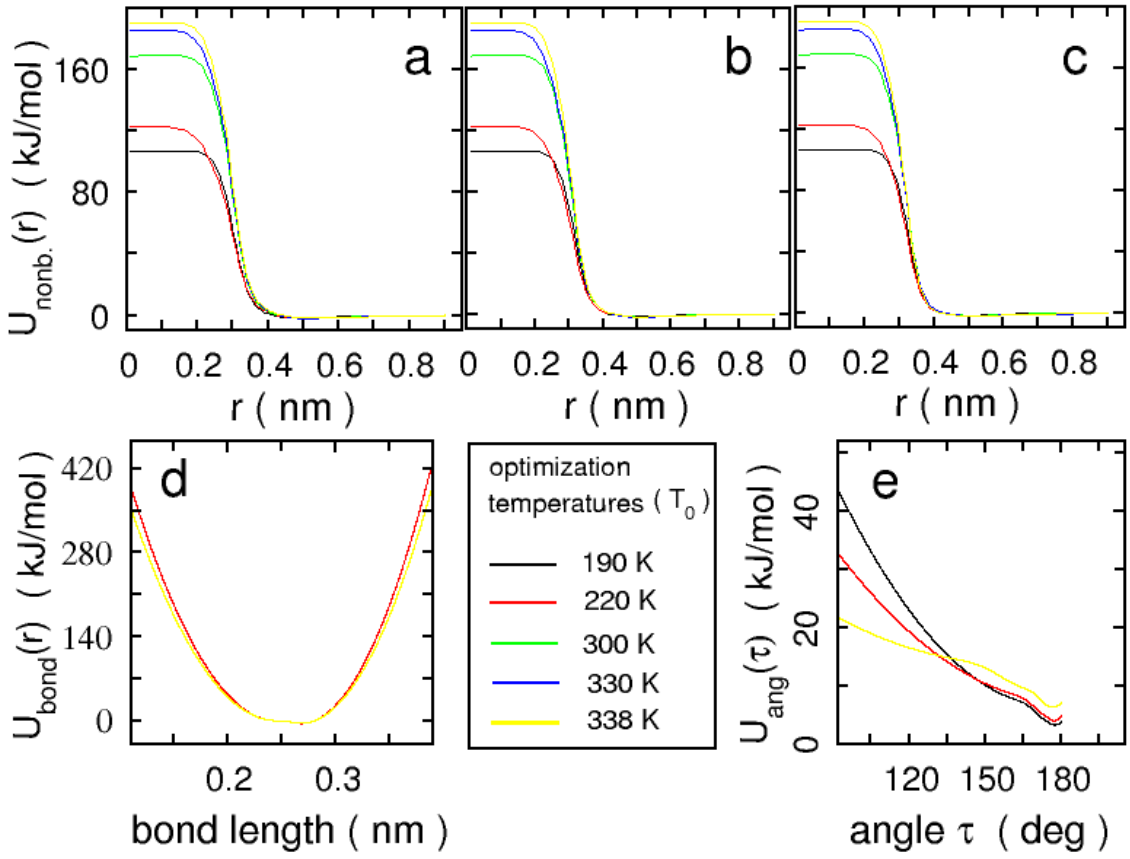


***Figure A.3.2.*** *Coarse-grained potentials resulting from the Iterative Boltzmann Inversion for the five optimization temperatures $T_0$ considered. The mapping scheme employed is displayed in Figure 3.1 of chapter 3. The diagrams a, b and c show the nonbonded potentials between the beads of type 1-1, 1-2 and 2-2. The bond and angle potentials are displayed in diagrams d and e. Note that the potentials in diagram a are different from the ones in b and c (even if this is not completely apparent from the plots). In diagram d the potentials optimized at $T_0$ = 300, 330 and 338 K completely overlap. The same holds for the potentials optimized at 190 and 220 K. In diagram e the overlap is again between the potentials optimized at $T_0$ = 300, 330 and 338 K.*

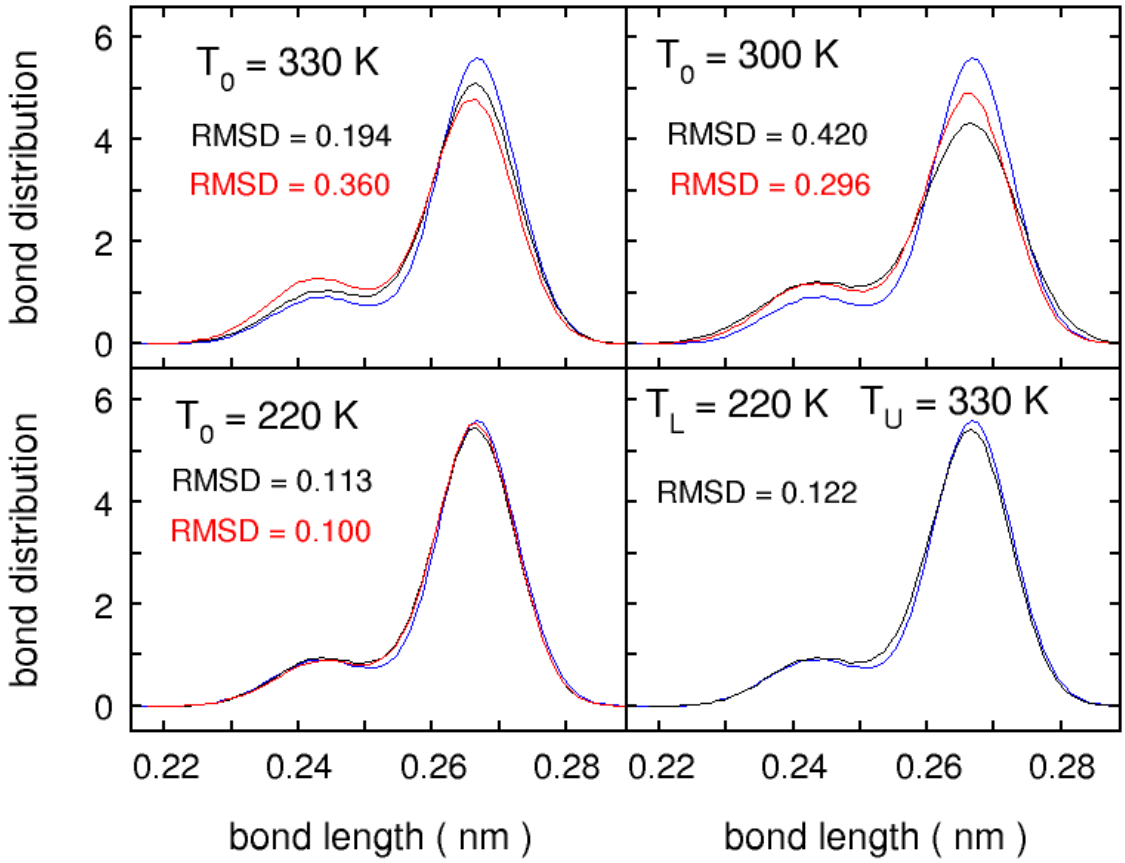


***Figure A.3.3.*** *Comparison between the target bond distribution derived from the atomistic trajectory at T = 240 K and the results of the different scaling methods. The curves are colored according to the coloring scheme in Figure 3.6. of chapter 3. Therefore, the target distribution derived at T = 240 K is plotted in blue in all four diagrams of the figure. The black curve in the bottom-right diagram is the bond distribution resulting from the use of the 2-point interpolation. In the three other diagrams the black curves correspond to the direct use of the potentials (f(T) = 1). The red curves are the output of the simulations in which the best factor f(T) for each $T_0$ has been employed. The RMSD values between the target function and the simulated ones have been symbolized following the coloring scheme defined above.*

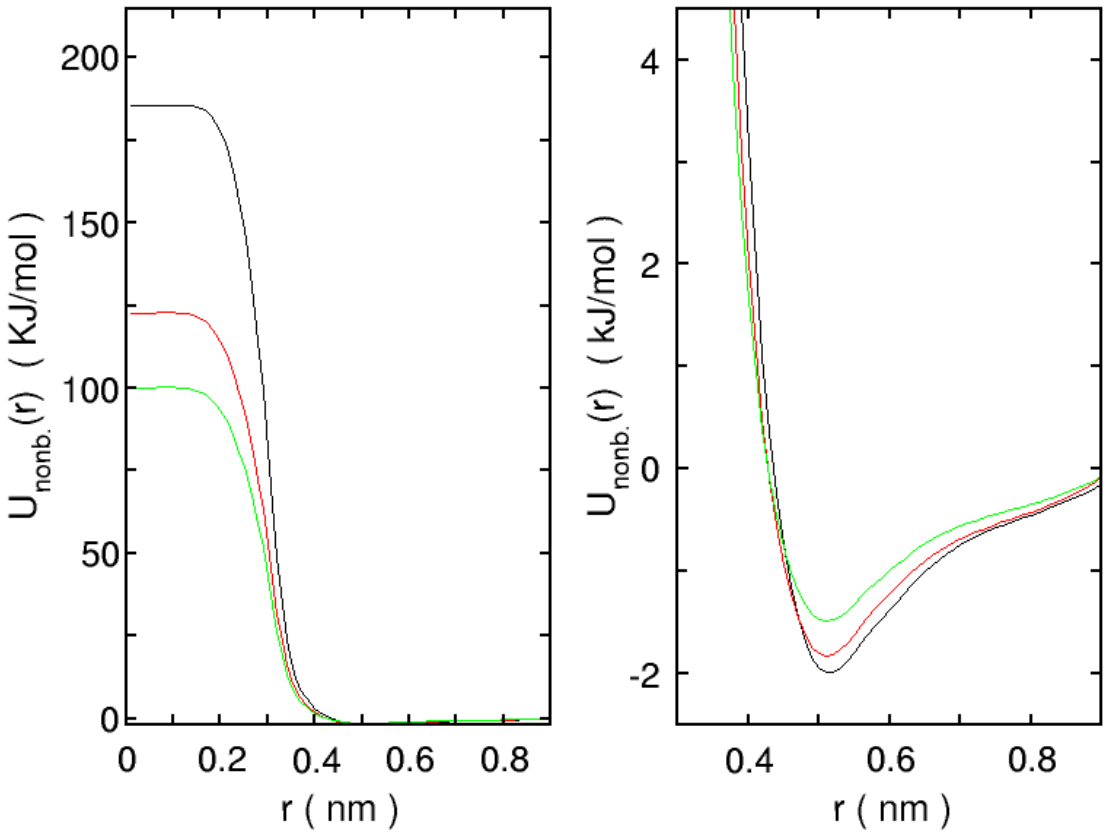


***Figure A.3.4.*** *Effect of the scaling factor* $f(T) = ( T_0 / T )^{1/2}$ *on the nonbonded coarse-grained interaction potential between two beads of type 1 resulting from the IBI optimization. The same potentials are plotted in the left and right diagrams. The right one is zoomed to emphasize the curve shapes in the vicinity of the minimum. The black and red curves are the potentials optimized with the Iterative Boltzmann Inversion at 330 K and 220 K. The green curve is the potential resulting from the scaling process using* $f(T) = ( T_0 / T )^{1/2}$ *with* $T_0 = 220$ *K and* $T = 330$ *K (Equation (3.1) of chapter 3).*

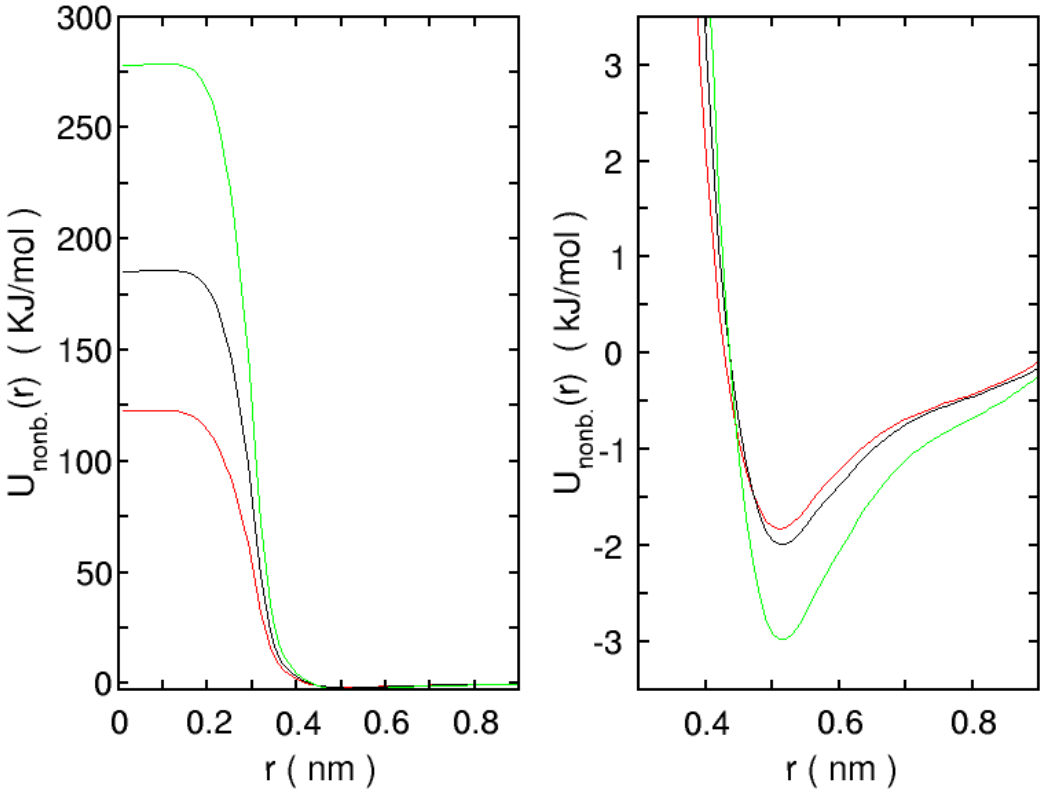


***Figure A.3.5.*** *Effect of the scaling factor f(T) = $T_0$ / T on the nonbonded coarse-grained interaction potential between two beads of type 1 resulting from the IBI optimization. The same potentials are plotted in the left and right diagrams. In analogy with Figure A.3.4 the right one is zoomed. The black and red curves are the potentials resulting from the Iterative Boltzmann Inversion at 330 K and 220 K. The green curve is the potential resulting from the scaling process using f(T) = $T_0$ / T with $T_0$ = 330 K and T = 220 K (Equation. (3.1) of chapter 3).*

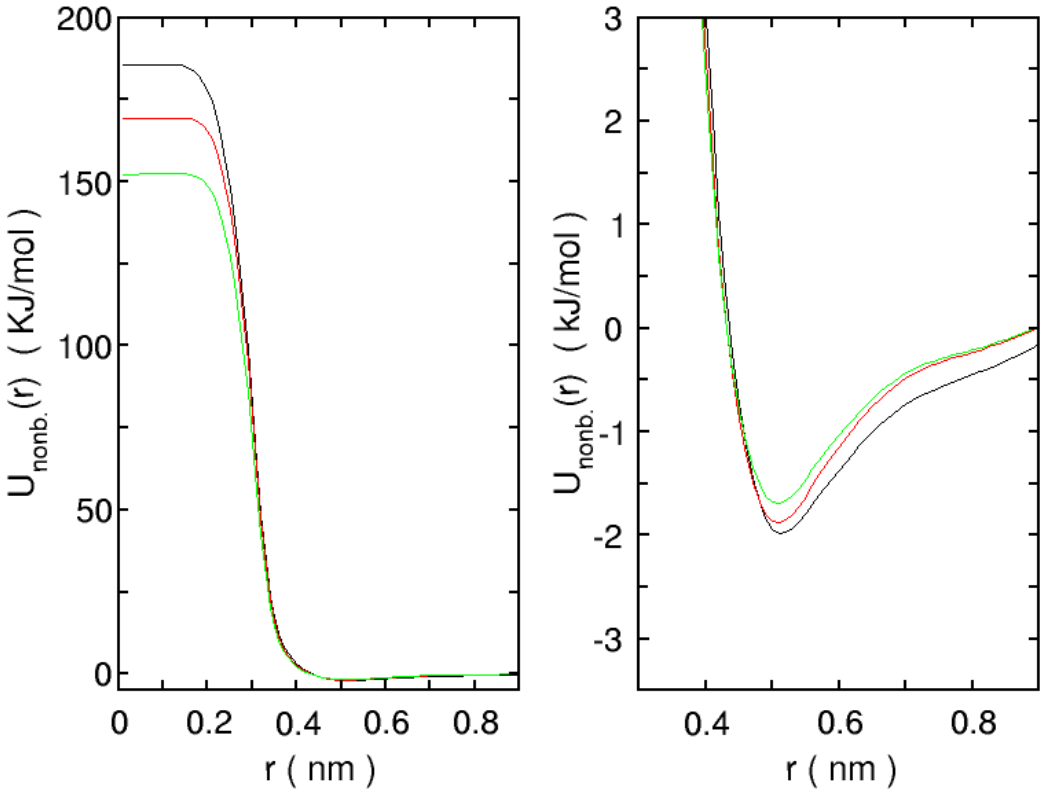


***Figure A.3.6.*** *Effect of the scaling factor f(T) = $T_0$ / T on the nonbonded coarse-grained interaction potential between two beads of type 1 resulting from the IBI optimization. The same potentials are plotted in the left and right diagrams. In analogy with Figure A.3.4 the right one is zoomed. The black and red curves are the potentials resulting from the Iterative Boltzmann Inversion at 330 K and 300 K. The green curve is the potential resulting from the scaling process using f(T) = $T_0$ / T with $T_0$ = 300 K and T = 330 K (Equation. (3.1) of chapter 3).*

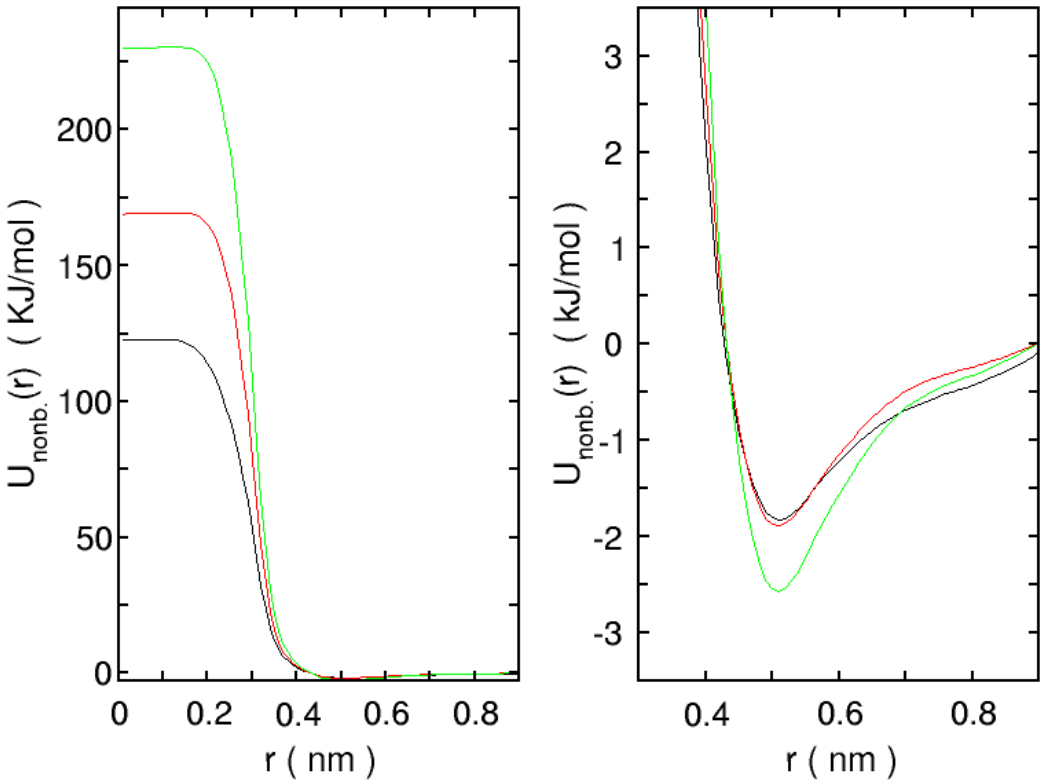


***Figure A.3.7.*** *Effect of the scaling factor on the nonbonded coarse-grained interaction potential between two beads of type 1 resulting from the IBI optimization. The same potentials are plotted in the left and right diagrams. In analogy with Figure A.3.4 the right one is zoomed. The black and red curves are the potentials resulting from the Iterative Boltzmann Inversion at 220 K and 300 K. The green curve is the potential resulting from the scaling process using* $f(T) = T_0 / T$ *with* $T_0 = 300$ *K and* $T = 220$ *K (Equation (3.1.) of chapter 3).*

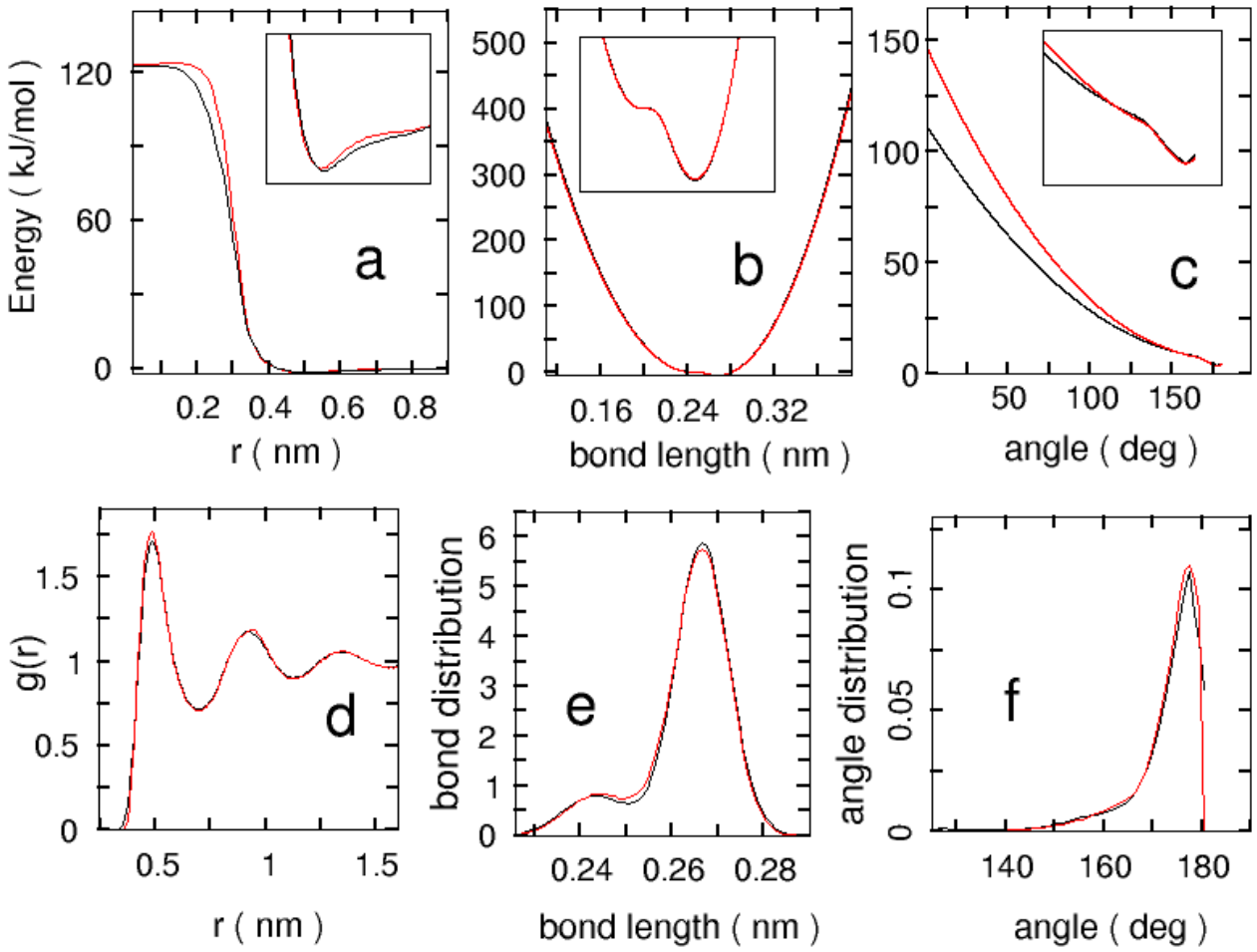


***Figure A.3.8.*** *Comparison between the coarse-grained potentials obtained from the IBI optimization at 220 K (black curves in diagrams a, b and c) and the potentials generated for CG simulations at T = 220 K by the 2-point interpolation with $T_L$ = 190 K and $T_U$ = 338 K (red curves in the diagrams). The energy values of the nonbonded potential for two beads of type 1 (diagram a) and of the bond and angular potentials (b and c) are expressed in kJ/mol. The small pictures inserted in the three diagrams are only a zoom around the minimum of the potentials. In the diagrams d, e and f we have plotted the target distributions associated with the potentials mentioned above. These distributions are derived from the IBI optimization at 220 K (black curves) and from the simulation which has used the CG potentials generated by the 2-point interpolation at T = 220 K (red curves).*

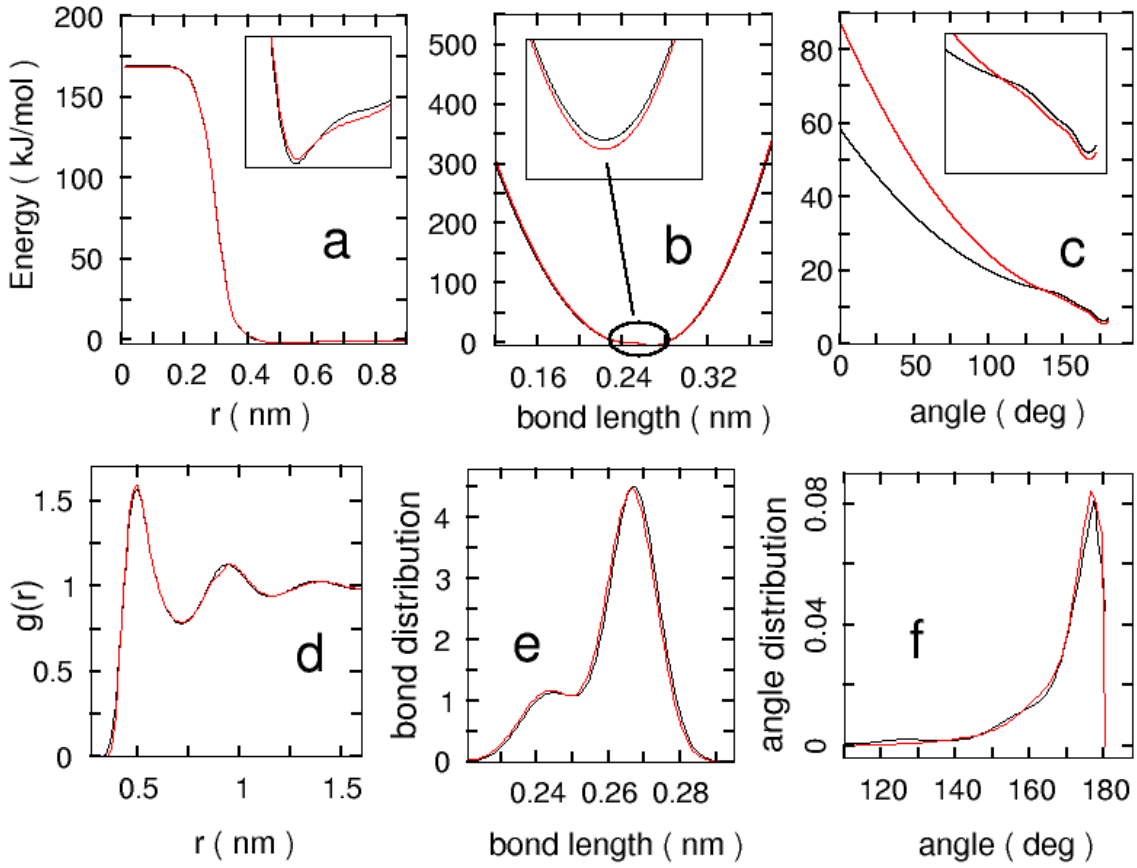


***Figure A.3.9.*** *Comparison between the coarse-grained potentials obtained from the IBI optimization at 300 K (black curves in diagrams a, b and c) and the potentials generated for CG simulations at T = 300 K by the 2-point interpolation with $T_L$ = 190 K and $T_U$ = 338 K (red curves in the diagrams). The energy values of the nonbonded potential for two beads of type 1 (diagram a) and of the bond and angular potentials (b and c) are expressed in kJ/mol. The small pictures inserted in the three diagrams are only a zoom around the minimum of the potentials. In the diagrams d, e and f we have plotted the target distributions associated with the potentials mentioned above. These distributions are derived from the IBI optimization at 300 K (black curves) and from the simulation which has used the CG potentials generated by the 2-point interpolation at T = 300 K (red curves).*

# 7. Simulation Packages and Super-Computers

The molecular dynamics simulation package YASP developed by Prof. Dr. Florian Müller-Plathe [1] has been used to perform all the required atomistic simulations. All equilibrium coarse-graining simulations have been performed with the IBIsCO package developed in the group of Prof. Dr. Florian Müller-Plathe by Dr. Hossein Ali Karimi-Varzaneh. [2] The Reactive Molecular Dynamics tool [3] developed for the purpose of the present PhD thesis is an extended version of the IBIsCO package.

The simulations have been run on two clusters supplied by the companies TRANSTEC and RAID MEDIA. They are both located in the theoretical physical chemistry group of Prof. Dr. Florian Müller-Plathe. We are grateful to the SPP1369 priority program on “Polymer-solid contacts: Interphases and Interfaces” for the financial support of the RAID MEDIA cluster. The present PhD project has been achieved in the framework of this priority program.

## References

[1] F. Müller-Plathe, *Comput. Phys. Commun.* **1993**, *78*, 77.

[2] H. A. Karimi-Varzaneh, H.–J. Qian, X. Chen, P. Carbone, F. Müller-Plathe, *J. Comput. Chem.*, **2011**, *32*, 1475.

[3] K. Farah, H. A. Karimi-Varzaneh, F. Müller-Plathe, M. C. Böhm, *J. Phys. Chem. B* **2010**, *114*, 13656.

# 8. Publications

The present PhD project has led to published articles [1-3], to a recently submitted review [4] and to an article that is currently in preparation [5]. The publications [1-3] and the submitted review [4] are presented in the dissertation.


[1] K. Farah, H.A. Karimi-Varzaneh, F. Müller-Plathe and M.C. Böhm, *J. Phys. Chem. B,* **2010**, *114*, 13656.

[2] K. Farah, A. C. Fogarty, M. C. Böhm and F. Müller-Plathe, *Phys. Chem. Chem. Phys.*, **2011**, *13*, 2894.

[3] K. Farah, F. Leroy, F. Müller-Plathe and M.C. Böhm, *J. Phys. Chem. C* **2011**, *115*, 16451.

[4] K. Farah, F. Müller-Plathe and M.C. Böhm, *ChemPhysChem, "Classical Reactive Molecular Dynamics Implementations: State of the Art "*, ***submitted to the editorial office.***

[5] K. Farah, M. Langeloth, M.C. Böhm and F. Müller-Plathe, *'Epoxy-like Curing and Surface-Induced Interphases: Reactive Coarse-Grained Molecular Dynamics Simulations'****, in preparation for the Journal of Adhesion.***

# 9. Financial Support

I am grateful to the "*Deutsche Forschungsgemeinschaft*" (DFG) organism that has funded the priority program SPP1369 on *"Polymer-solid contacts: Interphases and Interfaces"* to which the present PhD project belongs. I would like to thank the organization committee of this priority program for giving the opportunity to PhD students to perform oral and poster presentations during the annual meetings and for organizing summer schools.

# Acknowledgements

I am very grateful to my supervisor Prof. Dr. Florian Müller-Plathe who offered me the chance to do a PhD thesis. His knowledge, patience, and energy have been crucial during my PhD time. I have enjoyed our scientific discussions; they have been for me a rich source of information. He always motivates PhD students to take up new challenges and this has been, for me, a source of continuous professional and personal improvements.

Thanks to Prof. Dr. Nico Van der Vegt who has accepted to be the co-referent of my PhD dissertation. His questions and comments during our joined weekly seminars have also been a rich source of learning. Thanks to Prof. Dr. Berger and Prof. Dr. Stühn for participating as referees at the oral presentation.

My deep gratitude goes to Prof. Dr. Michael C. Böhm for the daily attention that he has given to me. He has been, for me, more than a supervisor. I have really enjoyed our collaboration. Our scientific discussions and his guidance have been crucial. I would like to thank him for his generosity and the time that he has taken to help me improve in many areas. I would also like to thank S. Philipp for taking the time to read and improve the first chapter of the dissertation.

Many thanks to Dr. Frédéric Leroy for the theoretical and technical supports that he has brought to me all along my PhD time and for the moments that we have shared during three years. The presence of Dr. Hossein Ali Karimi-Varzaneh has also been important; building-up the reactive tool would have been a much more tedious process without his support. I would like to thank also Dr. Thomas Mueller and Dr. Volker Weiss for their assistance at the very beginning of my thesis and the warm atmosphere of the office that we shared.

The patience of Jessica Ahluwalia and Kristin Adolph in dealing with some of our administrative issues is really appreciable; thanks to them.

My deep gratitude is addressed to my colleague and friend Tinashe Ndoro for our discussions on several topics and the nice relationship that we have maintained for more than two years. He gave an ear to me each time that it has been necessary. Finally, I would like to thank all my colleagues for the different moments that we have shared during these years.

As no achievement is possible without the presence of family and friends, I address a special thanks to my friends that are in Strasbourg.

Many thanks to my uncle and aunt for taking care of me and my brothers when we arrived in Strasbourg for our university studies.

There is no word to express what a son owes to his parents; to mine I just want to tell that they are wonderful parents for me. The same holds for my two brothers. They all belong to the best parts of my life.

An important person for me during these last years is certainly my girl-friend. Without her my PhD time would have been lonely during the week-ends. She is the person who has really suffered me during the difficult periods and also shared the exciting moments. I would like to express how much her presence, patience, and kindness have been important to me during these last years.

# Curriculum Vitae

**Name:** karim Frédéric

**Last Name:** FARAH

**Place of Birth:** Dakar (Sénégal)

**Date of Birth:** 02/10/1982

**Nationality:** French

**Education**

**1998-2001:** "Cours Sainte-Marie de Hann" high school of Dakar.

**2001-2004:** "Louis Pasteur" University of Strasbourg.

**2004-2006:** "Louis Pasteur" University of Strasbourg.

**2008-2011:** PhD student in theoretical physical chemistry, Technical University of Darmstadt, Germany.

_____

(Karim Frédéric Farah)

Karim Frédéric Farah
Bleichstr. 30
64283 Darmstadt
Germany

Darmstadt, Montag, den 12. September 2011

# Erklärung

Ich erkläre hiermit, noch keinen Promotionsversuch unternommen zu haben.

_____

(Karim Frédéric Farah)

Karim Frédéric Farah
Bleichstr.. 30
64283 Darmstadt
Germany

Darmstadt, Montag, den 12. September 2011

# Eidesstattliche Erklärung

Ich erkläre hiermit an Eides Statt, dass ich meine Dissertation selbständig und nur mit den angegebenen Hilfsmitteln angefertigt habe.

_____

(Karim Frédéric Farah)